Cai Tian

# Numerical studies of viscous flow around step cylinders

Doctoral thesis

Cai Tian

**NTNU**
Norwegian University of
Science and Technology

**NTNU**
Norwegian University of
Science and Technology

Cai Tian

# Numerical studies of viscous flow around step cylinders

Thesis for the degree of Philosophiae Doctor

Trondheim, March 2021

Norwegian University of Science and Technology
Faculty of Engineering
Department of Marine Technology

**NTNU**
Norwegian University of
Science and Technology

PRINTED IN
NORWAY
NO - 1598

NORDIC SWAN ECOLABEL
Printed matter
2041 0731

# Contents

# Abstract

A step cylinder consists of a small diameter cylinder ($d$) attached coaxially to a large diameter cylinder ($D$). Structures with a similar shape as the step cylinder have been extensively used in many marine engineering applications, for example, the underwater hull of a semi-submersible offshore platform, the supporting structures for a floating wind turbine, and the marine riser with staggered buoyance elements. In recent years, there has been an increasing interest in the flow around step cylinders. Previous studies investigated dominating vortex cells in step cylinder wakes, the vortex interactions between them, and the force distributions on the surface of step cylinders. However, there has been little discussions about the formation mechanism and detailed process of vortex interactions, the diameter ratio ($D/d$) effects in the wake, and the vortex system around the step cylinder under a sub-critical Reynolds number ($Re_D$). To focus on these aspects, in the present thesis, the flow around step cylinders with diameter ratios $2 \leq D/d \leq 3$ at two Reynolds numbers $Re_D$=150 and 3900 were investigated by directly solving the three-dimensional Navier-Stokes equations.

The new findings can be mainly divided into two parts. In the first part, we investigated the vortex interactions in the wake behind step cylinders with $2 \leq D/d \leq 3$ at $R_D$=150. Two types of N-cell cycles: the long N-cell cycle, and the fundamental N-cell cycle, were first identified beside the conventional N-cell cycle. Moreover, two newly observed vortex loop structures were observed to antisymmetrically or symmetrically appear between the neighboring N-cell cycles in a long N-cell cycle. After developing a reliable method that can be used to calculate the phase information of vortices, the vortex interactions, especially the vortex dislocations were analyzed in detail. A vortex dislocation mechanism, together with its effects in the newly identified symmetric and antisymmetric vortex interactions, were described.

In the second part, the flow around a step cylinder with $D/d$=2 at $Re_D$=3900 was investigated. Four horseshoe vortices were observed to form

vii

above the step surface in front of the upper small cylinder in the time-averaged flow. Their developments were analyzed. Moreover, a pair of base vortices and a backside horizontal vortex in the rear part of the step surface behind the small cylinder were captured. For the instantaneous flow, hairpin vortices were found to form between the legs of two counter-rotating horseshoe vortices located on the same side of the step cylinder. Furthermore, in the small cylinder wake, Kelvin-Helmholtz vortices were observed to shed at an unexpectedly high shedding frequency.

The present thesis contributes a deeper and more complete physical understanding of the wake behind step cylinders.

# Preface

This thesis is submitted to the Norwegian University of Science and Technology (NTNU) for partial fulfillment of the requirements for the degree of philosophiae doctor.

# Acknowledgment

First of all, I would like to express my deepest gratitude to my supervisor, Professor Bjørnar Pettersen, for his patient guidance, warm care, and continuous encouragement throughout my whole PhD study. Under his guidance and support, I become an self-motivated researcher with logical and critical thinking. His rich experiences have always provided valuable comments for all the scientific papers published during my PhD study. Furthermore, his optimistic and energetic attitudes toward life also provide a remarkable example of my daily work.

I also greatly appreciate my co-supervisor Professor Helge Ingolf Andersson. He is kind and supportive but also critical of all research problems. He provided countless valuable and constructive suggestions on both the theoretical and scientific writing aspects of all my papers. Sincere thanks are extended to my co-supervisor Doctor Fengjian Jiang. With his patience, enthusiasm, and solid background knowledge about the bluff body wakes, we had many insightful discussions. When I met problems, his valuable and quick responses helped me a lot. My gratitude also goes to Doctor Håkon Strandenes, for his strong support of installing the hardware and implementing software code.

Special thanks go to Shuaishuai Wang and Jianxun Zhu for many enjoyable moments at basketball court, tyholt billiard room and gym. I would also like to express my appreciation all my friends for making this long study trip a fun and pleasant experience.

Finally, I am truly grateful to my parents Lijuan Peng and Daiyou Tian, and my fiancee Zijing Cao. They have always encouraged and supported me to overcome difficulty and pursue my dreams. Their love and understanding mean everything to me.

<div align="right">

Cai Tian
January 2021
Trondheim, Norway

</div>

# Publication List

**List of Appended Articles**

**Article 1:**
Tian C, Jiang F, Pettersen B, Andersson HI. Numerical investigation of flow around a step cylinder. *Proceedings of 9th National Conference on Computational Mechanics (CIMNE), Trondheim, Norway, May 11-12*, 2017; 369-384.

**Article 2:**
Tian C, Jiang F, Pettersen B, Andersson HI. Antisymmetric vortex interactions in the wake behind a step cylinder. *Physics of Fluids*, 2017; **29**(10): 101704.

**Article 3:**
Tian C, Jiang F, Pettersen B, Andersson HI. The long periodicity of vortex dislocations in the wake behind a step cylinder. *Proceedings of 10th National Conference on Computational Mechanics (CIMNE), Trondheim, Norway, June 3-4*, 2019; 81-99.

**Article 4:**
Tian C, Jiang F, Pettersen B, Andersson HI. Vortex dislocation mechanisms in the near wake of a step cylinder. *Journal of Fluid Mechanics*, 2020; **891**.

**Article 5:**
Tian C, Jiang F, Pettersen B, Andersson HI. Diameter ratio effects in the wake flow of single step cylinders. *Physics of Fluids*, 2020; **32**(9): 093603.

**Article 6:**
Tian C, Jiang F, Pettersen B, Andersson HI. Vortex system around a step cylinder in a turbulent flow field. *Accepted for publication in Physics of*

*Fluids, DOI: 10.1063/5.0041234.*

# Chapter 1

# Introduction

## 1.1 Viscous flow around a circular cylinder in steady flow

Cylindrical structures are widely used in the marine offshore industry, for example, the hull of a Spar platform [1] and deep-water risers [2]. As flow separates from a cylindrical structure's surface, the subsequent well-known vortex shedding generates significant flow-induced periodic loading on the structure. Consequently, wake flow around circular cylinders has been a popular research topic for engineers and scientists for decades. In this section, a brief review of flow around a circular cylinder is described.

### 1.1.1 Flow regimes around a circular cylinder

To describe the flow around a circular cylinder, a governing non-dimensional parameter, namely the cylinder Reynolds number, is introduced:

$$Re_D = \frac{UD}{\nu},\tag{1.1}$$

where $U$ is the flow velocity, $D$ represents the diameter of the cylinder, and $\nu$ is the kinematic viscosity. The wake flow tremendously changes when $Re_D$ increases from zero. The detailed information about the flow regimes at different regimes of $Re_D$ is shown in Figure 1.1.

One can see that, when $Re_D$ is less than 5 (Figure 1.1 (a)) there is no flow separation around the cylinder. As the Reynolds number increases to the range $5 < Re_D < 40$ (Figure 1.1 (b)), the flow separates on the cylinder wall to form a fixed pair of vortices behind the cylinder, and there is no vortex shedding. For $40 < Re_D < 200$ (Figure 1.1 (c)), periodic two-dimensional vortex shedding occurs, i.e., the vortex street does not vary
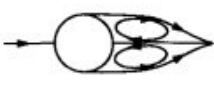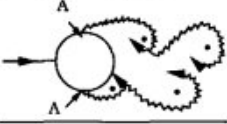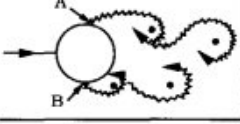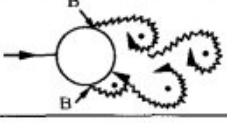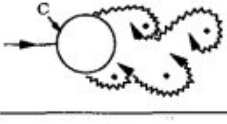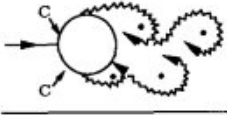
| | Description | Reynolds number |
|---|---|---|
| a) | No separation. Creeping flow | Re < 5 |
| b) | A fixed pair of symmetric vortices | 5 < Re < 40 |
| c) | Laminar vortex street | 40 < Re < 200 |
| d) | Transition to turbulence in the wake | 200 < Re < 300 |
| e) | Wake completely turbulent. A:Laminar boundary layer separation | $300 < Re < 3 \times 10^5$ Subcritical |
| f) | A:Laminar boundary layer separation B:Turbulent boundary layer separation;but boundary layer laminar | $3 \times 10^5 < Re < 3.5 \times 10^5$ Critical (Lower transition) |
| g) | B: Turbulent boundary layer separation;the boundary layer partly laminar partly turbulent | $3.5 \times 10^5 < Re < 1.5 \times 10^6$ Supercritical |
| h) | C: Boundary layer completely turbulent at one side | $1.5 \times 10^6 < Re < 4 \times 10^6$ Upper transition |
| i) | C: Boundary layer completely turbulent at two sides | $4 \times 10^6 < Re$ Transcritical |

Figure 1.1: Regimes of flow around a smooth, circular cylinder in steady current (Images reproduced from Sumer and Fredsøe [4]).

in the spanwise direction [3]. As $Re_D$ exceeds 200, the wake flow starts to transit into turbulent. Gerard and Williamson [3] reported distinctly three-dimensional vortex shedding at $200 < Re_D < 300$.
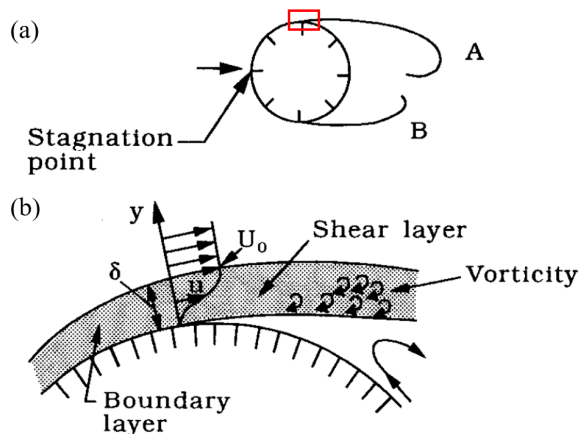
Figure 1.2: (a) Schematic sketch illustrating flow around the circular cylinder. (b) A zoom-in sketch of flow near the separation region highlighted by the red rectangular in (a) (Images reproduced from Sumer and Fredsøe [4]).

When the Reynolds number becomes larger than $Re_D \approx 300$, the cylinder wake flow becomes completely turbulent as shown in Figure 1.1 (e). In the meantime, the boundary layer over the cylinder surface stays laminar in a wide Reynolds number regime $300 < Re_D < 2 \times 10^5$, which is known as the subcritical flow regime. As $Re_D$ further increases, the region of transition to turbulence first occurs at the separation point in Figure 1.1 (f) at $3 \times 10^5 < Re_D < 3.5 \times 10^5$. Then it moves upstream toward the stagnation point when $Re_D$ continues to increase.

The boundary layer and wake flow of the circular cylinder become completely turbulent at $Re_D > 4.5 \times 10^6$, which is referred to as the transcritical regime.

### 1.1.2  Vortex shedding

For all the flow regimes when $Re_D > 40$ (Figure 1.1), one dominating phenomenon is the vortex shedding. Sumer and Fredsøe [4] concluded that, due to the adverse pressure gradient caused by the divergent flow at the rear side of the cylinder, the boundary layer over the cylinder surface would separate. As a consequence, a shear layer is formed. As shown in Figure 1.2, the velocity distribution in the boundary layer along the cylinder surface creates a significant amount of vorticity. When this vorticity convects into the shear layer formed downstream of the separation point, it causes the shear layer to roll up into a vortex with the same sign compared to that of
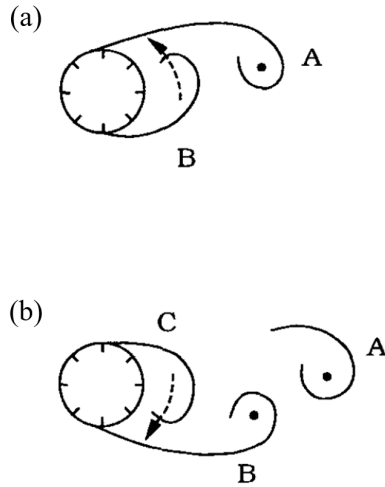
*Figure 1.3: (a) Prior to shedding of Vortex A, Vortex B is being drawn across the wake. (b) Prior to shedding of Vortex B, Vortex C is being drawn across the wake (Images reproduced from Sumer and Fredsøe [4]).*

the incoming vorticity.

The vortex shedding process behind a circular cylinder was first systematically described by Gerrand [5]. According to his research, when the small disturbances are introduced to the flow around a circular cylinder at $Re_D > 40$, the vortex at one side of the cylinder will grow larger than the other side vortex. Then the alternative vortex shedding follows. As shown in Figure 1.3 (a), when Vortex A becomes larger and stronger, it draws the oppositely rotating Vortex B across the wake. The vorticity in Vortex A is in the clockwise direction as indicated in Figure 1.2, while that in Vortex B is in the anti-clockwise direction. As Vortex B approaches to Vortex A, it will cut off the further supply of vorticity from the boundary layer to Vortex A, and further cause Vortex A to shed. Then Vortex A convects downstream as a free vortex. After Vortex A shed from its shear layer, a new vortex (Vortex C) forms at the same side of the cylinder in Figure 1.3. Now, the size and strength of Vortex B will increase. It plays the same role as Vortex A did. Therefore Vortex C will be drawn across the wake and finally lead to Vortex B's shedding. This shedding process will continue to occur alternatingly between the sides of the cylinder.

To describe the vortex shedding behind a circular cylinder, the normalized vortex shedding frequency, namely the Strouhal number ($St$) is
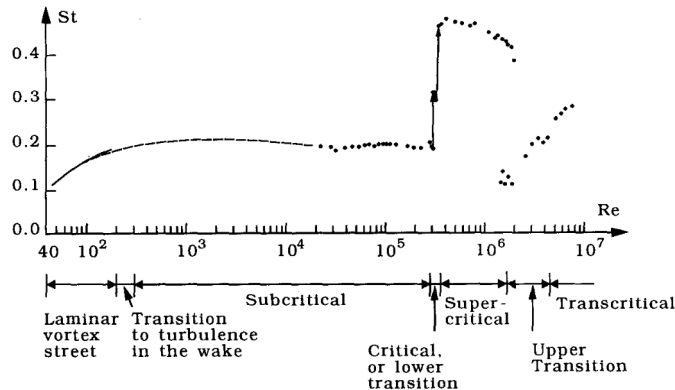
*Figure 1.4: Strouhal number for a smooth circular cylinder. The solid curve is from Williamson [3]. The dashed curve is from Roshko [6]. The dotted curve is from Schewe [7]. (This image reproduced from Sumer and Fredsøe [4]).*

introduced:

$$St = \frac{f_v D}{U}, \tag{1.2}$$

where $f_v$ is the vortex shedding frequency, $D$ is the diameter of the circular cylinder, and $U$ is the velocity of the steady current. Figure 1.4 shows how the Strouhal number varies with the Reynolds number.

## 1.2   Vortex shedding behind step cylinders

Besides the uniform cylindrical structures, the structures with a similar shape of the step cylinder illustrated in Figure 1.5 have been used in many engineering applications, for example, the underwater hull of a semisubmersible offshore platform, the underwater support structure of a spar floating wind turbine (Figure 1.6 (a)), and the steel lazy wave risers (Figure 1.6 (b)). In recent years, the flow around step cylinders has drawn a lot of attention.

For a long step cylinder, there are two important parameters for the flow past a single step cylinder, i.e., the Reynolds number $Re_D$ and the diameter ratio ($D/d$). $D/d$ is the ratio between the large- and small-diameter parts of the step cylinder, and $Re_D$ is the Reynolds number introduced in Equation 1.1. The first systematic investigation of the wake flow behind a single step cylinder is given by Lewis and Gharib [9]. Based on experimental analyses in the wake of step cylinders with $1.44 < D/d < 1.76$ at $67 < Re_D <$
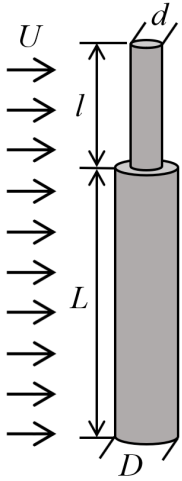
*Figure 1.5: A sketch of step cylinder geometry used in Article 1 ∼ 6 in the present thesis. The diameter of the small and large cylinders are d and D, respectively. l and L denote the length of the small and large cylinders, respectively.*

200, they first defined three main vortex interaction modes: a *direct mode* when $D/d < 1.25$, a *indirect mode* when $D/d > 1.55$, and a *transition mode* when $1.25 < D/d < 1.55$. In the *direct mode*, vortices shed from the small cylinder directly interact with those from the large cylinder in a narrow region, which is referred to as the interface. While in the *indirect mode*, one more frequency $f_3$ (which is referred to as $f_N$ in the present work) was identified in a so-called modulation zone, in which no direct interaction was found between vortices with $f_S$ and $f_L$. Figure 1.7 (a) and (b) illustrate the *direct* and *indirect modes*, respectively. Meanwhile, Lewis and Gharib [9] mentioned that the corresponding regions of $D/d$ to the different vortex interaction modes varied with the varying Reynolds number. In 2006, Dunn and Tavoularis [10] validated the *indirect mode* through experimental investigations in the wake of a step cylinder with $D/d \approx 2$ at $63 \leq Re_D \leq 1100$. Based on the three dominating shedding frequencies, they identified three types of spanwise vortex cells: (1) S-cell vortex with the highest shedding frequency $f_S$ behind the small cylinder, (2) L-cell vortex shed from the large cylinder with shedding frequency $f_L$, and (3) N-cell vortex with the lowest shedding frequency $f_N$ located between the S- and L-cell regions. The terminologies S-, N-, and L-cell vortices were thereafter adopted in many studies [11, 12, 13] and are also used in all articles included in the present thesis. The regions where these three vortex cells occur are indicated in Figure 1.7.

The formation of the N-cell vortex is an essential feature in the wake behind the step cylinder. The N-cell vortex has the lowest shedding frequency among the three dominating vortex cells, i.e., the S-, N- and L-cell vortices.
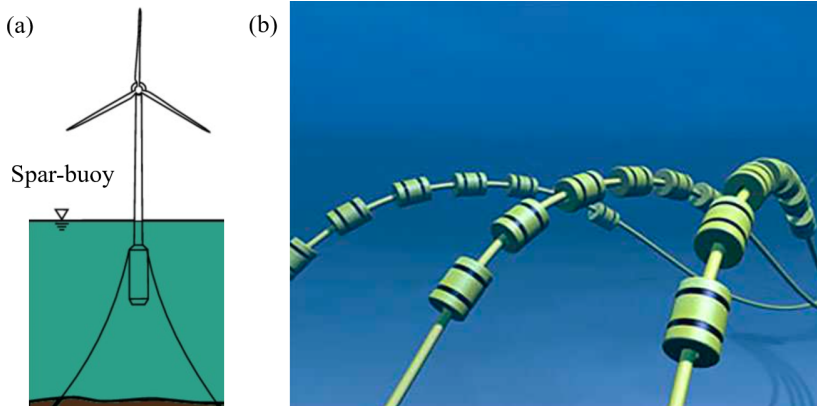
Figure 1.6: (a) A sketch of the SPAR-buoy floating offshore wind turbine [8]. (b) A typical view of steel lazy wave risers (SLWR) (Retrieved from: https:www.kongsberg.com).
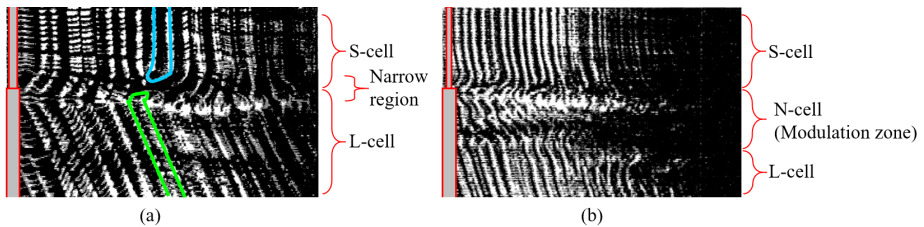


Figure 1.7: (a) Flow visualization of the direct mode at Reynolds number $Re_D = 76$ for the diameter ratio $D/d=1.34$. The S-S and L-L half-loop structures are marked by the blue and green curves, respectively. (b)Flow visualization of the indirect mode at Reynolds number $Re_D = 99$ for the diameter ratio $D/d=1.76$. Images reproduced from Lewis and Gharib [9].

Similar low-frequency cells were also observed in the wake behind several other configurations, e.g., the wake behind a free-end cylinder [14], the wake behind a circular cylinder with flat end-plat [3], and the wake behind a concave curved cylinder [15]. The previous studies [3, 10, 12, 16] attributed the appearances of such low-frequency cells (N-cell-like vortex) to 3D effects, which include mainly two mechanisms: downwash and increased base pressure. Bearman [17] and Williamson [3] found that the increased base pressure could increase the vortex formation region and cause the vortex shedding frequency to decrease. Zdravkovich [16] and Williamson [3] found that the spanwise velocity (downwash) could not merely displace the vortex formation region further downstream but also widen the separated shear
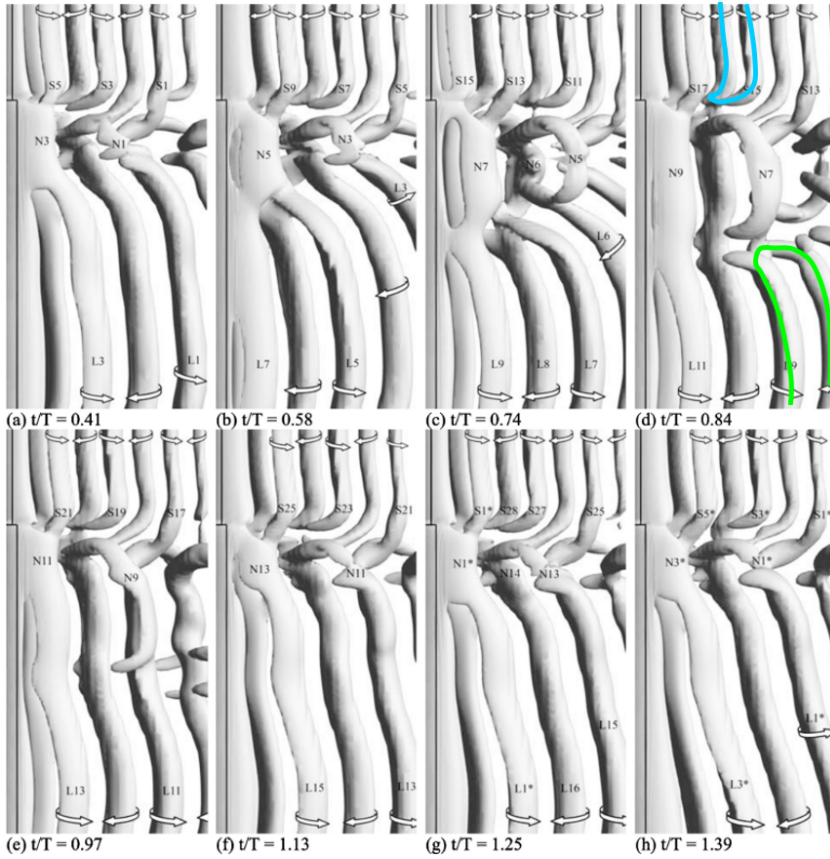
Figure 1.8: Isosurfaces of $Q = 2 \times 10^{-3}$ showing vortex structures' development in the wake behind a step cylinder with $D/d = 2$ at $Re_D = 150$. $T$ is the period of one N-cell cycle. In (d) the S-S and L-L half-loop structures are marked by the blue and green curves, respectively. Images reproduced from Morton and Yarusevych [11].

layers before they roll up into vortices. These effects would also decrease the vortex shedding frequency. For the wake behind the step cylinder, by doing experiments and numerical simulations, Dunn & Tavoularis [10] and Morton & Yarusevych [12] also suggested that the 3D effect is a plausible explanation of the formation of the N-cell vortex.

Besides the formation mechanism of the N-cell vortex, Morton and Yarusevych [11] further defined a cyclic feature in N-cell shedding. They found that the spanwise extension of N-cell vortices sharply decreases after the vortex dislocation occurs between the N- and L-cell vortices. Then the

spanwise extension of the following N-cell vortices increases again until the next vortex dislocation happens. They defined this cyclic change in the spanwise length of N-cell vortices as the N-cell cycle. As an example, in the N-cell cycle shown in Figure 1.8 (a), (b), (c), and (d), the length of the N-cell vortices increases from N3 to N9. After the vortex dislocation occurs in Figure 1.8 (d) and (e), at the beginning of the subsequent N-cell cycle. the length of N13 (Figure 1.8 (f)) is clearly smaller than that of N9 (Figure 1.8 (e)).

## 1.3    Vortex dislocation

The phrase *vortex dislocation* was first introduced by Williamson [3] when he investigated multiple vortex cells with different shedding frequencies in his experiments of flow past a circular cylinder at $Re_D < 200$. Neighboring vortex cells were observed to move either in-phase or out-of-phase with each other due to their different shedding frequencies. When these vortex cells move out of phase, at the boundary between them, the contorted 'tangle' of vortices appears and looks like dislocations that occur in solid materials. Williamson [3] defined this kind of flow phenomenon as *vortex dislocation*. He reported that, at $Re_D = 100$, vortex dislocations occur at the boundary between vortex cells (the end-plate cell of frequency $f_e$ and the single cell of frequency $f_L$) at a constant beat frequency $f_L - f_e$, accompanied by an obvious minimum amplitude of the velocity fluctuations at the boundary. In addition, the time trace of phase differences was plotted by comparing velocity signals from different vortex cell regions. In 1992, Williamson [18] further investigated the dislocation by adding a small 'ring' on a circular cylinder to force the dislocation to happen. This study revealed more detailed features of vortex dislocations, such as the vortex dynamics and the effects of vortex dislocations in the wake flow.

Behind step cylinders, vortex dislocations appear in the wakes with both the *direct* and the *indirect modes*. For the *direct mode*, Lewis and Gharib [9] found that, when S- and L-cell vortices are in phase, they connect to each other one by one across the interface. However, due to their different shedding frequencies, the phase difference between the corresponding S- and L-cell vortices gradually increases. When they become out of phase, the direct connection will be interrupted. At the same time, as shown in Figure 1.7 (a), the S-S and L-L half-loop connections form between oppositely rotating S-cell vortices and L-cell vortices, respectively. The period between two such interruptions is called a *beat cycle*. The corresponding beat frequency can be calculated as $f_S$-$f_L$. The similar vortex dislocations

and half-loop structures were also observed in Ref. [19].
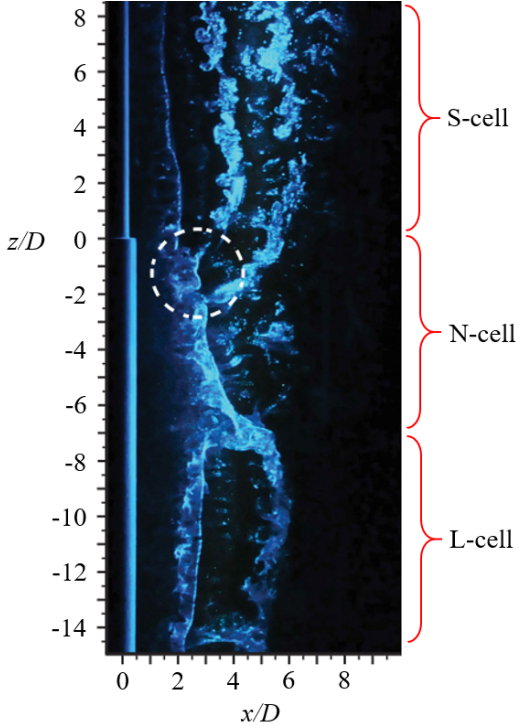


Figure 1.9: A hydrogen bubble flow visualization image showing vortex structures in the wake behind the step cylinder with $D/d = 2$ at $Re_D = 1050$. The S-, N-, and L-cell vortices are indicated. The white dashed circle marks the vortex dislocation between the S- and N-cell vortices. Image reproduced from Morton and Yarusevych [13].

For the *indirect mode*, the vortex dislocation was mainly investigated in the wake behind a single step cylinder with $D/d = 2$ at $Re_D \approx 150$ in Refs. [10, 11]. These studies concluded that the S-N cell boundary (the region between the S- and N-cell vortices) is stable and slightly deflects spanwise to the large cylinder direction. At this boundary, the vortex dislocations between the S- and N-cell vortices occur at a beat frequency $f_S$-$f_N$. One N-cell vortex always splits into two filaments in this dislocation process. One of these filaments connects to a counter-rotating N-cell mate, and the other connects to a S-cell vortex. The rest of the S-cell vortices that have no connection with N-cell vortices form the S-S half-loop structures (the blue curve in Figure 1.8 (d)). Unlike the S-N cell boundary, due to the N-cell vortex's length varies during one N-cell cycle [12], the N-L cell boundary (the region between the N- and L-cell vortices) is unstable. When the phase difference between the corresponding N- and L-cell vortices is small, every L-cell vortex directly connects to its counterpart N-cell vortex. As the corresponding N-L vortex pair gradually becomes out of phase, in parallel with the appearance of vortex dislocations, the spanwise extensions of the N-cell vortices and the position of the N-L cell boundary vary periodically with a

beat frequency $f_N$-$f_L$. During the vortex dislocation, half-loop connections form between the L-cell vortices (the green curve in Figure 1.8 (d)). Furthermore, as presented in Figure 1.9, Morton and Yarusevych [13] showed that even in the wake behind a step cylinder with $D/d = 2$ at a higher Reynolds number $Re_D = 1050$, similar vortex cells and vortex dislocations can be found.

An interesting long-period characteristic of the vortex dislocation was first reported by McClure et al. [20] based on investigating flow past dual step cylinders. They defined the period between two identical vortex dislocations as the fundamental dislocation cycle. Vortex dislocations in other types of wakes and mixing layers have been reported by many others. For details, the reader is referred to the works of Refs. [21, 22, 23].

## 1.4   Vortex system around the step surface

In addition to the three main spanwise vortices mentioned in Sec. 1.2, the streamwise vortex system around the horizontal step surface of step cylinder has also been investigated in some previous studies[10, 12, 24, 25, 26]. By
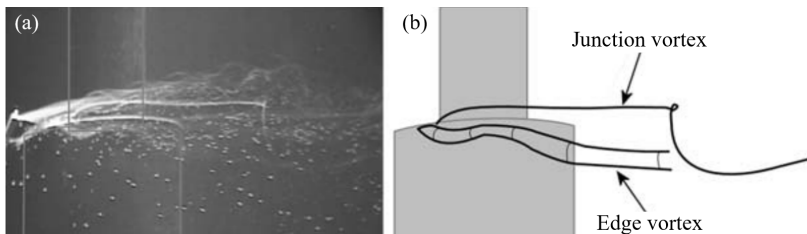


*Figure 1.10: (a) A hydrogen bubble flow visualization image showing the streamwise vortex structures around the step cylinder with $D/d = 2$ at $Re_D = 1100$. (b) A simplified sketch of (a) indicating the junction and edge vortices. Images reproduced from Dunn and Tavoularis [10].*

using hydrogen bubble visualization method in the flow around a single step cylinder with $D/d = 2$ at $Re_D = 1100$, Dunn and Tavoularis[10] identified two types of streamwise vortices, as indicated in Figure 1.10: (1) a pair of edge vortices form at the edge of the step surface and toward the large cylinder, (2) a junction vortex forms in front of the base of the small cylinder and then wraps around the small cylinder to the downstream. They found that the recirculating flow in front of the step cylinder causes the formation of the junction vortex. The induced rotating flow by the junction vortex and the blockage by the small cylinder together induce the forthcoming

fluid sideways and spill over the edges of the step cylinder to form the edge vortex. Moreover, they pointed out that, on the same side of the step cylinder, the edge vortex is counter-rotating to the adjacent branch of the junction vortex. By numerically investigating flow over a step cylinder with $D/d = 2$ at $Re_D = 2000$, Morton et al.[12] verified the existence of the junction and edge vortices.

Besides, similar streamwise vortex system was also observed in the flow around dual-step cylinders[24, 25, 26]. Based on numerically investigations of the flow around dual-step cylinders with $1.1 < D/d < 4$, $0.2 < L/D < 5$ at $Re_D = 150$, McClure et al. [24] captured the junction and edge vortices. They further concluded that the junction vortex primarily connects to the vortices shed from the large cylinder, while the edge vortex mainly connects to the small cylinder vortices, as indicated in Figure 1.11. Ji et al. [25] first numerically investigated the flow around a dual step cylinder undergoing vortex induced vibrations. They also captured the junction and edge vor-
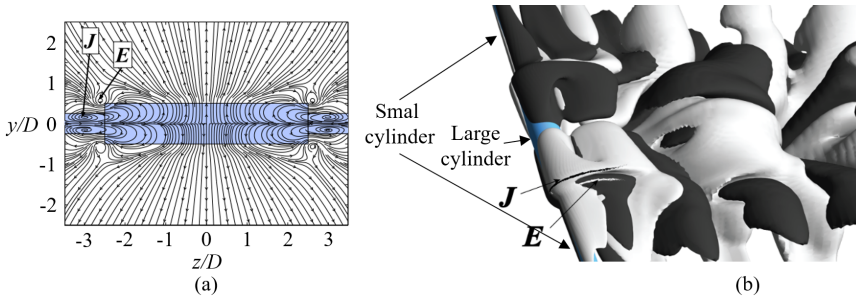


*Figure 1.11: Streamwise vortical structures in the wakes of a dual step cylinder with $D/d = 2$, $L/D = 5$ at $Re_D = 150$ visualized with (a) planar streamlines in the front-back view, (b) isosurfaces of streamwise vorticity $\omega_x = \pm 0.06 U/D$: $+gray$, $-white$. The junction vortex and edge vortex are indicated by the capital letter 'J' and 'E', respectively. Images reproduced from McClure et al.,[24].*

tices. By plotting the consecutive instantaneous vortex structures, Ji et al., [25] reported that the junction and edge vortices induce the L-cell vortices with opposite rotating directions to connect to each other. Moreover, by absorbing the strength of S-cell vortices, these streamwise vortices' strength increases as they convect downstream.

A nice sketch of the flow around a step cylinder in indirect vortex dislocation mode is made by Dunn and Tavoularies [10], and reprinted here in Figure 1.12. This sketch is a good summary to discussions in Chapter 1.2 and 1.4.
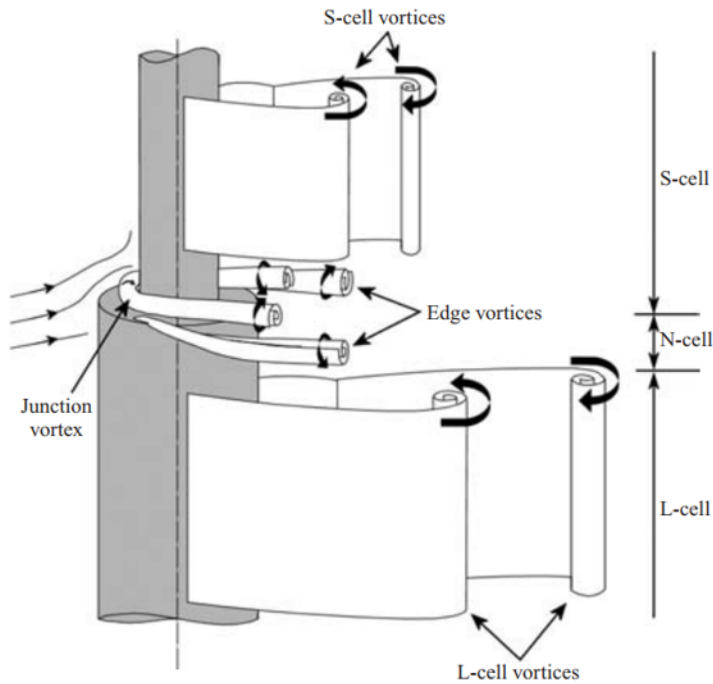
*Figure 1.12: Sketch of the junction vortex and edge vortex shed from a step cylinder. This image reproduced from Dunn and Tavoularis [10].*

## 1.5 Motivation and objective

As described in Section 1.2, 1.3, and 1.4, the previous investigations in the step cylinder wakes can be briefly divided into two aspects: 1. Vortex interactions behind step cylinders; 2. Vortex system around the step surface of step cylinders.

For the first aspect, due to the different shedding frequencies of the neighboring vortex cells, complex vortex interactions, especially the vortex dislocations, appear in both the direct and indirect modes of the step cylinder wakes. Although the previous papers successfully outlined vortex interactions between the S-, N-, and L-cell vortices, there are still several fundamental questions that require explanations. For example:

- What is the formation mechanism of the N-cell vortex?

- How does phase difference accumulate between the corresponding S-, N-, and L-cell vortices?

- How does phase difference between the neighboring vortices trigger

the vortex dislocations between them?

For the second aspect, the previous numerical studies mainly focused on the vortex system around the step surface of step cylinders at relatively low Reynolds number. In the experimental studies, due to the limitation of the hydrogen bubble and electrolytic precipitation visualization methods, to clearly illustrate vortices' developments around the step surface is difficult. Although the junction and edge vortices were identified, some fundamental questions were left:

- What is the formation mechanisms of the horseshoe vortices around the step cylinder?

- How do these streamwise vortices develop and interact with each other?

- How many types of streamwise vortices generating around the step cylinder?

The overall objective of the present thesis is to offer a deeper and more complete understanding of the vortex formations and vortex interactions in the flow around step cylinders. This is achieved by the following sub-objectives.

1. Use direct numerical simulations to visualize and investigate vortex interactions between the main spanwise vortices in the wake behind single step cylinders. Try to identify new vortex structures.

2. Develop a reliable method to monitor the phase information of every S-, N-, and L-cell vortex.

3. Investigate the accumulation process of the phase difference between neighboring vortex cells during their vortex dislocation processes. Explore the physical mechanism behind the vortex dislocation in the step cylinder wakes.

4. Compare the wake flows behind step cylinders with different diameter ratios. Investigate the diameter ratio effects in vortex formations and vortex interactions in the step cylinder wake.

5. Use direct numerical simulations to investigate both the time-averaged and instantaneous flows around the step cylinder at a relative high Reynolds number. Try to identify different components of vortices around the step cylinder, and investigate their developments and interactions.

## 1.6   Thesis organization

The present thesis is based on a collection of six articles, which are appended in full-length at the end. Chapter 1 presents the introduction of this thesis, which gives the overall background, motivation, and objectives. The other chapters are as follows:

Chapter 2 gives a brief description of the numerical simulation technique used in all investigations during my Ph.D. period.

Chapter 3 gives the summaries of the six appended articles.

Chapter 4 concludes the main original contributions of my Ph.D. study and gives recommendations for potential future works.

Chapter 5, 6, 7, 8, 9, and 10 present article 1, 2, 3, 4, 5, and 6, respectively.

# References

[1] Saiful-Islam ABM, Jameel M, Jumaat MZ, Shirazi SM, Salman F. Review of offshore energy in Malaysia and floating spar platform for sustainable exploration. *Renew Sust. Energ. Rev.* 2012; **16**:6268–6284.

[2] Carter BA, Ronalds BF. Deepwater riser technology. *SPE Asia Pacific Oil and Gas Conference and Exhibition, Perth, Australia, October 12-14*, 1998; 461–470.

[3] Williamson CHK. Oblique and parallel modes of vortex shedding in the wake of a circular cylinder at low Reynolds numbers. *J. Fluid Mech.* 1989; **206**:579–627.

[4] Sumer B, Fredsøe J. *Hydrodynamics around cylindrical structures-Volume 26.* World Scientific: Singapore, 1997.

[5] Gerrard J. The mechanics of the formation region of vortices behind bluff bodies. *J. Fluid Mech.* 1966; **25**:401–413.

[6] Roshko A. Experiments on the flow past a circular cylinder at very high reynolds number. *J. Fluid Mech.* 1961; **10**:345–356.

[7] Schewe G. On the force fluctuations acting on a circular cylinder in crossflow from subcritical up to transcritical Reynolds numbers. *J. Fluid Mech.* 1983; **133**:265–285.

[8] Rodriguez S, Jaworski J. Strongly-coupled aeroelastic free-vortex wake framework for floating offshore wind turbine rotors. part 2: Application. *Renew. Energy* 2019; **149**:1018–1032.

[9] Lewis CG, Gharib M. An exploration of the wake three dimensionalities caused by a local discontinuity in cylinder diameter. *Phys. Fluids A: Fluid Dynamics* 1992; **4**(1):104–117.

[10] Dunn W, Tavoularis S. Experimental studies of vortices shed from cylinders with a step-change in diameter. *J. Fluid Mech.* 2006; **555**:409–437.

[11] Morton C, Yarusevych S. Vortex shedding in the wake of a step cylinder. *Phys. Fluids* 2010; **22**(8):083 602.

[12] Morton C, Yarusevych S, Carvajal-Mariscal I. Study of flow over a step cylinder. *Appl. Mech. Mater.* 2009; **15**:9–14.

[13] Morton C, Yarusevych S. Vortex dynamics in the turbulent wake of a single step cylinder. *ASME J. Fluids Eng.* 2014; **136**(031204).

[14] Ayoub A, Karamcheti K. An experiment on the flow past a finite circular cylinder at high subcritical and supercritical Reynolds numbers. *J. Fluid Mech.* 1982; **118**:1–26.

[15] Jiang F, Pettersen B, Andersson HI, Kim J, Kim S. Wake behind a concave curved cylinder. *Phys. Rev. Fluids* 2018; **3**(9):094 804.

[16] Zdravkovich MM, Brand VP, Mathew G, Weston A. Flow past short circular cylinders with two free ends. *J. Fluid Mech.* 1989; **203**:557–575.

[17] Bearman PW. Investigation of the flow behind a two-dimensional model with a blunt trailing edge and fitted with splitter plates. *J. Fluid Mech.* 1965; **21**(2):241–255.

[18] Williamson CHK. The natural and forced formation of spot-like vortex dislocations in the transition of a wake. *J. Fluid Mech.* 1992; **243**:393–441.

[19] Vallès B, Andersson HI, Jenssen CB. Direct-mode interactions in the wake behind a stepped cylinder. *Phys. Fluids* 2002; **14**(4):1548–1551.

[20] McClure J, Morton C, Yarusevych S. Flow development and structural loading on dual step cylinders in laminar shedding regime. *Phys. Fluids* 2015; **27**:063 602.

[21] Eisenlohr H, Eckelmann H. Vortex splitting and its consequences in the vortex street wake of cylinders at low Reynolds number. *Phys. Fluids A-Fluids* 1989; **1**:189–192.

[22] Gaster M. Vortex shedding from slender cones at low Reynolds numbers. *J. Fluid Mech.* 1969; **38**:565–576.

[23] Dallard T, Browand F. The growth of large scales at defect sites in the plane mixing layer. *J. Fluid Mech.* 1993; **247**:339–368.

[24] McClure J, Morton C, Yarusevych S. Flow development and structural loading on dual step cylinders in laminar shedding regime. *Phys. Fluids* 2015; **27**(6):063 602.

[25] Ji C, Cui Y, Xu D, Yang X, Srinil N. Vortex-induced vibrations of dual-step cylinders with different diameter ratios in laminar flows. *Phys. Fluids* 2019; **31**(7):073 602.

[26] Ji C, Yang X, Yu Y, Cui Y, Srinil N. Numerical simulations of flows around a dual step cylinder with different diameter ratios at low Reynolds number. *Eur. J. Mech. B/Fluids* 2020; **79**:332–344.

# Chapter 2

# Numerical simulation technique

All investigations during my Ph.D. period are based on numerical simulations. In this chapter, the basic details of the numerical simulation methodology used in my researches are briefly described.

## 2.1 Governing equation

The governing equations for the three-dimensional incompressible Newtonian fluid flow contain a mass conservation equation (2.1) and a time-dependent full three-dimensional incompressible Navier-Stokes equation (2.2):

$$\frac{\partial u_i}{\partial x_i} = 0, \tag{2.1}$$

$$\frac{\partial u_i}{\partial t} + u_j \frac{\partial u_i}{\partial x_j} = -\frac{1}{\rho} \frac{\partial p}{\partial x_i} + \nu \frac{\partial^2 u_i}{\partial x_j \partial x_j} + f_i, \tag{2.2}$$

where $x_i$ stands for the three Cartesian directions ($i$=1, 2, 3), $u_i$ represents the velocity in each of the three Cartesian direction, $p$ is pressure, $\rho$ is the fluid density, $\nu$ is the kinematic viscosity of the fluid, $f_i$ represents the body forces. Both $\rho$ and $\nu$ are assumed to be constant.

For all simulations in my Ph.D. study, a thoroughly validated finite-volume-based numerical code MGLET [1, 2] is used to directly solve the governing equations without introducing any turbulent models. In this finite volume method, the governing equations (2.1 and 2.2) are transferred to their integral form (2.3 and 2.4) through integration over a control volume

19

$\Omega$ bounded by a surface $A$:

$$\oint_A u_i n_i \; dA = 0, \tag{2.3}$$

$$\frac{\partial}{\partial t} \iiint_\Omega u_i \; d\Omega + \oint_A u_i u_j n_j \; dA = -\frac{1}{\rho} \oint_A p n_i \; dA + \oint_A \nu \frac{\partial u_i}{\partial x_j} n_j \; dA. \tag{2.4}$$

Here, $n$ represents the unit vector pointing out the control surface ($dA$) of the control volume ($d\Omega$). Note: The body force term $f_i$ in Eq. 2.2 is neglected during the integration, because there is no external force applying in the bulk of the fluid in my simulations.

## 2.2 Computational method

In MGLET, Eq. 2.3 and Eq. 2.4 are first discretized on a three-dimensional staggered Cartesian grid. By using the midpoint rule and the central difference, the governing equations are integrated over the surfaces of the discrete volumes. It leads to a second-order accuracy in space. In time, the integration is done by Williamson's explicit low-storage three-order Runge-Kutta scheme [3]. The pressure corrections are achieved by using Stone's implicit procedure (SIP)[4].

The use of a staggered Cartesian grid could cause the problem of interpreting the solid surface of the configuration in the computational domain. MGLET solves this problem by introducing an immersed boundary method (IBM). The surface of the geometry is represented by an unstructured triangular mesh. The information of this mesh is directly transferred to IBM to block the grid cells bounded by the meshed surface. Then, the quantities on the grid cell at the fluid-solid interface are determined by interpolation from the neighboring grid cells. A more detailed description and validation of the IBM used in MGLET can be found in Ref. [5, 6].

For more detailed information regarding the computational domain, grid resolution, and boundary conditions, please check individual articles.

# References

[1] Manhart M, Friedrich R. DNS of a turbulent boundary layer with separation. *Int. J. Heat Fluid Flow* 2002; **23**(5):572–581.

[2] Manhart M. A zonal grid algorithm for DNS of turbulent boundary layers. *Computers & Fluids* 2004; **33**(3):435–461.

[3] Williamson JH. Low-storage Runge-Kutta schemes. *J. Comput. Phys.* 1980; **35**:48–56.

[4] Stone HL. Iterative solution of implicit approximations of multidimensional partial differential equations. *SIAM J. Numer. Anal.* 1968; **5**:530–558.

[5] Peller N, Duc AL, Tremblay F, Manhart M. High-order stable interpolations for immersed boundary methods. *Int. J. Numer. Meth. Fl.* 2006; **52**:1175–1193.

[6] Peller N. Numerische simulation turbulenter strömungen mit immersed boundaries. PhD Thesis, Technische Universität München, München, Germany 2010.

# Chapter 3

# Summary of the articles

This chapter gives a brief description of the six articles in the present thesis, which focuses on two main topics. The first topic is treated in the first five articles, which concentrate on vortex interactions, especially the vortex dislocations, in the wake flow behind single step cylinders at $Re_D = 150$. The sixth article mainly focuses on the vortex system around the step cylinder at $Re_D = 3900$, constituting the second topic in this thesis.

## 3.1 Part 1 - Vortex interaction behind single step cylinders

### Article 1 - Numerical investigation of flow around a step cylinder [1]

In this article, the flow around a single step cylinder with $D/d = 2$ at $Re_D = 150$ is investigated by using direct numerical numerical simulation (DNS). As the first conference paper in my doctoral period, the main objectives are to investigate the flow past single step cylinder and familiarize myself with the numerical code MGLET. In general, the results in this article show good agreement with the previous similar studies [2, 3], including the three dominating vortex cells (the S-, N-, and L-cell vortices), the vortex dislocation between neighboring vortex cells, and the formation of streamwise vortices. The speculated repetition of the N-cell cycle in Ref. [3] is verified in this article by capturing similar-shaped vortex loop structures in the neighboring N-cell cycles. Moreover, these vortex loop structures are observed to be antisymmetric in the neighboring N-cell cycles for the first time. The desire to figure out how these vortex loop structures develop and why they become antisymmetric motivated me to do further investigations.

## Article 2 - Antisymmetric vortex interactions in the wake behind a step cylinder [4]

The primary goal of Article 2 is to investigate the remaining unsolved questions in Article 1: (1) How do the vortex loop structures form in every N-cell cycle, (2) Why are the vortex loop structures antisymmetric in the neighboring N-cell cycles. By illustrating the consecutive snapshots of the vortex structures in one N-cell cycle, two types of vortex loop structures are identified in one N-cell cycle: the *fake loop* (NL-loop) between N- and L-cell vortices (the red curves in Figure 3.1) and the *real loop* (NN-loop) between two N-cell vortices (the blue curves in Figure 3.1). Detailed observations
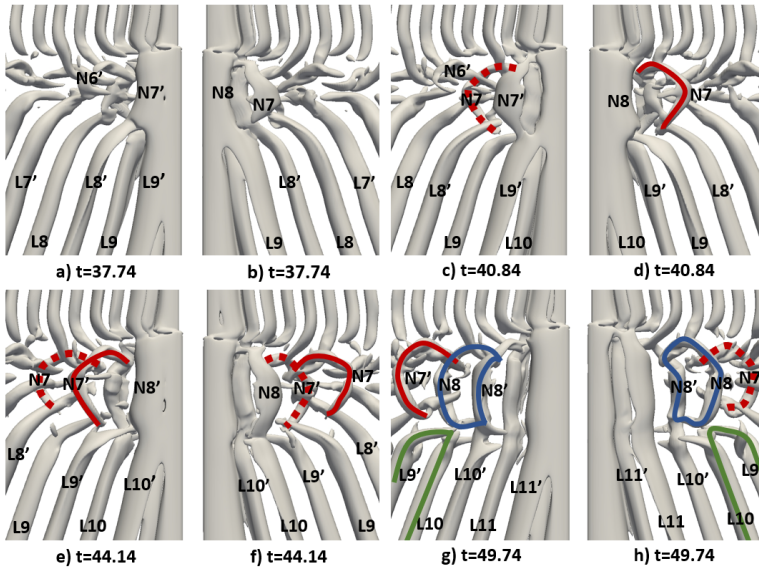


*Figure 3.1: Isosurfaces of $\lambda_2$=-0.15 showing vortex interactions occurring at the N-L cell boundary during the vortex dislocation process. (a), (c), (e), and (g) are observed from '+Y' to '-Y' sides, while (b), (d), (f), and (h) are observed from the opposite side. The solid and dashed red curves indicate NL-loops, the blue closed curve show NN-loop, and the green curves show L-L half loops. Images reproduced from Article 2 [4].*

show that there are, in total, two fake loops, one real loop, and one L-L half loop generated during the vortex dislocation process in each N-cell cycle. Additionally, after defining the side of the N-cell vortex in an NL-loop structure as the side of the loop itself, an antisymmetric phenomenon between two adjacent N-cell cycles is clearly presented and defined. As shown in Figure 3.2, the NL- and NN-loop structures occur antisymmetrically in the
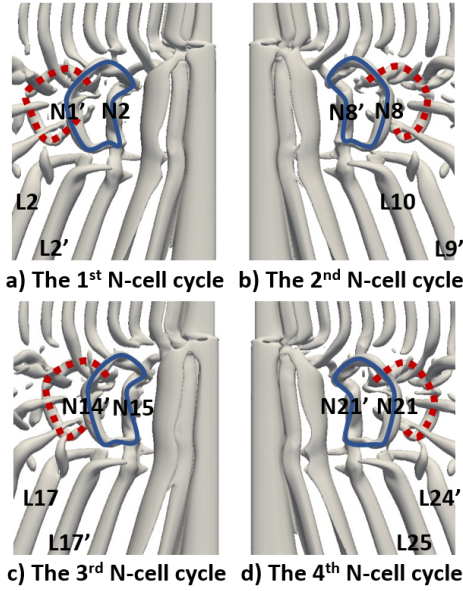
*Figure 3.2: Isosurfaces of $\lambda_2$=-0.2 in four neighboring N-cell cycles showing features and repetition of the NL- and NN-loop structures. (a) and (c) are observed from '+Y' to '-Y' sides, while (b) and (d) are observed from the opposite side. The NL- and NN-loop structures are marked by the red and blue curves, respectively. Images reproduced from Article 2 [4].*

neighboring N-cell cycles. Furthermore, the boundary between two neighboring N-cell cycles is redefined. With the new boundary, 13 N-cell vortices and 15 L-cell vortices are observed in every N-cell cycle in the 2:1 step cylinder wake at $Re_D = 150$ and $D/d = 2$.

More detailed descriptions and discussions related to the vortex dislocations and the formation process of the NL- and NN-loop structures are referred to Article 2.

## Article 3 - The long periodicity of vortex dislocations in the wake behind a step cylinder [5]

Article 3 follows the work presented in Article 2 and extended it further. The main objective is to examine the long periodicity of the vortex interactions, especially the vortex dislocations between the N- and L-cell vortices. Several long time numerical simulations (more than 3000 time units $(D/U)$) are conducted to illustrate and analyze the wake flow.

Following Article 2, this article presents more detailed and in-depth investigations on the antisymmetric vortex loop structures in the N-cell cycles. First, the vortex loop structures, i.e., the NL-loops and the NN-loops, in two neighboring N-cell cycles are illustrated by plotting the isosurfaces of $\lambda_2$. Careful observations indicate that the antisymmetry defined in Article 2 is not perfect. Figure 3.3[(a), (b)] and [(c), (d)] show that, between the neighboring 1st and 2nd N-cell cycles, the corresponding NL-loops marked

by the same color have small differences when comparing their detailed structures as highlighted by black circles. Long time observations reveal
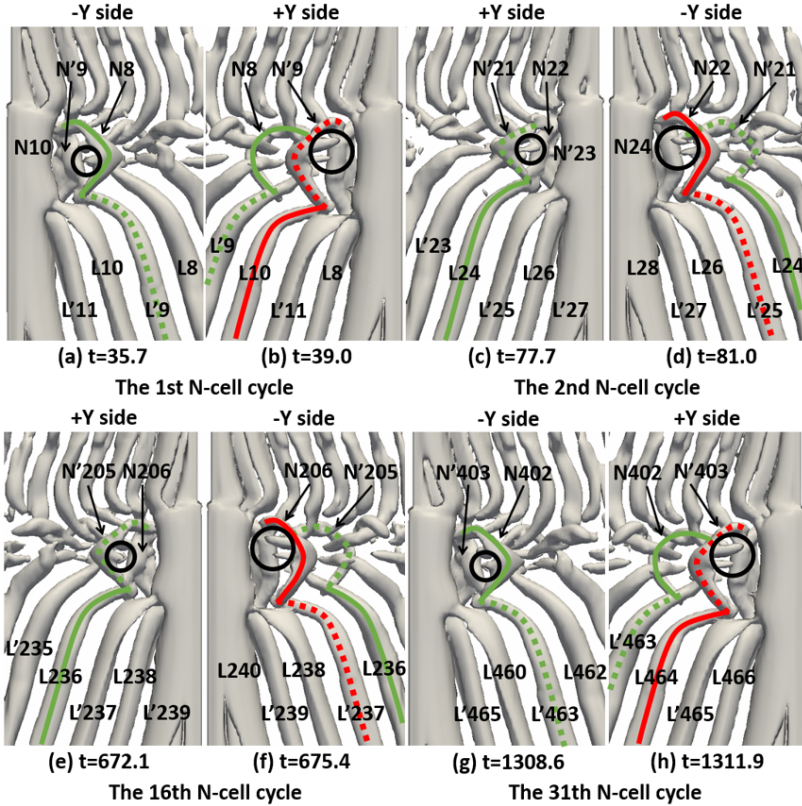


*Figure 3.3: NL-loop structures at the 1st, 2nd, 16th, and 31th N-cell cycles are plotted in [(a), (b)], [(c), (d)], [(e), (f)], and [(g), (h)], respectively. In each N-cell cycle, the first appeared loop structure (NL-loop 1) is marked by the green curve, and the second appeared loop structure (NL-loop 2) is marked by the red curve. Solid and dashed curves indicate the loop structures on the '-Y' and '+Y' sides, respectively. Images reproduced from Article 3 [5].*

that the perfect antisymmetric NL-loop structures only appear after every 15 N-cell cycles. As presented in Figure 3.3[(a), (b)], [(e), (f)], and [(g), (h)], the corresponding NL-loops are approximately perfect antisymmetric between the 1st, 16th and 31th N-cell cycles, even when comparing their detailed structures highlighted by the black circles. This long cyclic process, served as a supplementary part, makes the definition of 'fundamental dislocation cycle' in Ref. [6] more complete: there are two types of the fun-

damental dislocation cycles, i.e., the perfect symmetric cycle and the perfect antisymmetric cycle. Moreover, the different duration of all the N-cell and L-cell vortices in one N-cell cycle is found to brings the small phase shift to every N-L vortex pair in the neighboring N-cell cycles, and further cause the fundamental vortex dislocation cycle.

Last but not least, detailed discussions about the challenges of the grid resolution on investigating the long period characteristic are given. For the present case, although the detailed information (e.g., the number of N- and L-cell vortices) in one fundamental vortex dislocation cycle varies when continuing to refine the grid, the phenomenon and mechanism of the fundamental vortex dislocation cycle are proved to be valid for all investigated cases.

More detailed descriptions and discussions related to the fundamental vortex dislocation cycle and computational challenges are referred to Article 3 [5].

## Article 4 - Vortex dislocation mechanisms in the near wake of a step cylinder [7]

Article 4 focuses on physical interpretation of the mechanisms in vortex dislocations between the N- and L-cell vortices. To achieve this, vortex dislocation processes in the near wake behind two single step cylinders with diameter ratio $D/d = 2$ and 2.4 at $Re_D = 150$ are studied in depth. The main objective is to thoroughly investigate the mechanisms of phase difference accumulation in the step cylinder wake, and their effect on vortex interactions.

First, to monitor the phase information and phase difference of corresponding N- and L-cell vortices, a phase-tracking method is developed and validated. By using this method, Article 4 presents more detailed information on how the phase difference ($\Phi$) between the corresponding N- and L-cell vortices is accumulated and finally triggers the formation of vortex dislocations and concomitant NL-loop structures. A phase difference accumulation mechanism is identified for the first time, i.e., $\Phi = \Phi_f + \Phi_c$. There are two qualitatively different physical factors contributing to the accumulation of $\Phi$, one is different shedding frequencies ($\Phi_f$), the other one is varying convective velocities in the different vortex cell regions ($\Phi_c$). While $\Phi_f$ is relatively well-known, the contribution from convective velocity $\Phi_c$ has never been examined before.

Based on this new understanding of the phase difference accumulation mechanism, the variations of the formation position of the NL-loop 1 and
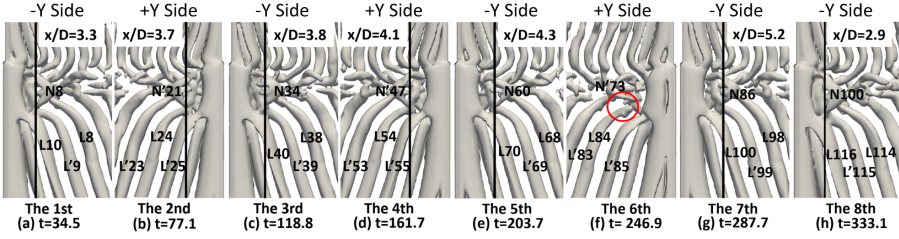
*Figure 3.4: The just-formed NL-loop 1 structures in the first to the eighth N-cell cycle are plotted from both the -Y and +Y sides. The black line marks the formation position of NL-loop 1. Images reproduced from Article 4 [7].*

NL-loop 2, and the irregularity of the NL-loop 1 formation are fully explained. For a pair of N- and L-cell vortices, as $\Phi_f$ decreases, $\Phi_c$ must contribute more to ensure a sufficiently large $\Phi$ (we refer to it as the *trigger value*) that can trigger the vortex dislocations. This makes the formation position of the corresponding NL-loop structure move downstream. The just-formed NL-loop 1 structures in the 1st to 8th N-cell cycles are plotted from both the $-Y$ and $+Y$ sides in Figure 3.4(a-h). The corresponding time trace of phase difference ($\Phi_f U/D$) is plotted in Figure 3.5. One can see that, except for the sixth N-cell cycle, as $\Phi_f U/D$ decreases from G1 to G7 in Figure 3.5 the formation position of the corresponding NL-loop 1 structure continues to move downstream from the 1st to the 7th N-cell cycle in Figure 3.4(a-g).

Moreover, a long-time trace of the accumulation of $\Phi_f$ in Figure 3.5 clearly shows cyclic trends, which are caused by the phase shift of every vortex pair in one N-cell cycle, as compared to the N-cell cycle before it. The phase shift ($S$) can be expressed as

$$S = \alpha \frac{1}{2f_L} - \beta \frac{1}{2f_N}, \tag{3.1}$$

where $\alpha$ and $\beta$ represent the number of L- and N-cell vortices in one N-cell cycle; and $f_L$ and $f_N$ are the shedding frequencies of L- and N-cell vortices. Due to the accumulation of this phase shift, the antisymmetric phenomenon reported in Article 2 will be cyclically interrupted when $\Phi_f$ decreases below a certain value. This value is referred to as the *threshold value* (the yellow line in Figure 3.5). When $\Phi_f$ continues to decrease along the green line from G1 to C8 in Figure 3.5, even by including the contribution of $\Phi_c$, $\Phi$ is still not large enough to induce the formation of the expected NL-loop 1 (N'99-L114). In this N-cell cycle, one additional vortex pair shedding is needed to make $\Phi$ sufficiently large to induce the formation of the NL-loop 1 (N100-
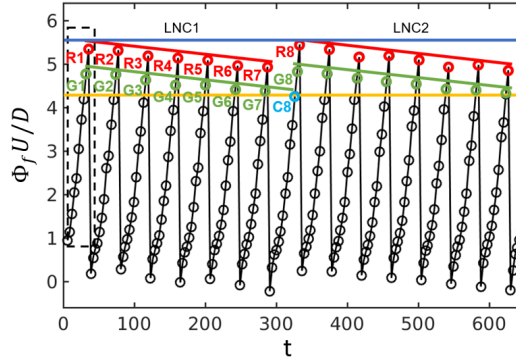
*Figure 3.5: Time trace of $\Phi_f$ between corresponding N- and L-cell vortices in the first (LNC1) and second (LNC2) long N-cell cycles. The circles represent $\Phi_f$ between an N-cell vortex ans its counterpart L-cell vortex. The green and red circles indicate $\Phi_f$, which eventually causes formation of the NL-loop 1 and NL-loop 2 structures, respectively. From the first to the eighth N-cell cycle, the green and red circles are numbered. Images reproduced from Article 4 [7].*

L'115 in Figure 3.4(h)). The additional one pair of N- and L-cell vortices makes the number of N-cell vortices in the 8th N-cell cycle become even, thereby interrupting the antisymmetric phenomenon. The NL-loop 1 forms at the $+Y$ side in both the 7th and 8th N-cell cycles in 3.4(g and h). This interruption of the antisymmetric phenomenon is observed to appear after every 7 or 8 N-cell cycles. Based on this phenomenon, the uninterrupted series of antisymmetric N-cell cycles are defined as the long N-cell cycle. As an example, the first two long N-cell cycles (LNC1 and LNC2) are indicated in Figure 3.5.

In the last part of this article, the universality of our discussions and conclusions from the $D/d = 2$ case is justified by investigating the $D/d = 2.4$ case.

## Article 5 - Diameter ratio effects in the wake flow of single step cylinder [8]

As an important extension of Article 2 and Article 4, Article 5 applies the new findings in the previous two articles to a wider range of parameter space. Article 5 reveals important tendencies as the diameter ratio ($D/d$) changes. It also further validates the universality of all physical mechanisms concluded in Article 2 and Article 4. In article 5, the near wake behind

ten single cylinders with $D/d$ ranging from 2 to 3 are studied at a fixed $Re_D = 150$.

First, the antisymmetric phenomenon in the $D/d = 2$ and 2.4 cases mentioned in Article 2 and Article 4 is verified in the $D/d = 2.6$ case. Moreover, in the $D/d$=2.2, 2.8, and 3.0 cases, the NL-loop 1 structure is found to continuously appear at either the +Y or -Y side of the step cylinder. Figure 3.6 shows that the NL-loop 1 structure continues to form at the $-Y$ side in the $D/d = 2.2$ case. This phenomenon is referred to
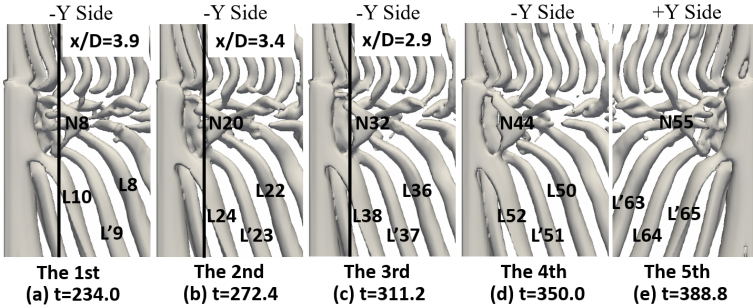


Figure 3.6: *The just-formed NL-loop 1 structures in the 1st to 5th N-cell cycles are plotted from both the -Y and +Y sides in the $D/d = 2.2$ case at $Re_D = 150$. Images reproduced from Article 5 [8].*

as symmetric vortex interaction, in comparison with the already known antisymmetric phenomenon. Further investigation shows that it is the parity of the number of N- and L-cell vortices, i.e., $\beta$ and $\alpha$, in one N-cell cycle in different $D/d$ cases that determine whether symmetric or antisymmetric vortex interactions appear in a specific $D/d$ case. When $\beta$ and $\alpha$ are even numbers, symmetric vortex interactions will occur. Oppositely, when $\beta$ and $\alpha$ are odd numbers, antisymmetric vortex interactions will happen.

Moreover, by using the phase tracking method developed in Article 4, the time traces of $\Phi_f$ in the $D/d$=2.0, 2.2, 2.4, 2.6, 2.8, and 3.0 cases are monitored. An increasing tendency of $\Phi_f$ is first captured in the $D/d$=2.2, 2.6, and 3.0 cases. In these cases, the formation position of NL-loop 1 structure is observed to continuously move upstream as $\Phi_f$ increases. One can see that, as $\Phi_f$ increases from G1 to G4 in Figure 3.7, the formation position of the corresponding NL-loop 1 structure continues to move downstream from the 1st to the 4th N-cell cycles in Figure 3.6(a-d). Similar to the decreasing tendency of $\Phi_f$ reported in Article 4, the discovered increasing $\Phi_f$ tendency also can cause the interruption of continuous antisymmetric or symmetric vortex interaction phenomena. For example, as shown in Figure 3.6(d) and (e), the continuous symmetric interactions are interrupted between the 4th
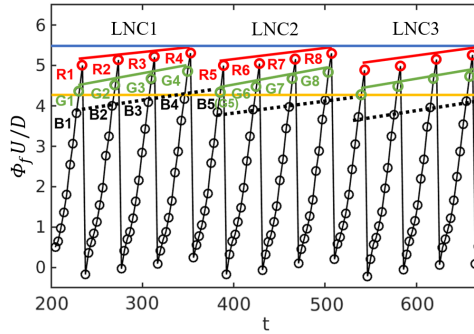
*Figure 3.7: Time trace of $\Phi_f$ between corresponding N- and L-cell vortices in the first (LNC1), second (LNC2), and third (LNC3) long N-cell cycles. The circles represent $\Phi_f$ between an N-cell vortex and its counterpart L-cell vortex. The green and red circles indicate $\Phi_f$, which eventually causes formation of the NL-loop 1 and NL-loop 2 structures, respectively. From the first to the eighth N-cell cycle, the green and red circles are numbered. Images reproduced from Article 5 [8].*

and 5th N-cell cycles in the $D/d = 2.2$ case. According to the time trace of $\Phi_f$, the trigger value of vortex dislocations is found to remain constant when $D/d$ varies. The threshold value of vortex dislocations decreases as $D/d$ increases, which further causes the number of NL-loop structures in one N-cell cycle to increase from 2 in the $D/d=2.0$ case to 4 in the $D/d=3.0$ case.

Furthermore, the likelihood of the appearance of antisymmetric or symmetric vortex interactions, and the likelihood of increasing or decreasing phase differences are analyzed. Based on the investigations on the $D/d=2.0$, 2.2, 2.4, 2.6, 2.8 and 3.0 cases, Article 4 gives a predictio: when $2 \leq D/d \leq 3$ the likelihood of increasing $\Phi_f$ and decreasing $\Phi_f$ are almost the same, but the antisymmetric phenomenon is more likely to appear than the symmetric phenomenon. Further observations in $D/d=2.1$, 2.3, 2.5 and 2.7 cases prove our anticipation.

Last but not least, careful observations on the distributions of $-w/U$ and base pressure coefficient ($C_{pb}$) show that the formation of N-cell vortices are caused by the joint influence of both increased $-w/U$ and increased $C_{pb}$, but the latter one plays a major role.

## 3.2    Part 2 - Vortex system around a single step cylinder

### Article 6 - Vortex system around a step cylinder in a turbulent flow field [9]

For the flow past a uniform circular cylinder, the particular Reynolds number 3900 is a benchmark, at which there are many accurate numerical simulations [10, 11, 12, 13] and experimental studies [14, 15]. However, until now, no one has investigated flow around a step cylinder at such Reynolds number. As a pioneer, the present study investigates the flow around a single step cylinder with $D/d = 2$ at $Re_D = 3900$ by using direct numerical simulations (DNS). The main objective is to investigate the development and interaction of the vortices around the step position.

In general, the results in this article show good agreement with previous studies [2, 6, 6, 16, 17] with respect to the formation of the junction and edge vortices around the step surface of the step cylinder. Meantime, the similar base vortices identified in the flow past a wall-mounted cylinder by Ref. [18, 19, 20] are also captured in the rear part of the step surface. Furthermore, the numerical results provide more complete and detailed information in the flow around the step surface.
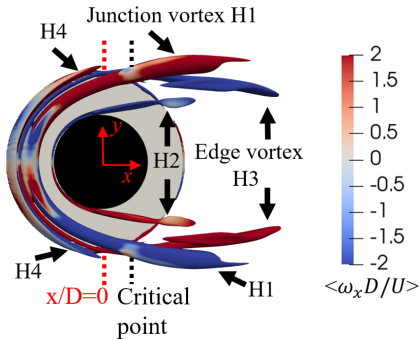


Figure 3.8: The time-averaged vortex structures around the step surface are illustrated by the isosurface of the time-averaged $\lambda_2 = -9$ at the top-down viewpoint coloured by the time-averaged streamwise vorticity $\omega_x$. Images reproduced from Article 6 [4].

First, the time-averaged iso-surfaces of $\lambda_2$ and streamlines show that four horseshoe vortices (H1, H2, H3, and H4) form in front of the step cylinder, due to the flow recirculations and the flow separations on the junction surfaces between the root of the small cylinder and the step surface. As shown in Figure 3.8, besides the conventional junction vortex H1 and the edge vortex H3, two more horseshoe vortices H2 and H4 are clearly illustrated. The corresponding *Octupole Type* of the time-averaged vortex structures is also identified. Under the influence of the different flow tendencies in the small and large cylinders' wakes, the development tendencies of H1, H2, and H3

become different when they extend to $x/D > 0$. Consequently, a critical point for H1 and H3 is identified in Figure 3.8.
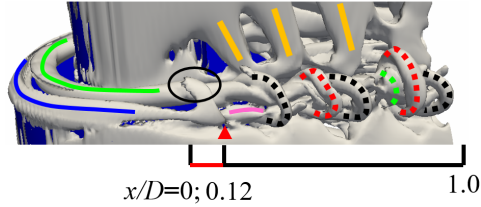


*Figure 3.9: Instantaneous isosurface of $\lambda_2 = -0.2$ showing vortex structures around the step position in the $D/d = 2$ case at $Re_D = 3900$. The vortices H1, H3, and H4 are marked by the green, pink, and blue curves, respectively. The vortex bridge between H1 and H4 are indicated by the black circle. Different hairpin vortices are marked by dotted curves with different colors. Kelvin-Helmholtz vortex is represented by the yellow straight lines. Images reproduced from Article 6 [9].*

Moreover, the consecutive instantaneous iso-surfaces of $\lambda_2$ and the animation attached in the supplementary file indicate that the four horseshoe vortices exist in both the time-averaged and instantaneous flows. In the forepart of the step surface ($x/D < 0$), the vortices H1, H2, H3, and H4 keep their own vortical structure stable and slightly fluctuated as time varies. As H4 extends to $x/D > 0$, a vortex bridge gradually forms between H4 and H1, as marked by the black circle in Figure 3.9. When this vortex bridge sheds from the end of H4 and connects to H3, a hairpin vortex forms. In the neighboring region upstream of this hairpin vortex, other two or three hairpin vortices form before the small turbulent eddies dominates the wake. These hairpin vortices are shown by different dotted curves in Figure 3.9.

In the rear part of the step surface ($x/D > 0$), another remarkable phenomenon is the appearance of Kelvin-Helmholtz (KH) vortex, which is indicated by the solid yellow lines in Figure 3.9. These KH vortices shed in an unexpected high shedding frequency behind the small cylinder. Our results suggest that it is the formation of the hairpin vortex that amplifies the convection of perturbations and further accelerates the formation of KH vortices.

# References

[1] Tian C, Jiang F, Pettersen B, Andersson HI. Numerical investigation of flow around a step cylinder. *Proceedings of 9th National Conference on Computational Mechanics (CIMNE), Trondheim, Norway, May 11-12*, 2017; 369–384.

[2] Dunn W, Tavoularis S. Experimental studies of vortices shed from cylinders with a step-change in diameter. *J. Fluid Mech.* 2006; **555**:409–437.

[3] Morton C, Yarusevych S. Vortex shedding in the wake of a step cylinder. *Phys. Fluids* 2010; **22**(8):083 602.

[4] Tian C, Jiang F, Pettersen B, Andersson HI. Antisymmetric vortex interactions in the wake behind a step cylinder. *Phys. Fluids* 2017; **29**(10):101 704.

[5] Tian C, Jiang F, Pettersen B, HI Andersson. The long periodicity of vortex dislocations in the wake behind a step cylinder. *Proceedings of 10th National Conference on Computational Mechanics (CIMNE), Trondheim, Norway, June 3-4*, 2019; 81–99.

[6] McClure J, Morton C, Yarusevych S. Flow development and structural loading on dual step cylinders in laminar shedding regime. *Phys. Fluids* 2015; **27**(6):063 602.

[7] Tian C, Jiang F, Pettersen B, Andersson HI. Vortex dislocation mechanisms in the near wake of a step cylinder. *J. Fluid Mech.* 2020; **891**.

[8] Tian C, Jiang F, Pettersen B, Andersson HI. Diameter ratio effects in the wake flow of single step cylinders. *Phys. Fluids* 2020; **32**(9):093 603.

[9] Tian C, Jiang F, Pettersen B, Andersson HI. Vortex system around a step cylinder in a turbulent flow field. Submitted to Phys. Fluids.

[10] Lehmkuhl O, Rodríguez I, Borrell R, Oliva A. Low-frequency unsteadiness in the vortex formation region of a circular cylinder. *Phys. Fluids* 2013; **25**(8):085 109.

[11] Rajani BN, Kandasamy A, Majumdar S. LES of flow past circular cylinder at Re= 3900. *J. Appl. Fluid Mech.* 2016; **9**(3).

[12] Strandenes H, Pettersen B, Andersson HI, Manhart M. Influence of spanwise no-slip boundary conditions on the flow around a cylinder. *Comput. Fluids* 2017; **156**:48–57.

[13] Tian G, Xiao Z. New insight on large-eddy simulation of flow past a circular cylinder at subcritical Reynolds number 3900. *AIP Adv.* 2020; **10**(8):085 321.

[14] Parnaudeau P, Carlier J, Heitz D, Lamballais E. Experimental and numerical studies of the flow over a circular cylinder at Reynolds number 3900. *Phys. Fluids* 2013; **20**(8):085 101.

[15] Molochnikov VM, Mikheev NI, Mikheev AN, Paereliy AA, Dushin NS, Dushina OA. SIV measurements of flow structure in the near wake of a circular cylinder at Re= 3900. *Fluid Dyn. Res.* 2019; **51**(5):055 505.

[16] Morton C, Yarusevych S, Carvajal-Mariscal I. Study of flow over a step cylinder. *Appl. Mech. Mater.* 2009; **15**:9–14.

[17] Ji C, Cui Y, Xu D, Yang X, Srinil N. Vortex-induced vibrations of dual-step cylinders with different diameter ratios in laminar flows. *Phys. Fluids* 2019; **31**(7):073 602.

[18] Sau A, Hwang RR, Sheu TW, Yang WC. Interaction of trailing vortices in the wake of a wall-mounted rectangular cylinder. *Phys. Rev. E* 2003; **68**(5):056 303.

[19] Palau-Salvador G, Stoesser T, Fröhlich J, Kappler M, Rodi W. Large eddy simulations and experiments of flow around finite-height cylinders. *Flow Turbul. Combust.* 2010; **84**(2):239.

[20] Dousset V, Pothérat A. Formation mechanism of hairpin vortices in the wake of a truncated square cylinder in a duct. *J. Fluid Mech.* 2010; **653**:519–536.

# Chapter 4

# Conclusions and Recommendations for Future Work

In this chapter, the main findings in the present thesis are summarized. Moreover the recommended future works are presented.

## 4.1 Main finding in the present thesis

For the flow past step cylinders, different types of vortex cells and their interactions have been investigated in many studies. Especially for the three dominating spanwise vortex cells, i.e., the S-, N, and L-cell vortices, due to their different shedding frequencies, complex vortex interactions, vortex dislocations, and concomitant vortex structures were observed and analyzed in the step cylinder wakes by previous studies [1, 2, 3, 4, 5, 6]. However, the formation mechanism of the vortex dislocations and how different diameter ratios affect the vortex interactions in the step cylinder wakes still require a thorough investigation. For these two parts, the most important original observations in the present thesis are summarized as follows:

1. There are mainly three types of N-cell cycle in the wake behind single step cylinders with $2 \leq D/d \leq 3$ at $Re_D = 150$:

    (a) The N-cell cycle: as the N- and L-cell vortices move out-of-phase, in parallel with the appearance of the vortex dislocations, the spanwise length of the N-cell vortices and the position of the N-L cell interface change periodically. This cyclic variation is defined as the N-cell cycle. (Ref. [4])

(b) The long N-cell cycle: the uninterrupted series of antisymmetric or symmetric N-cell cycles are defined as the long N-cell cycle. (*Article 4*)

(c) The fundamental N-cell cycle (the fundamental dislocation cycle): when the vortex alignments and vortex loop structures at one side of the step cylinder in a N-cell cycle identically repeat at either the same side or the opposite side of the step cylinder in other subsequent N-cell cycle, the symmetric fundamental N-cell cycle or the antisymmetric N-cell cycle appear, respectively. (*Article 3*)

2. The vortex dislocation in one N-cell cycle is caused by the accumulation of phase difference ($\Phi$) between the corresponding N- and L-cell vortices. There are two distinct physical mechanisms contributing to the accumulation of $\Phi$: one is different shedding frequencies ($\Phi_f$), the other one is varying convective velocities in the different vortex cell regions ($\Phi_c$). Then, the phase difference accumulation mechanism can be presented as $\Phi = \Phi_f + \Phi_c$. (*Article 4*)

3. During the vortex dislocation process in one N-cell cycle, there are several NL-loop structures, NN-loop structures, SS- and LL-half loop structures form. At $Re_D = 150$, in one N-cell cycle, the number of NL-loop structures increases as $D/d$ increases. (*Article 2 and Article 5*)

4. Two different vertex interaction scenarios are identified between the neighboring N-cell cycles, namely antisymmetric and symmetric N-cell cycles. (*Article 2 and Article 5*)

Antisymmetry: when the NL-loop structure first forms at the different side of the step cylinder in the neighboring N-cell cycles.

Symmetry: when the NL-loop structure first forms at the same side of the step cylinder in the neighboring N-cell cycles.

5. Within one long N-cell cycle, the continuous antisymmetric or symmetric vortex interactions appear between subsequent N-cell cycles. It is the parity of the number of N-cell vortex ($\beta$) and L-cell vortex ($\alpha$) in one N-cell cycle that determines whether symmetric or antisymmetric vortex interactions appears in a certain $D/d$ case. (*Article 5*)

6. The trigger value and threshold value are defined. Both are important parameters that control the vortex dislocation process. (*Article 4 and Article 5*).

The trigger value: when $\Phi$ becomes larger than the trigger value, the vortex dislocation between the corresponding N- and L-cell vortices happens.

The threshold value: Only when $\Phi_f$ becomes larger than the threshold value, the vortex dislocation can occur between the corresponding N- and L-cell vortices.

Moreover, as $D/d$ increases from 2 to 3, the threshold value is found to decrease, but the trigger value remains constant. Based on the application of the constant trigger value, several equations are purposed to measure the number of N-cell vortex ($\beta$) and L-cell vortex ($\alpha$) in one N-cell cycle.

7. As the decreasing or increasing tendencies of $\Phi_f$ appears in one long N-cell cycle, the formation position of the corresponding NL-loop structure is found to move downstream or upstream, respectively. (*Article 4 and Article 5*)

As an example, in Figure 4.1, the long-time history of the vortex connection topology behind the step cylinder with $D/d = 2$ at $Re_D = 150$ schematically illustrates the vortex dislocation between the N- and L-cell vortices, the different NL-loop structures, and the three types of N-cell cycles.
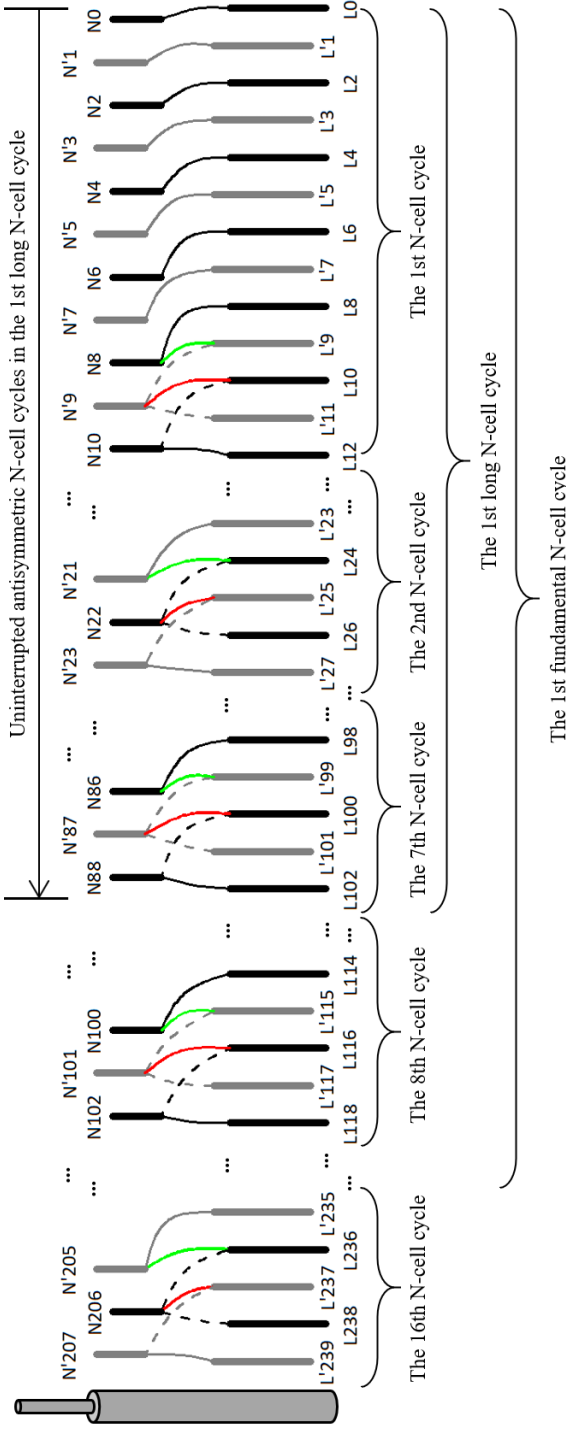
Figure 4.1: *Schematic topology sketches illustrating the long-time history of the vortex connection topology and the vortex shedding behind step cylinder with $D/d = 2$ at $Re_D = 150$. The thick black and grey straight lines represent vortices on the $-Y$ and $+Y$ side, respectively. Only the N- and L-cell vortices are shown by short and long straight lines. The connections between them are depicted by thin solid curves. Black and grey solid curves indicate the connections between an N-cell vortex and its counterpart L-cell vortex. The red and green curves reveal NL-loop 1 and NL-loop 2 structures, respectively. The dashed curves, on the other hand, indicate broken connections that are not able to persist due to dislocations.*

For the flow past step cylinders, the characteristics of the three main spanwise vortex cells, i.e., the S-, N-, and L-cell vortices, have been discussed in many previous studies [1, 2, 3, 4, 5, 6]. On the other hand, only a few studies have analyzed the vortex system around step cylinders [2, 4, 7]. To make this part of knowledge more complete, the vortex system around the step cylinder with $D/d = 2$ at $Re_D = 3900$ is investigated. The main observations are as follows:

1. Due to the flow recirculations and the flow separations on the junction surfaces between the small cylinder's root and the step surface, four horseshoe vortices (H1, H2, H3, and H4) form on the step surface in front of the small cylinder.

2. Under the influence of the different flow tendencies in the small and large cylinders' wakes, the spacial evolution of H1, H2, and H3 become different. When they warp around the small cylinder and extend downstream, the crossflow width of H2 and H3 continues to increase. However, the crossflow width of H1 decreases. Consequently, a critical point for H1 and H3 is defined.

3. As the vortex bridge between H1 and the end of H4 sheds from H4 and connects to H3, a hairpin vortex forms. In the neighboring region upstream of this hairpin vortex, other two or three hairpin vortices generate before the small turbulent eddies dominate the wake.

4. In the rear part of the step surface, a pair of base vortices and a backside horizontal vortex are captured in the time-averaged flow.

5. Behind the small cylinder, the Kelvin-Helmholtz (KH) vortices form in an unexpected high shedding frequency, comparing to the KH vortices behind the circular cylinder with the same $Re_d$ in Refs. [8, 9]. An speculated explanation is that the formation of the hairpin vortex amplifies the convection of perturbations and further accelerates the formation of KH vortices.

An overall schematic of the flow around the step surface of the step cylinder with $D/d = 2$ at $Re_D = 3900$ is illustrated in Fig. 4.2, where the main time-averaged vortex structures and flow features are identified.
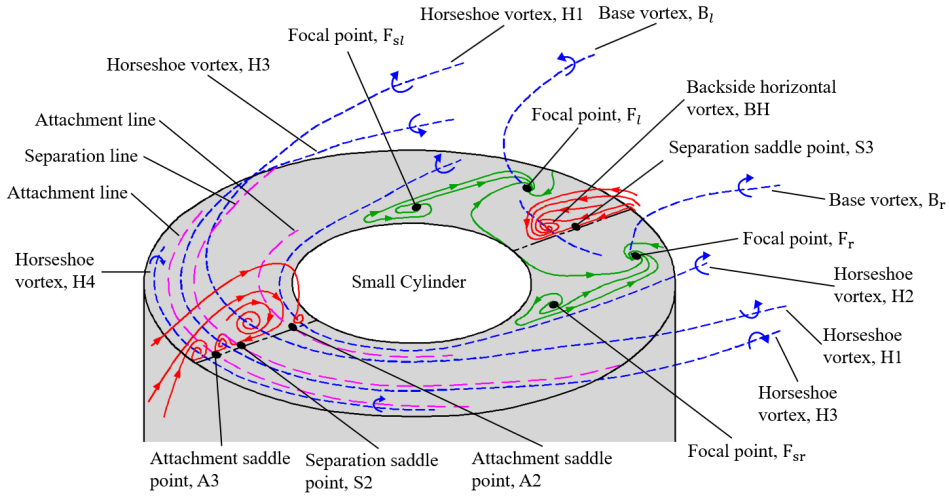
*Figure 4.2: Schematic of the flow field for the single step cylinder with $D/d = 2$ at $Re_D = 3900$ showing the main flow features. To ease observations, the surface of the small cylinder is omitted.*

## 4.2 Recommendation for future work

### 4.2.1 Vortex interactions in the direct mode wake of the step cylinder with small diameter ratios

Most of the existed studies, including the present thesis, focused on the vortex interactions in the indirect mode wake behind the step cylinders, where the complex vortex interactions, vortex dislocations, and consequent vortex loop structures were observed and discussed in detail. However, the characteristics of the direct mode wake behind the step cylinders with $D/d < 1.25$ have been seldomly analyzed. The smallest diameter ratio that has been investigated is 1.13 by Lewis and Gharib in 1992 [1]. The study related to the step cylinder cases with $D/d < 1.1$ is still blank. More investigations in such wakes can be done in the future.

### 4.2.2 Reynolds number and diameter ratio effects in the vortex system around the step cylinder

As described in Article 6 in the present thesis, four horseshoe vortices were identified around the step cylinder with $D/d = 2$ at $Re_D = 3900$. However, the previous studies only observed one horseshoe vortex and one edge vortex around the step cylinder at a relative low Reynolds number $Re_D = 150$ and

200. How the vortex system transfers from a step cylinder case at low Reynolds number to a case at high Reynolds number, and how the different diameter ratios affect the vortex system require a thorough investigation.

### 4.2.3 Turbulent wake behind step cylinders

For the wake flow behind step cylinders at sub-critical Reynolds numbers ($Re_D > 300$), the existed studies, including the present thesis, focused on the main types of vortex cells, the vortex interactions between these vortex cells, and the force distribution on the step cylinder surface. The detailed turbulent wake characteristics, e.g., the shear-layer instability and the statistical study of physical quantities, have never been studied yet.

### 4.2.4 Oscillatory flow around step cylinders

In marine hydrodynamics, the oscillatory flow around a bluff body is a popular and classical topic. With different Reynolds numbers ($Re$) and Keulegan–Carpenter number ($KC$), many fascinating flow patterns have been reported around uniform circular cylinders under the sinusoidal flow. Moreover, the lift coefficients at a particular series of $KC$ and $Re_D$ are of interest for many VIV prediction methods. However, until now, there is no study focusing on the oscillatory flow around step cylinder.

# References

[1] Lewis CG, Gharib M. An exploration of the wake three dimensionalities caused by a local discontinuity in cylinder diameter. *Phys. Fluids A: Fluid Dynamics* 1992; **4**(1):104–117.

[2] Dunn W, Tavoularis S. Experimental studies of vortices shed from cylinders with a step-change in diameter. *J. Fluid Mech.* 2006; **555**:409–437.

[3] Morton C, Yarusevych S. Vortex shedding in the wake of a step cylinder. *Phys. Fluids* 2010; **22**(8):083 602.

[4] Morton C, Yarusevych S, Carvajal-Mariscal I. Study of flow over a step cylinder. *Appl. Mech. Mater.* 2009; **15**:9–14.

[5] Morton C, Yarusevych S. Vortex dynamics in the turbulent wake of a single step cylinder. *ASME J. Fluids Eng.* 2014; **136**(031204).

[6] Norberg C. An experimental study of the flow around cylinders joined with a step in diameter. *Proceedings of the 11th Australasian Fluid Mechanics Conference, Hobart, Australia*, vol. 1, 1992; 507–510.

[7] McClure J, Morton C, Yarusevych S. Flow development and structural loading on dual step cylinders in laminar shedding regime. *Phys. Fluids* 2015; **27**:063 602.

[8] Wei T, Smith C. Secondary vortices in the wake of circular cylinders. *J. Fluid Mech.* 1986; **168**:513–533.

[9] McClure J, Pavan C, Yarusevych S. Secondary vortex dynamics in the cylinder wake during laminar-to-turbulent transition. *Phys. Rev. Fluids* 2019; **4**(12).

# Chapter 5

# Article 1: Numerical investigation of flow around a step cylinder

Cai Tian[1], Fengjian Jiang[2], Bjørnar Pettersen[1], Helge I. Andersson[3]

## Abstract

Flow past a step cylinder with diameter ratio $D/d = 2$ at Reynolds number $Re_D = 150$ was simulated by directly solving the three-dimensional unsteady Navier-Stokes equations. The vortical structures and shedding frequencies of the wake flow were studied in details. One kind of streamwise vortices, i.e. the 'edge vortex' was observed. Three main vortex cells (S-cell vortex behind the small cylinder, L-cell vortex behind the large cylinder and N-cell vortex in between) and the beat frequency which were reported by previous papers were also precisely captured in the present simulation. Additionally, half-loop connection between two L-cell vortices and loop connection between two N-cell vortices were captured. Specially, we noticed antisymmetric topology between two adjacent N-cell cycle periods.

[1]Department of Marine Technology, Norwegian University of Science and Technology, No-7491 Trondheim, Norway
[2]SINTEF Ocean, NO-7052 Trondheim, Norway
[3]Department of Energy and Process Engineering, Norwegian University of Science and Technology, No-7491 Trondheim, Norway

## 5.1   Introduction

In recent years, interfering effects in the wake of a step cylinder Fig 5.1 a) have received a lot of attention. Structures with similar shape of a step cylinder are used in many industrial applications, for example, the hull of a SPAR-platform, the outer wall of TV-towers, the supporting structures for offshore wind turbines (fixed and floating), and so on.

There are two important variables when considering flow past a step cylinder, i.e. the Reynolds number $Re_D$ and the ratio between diameters of large cylinder and small cylinder (diameter ratio D/d). Many experimental and numerical investigations have been out based on these two parameters. Lewis and Gharib [1] reported two vortex interaction modes in the wake, direct and indirect modes. The direct mode happens when the diameter ratio is smaller than 1.25 ($D/d < 1.25$). In this mode, vortices shed from the large cylinder and the small cylinder have direct connections, and the vortex interaction between them takes place in a very narrow region around the step. Only two dominating vortex shedding frequencies could be detected. When the diameter ratio becomes larger than 1.55 ($D/d > 1.55$), the indirect mode takes place. Except for the two dominated vortex shedding frequencies of the large and the small cylinder, another low vortex shedding frequency could be captured in the wake region downstream of the step. The vortex cell corresponding to this frequency was defined as N-cell by Dunn and Tavoularis [2]. In paper [2], three types of spanwise vortices were identified based on the shedding frequency: 1) S-cell vortex shedding from the small cylinder with the highest vortex shedding frequency; 2) N-cell vortex shedding in the interaction region [1] with the lowest vortex shedding frequency; 3) L-cell vortex shedding from the large cylinder. Moreover, Dunn and Tavoularis [2] also defined two kinds of streamwise vortices; the edge vortex and the junction vortex. The junction vortex was caused by the recirculation in the step region. The downwash of incoming fluid at the step region induced the edge vortex. They used hydrogen bubbles to visualize these two vortices by doing experiments with a step cylinder (D/d=2) for $Re_D = 1230$. Similar vortices were also observed by Morton and Yarusevych [3]. However, they did not show them directly by numerical simulations.

All of the papers [1, 2, 3] mentioned that the N-cell is a cyclic phenomenon (N-cell cycle). In [3], a detailed description and explanation were given. Morton and Yarusevych [3] suggested that it is the dislocation [4] in N-L cell boundary that causes the N-cell cycle. In their report, during this dislocation, a half-loop connection between two L-cell vortices was captured, but the repetition of L-cell half-loop connection was not shown.

Weak cross-boundary or half-loop connections between N-cell vortices were assumed to exist, but they did not observe it.

The primary aim of the present work is to show the structure of streamwise vortices and to investigate the dislocation process in the N-L cell boundary. In order to achieve this, the flow past a step cylinder (D/d=2) at Reynolds number 150 has been studied by means of solving the full three-dimensional unsteady Navier-Stokes equations. The isosurface of $\lambda_2$ [5] and velocity spectra were plotted for detailed discussions.

## 5.2 Flow configuration and computational method

### 5.2.1 Introduction to MGLET

All simulations in this study were conducted by directly solving the full three-dimensional unsteady Navier-Stokes equations for an incompressible fluid. This is achieved with the code MGLET [6, 7]. In this second-order finite-volume solver, the governing equations are in integral form:

$$\int_A \mathbf{u} \cdot \mathbf{n} \, dA = 0 \tag{5.1}$$

$$\frac{\partial}{\partial t} \iiint_\Omega u_i \, d\Omega + \oint_A u_i \, \mathbf{u} \cdot \mathbf{n} \, dA = -\frac{1}{\rho} \oint_A p \, \mathbf{i_i} \cdot \mathbf{n} \, dA + \nu \oint_A grad \, u_i \cdot \mathbf{n} \, dA \tag{5.2}$$

where $\Omega$ is the control volume and A is the control surface, $n$ is the unit vector on $dA$ pointing out of $\Omega$, and $i_i$ is the Cartesian unit vector in $x_i$ direction. The governing equations (5.1) and (5.2) are solved on a staggered Cartesian grid. By discretizing equation (5.2), the following format could be obtained:

$$\frac{\partial u}{\partial t} = D(u) + C(u) + G(p) = f(u, p) \tag{5.3}$$

In equation (5.3), D(u) represents the discretized diffusive term, C(u) represents the discretized convective term, and G(p) represents the discretized pressure term. The surface integral is approximated by the midpoint rule which is of second-order accuracy. The derivative in the integrand of the diffusive term is approximated by a central-difference formulation, which preserves the second-order accuracy. The volume integral in equation (2) is simply approximated by the product of the value of the integrand in the grid center and the control volume of the grid cell. The time integration of equation (3) is done by an explicit low-storage third-order Runge-Kutta

scheme [8] (details can be found in [9]). The general idea is to use an explicit time advancement scheme and correct the pressure through solving a Poisson equation to fulfill a divergence-free velocity field:

$$div[(G(\delta p))]\Delta t = div(u^*) \tag{5.4}$$

Equation (5.4) is referred to as the discrete analog of the Poisson equation, in which $\delta p$ is the pressure correction, and $u^*$ is an intermediate velocity field calculated by omitting the pressure term in equation (5.3). This discretized Poisson equation is represented by a linear equation system at every time marching step. This linear equation system is solved iteratively by Stone's Strongly Implicit Procedure (SIP) [10].

The use of a staggered Cartesian grid brings the problem of interpreting the solid boundaries of the step cylinder in the computational domain. This problem is solved in MGLET by introducing a direct-forcing Immersed Boundary Method (IBM). In MGLET, the surface of the geometry is represented by an unstructured triangular mesh and read directly to IBM to block grid cells bounded by this surface. Then the cells at the fluid-solid interface will be transformed into internal boundary conditions by interpolation [11] from the fluid cells in the vicinity of the bluff body geometry. A more detailed description of the IBM used in MGLET can be found in [11].

### 5.2.2   Flow configuration and coordinate system

Figure 5.1 a) shows the shape of the step cylinder, in which $D = 1m$ represents the diameter of the large circular cylinder and $d = 0.5D$ represents the diameter of the small circular cylinder. $l$ and $L$ represent the length of the small and large cylinder, respectively. The computational domain is depicted in Figure 5.1 b). The step cylinder was placed in a continuous uniform flow, $U = 1m/s$, flowing in the X-direction. The inlet plane is placed 10D upstream from center of the cylinder, while the outlet plane is placed 20D downstream. The width of the domain in y-z plane is 20D. The height of the domian is 30D, with the small and the large cylinders occupying 5D and 25D, respectively. Morton and Yarusevych [3] used the same domain size and cylinder length to model flow over a stepped cylinder with the same Reynold number [3]. The following boundary conditions are used in all simulations:

- The inflow boundary: uniform velocity profile u=U, v=0, w=0;

- The outlet boundary: Neumann boundary condition ($\frac{\partial u}{\partial x} = \frac{\partial v}{\partial x} = \frac{\partial w}{\partial x} = 0$) and constant zero pressure condition;
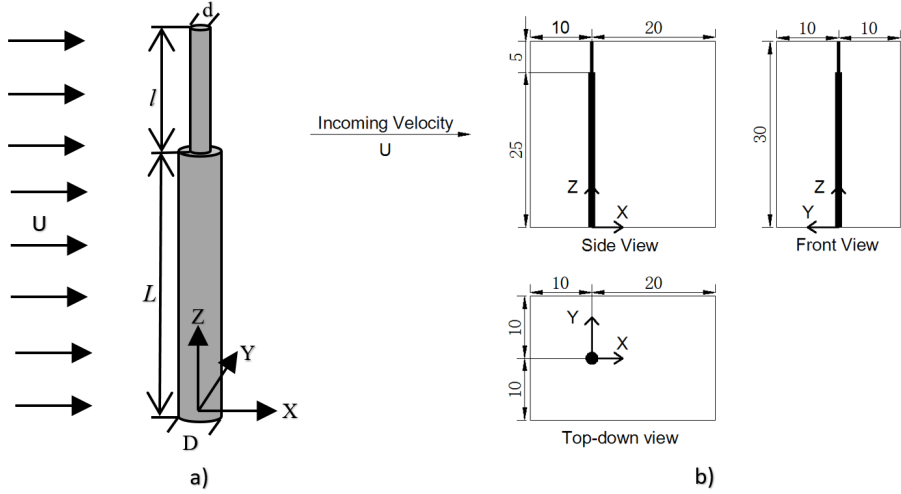
*Figure 5.1: a) The stepped cylinder geometry considered in the present study; b) Domain size illustrated from different viewpoints (Diameter of large cylinder D is the length unit).*

  - The body surfaces: no-slip and impermeable wall;

  - The other four surfaces: free-slip boundary condition;

## 5.3 Case summary and grid study

### 5.3.1 Case overview

*Table 5.1: Case information of all simulations*

| Case | $Re_D$ | Min Grid Spacing $\frac{\Delta}{D}$ | Grid cells $N_x \times N_y \times N_z$ | Total grid number | $\overline{C_D}$ |
|------|--------|------------------|------------------------|-------------------|-------|
| 1 | 150 | 0.01 | 414×356×384 | 56.59 million | 0.645 |
| 2 | 150 | 0.02 | 264×204×356 | 19.17 million | 0.641 |
| 3 | 150 | 0.05 | 244×184×336 | 15.09 million | 0.636 |
| 4 | 150 | 0.08 | 196×140×324 | 8.89 million | 0.632 |
| 5 | 150 | 0.1 | 174×124×304 | 6.56 million | 0.628 |

Specific details of all cases are summarised in Table 5.1. The Reynolds number ($Re_D$) in this study is defined based on the diameter of large cylinder $D$ and free-stream velocity $U$, i.e. $Re_D = \frac{UD}{\nu}$ where $\nu$ is the kinematic
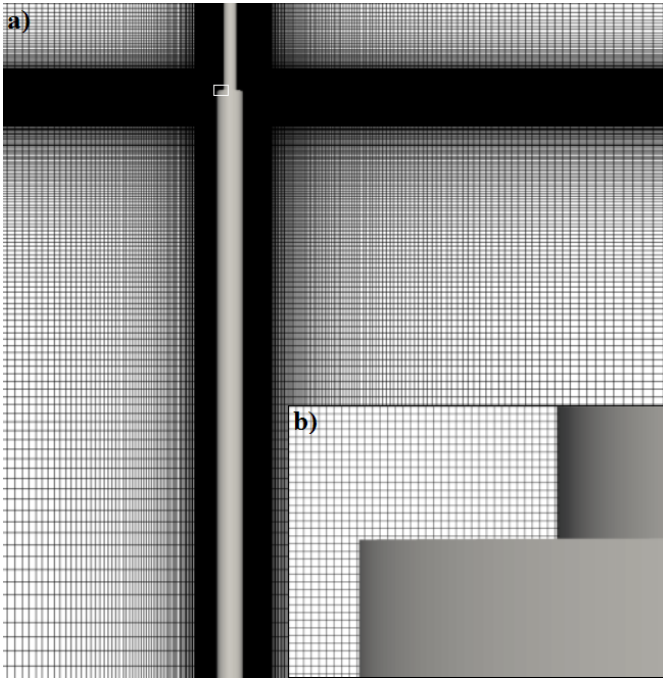
*Figure 5.2: a) Mesh structures in x-z plane at y=0; b) A zoom-in plot of mesh in the step region (white rectangle)*

viscosity of the fluid. For all five cases, $Re_D = 150$. The size of the computational domain for all cases is $30D \times 20D \times 30D$. All cases are simulated on a staggered Cartesian grid. In Fig 5.2 a), x-z plane view of the mesh structure at y=0 is presented. It is clear that there are two black bands. The quality of the grid in these two bands are better than the rest of the domain. These two bands make sure that the grid resolution near the step cylinder is good enough to resolve the flow phenomenon properly. Because of the abrupt change of cylinder diameter, the flow around the step is expected to be very complicated. A $2D \times 2D \times 2D$ "central block" wrapping the step area was built up. Uniform grid spacing (given in Table 5.1 as "Min Grid Spacing") is used in the "central block". A part of the uniform grid in the "central block" is plotted in the zoom-in plot, as shown in Fig 5.2 b). The approximate position of this grid is indicated by a white rectangle in Fig 5.2 a). The grid is gradually stretched outside of the central block to the far field and the max expansion rate is lower than 1.04. An immersed boundary method (IBM) [9, 11] is used to deal with the intersection between the Cartesian grid and the curved surface of the step cylinder. The same numerical method

was used recently by Jiang *et al.* [12] to simulate the wake behind a prolate spheroid. In Fig 5.3, the drag coefficient $C_D = F_X^{tot}/\rho u^2(dl + DL)$ and the lift coefficient $C_L = F_Y^{tot}/\rho u^2(dl + DL)$ of the step cylinder for case 1 are plotted. It can be observed that fully developed flow was obtained after 250 time units($D/U$). All cases have been running for at least 600 time units in parallel on a *SGI Altix ICE X SLES − 11sp3* cluster system. The time-step was set to guarantee the maximal CFL number lower than 0.6.
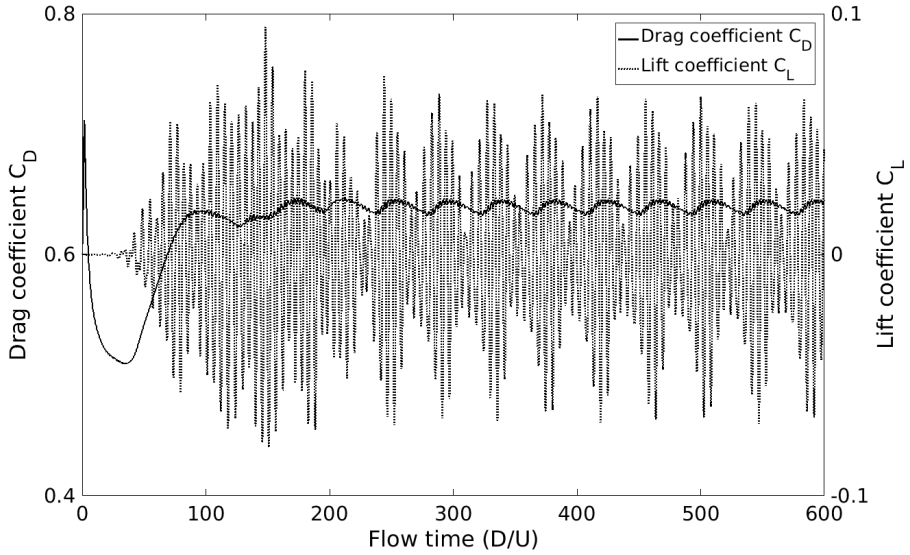


*Figure 5.3: Drag coefficient and lift coefficient of step cylinder for Case* 1.

### 5.3.2 Grid independence study

In order to ensure that the grid resolution is good enough to capture all important fluid phenomena, especially the complicated flow close to the step, five grids were generated for grid study, as shown in Table 5.1. First, a rough check was done. Based on the data of mean total drag coefficients $\overline{C_D} = \overline{F_X^{tot}}/\rho U^2(dl + DL)$ in Table 5.1, an convergence tendency can be found. Additionally, the difference between *Case* 1 and *Case* 2 is smaller than 0.6% Then, mean streamwise velocity distributions along line AB (as indicated in the subplot of Fig 5.4 b)) are calculated to illustrate the flow field near the step. The distribution curves of $\frac{\bar{u}}{U}$ are shown in Figure 5.4 a). It can be observed that the finer the grid is, the more smoothly the curve becomes (*Case* 1 and *Case* 2). The convergence tendency is clear by comparing the discrepancy between adjacent curves. Moreover, the difference between
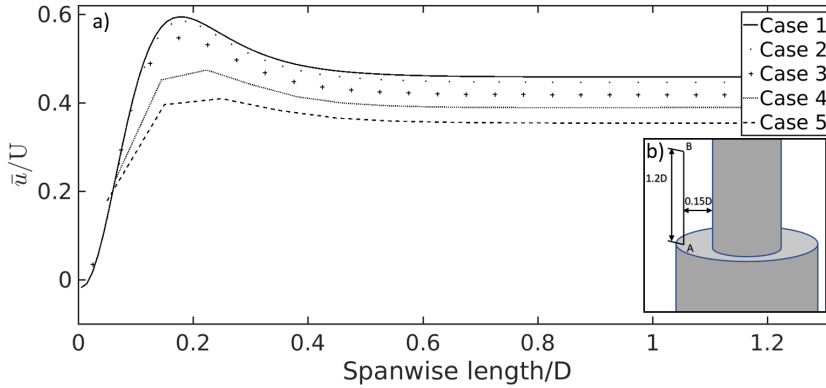
Figure 5.4: a) Mean streamwise velocity $\frac{\bar{u}}{U}$ distribution along line AB shown in Fig (b); b) Coordinates and length of line AB (in x-z plane with y=0).

Case 1 and Case 2 is almost negligible. It is therefore safe to conclude that the Case 1 has a fine enough grid resolution. All results presented in the following discussions are therefore based on resolution Case 1.

## 5.4   Results

### 5.4.1   Overview of flow development
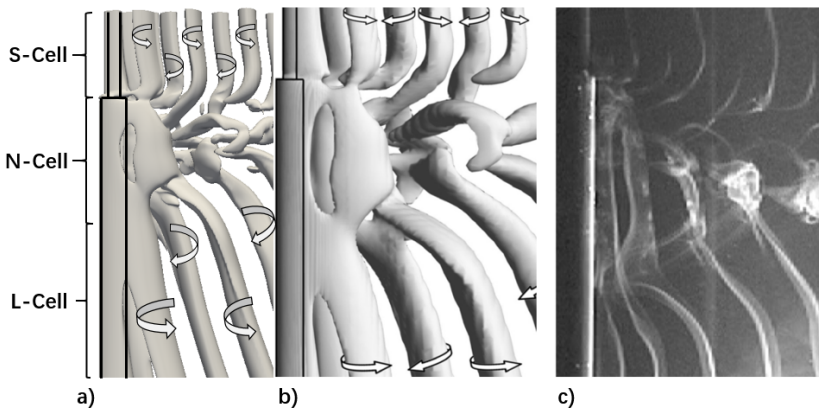


Figure 5.5: Vortex shedding in the wake of a step cylinder: a) Isosurfaces $\lambda_2 = -0.1$ for $Re_D = 150$ and $D/d=2$; b) Isosurfaces by Morton and Yarusevych [3] of $Q \approx 2 \times 10^{-3}$ c) Flow visualization image by Dunn and Tavoularis [2] for $Re_D = 150$ and $D/d=1.98$.

Overview of the vortical structures in the wake for $Re_D = 150$ is illustrated in Fig 5.5 a) by using isosurface of $\lambda_2 = -0.1$. Similar to the results of Morton and Yarusevych [3] and Dunn and Tavoularis [2], the vortex structures can be mainly divided into three types, namely, the S-cell, the N-cell and the L-cell. Comparing Fig 5.5 a), b) and c), we observed that the overall wake structures obtained by the present numerical simulation agrees well with previous numerical simulation [3] and experimental results[2]. Although the streamwise vortices is not detectable in Fig 5.5, the edge vortex was observed in the vicinity of the step. The junction vortex which was observed in [2, 3] was not captured by the present study. As can be observed in Fig 5.5, vortex structures in the N-cell area are far more complicated than those in the S-cell and L-cell areas. Moreover, it seems like all N-cell structures appear in the wake behind the large cylinder. Detailed discussions are presented in section 4.3.

### 5.4.2  Streamwise vortices
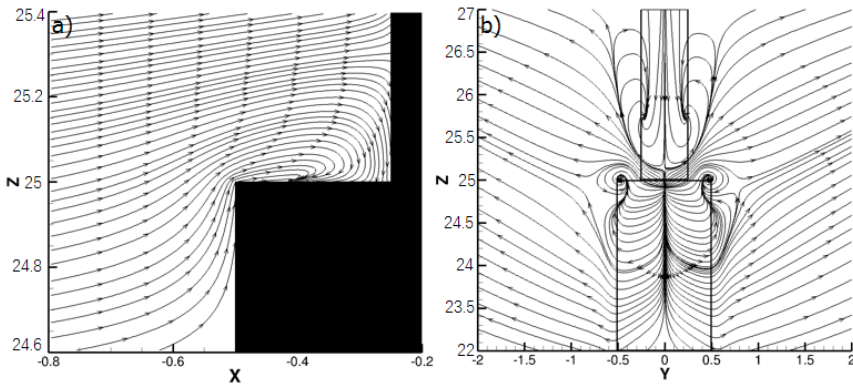


*Figure 5.6: a) Streamline near the step area at x-z plane with y=0; b) Streamline of projected velocity vector in the y-z plane at a downstream position of x=0.6 (i.e. Plane 2 shown in Fig 5.7 a))*

As the flow reaches the region near the step, the streamlines at the symmetry plane tend to separate at the leading edge of the small cylinder and produce a recirculation at the step surface of the large cylinder, which is shown in Fig 5.6 a). Due to this recirculation, a peak value of vorticity $\omega_y$ at the corresponding position was found in Fig 5.7 b). Based on the vortex structure in Fig 5.7 a), the concentrated high vorticity region at the shoulder in Fig 5.7 c) d) and the streamlines in Fig 5.6 b), it is clear that there is a streamwise vortex pair near the step. As discussed in [2], there

might exist two different kinds of streamwise vortices in the step cylinder flow, i.e. the 'junction vortex' and the 'edge vortex', respectively. The 'junction vortex' is caused by recirculation, when viewing upstream, the left-hand vortex tube should rotate clockwise while the right-hand vortex should rotate counterclockwise. The 'edge vortex' has a different topology than the 'junction vortex'. Since the 'edge vortex' is essentially generated by downwash at the edge of the step, it has an opposite rotating direction compared to the 'junction vortex' on each side shoulder of the step [2]. In this way, we may identify the streamwise vortex in the present study. In Fig 5.6 b), by plotting streamlines in y-z plane just behind the step cylinder, it is easy to find that when viewing upstream from behind the step cylinder, the left-hand vortex rotates counterclockwise and the right-hand vortex rotates clockwise. It means that the streamwise vortex structure marked by a white circle in Fig 5.7 a) is not the branch of a 'junction vortex', but the 'edge vortex'. Furthermore, the contours of $\omega_x$ in y-z plane at different x positions were presented in Fig 5.7 c) and d).
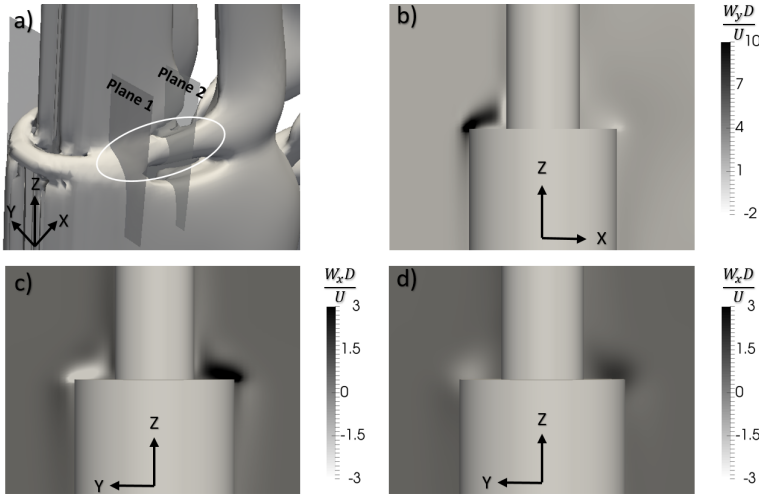


*Figure 5.7: a) Isosurface $\lambda_2 = -0.1$ showing vortex structure near the step; b) Vorticity contour of $\omega_y$ at x-z plane of y=0 ; c) Vorticity contour of $\omega_x$ at y-z plane of x=0 (i.e. Plane 1 in a)); d) Vorticity contour of $\omega_x$ at y-z plane of x=0.6D (i.e. Plane 2 in a))*

### 5.4.3   Spanwise vortex

Figure 5.8 shows the streamwise velocity spectra obtained to analyze the frequency and compositions of spanwise vortices. Also, by plotting the $\lambda_2$
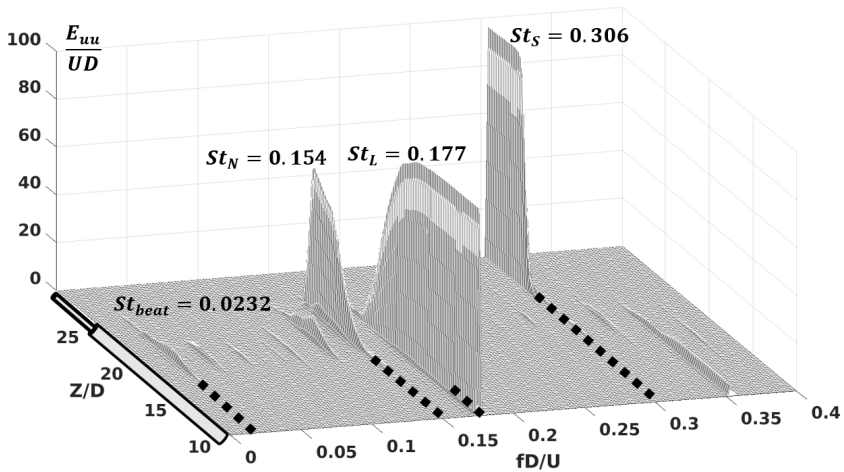
*Figure 5.8: Streamwise velocity spectra for x/D=2.5 and y/D=0.75*

isosurfaces in Fig 5.9, the spanwise vortex structures in the wake can be clearly observed. In order to analyze the generation of N-cell cycle (definition of N, S, L cell can be seen in Fig 5.5), we present consecutive images through a N-cell cycle in Fig 5.9. Moreover, the features and repetitions of N-cell cycle are shown in Fig 5.10. It is worthy to mention that the N-cell cycle refers to the cyclic changes in the N-cell instead of the N-cell vortex shedding, the differences will be explained in the following discussions.

- *Spanwise vortex shedding frequency*

  The streamwise velocity data is sampled at discrete points along a line parallel to z-axis at x/D=2.5 and y/D=0.75. By Fast Fourier Transform of the time-series of $u$, streamwise velocity ($E_{uu}$) spectra are presented in Fig 5.8. From this figure, three dominating peaks can be observed, corresponding to S-cell $St_S = f_S D/U = 0.306$, N-cell $St_N = f_N D/U = 0.154$ and L-cell vortices $St_L = f_L D/U = 0.177$. Additionally a smaller peak at the beat frequency $St_{beat} = f_{beat} D/U = 0.0232$ is also captured. The beat frequency is caused by linear combinations and harmonics of the shedding frequencies of the adjacent vortices, which is commonly observed in quasiperiodic spectra associated with spanwise vortex cells [4, 13]. In comparision, [3] reported $St_S = 0.320$, $St_N = f_N D/U = 0.157$, $St_L = f_L D/U = 0.179$ and $St_{beat} = 0.022$. The maximum discrepancy is smaller than 6%, which is totally acceptable.

- *Main spanwise vortex structures*

In Fig 5.9, first, behind the top half of the small cylinder, the S-cell vortex structures are shed, one by one, regularly and parallel to each other. This is similar to the wake structure behind a circular cylinder without a step. Secondly, behind the lower part of the small cylinder, due to the influence of the step, the complex connection between the N and S cell vortex appears. The connection can be mainly divided into two types: some of the S-cell vortices connected to the N-cell vortices, some of the S-cell vortices connected to the other side S-cell vortices forming a half-loop connection. For example, in Fig 5.9 a), the connection between vortex S2 and N1 belongs to the first type; while the connection between vortex S1 and S0 belongs to the second type.

$L - cell\ vortex$: Similar to the S-cell vortex, behind the lower part of the large cylinder, L-cell vortex structures are parallel to each other regularly. When we come closer to the step, we observed complex connections between the N-cell and L-cell vortices. In Fig 5.9, there are mainly two types of connections. The first one is characterized by a L-cell vortex connects to a corresponding N-cell vortex, like N5 to L5, N7 to L7 and so on. The other type is characterized by one L-cell vortex connects to the subsequent L-cell vortex forming a half-loop connection, like L1' to L0' and L2' to L3' in Fig 5.10.

$N - cell\ vortex$: There are two kinds of N-cell shedding: N-cell vortex shedding defined by $St_N$ and N-cell cycle shedding defined by $St_{beat}$. The time sequences in Fig 5.9 show the whole process of an N-cell cycle development. It is clear that the vortex structures in a) and h) are very similar, representing the same phase in two adjacent periods. From Fig 5.9, it can be found that around 14 N-cell vortices are shed during one N-cell cycle. This estimation agrees well with those reported in [2, 3].

$The\ features\ and\ repetition\ of\ N - cell\ cycle$: The N-cell cycle is caused by the dislocation between N-L boundary [3]. It means the period of the N-cell cycle is long, compared to the three main vortex cells. Moreover, during a N-cell cycle, the interactions and variations of three vortex cells are very complicated. It is necessary to find clear features that may help to identify the different cycles. Through long time observation (more than 200D/U), two distinct characteristics were captured, as shown in Fig 5.10. The first one is a half-loop connection generated between two L-cells, like L1' and L0' in Fig 5.10 a). The other is that a N-cell vortex on one side connected to the
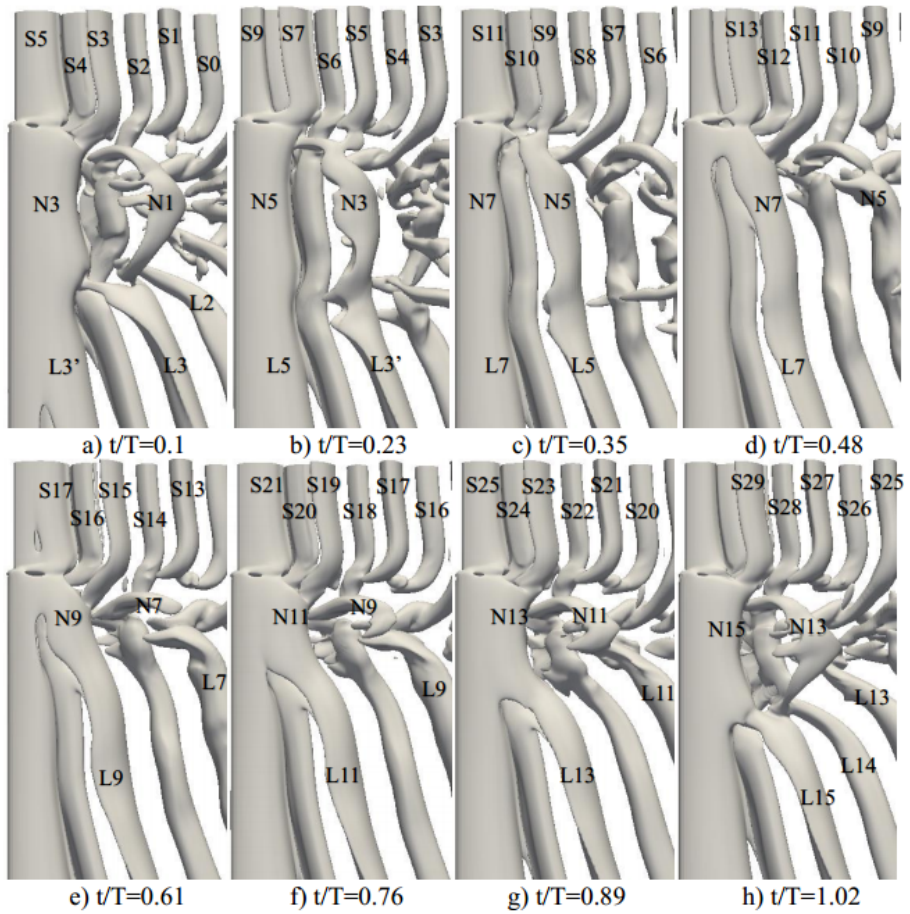
*Figure 5.9: Isosurface of $\lambda_2 = -0.1$ showing N-cell development. T is the period of one N-cell cycle defined by the beat frequency.*

subsequent N-cell vortex on the other side, forming a loop connection, like N0' and N1' in Fig 5.10 a). These two features always appear together and only once during every N-cell cycle. The half-loop connection was also captured by Morton and Yarusevych [3], but they did not show the repetition of this feature. Meanwhile, they speculated that the weak cross-boundary or half-loop N-cell vortex connections may persist but they couldn't observed it. The N-cell loop in Fig 5.10 nicely proves this speculation. To the authors' knowledge, this is the first time that the beat frequency is clearly identified and shown by the L-cell half-loop and N-cell loop.
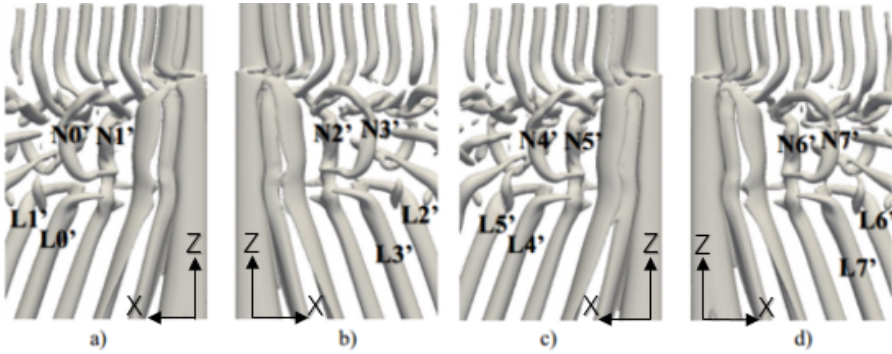
Figure 5.10: Isosurface of $\lambda_2 = -0.2$ showing features and repetitions of N-cell cycle a) t=659; b) t=701; c) t=743; d) t=785 ('D/U' is the time unit).

## 5.5   Conclusion

The study shows good agreement with previous researches [2, 3]. For streamwise vortices, the 'jucntion vortex' which was captured in [2] was not observed in the present study. This may be explained by a Reynolds number effect. Dunn and Tavoularis [2] observed the 'junction vortex' for $Re_D = 1230$ which is much higher than in the present study. However, the 'edge vortex' mentioned in [2] is captured in the present case and clearly shown in Fig 5.7 a). By calculating the streamwise velocity spectra, shedding frequencies of three main vortex cells together with the beat frequency were captured. The discrepancy is smaller than 6% compared to previous study [3]. The repetition of N-cell cycle was shown clearly in Fig 5.10. This phenomenon was speculated to exist in [3], but haven't been presented by any results. Another interesting observation is that the vortex structure is antisymmetric. Finally, different from the speculation about half-loop connection in [3], a full-loop connection between two N-cell vortices was observed.

In the future, higher Reynolds numbers (e.g. extending to $10^4$) and higher diameter ratios between large cylinder and small cylinder will be investigated to explore when a 'junction vortex' can be observed. Additionally, a study about how the loop connection for N-cell vortices is generated and why the vortex structure become anti-symmetric would be of interest.

## Acknowledgements

## References

[1] Lewis CG, Gharib M. An exploration of the wake three dimensionalities caused by a local discontinuity in cylinder diameter. *Phys. Fluids A: Fluid Dynamics* 1992; **4**(1):104–117.

[2] Dunn W, Tavoularis S. Experimental studies of vortices shed from cylinders with a step-change in diameter. *J. Fluid Mech.* 2006; **555**:409–437.

[3] Morton C, Yarusevych S. Vortex shedding in the wake of a step cylinder. *Phys. Fluids* 2010; **22**(8):083 602.

[4] Williamson CHK. Oblique and parallel modes of vortex shedding in the wake of a circular cylinder at low Reynolds numbers. *J. Fluid Mech.* 1989; **206**:579–627.

[5] Jeong J, Hussain F. On the identification of a vortex. *J. Fluid Mech.* 1995; **285**:69–94.

[6] Manhart M. A zonal grid algorithm for DNS of turbulent boundary layers. *Computers & Fluids* 2004; **33**(3):435–461.

[7] Manhart M, Friedrich R. DNS of a turbulent boundary layer with separation. *Int. J. Heat Fluid Flow* 2002; **23**(5):572–581.

[8] Williamson JH. Low-storage Runge-Kutta schemes. *J. Comput. Phys.* 1980; **35**:48–56.

[9] Peller N. Numerische simulation turbulenter strömungen mit immersed boundaries. PhD Thesis, Technische Universität München, München, Germany 2010.

[10] Stone HL. Iterative solution of implicit approximations of multidimensional partial differential equations. *SIAM J. Numer. Anal.* 1968; **5**:530–558.

[11] Peller N, Duc AL, Tremblay F, Manhart M. High-order stable inter-
     polations for immersed boundary methods. *Int. J. Numer. Meth. Fl.*
     2006; **52**:1175–1193.

[12] Jiang F, Gallardo JP, Andersson HI. The laminar wake behind
     a 6:1 prolate spheroid at 45 incidence angle. *Phys. Fluids* 2014;
     **26**(11):113 602.

[13] Gerich D, Eckelmann H. Influence of end plates and free ends on the
     shedding frequency of circular cylinders. *J. Fluid Mech.* 1982; **122**:109–
     121.

# Chapter 6

# Article 2: Antisymmetric vortex interactions in the wake behind a step cylinder

Cai Tian[1], Fengjian Jiang[2], Bjørnar Pettersen[1], Helge I. Andersson[3]

## Abstract

Flow around a step cylinder at Reynolds number 150 was simulated by directly solving the full Navier-Stokes equations. The configuration was adopted from [Morton and Yarusevych, Physics of Fluids 22, 083602(2010)], in which the wake dynamics were systematically described. A more detailed investigation of the vortex dislocation process has now been performed. Two kinds of new loop vortex structures were identified. Additionally, antisymmetric vortex interactions in two adjacent vortex dislocation processes were observed and explained. The results in this Letter serve as a supplement for a more thorough understanding of the vortex dynamics in the step cylinder wake.

In recent years, interfering effects in the wake of a step cylinder, as shown in Fig 6.1, have received considerable attention. Structures with a

[1]Department of Marine Technology, Norwegian University of Science and Technology, No-7491 Trondheim, Norway
[2]SINTEF Ocean, NO-7052 Trondheim, Norway
[3]Department of Energy and Process Engineering, Norwegian University of Science and Technology, No-7491 Trondheim, Norway
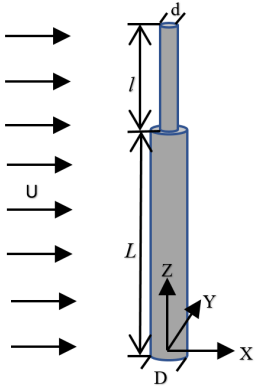
Figure 6.1: Step cylinder geometry considered ($D/d = 2, l = 5D, L = 25D$). The origin of the coordinate system locates in the center at the bottom of the large cylinder.

similar shape have been used in many industrial applications, for example, the hull of a SPAR-buoy, the outer wall of TV-towers, the supporting structures for fixed and floating offshore wind turbines, *etc.* There are two important parameters for flow past a step cylinder, *i.e.* the ratio between the large and the small cylinder diameter, $D/d$, and the Reynolds number $Re_D = UD/\nu$ (where $U$ denotes the free-stream velocity and $\nu$ denotes the kinematic viscosity). There exist many papers on the wake dynamics behind a step cylinder, both experimentally [1, 2, 3, 4, 5, 6] and numerically[7, 8, 9]. Lewis and Gharib [3] reported two vortex interaction modes in the wake, direct and indirect modes. The direct mode occurs when $D/d < 1.25$, where vortices shed from the large cylinder and the small cylinder have direct connections, and the vortex interaction between them takes place in a narrow region around the step. Only two dominating vortex shedding frequencies could be detected in this mode. When $D/d > 1.55$, the indirect mode takes place. In addition to the two dominating shedding frequencies of the large and small cylinder, another low shedding frequency could be captured in the wake downstream of the step. The vortex cells corresponding to this frequency were named N-cell by Dunn and Tavoularis [6]. They identified three types of spanwise vortices based on the shedding frequency: 1) S-cell vortex shedding from the small cylinder with the highest shedding frequency; 2) N-cell vortex shedding in the interaction region with the lowest shedding frequency; 3) L-cell vortex shedding from the large cylinder. Based on the different shedding frequencies and vortex interactions, Morton and Yarusevych[9] defined *vortex splitting* and *vortex dislocation* in the two interaction regions located between adjacent cells. In their paper, vortex interactions between S-cell and N-cell vortices were specifically described. However, vortex interactions between L-cell and N-cell vortices, and the vortex dynamics during the dislocation at the N-L cell boundary, still require a

complete explanation. The N-cell vortices shedding is a cyclic phenomenon (N-cell cycle) [3, 6, 9], and Morton and Yarusevych [9] suggested that it is the dislocation in the N-L cell boundary that causes the N-cell cycle. They moreover inferred that there will be 28 S-cell vortices, 14 N-cell vortices, and 16 L-cell vortices shed from the step cylinder during one N-cell cycle at $Re_D = 150$. This estimate is in good agreement with the results reported by Dunn and Tavoularis [6].

The primary aim of the present Letter is to investigate the vortex interactions and the vortex dislocations at the N-L cell boundary in the step cylinder wake in detail. To achieve this, the flow past a step cylinder (D/d=2) at $Re_D = 150$ was studied by using a well-validated [10, 11] Direct Numercial Simulation ($DNS$) code $MGLET$ [12] to directly solve the full Navier-Stokes equations. All aspects of the numerical details can be found in a conference paper [13].
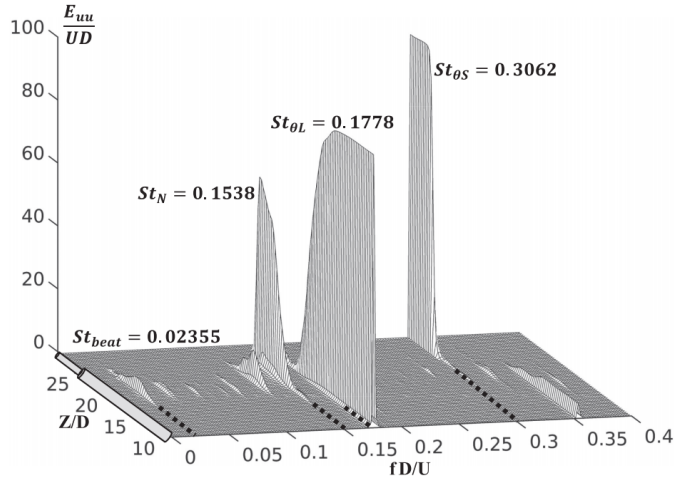


*Figure 6.2: Streamwise velocity spectra of a sample line at x/D=2.5 and y/D=0.75. The spectra were sampled over more than 50 N-cell cycles. We have verified that this plot will not at all be influenced by the choice of the sampling location in the near wake.*

The streamwise velocity is sampled at discrete points along a line parallel to the z-axis at $x/D$=2.5 and $y/D$=0.75 (the same as in Morton and Yarusevych [9]). The energy spectrum $E_{uu}$ is presented in Fig 6.2, from which three dominating peaks are clearly observed, corresponding to S-cell $St_{\theta_S} = f_S D/U = 0.3062$, N-cell $St_N = f_N D/U = 0.1538$ and L-cell vortices $St_{\theta_L} = f_L D/U = 0.1778$. In addition, a minor peak at the beat frequency, *i.e.* the frequency of vortex dislocations at the N-L boundary[9],

Table 6.1: *The present simulation results compared with Eq 6.1.  (Note: $St_{\theta_S}$ in Fig 6.2 is calculated based on the large cylinder diameter(D), $St'_{\theta_S}$ is based on the small cylinder diameter (d))*

|          | $\theta_L$ | $\theta_S$ | $St_{\theta_L}$ | $St'_{\theta_S}$ | $St_L$ | $St_S$ |
|----------|------------|------------|-----------------|------------------|--------|--------|
| Present  | 17         | 0          | 0.1778          | 0.1531           | 0.1859 | 0.1531 |
| Eq.(6.1) | -          | -          | -               | -                | 0.1854 | 0.151  |

$St_{beat} = f_{LN}D/U = (f_L - f_N)D/U = 0.02355$ is also captured. It is estimated from Fig 6.3 c), that the shedding angle $\theta_L$ in the wake behind the large cylinder is about $17°$, which means oblique shedding occurred. This is consistent with the findings of Dunn and Tavoularis [6], who used the same $D/d = 2$ in a wide range of $Re_D$ ($63 < Re_D < 1100$) and noticed that the vortex inclination in the wake behind the step cylinder is between $0°$ and $30°$ with respect to the cylinder axis. Morton and Yarusevych [9] also reported that, due to oblique vortex shedding, the Strouhal numbers ($St$) of the S- and L-cell are lower than those obtained in simulations of the wake behind a uniform cylinder at the same $Re_D$. If the oblique shedding data are recast into a parallel-shedding Strouhal number $St = St_\theta/cos(\theta)$, the comparison with the empirical formula from Williamson and Brown [14]

$$St = 0.2731 - 1.1129/Re^{0.5} + 0.4821/Re. \tag{6.1}$$

in Table 6.1 shows that the $St$ values deduced from this study fit closely with Eq 6.1.

The generation of S-cell vortices and the vortex interactions between S- and N-cell vortices have been discussed in detail by Morton and Yarusevych [9]. Based on their work, the present study focuses on the complex interaction between L- and N-cell vortices, of which some interesting features, not reported before, will be presented and discussed.

The vortex structures of isosurface of $\lambda_2$ [15] in the near wake are illustrated by consecutive snapshots in Fig 6.3, where selected N- and L-cell vortices are numbered. The time instant of Fig 6.3 a), $t = 651.06D/U$, was set as $t = 0$ to ease the discussion. We use a combination of capital letters and numbers to label all N- and L-cell vortices, 'N' or 'L' denote vortices belonging to N-cell or L-cell, respectively, while the number denotes the shedding order. To distinguish vortices shed from different sides of the cylinder, we use numbers, *e.g.* 1, 2... indicating vortices shed from the "-Y" side, and numbers with prime, *e.g.* 1', 2'..., to indicate vortices
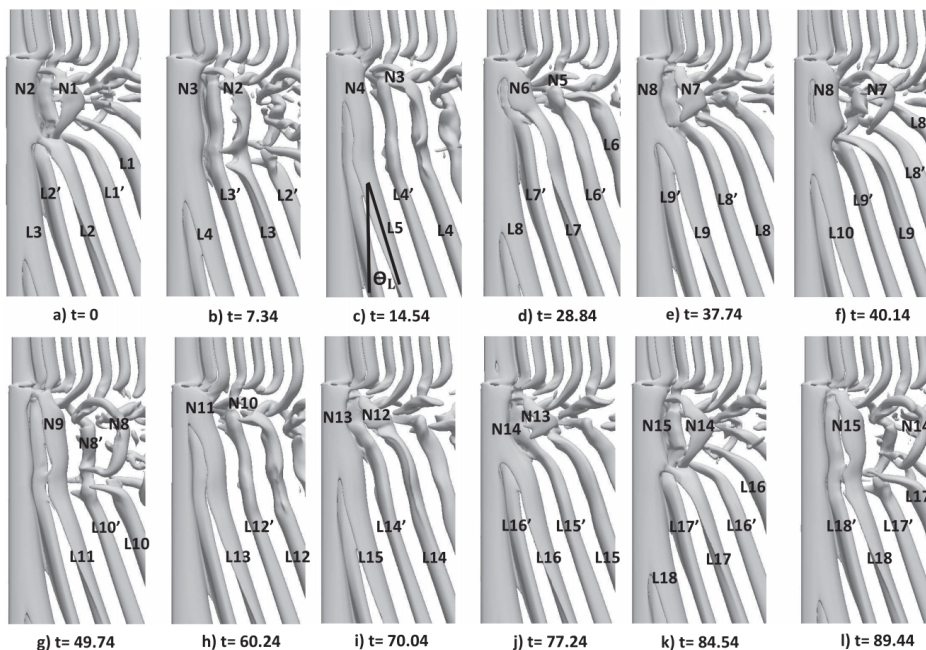
*Figure 6.3: Isosurfaces of $\lambda_2$=-0.15 showing vortex structures development. The actual time $t = 651.06D/U$ in a) is set to $t = 0$ to ease the disussions. There are about two N-cell cycles from a) to l).*

shed from the "+Y" side. We have learned from previous studies [6, 9] that the N-cell vortices change cyclically, referred to as *N-cell cycles*, and are characterized by vortex dislocations between N- and L-cell vortices. Before a vortex dislocation occurs, L-cell vortices shed in phase with N-cell vortices. In other words, each L-cell vortex forms a direct connection with one corresponding N-cell vortex, like N2-L3, N3-L4 *etc.* in Fig 6.3 b) and 6.3 c). When a dislocation happens, complex vortex interactions take place, and we call this process a *vortex dislocation process*. It has been reported in a previous study [9] that, during the vortex dislocation process, two L-cell vortices disconnect with their counterpart N-cell vortices and form a *L-L half loop* as shown by the green curves in Fig 6.4 h)(*i.e.* L9'-L10). Through the present study, we observed additional interesting features:

**1.** In addition to the L-L half loop, we have identified two other types of loop structures in every N-cell cycle: the *real loop* (also called a N-N loop) and the *fake loop* (also called a N-L loop).

**2.** The vortex interactions show distinct anti-symmetrical features between two adjacent N-cell cycles.

These phenomena can be observed in the consecutive snapshots in Fig 6.4, where the vortex structures are shown from both '+Y' and '-Y' sides of the step cylinder in order to facilitate the discussion. In the fake loop structure, a N-cell vortex connects to a L-cell vortex as shown by the red curves (both solid and dotted) in Fig 6.4. We name this kind of loop a 'fake loop', because it has a similar appearance, *i.e.* a vortex-ring-like structure, as the following 'real loop'. However, their connection topology is essentially different. This is very important for understanding the dislocation process. During the dislocation process, when a L-cell vortex breaks away from the corresponding N-cell vortex from the same side (L8' and N7' in Fig 6.4 a) and Fig 6.4 c)), the L-cell vortex can not just end in the fluid and must therefore connect with the N-cell vortex from the other side (L8'-N7 in Fig 6.4 c)). This leads to the generation of a fake loop structure shown by the red curve in Fig 6.4 d). Following this process, the formation of the second fake loop L9 and N7', and a L-L half-loop (L10-L9') becomes unavoidable for topological reasons.
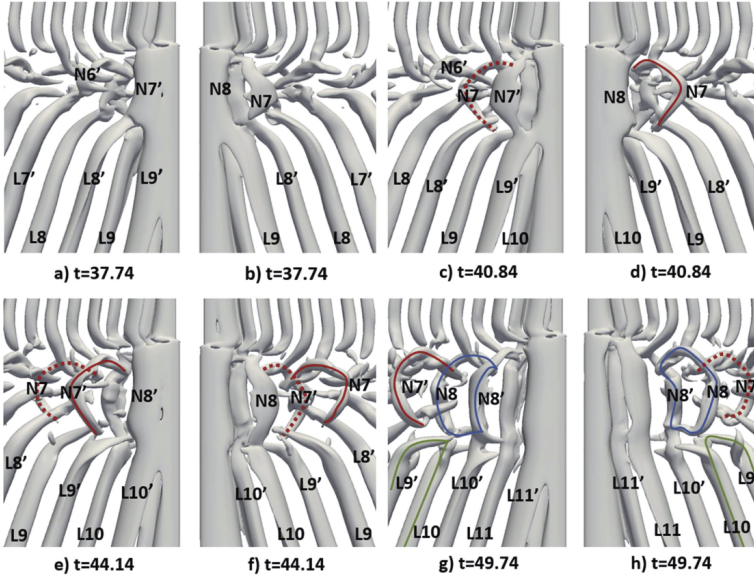


*Figure 6.4: Isosurfaces of $\lambda_2 = -0.15$ showing vortex interactions occurring at the N-L cell boundary during the dislocation process. (a, c, e, g) are observed from '+Y' to '-Y' side, while (b, d, f, h) are observed from the opposite side. Solid and dashed red curves indicate fake loops (N-L loop) from different sides, blue closed curves show real loops (N-N loop) and green curves show L-L half loops.*

Different from the fake loop, the real loop is formed by two N-cell vortices

shed from opposite sides connecting to each other. With the development of the L-L half loop L10-L9' in Fig 6.4 h), the N-cell vortex N8 looses its counterpart L-cell vortex L10. Meanwhile, there is no isolated L-cell vortex on the other side (L10' connects neatly to N8'), which means that no fake loop can be generated. However, the N8 vortex can not just end in the fluid. Therefore two N-cell vortices shed from opposite sides inevitably connect to each other to form a real loop structure, as indicated by the blue closed curve in Fig 6.4 h).
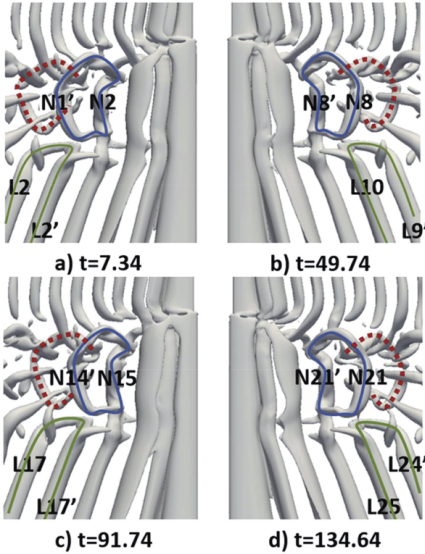


*Figure 6.5: Isosurface of $\lambda_2 = -0.2$ showing features and repetitions of the N-cell cycle.(a, c) are observed from '+Y' to '-Y' side, while (b, d,) are observed from the opposite side. Similar colors as used in Fig 6.4 represent different kinds of vortex loop structures.*

The recognition of the real and fake loops further help us to observe another interesting phenomenon in this wake, namely the antisymmetry. In Fig 6.5, the snapshots from the wake in the same phase of four continuous N-cell cycles are shown. It is clear that the L-L half loop and the loop structures (both real and fake) all occurred anti-symmetrically instead of symmetrically. In other words, real loops (N-N loop) from two adjacent dislocation processes are led by N-vortices shed from opposite sides. The same phenomenon occurs for the L-L half loop and the fake loop (N-L loop). For example, in Fig 6.5 a) and c), the real loop is led by N1' and N14' from '+Y' side, while the real loop in Fig 6.5 b) and d) is led by N8 and N21 from the '-Y' side. A similar sequence occurs for the L-L half loop. To the authors' best knowledge, this antisymmetric phenomenon, caused by the intrinsically different vortex connection topology in adjacent dislocation processes, has never been reported before.

The time history and vortex connection topology of the vortices in the
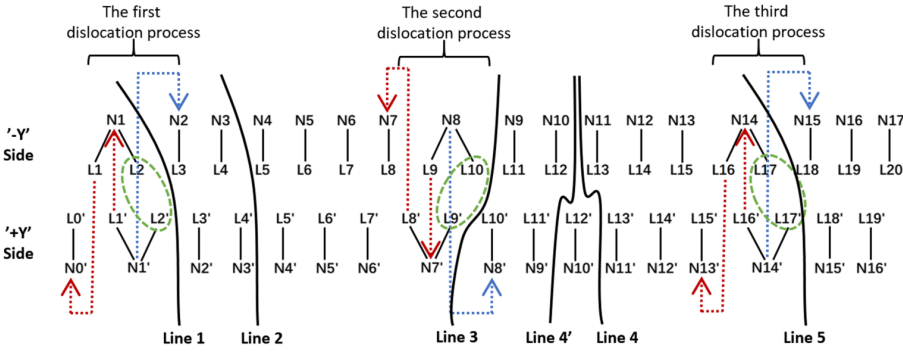
*Figure 6.6: Time history of the vortex shedding. The short straight black lines represent the connection between the L-cell vortex and its counterpart N-cell vortex. The same colors as used in Fig 6.4 reveal different kinds of loop vortex structures.*

wake are sketched in Fig 6.6 based on long-time observations. The corresponding time sequence of the instantaneous iso-surfaces of $\lambda_2$ can also be seen in Fig 6.3. The straight short black lines in Fig 6.6 indicate connections between the L-cell vortex and its N-cell vortex counterpart. When one N-cell vortex is connected to two L-cell vortices (*e.g.* N1 is connected to L1 and L2), a dislocation occurs.

In Fig 6.6, the first dislocation process begins from the '-Y' side (N1 connects to two L-cell vortices L1 and L2). This dislocation caused the fake loop to appear firstly at the '+Y' side (L1 and N0' connection). Then another fake loop (L1'-N1), a L-L half-loop (L2-L2') and a real loop (N1'-N2) were generated in succession. This scenario can be observed in Fig 6.5 a). Contrary, the second dislocation process begins from the '+Y' side (N7' connected to two L-cell vortices L8' and L9'). The fake loop vortex structure therefore firstly appeared on the -Y' side (L8 - N7). The other loop structures are also antisymmetric with respect to the first dislocation process. This scenario is shown in Fig 6.5 b). The third dislocation process is exactly the same as the first one, e.g. Fig 6.5 c) compared with Fig 6.5 a). The antisymmetrical periodic phenomenon can also be observed in Fig 6.7, in which the time trace of a velocity time trace is plotted. This anti-symmetry system gives the ratio of numbers of N-cells to L-cells $26/30 \approx 0.867$, which agrees well with the ratio between the shedding frequencies $f_N/f_L = 0.865$.

By knowing the antisymmetric feature, one may incorrectly infer that fig 5a) and 5c) form a complete N-cell cycle period. However, it is noteworthy to mention that although two adjacent dislocation processes are
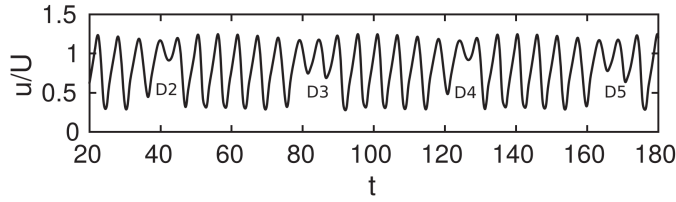
*Figure 6.7: Time trace of the streamwise velocity at a sample point $(x, y, z)/D = (2.5, 0.75, 19.5)$. 'D2' means the second dislocation process defined in Fig 6.6, same for D3, etc.*

antisymmetric, the frequency of the N-cell cycle is still decided by the beat frequency $(f_{LN}=f_N-f_L)$ rather than by twice the beat frequency. In other words, although fig 5a) and b) are antisymmetric, they form a complete N-cell cycle. The dislocation process is complicated and continues over four L-cell vortices. We believe that the generation of the L-L half loops (*e.g.* L2-L2') should serve as the bound between two N-cell cycles. Based on this, the period of the N-cell cycle is defined as the time between Line 1 and Line 3 (or Line 3 and line 5), shown in Fig 6.6. It is found that the duration between two L-L half loops (the green dashed circle in Fig 6.6) is constant, equal to 7.5 times the shedding period of L-cell vortices $T_L$, regardless of the antisymmetric scenario. This fits well with $f_L/f_{LN}=7.55$ from Fig 6.2. This particular frequency ratio causes the observed antisymmetries. On the other hand, if the frequency ratio had happened to be an integer, we believe that the dislocation process would have been symmetric.

Previous studies [6, 9] reported that there are 14 N-cell vortices and 16 L-cell vortices during one N-cell cycle. However, after now having uncovered the antisymmetry of two adjacent dislocation processes, we realize there are actually 13 N-cell vortices and 15 L-cell vortices in one N-cell cycle. Without paying attention to the antisymmetry of the vortex interaction, one may conclude that the period from Line 2 to Line 4 in Fig 6.6 is a N-cell cycle based on the fact that Fig 6.3 c) and Fig 6.3 h) correspond to the same phase of the N-cell cycle, in which there are 14 N-cell vortices and 16 L-cell vortices (as reported by Morton and Yarusevych [9]). However, by considering the antisymmetry, it is clear that, instead of Line 2 and Line 4, the time lapse between Line 2 and Line 4' should be counted as the N-cell cycle period, during which there are 13 N-cell vortices and 15 L-cell vortices, as documented in Fig 6.6.

In summary, our present results show good agreement with previous studies, including distinct spanwise vortices, S-, N- and L-cells [6], and the vortex dislocations [3, 6, 9] occurring at the N-L boundary. More impor-

tantly, the numerical results provid more detailed information about the vortex dislocation process, from which two new loop structures in this wake were identified, *i.e.* the *fake loop* between N- and L-cell vortices, and the *real loop* between two N-cell vortices. We have clearly shown that there are in total two fake loops, one real loop, and one L-L half loop generated during each dislocation process. Additionally, based on the new understanding of the intrinsically different connection topology of real and fake loops, an antisymmetry between two adjacent N-cell cycles has been observed and reported for the first time. Due to this antisymmetric feature, different from previous experiment [6] and simulation [9], we found that there are 13 N-cell vortices and 15 L-cell vortices in every N-cell cycle in the 2:1 step cylinder wake at $Re_D = 150$. The identification of the real and fake loop, together with the observation of the antisymmetric features in the dislocation process, offer a deeper and more complete understanding of this wake phenomenon. Although vortex dislocations are common in bluff body wakes, we should mention the particularity of the phenomena reported in this Letter, for which N-cell vortices play a central role. The N-cell vortex is probably a unique feature of step cylinder wakes. Yet there exist the possibility that similar vortical structures may appear in other wakes, albeit with different appearances. We leave this as an open question for further investigation.

# References

[1] Yagita M, Kojima Y, Matsuzaki K. On vortex shedding from circular cylinder with step. *Bulletin of JSME* 1984; **27**(225):426–431.

[2] Ko NWM, Chan ASK. In the intermixing region behind circular cylinders with stepwise change of the diameter. *Experiments in Fluids* 1990; **9**(4):213–221.

[3] Lewis CG, Gharib M. An exploration of the wake three dimensionalities caused by a local discontinuity in cylinder diameter. *Phys. Fluids A: Fluid Dynamics* 1992; **4**(1):104–117.

[4] Norberg C. An experimental study of the flow around cylinders joined with a step in diameter. *Proceedings of the 11th Australasian Fluid Mechanics Conference, Hobart, Australia*, vol. 1, 1992; 507–510.

[5] Ko NWM, Chan ASK. Wakes behind circular cylinders with stepwise change of diameter. *Experimental Thermal and Fluid Science* 1992; **5**(2):182–187.

[6] Dunn W, Tavoularis S. Experimental studies of vortices shed from cylinders with a step-change in diameter. *J. Fluid Mech.* 2006; **555**:409–437.

[7] Vallès B, Andersson HI, Jenssen CB. Direct-mode interactions in the wake behind a stepped cylinder. *Phys. Fluids* 2002; **14**(4):1548–1551.

[8] Morton C, Yarusevych S, Carvajal-Mariscal I. Study of flow over a step cylinder. *Appl. Mech. Mater.* 2009; **15**:9–14.

[9] Morton C, Yarusevych S. Vortex shedding in the wake of a step cylinder. *Phys. Fluids* 2010; **22**(8):083 602.

[10] Jiang F, Gallardo JP, Andersson HI, Zhang Z. The transitional wake behind an inclined prolate spheroid. *Physics of Fluids* 2015; **27**(9):093 602.

[11] Gallardo JP, Andersson HI, Pettersen B. Turbulent wake behind a concave curved cylinder. *J. Fluid Mech.* 2014; **742**:192.

[12] Manhart M. A zonal grid algorithm for DNS of turbulent boundary layers. *Computers & Fluids* 2004; **33**(3):435–461.

[13] Tian C, Jiang F, Pettersen B, Andersson HI. Numerical investigation of flow around a step cylinder. *Proceedings of 9th National Conference on Computational Mechanics (CIMNE), Trondheim, Norway, May 11-12, 2017*; 369–384.

[14] Williamson CHK, Brown GL. A series in $1/\sqrt{Re}$ to represent the Strouhal–Reynolds number relationship of the cylinder wake. *J. Fluid Struct.* 1998; **12**(8):1073–1085.

[15] Jeong J, Hussain F. On the identification of a vortex. *J. Fluid Mech.* 1995; **285**:69–94.

# Chapter 7

# Article 3: The long periodicity of vortex dislocations in the wake behind a step cylinder

Cai Tian[1], Fengjian Jiang[2], Bjørnar Pettersen[1], Helge I. Andersson[3]

## Abstract

By directly solving the three-dimensional unsteady Navier-Stokes equations, the wake flow behind a step cylinder with diameter ratio $D/d = 2$ at Reynolds number $Re_D = 150$ was investigated. The dominating frequency components and vortex interactions in the wake were studied in detail. Same as in previous studies, three spanwise vortex cells (the S-cell vortex behind the small cylinder, the L-cell vortex behind the large cylinder and the N-cell vortex between them) with different shedding frequencies were precisely captured in the present paper. Complex vortex interactions occur between these vortex cells. We focused on the vortex dislocations between the N-

[1]Department of Marine Technology, Norwegian University of Science and Technology, No-7491 Trondheim, Norway
[2]SINTEF Ocean, NO-7052 Trondheim, Norway
[3]Department of Energy and Process Engineering, Norwegian University of Science and Technology, No-7491 Trondheim, Norway

and L-cell vortices. A long periodicity of the vortex dislocation is reported and analyzed. Several long time numerical simulations (more than 3000 $D/U$ time units) were conducted to illustrate and analyze the wake flow. Benefit from it, a long period characteristic of the vortex dislocation was reported and analyzed. Additionally, the challenges of the grid resolution for investigating the long period phenomenon were discussed.

## 7.1  Introduction

In recent years, the wake flow behind a step cylinder has attracted more and more attention from researchers. Due to the abrupt change in diameter, the vortical structures in the near wake behind the step cylinder are complex even at a low Reynolds number, e.g. $Re_D = 150$, as shown in figure 7.7.

When considering flow past a step cylinder, there are two important parameters, i.e. the ratio between the large cylinder and the small cylinder (diameter ratio $D/d$) and the Reynolds number ($Re_D$). By doing laboratory experiments, Lewis & Gharib [1] observed and reported two vortex interaction modes, direct and indirect modes. When the diameter ratio is smaller than 1.25, only two dominating vortex shedding frequencies can be captured in the wake of the step cylinder, corresponding to the vortices shed from the large cylinder and the small cylinder, respectively. These two vortex cells directly connect to each other, and the vortex interactions between them occur in a narrow region behind the step. This mode is called the direct mode. The indirect mode happens when the diameter ratio ($D/d$) becomes larger than 1.55. Besides the two dominating vortex shedding frequencies of the small and large cylinder, a distinct frequency can be detected in the region downstream of the step. Lewis & Gharib [1] defined the region containing this distinct frequency as the modulation zone (the N-cell area in the present paper, see figure 7.1). Based on the shedding frequencies and locations of different vortex cells, Dunn & Tavoularis [2] defined three vortex cells behind the step cylinder with $D/d = 2$: (1) S-cell vortex shedding from the small cylinder with the highest vortex shedding frequency; (2) L-cell vortex shedding from the large cylinder; (3) N-cell vortex shedding near the step position between the S- and L-cell vortices, with the lowest vortex shedding frequency. The shedding areas of these three vortex cells are illustrated in figure 7.1. The terminologies S-cell, N-cell and L-cell were later used in many studies [3, 4, 5, 6], and are also used in the present study.

Due to the different shedding frequencies, neighbouring vortex cells move either in-phase or out-of-phase with each other. When they move out-of-phase, the contorted 'tangle' of vortices appears at the boundary be-
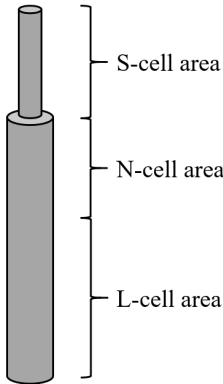
Figure 7.1: The shedding areas of the three vortex cells, i.e. S-, N- and L-cell area.

tween them, which looks like the dislocations that appear in solid materials. Williamson [7] defined this kind of vortex interaction as the vortex dislocation. The similar physical phenomena were also observed in the wake behind the step cylinder. In 1992, Lewis & Gharib [1] observed that an inclined interface between the N-cell and L-cell area appears at the beat frequency $(f_L - f_N)$. They suspected that this inclined interface might be caused by the variation of the actual spanwise length of the N-cell vortices. In 2010, Morton & Yarusevych [3] proved this suspicion. By doing numerical simulations, they clearly presented a cyclic variation of the N-cell vortices. In their studies, as N- and L-cell vortices move out-of-phase, in parallel with the appearances of the vortex dislocation, the spanwise length of the N-cell vortices and the position of the N-L cell interface change periodically with the beat frequency $(f_L$-$f_N)$. Morton & Yarusevych [3] defined these cyclic variations as the N-cell cycle. In 2017, Tian et al. [6] further investigated the vortex dislocation between N- and L-cell vortices in detail. They identified two new loop structures: the NL-loop (the fake loop) structure formed between a N-cell and a L-cell vortex, and the NN-loop (the real loop) structure formed between two adjacent N-cell vortices. Based on careful observations of the formation processes of these loop structures, an antisymmetric vortex interaction was also reported between two adjacent N-cell cycles.

In 2015, McClure et al. [8] were the first reported the long period characteristic of the vortex dislocation by investigating flow past dual step cylinders $(1 < D/d < 4)$ at $Re_D = 150$. They found that there is a continuous variation in the vortex dislocations, i.e. the neighboring vortex dislocations are not exactly the same. They also defined the time period between two identical vortex dislocations as the fundamental dislocation cycle.

Compare to the interesting observations in this wake, what was much less focus on in the literature is the computational challenges in conducting

simulations of the step cylinder wakes. Many complex and small vorti-
cal structures play important roles in the vortex interactions in this wake.
These vortices are far more difficult to capture compared to the primary
vortices. In addition, insufficient grid resolution may have little influence
on the primary vortices, but will have strong effects on the vortex dislo-
cations. When we discuss the long period phenomena, this becomes even
more critical.

In the present paper, we investigate and report some interesting long
period phenomena, and a subsequent computational challenge. In order
to achieve this, the flow past a step cylinder ($D/d = 2$) at $Re_D = 150$
is studied by means of solving the full three-dimensional unsteady Navier-
Stokes equations. The isosurface of $\lambda_2$ and the time trace of velocity are
plotted and observed for a relatively long time period (more than 2000
$D/U$). Last but not least, the challenges of investigating the long periodic
phenomenon are discussed.

## 7.2 Computational method and flow configuration

### 7.2.1 Computational method

For all simulations in the present study, the full three-dimensional incom-
pressible Navier-Stokes equations were directly solved by the code MGLET
[9, 10]. In this second-order finite-volume solver, the governing equations
are in integral form:

$$\int_A \mathbf{u} \cdot \mathbf{n} \, dA = 0 \tag{7.1}$$

$$\frac{\partial}{\partial t} \iiint_\Omega u_i \, d\Omega + \oint_A u_i \, \mathbf{u} \cdot \mathbf{n} \, dA = -\frac{1}{\rho} \oint_A p \, \mathbf{i_i} \cdot \mathbf{n} \, dA + \nu \oint_A grad \, u_i \cdot \mathbf{n} \, dA \tag{7.2}$$

where A and $\Omega$ are the control surface and the control volume, respec-
tively. $\mathbf{n}$ is the unit vector on $dA$ pointing out of $\Omega$, and $\mathbf{i_i}$ is the Cartesian
unit vector in $\mathbf{x_i}$ direction. All simulations are done on a staggered Cartesian
mesh. After discretizing equation (10.2), we get

$$\frac{\partial u}{\partial t} = D(u) + C(u) + G(p) = f(u, p) \tag{7.3}$$

in which D(u) represents the discretized diffusive term, C(u) represents
the discretized convective term, and G(p) represents the discretized pres-
sure term. The midpoint rule is used to approximate the surface integral,

leading to second-order accuracy in space. The diffusive term is approximated by a central-difference formulation, which preserves the second-order accuracy. The time integration of equation (7.3) is conducted by a third-order explicit low-storage Runge-Kutta scheme [11] (details can be found in [12]). The pressure term is corrected by solving a Poisson equation to fulfill a divergence-free velocity field:

$$div[(G(\delta p))]\Delta t = div(u^*) \tag{7.4}$$

where $\delta p$ is the pressure correction, $u^*$ is an intermediate velocity field calculated by omitting the pressure term in equation (7.3) and $\Delta t$ is the constant time step that ensures a CFL number smaller than 0.7. At every marching time step, this discretized Poisson equation is represented by a linear equation system, which is solved by Stone's Strongly Implicit Procedure (SIP) [13].

The solid boundaries of the step cylinder is handled by an immersed boundary method (IBM). In MGLET, we use an unstructured triangular mesh to represent the surface of the geometry, and directly transfer information to IBM to block grid cells bounded by this surface. Then the grid cells at the fluid-solid interface will be set as internal cells by interpolating the flow variables from the surrounding cells. A more detailed description of the IBM used in MGLET can be found in [14].

## 7.2.2  Flow configuration

The geometry of the step cylinder investigated in the present paper is shown in figure 7.2 (a), in which $D$ is the diameter of the large circular cylinder, and $d$ is the diameter of the small cylinder. $l$ and $L$ are the length of the small and large cylinder, respectively. The origin locates at the center of the interface between the small and large cylinder. In figure 7.2 (b), the coordinate system and the computational domain are shown, where $x-$, $y-$ and $z-$directions correspond to the streamwise, crossflow and spanwise direction, respectively. The computational domain is a rectangular box spanning $20D$ in the crossflow direction, $30D$ in the streamwise direction and $45D$ in the spanwise direction. The total length of the step cylinder equals $45D$. These parameters are larger than that used by Morton and Yarusevych [3] for modeling a step cylinder with the same $D/d$ and $Re_D$. Boundary conditions applied in the present study are as follow:

- The inlet boundary: uniform velocity profile $u=U$, $v=0$, $w=0$;

- The outlet boundary: Neumann boundary conditions for velocity components ($\partial u/\partial x = \partial v/\partial x = \partial w/\partial x = 0$) and constant zero pressure condition;

- The other four planes of the computational domain: free-slip boundary conditions. For the two vertical planes: $v = 0$, $\partial u/\partial y = \partial w/\partial y = 0$, For the two horizontal planes: $w = 0$, $\partial u/\partial z = \partial v/\partial z = 0$;

- The step cylinder surfaces: no-slip and impermeable wall condition;



(a)                                      (b)
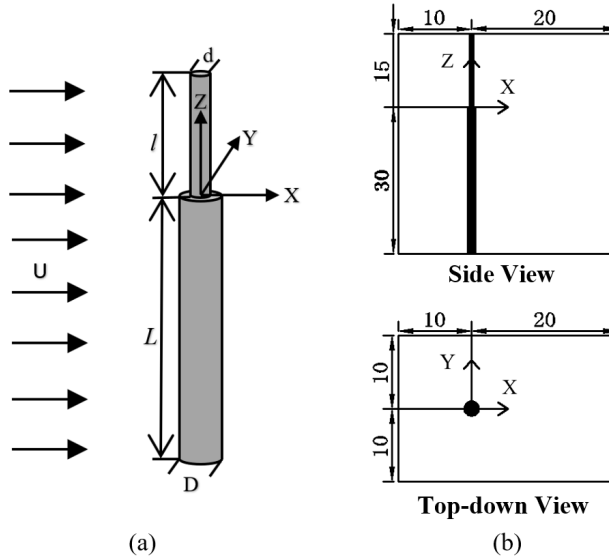
*Figure 7.2: (a) The step cylinder geometry investigated in the present study; (b) Computational domain size, origin and coordinate system illustrated from different viewpoints. Diameter of the large cylinder, D, is the length unit. The origin locates at the center of the interface between the small and large cylinder.*

## 7.3   Grid study

### 7.3.1   Grid overview

Detailed grid information of all cases simulated is summarized in table 7.1. The Reynolds number is calculated based on the uniform free-stream velocity ($U$) and the diameter of the large cylinder ($D$), i.e. $Re_D = UD/\nu = 150$ ($\nu$ is the kinematic viscosity of the fluid). The computational domain is

Table 7.1: *Grid information of all cases. The Reynolds number is 150 for all cases ($Re_D = UD/\nu = 150$). Grid levels are illustrated in figure 7.3.*

| Case | Min grid cell size | Number of grid levels | Number of grid cells in one grid box | Time step $\Delta t$ | Total number of grid cells (million) |
|---|---|---|---|---|---|
| 1 | 0.025 | 5 | $30 \times 30 \times 30$ | 0.0080 | 30.2 |
| 2 | 0.020 | 5 | $36 \times 36 \times 36$ | 0.0067 | 48.8 |
| 3 | 0.015 | 6 | $24 \times 24 \times 24$ | 0.0050 | 81.0 |
| 4 | 0.012 | 6 | $30 \times 30 \times 30$ | 0.0040 | 173.8 |

divided into many cubic Cartesian grid boxes. In each grid box, $N \times N \times N$ cubic Cartesian grid cells are uniformly distributed. In the areas where complex flow phenomena take place, such as in the region around the 'step', the area where the vortex dislocation happens, etc., the grid is refined by equally splitting grid boxes (e.g. the level-1 box) into eight smaller cubic grid boxes (i.e. the level-2 box). Hence, the grid resolution on level-2 is two times better than that on level-1. This refinement process goes on automatically until the finest grid level (varies with cases shown in table 7.1) is reached. In figure 7.3, a schematic illustration of the grid for $Case2$ is shown.

## 7.3.2 Grid convergence study

Motivated by ensuring that the grid resolution is good enough to resolve all important fluid phenomena, especially the complicated flow around the step, four grids were generated for thegrid study, as shown in table 7.1.

First, we did a rough check by comparing vortex shedding frequencies of the three vortex cells in all cases. In table 7.2, by conducting Fast Fourier Transform of the time-series of the streamwise velocity $u$ along a sampling line at $(x/D, y/D)=(0.6, 0.2)$, the Strouhal number ($St$) of the three dominating vortex cells (S-cell $St_S = f_S D/U$, N-cell $St_N = f_N D/U$ and L-cell $St_L = f_L D/U$) in the wake of the step cylinder are calculated and presented. One can see that the differences in $St$ of the same vortex cell are small among all cases. The largest difference is ($St_S$ of $Case2$-$St_S$ of $Case3$)/($St_S$ of $Case3$)=1.7%, which is considerably small. Moreover, the difference between $Case3$ and $Case4$ (the finest two cases) is smaller than 0.7%.

Table 7.2: The Strouhal number (St) of three dominating vortex cells (S-cell $St_S = f_S D/U$, N-cell $St_N = f_N D/U$ and L-cell $St_L = f_L D/U$) for all cases investigated. The results of one previous numerical study [3] and two previous laboratory experiments [15, 16] are also shown. [Note: in our case, $St_S$ is calculated based on the diameter of the large cylinder, a factor 2 is used when obtain data from [15, 16].]

| Case | $St_S$ | $St_N$ | $St_L$ |
|------|--------|--------|--------|
| 1 | 0.2943 | 0.1532 | 0.1769 |
| 2 | 0.2950 | 0.1531 | 0.1771 |
| 3 | 0.2895 | 0.1545 | 0.1780 |
| 4 | 0.2921 | 0.1549 | 0.1784 |
| Morton and Yarusevych [3] | 0.320 | 0.157 | 0.179 |
| Norberg [15] | 0.297 | - | - |
| Williamson [16] | 0.298 | - | - |

Second, the mean streamwise velocity ($\bar{u}/U$) distributions are checked along a line $AB$ (as indicated in the subplot figure 7.4 (c)) and a line $CD$ (as indicated in the subplot figure 7.5 (b)) to illustrate the time averaged flow conditions close to the step. The curves in figure 7.4 (a) are almost identical, and the zoom-in plot 7.4 (b) clearly shows a convergent tendency form $Case1$ to $Case4$. Additionally, the difference between $Case3$ and $Case4$ is negligible. The flow field behind the step is more complicated than that in front of the step. As shown in figure 7.5 (a), the curve from $Case1$ shows obvious differences compared with the curves from the other three cases. From the two zoom-in plots, figure 7.5 (c) and (d), one can see that the maximum difference in $\bar{u}/U$ between $Case2$, $Case3$ and $Case4$ is only around 0.005. This means that, except for $Case1$, the flow field from the other three cases fit each other well.

Furthermore, the time traces of the instantaneous spanwise velocity $w$ in the N-cell area where the velocity varies dramatically with time are plotted for $Case2$, $Case1$ and $Case4$ in figure 7.6. The mean values and the fluctuations of these curves coincide well.

### 7.3.3 Comparing with previous studies

In figure 7.7 (a), an overview of the vortex structures behind the step cylinder is illustrated by plotting the isosurface of $\lambda_2 = -0.05$ [17]. The overall
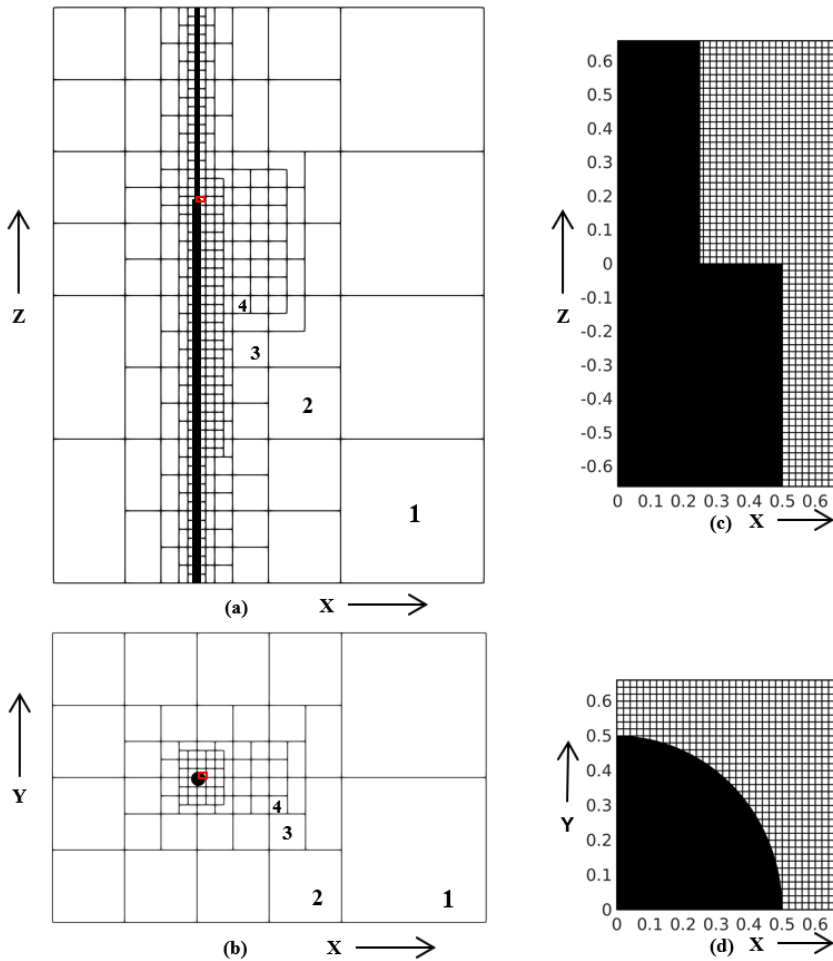
Figure 7.3: (a) A slice of the computational domain in the $x - z$ plane at $y/D = 0$. Each square represents the slice of a corresponding cubic Cartesian grid box which contains $N \times N \times N$ grid cells. In this figure, there are five levels of grid boxes, where the first four levels are indicated by numbers (1-4). Due to different minimum grid sizes, different cases have either five or six levels of grid boxes. (b) Same as (a) but the slice positioned in the $x - y$ plane at $z/D = 0^-$ (at the large cylinder area). (c) A zoom-in plot of the grid cells in the step region (red rectangle in (a)) for Case2; (d) Same as (c) but the zoom-in area is indicated by a red rectangle in (b).

vortical structures from previous numerical simulations [3] and laboratory experiments [2] are presented in figure 7.7 (b) and (c), respectively. The
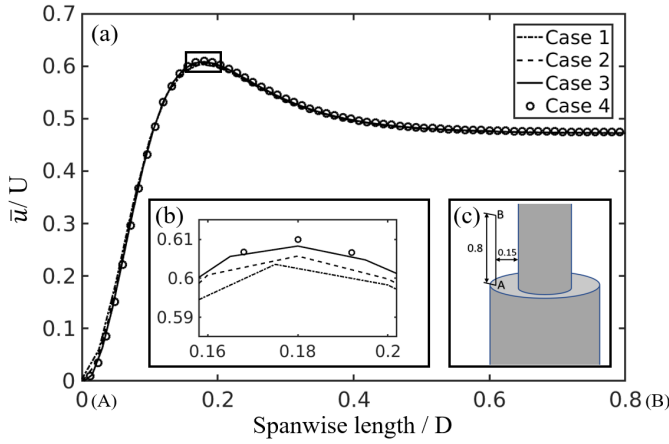
Figure 7.4: (a) Distributions of mean streamwise velocity $\frac{\bar{u}}{U}$ along a sampling line AB in the $x - z$ plane at $y/D = 0$; (b) A zoom-in plot of the upper part of curves in (a) (black rectangle in (a)); (c) A sketch of the sampling line AB of length $0.8D$, positioned $0.15D$ in front of the small cylinder.
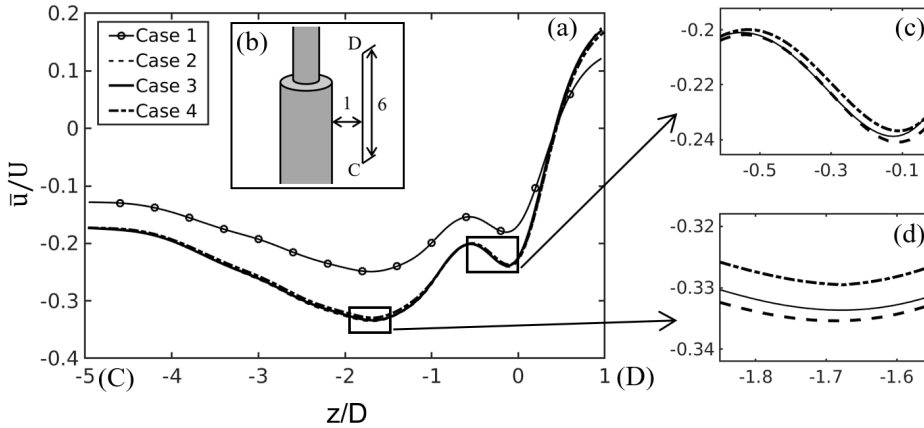


Figure 7.5: (a) Distributions of mean streamwise velocity $\frac{\bar{u}}{U}$ along a sampling line CD in the $x - z$ plane at $y/D = 0$; (b) A sketch of the sampling line CD of length $6D$, positioned $1D$ behind the large cylinder; (c) and (d) Zoom-in plots of the lower part of curves in (a) (black rectangles in (a)).

wake structures compare well with each other in these three plots. In figure 7.7 (a), three vortex cell areas (the S-, N- and L-cell areas) are also clearly illustrated. As Morton & Yarusevych [3], we also captured three dominating frequency components in the wake flow, as shown in table 7.2. The $St_L$
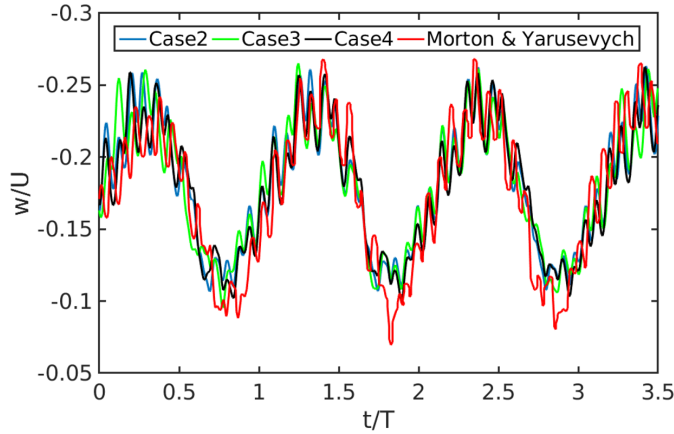
*Figure 7.6: Time traces of the spanwise velocity (w/U) at point (x/D, y/D, z/D)=(1, 0, -2.5) in the N-cell area. The red line is obtained from paper [3]. T is the period of one N-cell cycle which is the same time scale as Morton and Yarusevych used in [3].*
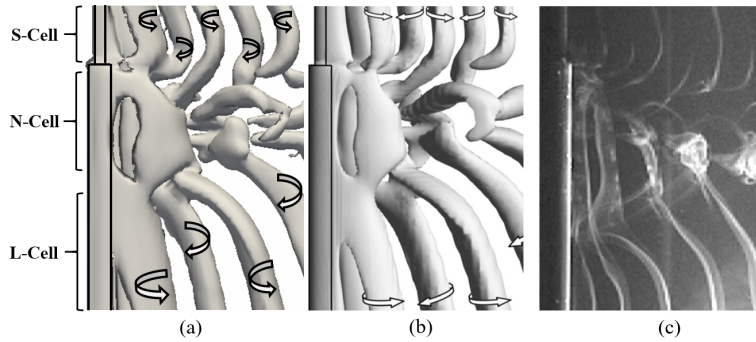


*Figure 7.7: Vortex shedding in the wake behind a step cylinder: (a) Isosurfaces of $\lambda_2 = -0.05$ [17] from our simulation, $Re_D = 150$ and $D/d = 2$; (b) Isosurfaces of $Q \approx 2 \times 10^{-3}$ from [3], $Re_D = 150$ and $D/d = 2$; (c) Flow visualization image from [2], $Re_D = 150$ and $D/d = 2$;*

from our simulations fits well with theirs. Our $St_S$ and $St_N$, however, are somewhat lower than that from their simulations. As mentioned in previous papers [2, 18, 19], the shedding of S-cell vortices is seldomly affected by the step. Two laboratory experiments [15, 16] are introduced to validate our $St_S$. From table 7.2, one can see that our results compare better with the experimental values. Moreover, the spanwise velocity data from paper [3] is inserted in figure 7.6. The match between the present study and Morton &

Yarusevych [3] is convincing, except for small differences in the lower part of the curves.

Based on all these careful comparisons, we believe that, except for *Case*1, the convergent tendency from *Case*2 to *Case*4 is clear. Moreover, the difference between *Case*3 and *Case*4 is small, and both of them fit well with previous results. However, due to the smaller time step size and large number of grid cells, the computational cost of *Case*4 is significantly higher that that of *Case*3. All discussions in the present paper are therefore based on data from *Case*3.

## 7.4 Results

### 7.4.1 Long periodicity of the vortex dislocations
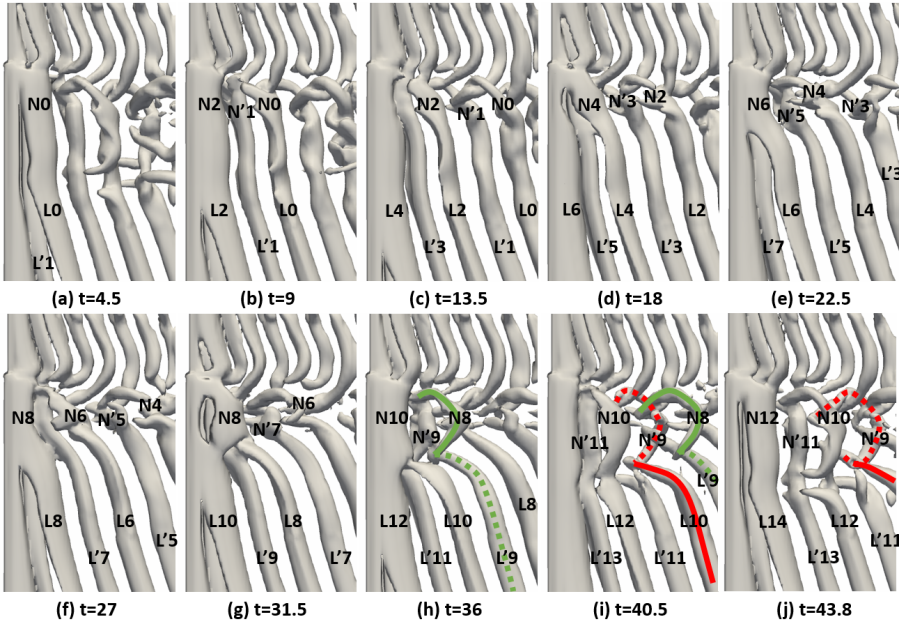


*Figure 7.8: Isosurface of $\lambda_2 = -0.05$ [17] showing the development of the 1st N-cell cycle on the '-Y' side of the step cylinder. The time t is set to t=t\*−2378.1D/U (t\* is the actual time). Solid and dashed curves indicate the loop structures on the '-Y' and '+Y' side, respectively.*

In the present study, as in the previous investigations [2, 3], three vortex cells (S-, N- and L-cell vortices) are captured in the wake behind the step cylinder. Complex vortex interactions occur between them, especially

between the N- and L-cell vortices. Due to different shedding frequencies, the N- and L-cell vortices move either in-phase or out-of-phase. During this process, vortex dislocations and vortex loop structures form. As shown in figure 7.8, the formation of the 1st N-cell cycle is illustrated by consecutive snapshots of isosurface of $\lambda_2$. The time $t$ is set to $t=t^*$-2378.1$D/U$, where $t^*$ is the actual time in the simulation (this applies through the paper). All N- and L-cell vortices are labeled by a combination of capital letters and numbers; 'N' and 'L' represent N- and L-cell vortices, respectively, while the number indicates the shedding order. To differentiate vortices shed from the different sides of the step cylinder, we use capital letters with primes (N' and L') to represent vortices shed from the '+Y' side; and capital letters (N and L) to represent vortices shed from the '-Y' side. From figure 7.8 (a) to (f), every N-cell vortex has one corresponding L-cell vortex shed from the same side (e.g. N0 and L0; N'1 and L'1...). As the phase difference between the N- and L-cell vortex accumulates [3], loop structures appear when corresponding N- and L-cell vortices are out of phase. From figure 7.8 (g) to (j), loop structures (N8-L'9) and (N'9-L10) form, and are indicated by green and red curves, respectively. Detailed descriptions of the formation process of those loop structures can be found in paper [6]. Based on the order of their appearances, we name the green curve as the NL-loop1, and the red curve as the NL-loop2. Meantime, we define the side of a NL-loop structure as the side of its N-cell vortex component. For example, the NL-loop1 N8-L'9 (shown by green curves) in figure 7.8 (h) is identified to form at the '-Y' side, because the N-cell vortex (N8) in this loop is at the '-Y' side.
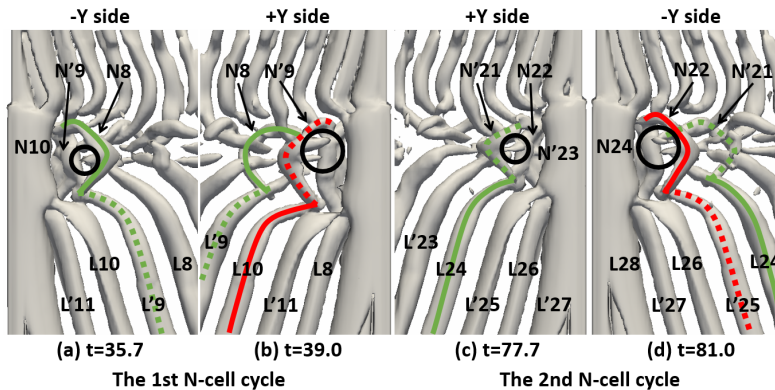


*Figure 7.9: NL-loop structures at the 1st and 2nd N-cell cycles are plotted in [(a), (b)] and [(c), (d)], respectively. The same colors and definitions used in figure 7.8 are also used here.*

In figure 7.9, by plotting the isosurface of $\lambda_2 = -0.05$, the NL-loop structures in the 1st and 2nd N-cell cycles are shown. The same colors and definitions in figure 7.8 are used here. One can see that the NL-loop1 (N8-L'9) in the 1st N-cell cycle (figure 7.9 (a)) and the NL-loop1 (N'21-L24) in the 2nd N-cell cycle (figure 7.9 (c)) are on different sides of the step cylinder. This is the antisymmetry reported in our previous paper [6]. However, by comparing figure 7.9 (a) and (c); (b) and (d), one can see that the corresponding NL-loops have small differences (highlighted by black circles), which means the conventional antisymmetry is not perfect. These differences are also reflected in the time traces of crossflow velocity ($v$) in the center plane. When a vortex dislocation occurs, the adjacent vortices move out phase. Meanwhile, the induced velocity fluctuations at the boundary between the adjacent vortex cells are excepted to diminish. For different dislocation processes, the corresponding distinct vortex alignments cause different amount of reductions in the induced crossflow velocity ($v$). In figure 7.10, the time trace of the crossflow velocity ($v/U$) is plotted at the position ($x/D$, $y/D$, $z/D$)=(1.5, 0, -6), which is at the boundary between the N- and L-cell vortices. The instants where the vortex dislocations in the 1st and 2nd N-cell cycle occur are marked by 'Dis1' and 'Dis2', respectively. One can see that the obvious reductions in the induced crossflow velocity are different at these two positions.
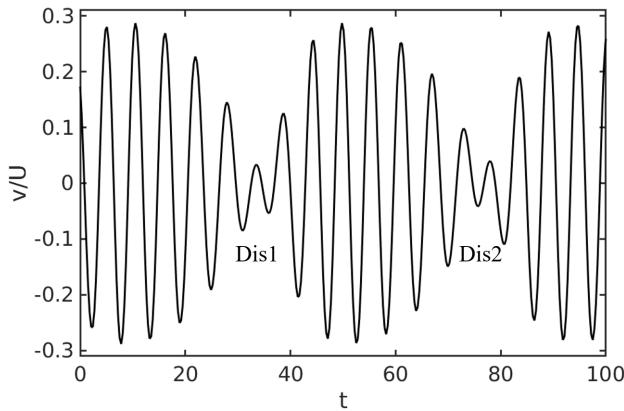


Figure 7.10: Time trace of the crossflow velocity (v) at a sampling point (x/D, y/D, z/D)=(1.5, 0, -6). "Dis1" represents the dislocation process that occurs in the 1st N-cell cycle defined in figure 7.9, same for "Dis2".

The different alignments of N- and L-cell vortices induce slightly different NL-loops and different reductions in the induced crossflow velocity in the 1st and 2nd N-cell cycles. From the NL-loop1 (N8-L'9) of the 1st N-cell

cycle in figure 7.9 (a) to the NL-loop1 (N'21-L24) of the 2nd N-cell cycle in figure 7.9 (c), there are 13 N-cell and 15 L-cell vortices. Compared to the vortex pairs in the 1st N-cell cycle, the fact that $15 \times \frac{1}{2f_L} - 13 \times \frac{1}{2f_N} = 0.064$ ($f_N$ and $f_L$ are obtained from table 7.2-$Case3$) induces a small phase shift to every vortex pair (a N-cell vortex and its counterpart L-cell vortex) in the 2nd N-cell cycle. It means that the vortex alignment varies from one N-cell cycle to another. Only when the vortex alignment becomes exactly the same in two N-cell cycles, the corresponding vortex dislocations can be exactly the same.

Considering vortices shed alternatingly from the '+Y' and '-Y' sides of the step cylinder, the exactly same vortex alignment can appear at the same side or different sides of the step cylinder. When the same vortex alignment appears at the same side of the step cylinder in two N-cell cycles, their subsequent NL-loop structures should be identical (i.e. perfect symmetric). On the other hand, perfect antisymmetric NL-loop structures are expected. We assume that there are two neighboring vortex cells: vortex cell-1 with a shedding frequency $f_1$, and vortex cell-2 with a shedding frequency $f_2$. If the number of cell-1 and cell-2 vortices are 'k' and 'j' between the two N-cell cycles which have the same vortex alignment, expression 7.5

$$k \times \frac{1}{2f_1} = j \times \frac{1}{2f_2} \qquad (7.5)$$

should be satisfied. We keep the number '2' as a factor in both sides of expression (7.5), because the shedding frequency should be doubled when we consider vortices from the '+Y' and '-Y' side separately (normally, the vortex shedding frequency in a Karman vortex street is the shedding frequency of a pair of vortices).
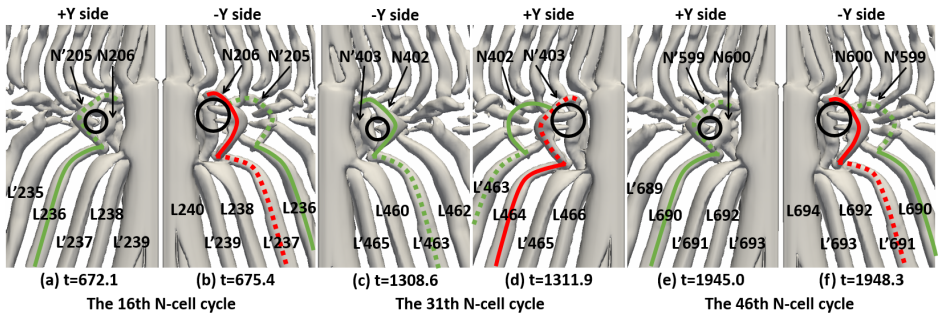


*Figure 7.11: NL-loop structures at the 16th, 31th and 46th N-cell cycles are plotted in [a), b)], [c), d)], and [e), f)]], respectively. The same colors and definitions as in figure 7.8 are used here.*

After long time of observation, we found that the corresponding NL-loop structures (NL-loop1: N8-L'9; NL-loop2: N'9-L10) in the 1st N-cell cycle, and (NL-loop1: N'205-L236; NL-loop2: N206-L'237) in the 16th N-cell cycle are perfect antisymmetric, as shown in figure 7.9 a), b) and figure 7.11 a) b). Details are highlighted by black circles. Between these two N-cell cycles, there are 183 N-cell vortices and 211 L-cell vortices which satisfy equation (7.5), i.e. $183 \times \frac{1}{2f_N} = 211 \times \frac{1}{2f_L} = 592$ ($f_N$ and $f_L$ are obtained from table 7.2-$Case3$).

In addition, the NL-loop structures in the 31th and the 46th N-cell cycle are plotted in figure 7.11 (c), (d), (e) and (f). One can see that, after every 15 N-cell cycles, the perfect antisymmetric phenomenon appears. In figure 7.12, the time traces of the crossflow velocity $v$ are plotted at the position $(x/D, y/D, z/D)$=(1.5, 0, -6). The y-coordinate of figure 7.12 (b) is reversed (from $v$ to $-v$) to ease the comparison. The position where a vortex dislocation happens is marked by a combination of the capital letter 'D' and its series number. One can see that these two plots almost coincide, which proves that all of the vortex alignments and the corresponding NL-loop structures are perfectly antisymmetric between D1-D15 and D16-D30.

This long cyclic process (around 650 $D/U$) is quite similar to the 'fundamental dislocation cycle' defined by McClure et al. [8]. They focused on the flow around a dual step cylinder. In their study, the same vortex dislocations appeared at the same side of the dual step cylinder at certain intervals, i.e. the perfect symmetry defined in the present paper. Moreover, they proposed equation (7.6) to measure the duration of the phase realignment process (the same assumption used in equation (7.5) is also used here).

$$\frac{f_1}{f_2} = \frac{m}{n} \tag{7.6}$$

The 'm' and 'n' are measured to the lowest possible integer value.

However, our observations clearly show that there is another type of the fundamental dislocation cycles, i.e. the perfect antisymmetric cycle. Behind the cylindrical structure, vortices alternatingly shed at the two sides of the structure. The alignment of vortices appears at one side of the structure is possible to repeat at either the same side or the other side of the structure. By using equation (7.6), the anticipated number of vortices in one fundamental vortex dislocation cycle can only be even (2m cell-1 vortices, and 2n cell-2 vortices). It makes equation (7.6) only suitable for the cases with perfectly symmetric fundamental dislocation cycles. In addition, when $f_1$ and $f_2$ are close, it is impossible to get the accurate value of 'm' and 'n'. For example, in our case, $f_1 = 0.1545$ and $f_2 = 0.1780$. It results in 197
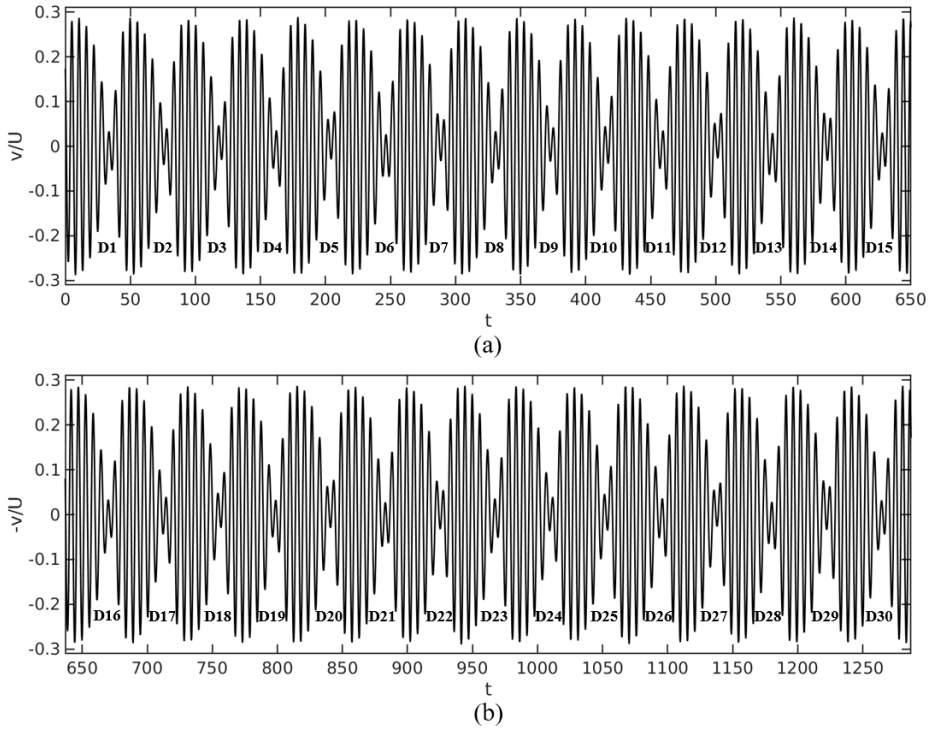
Figure 7.12: Time trace of the crossflow velocity (v) at a sample point (x, y, z)/D=(1.5, 0, -6). "D1" means the dislocation process that occurs in the 1st N-cell cycle defined in figure 7.9, same for "D2", etc.

N-cell vortices and 227 L-cell vortices in one fundamental vortex dislocation cycle. Without observations, it seems impossible to get the correct value of 'm' and 'n'.

In general, there are two types of the fundamental dislocation cycles, i.e. the perfect symmetric cycle and the perfect antisymmetric cycle. The different duration of 13 N-cell and 15 L-cell vortices brings the small phase shift to every vortex pair of the N- and L-cell vortex in neighboring N-cell cycles, and finally results in the 'fundamental dislocation cycle'. Ideally, the duration of the cycle can be measured by equation (7.5). But, in practice, it might be hard to get the accurate number of vortices without careful observations, especially when the shedding frequencies of neighboring vortices are close.

### 7.4.2  Computational challenges for investigating a long periodic phenomenon

As discussed in section 7.3.2, the results of our four cases show good convergence, and compare well with previous studies [3, 6]. However, considering the long periodicity of the fundamental dislocation cycle discussed in section 7.4.1, the simulation time of our convergence tests might not be long enough. Further investigations proves this.

Firstly, after another 1000 time units ($D/U$) simulation of Case 4, the exact same fundamental vortex dislocation was observed. However, different from Case 3, in Case 4, the same vortex dislocation appears at the same side of the step cylinder, and there are 131 N-cell and 151 L-cell vortices in one fundamental vortex dislocation cycle.

Furthermore, we set up a new case (named as $Case5$) to continue refining our grid size from $0.012D$ to $0.010D$. Still we cannot get exactly the same result as we obtained from the Case 4. In the Case 5, in one fundamental vortex dislocation cycle, the number of N- and L-cell vortices are 170 and 196, respectively.

Although, the number of vortices in one fundamental vortex dislocation cycle varies for different cases, further investigation proves that all the different cases converge to the same physical mechanism.

In figure 7.13, the isosurface of $\lambda_2 = -0.05$ is plotted to illustrate the NL-loop structures for different cases. Details of the loop structures are highlighted by black circles. The figure is divided into three parts by two dashed black lines: the left, middle and right part. As shown in the left part of figure 7.13 ((a), (b), (g), (h), (m) and (n)), the same NL-loop structures are observed in all three cases ($Case3$, $Case4$ and $Case5$). Even the details of the loop structures highlighted by black circles are almost exactly the same. It means, at this moment, all the three grid resolutions are able to give the same vortex alignments, and the same vortex structures. For all three cases, the N-cell cycle containing the NL-loop structures shown in the left part of figure 7.13, is set up to the 1*st N-cell cycle. By comparing the following N-cell cycles, we found that the differences between these three cases are gradually accumulated.

In the middle part of figure 7.13, the NL-loop structures in the 2*nd N-cell cycle are plotted for all three cases. One can see that the differences in details of the NL-loop structures are still very small between the different cases. However, as shown in the right part of figure 7.13, the loop structures in the 5*th N-cell cycle are completely different for all three cases. This transformation is caused by the accumulations of the minor differences in the vortex shedding frequencies ($f_N$ and $f_L$) between these three cases.
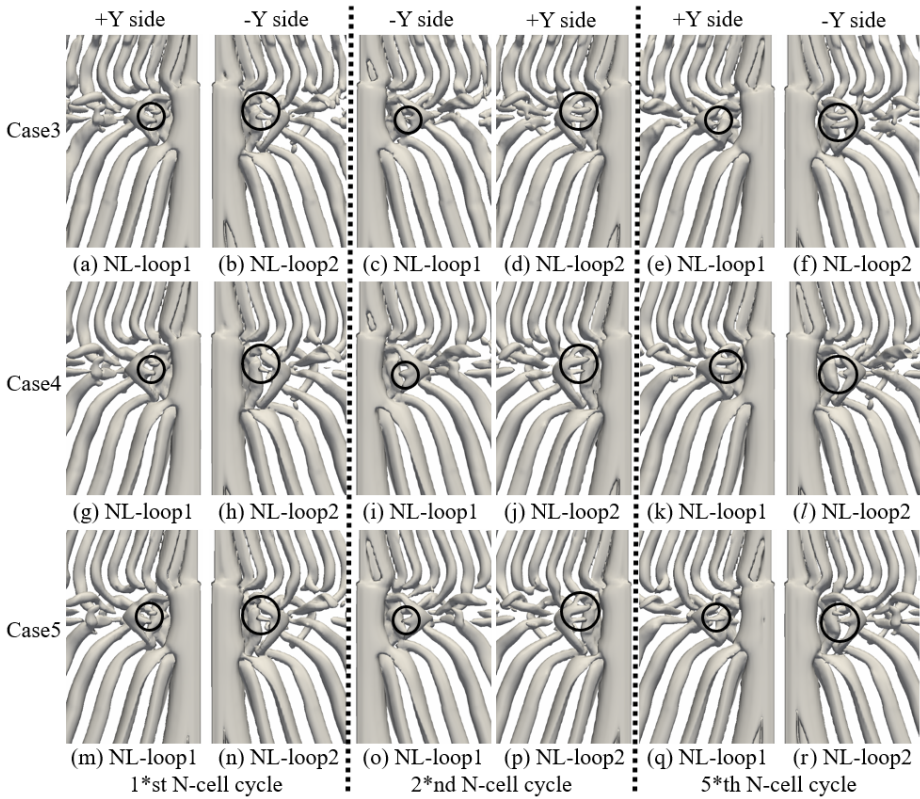
Figure 7.13: Isosurface of $\lambda_2 = -0.05$ [17] showing the NL-loop structures in Case3, Case4 and Case5 on both '+Y' and '-Y' sides. The details of the loop structures are highlighted by black circles. Two dashed lines divide the figure into three parts: the left part (the NL-loop structures in the 1*st N-cell cycle), the middle part (the NL-loop structures in the 2*nd N-cell cycle) and the right part (the NL-loop structures in the 5*th N-cell cycle).

As shown in table 7.3, the differences of the shedding frequencies ($f_L$ and $f_N$) are very small between these three cases. Normally, it is reasonable to claim that these three cases are already converged. Actually, in a relatively short time period, e.g. from the 1*st N-cell cycle (the left part of the figure 7.13) to the 2*nd N-cell cycle (the middle part of the figure 7.13), the wake flow and vortex structures agree well between Case3, Case4 and Case5. But after long time accumulations, e.g. from the 1*st N-cell cycle (the left part of figure 7.13) to the 5*th N-cell cycle (the right part of the figure 7.13), even the small differences in the shedding frequencies can affect the wake flow. Only when the shedding frequencies of different grid cases are

Table 7.3: The Strouhal number (St) of N-cell vortex ($St_N = f_N D/U$) and L-cell vortex ($St_L = f_L D/U$) for Case3, Case4 and Case5.

| Case | Mean grid size (D) | $St_N$ | $St_L$ |
|------|--------------------|--------|--------|
| 3    | 0.015              | 0.1545 | 0.1780 |
| 4    | 0.012              | 0.1547 | 0.1783 |
| 5    | 0.010              | 0.1549 | 0.1784 |

exactly the same, the vortex alignment and vortex structures can be exactly the same.

In general, we admit that even in *Case*5, the mesh resolution is still not fully converged for fundamental vortex dislocations. It is very difficult to get complete grid convergence when investigating the exceptionally long period phenomenon. After a long time accumulation, even a tiny difference could become big enough to affect the flow field. However we clearly show that *Case*3, *Case*4 and *Case*5 are all able to give the same instantaneous vortical structures in the near wake. The different detailed information (the number of N- and L-cell vortices) in one fundamental vortex dislocation cycle is caused by the accumulation of the minor difference in the vortex shedding frequencies between these cases. The mechanism and the existence of the two kinds of fundamental vortex dislocation cycles are valid for all cases.

## 7.5    Conclusion

The present results show good agreement with previous studies [3, 6, 8], such as the three dominating spanwise vortices (i.e. S-, N- and L-cell vortices), vortex dislocations between the N- and L-cell vortex, loop structures (NL-loop1 and NL-loop2) generated during the vortex dislocation process and the antisymmetric phenomena between the neighboring N-cell cycles. In addition, the long period characteristic of the vortex dislocation, i.e. the fundamental dislocation cycle, was for the first time captured and analyzed in the wake of the single step cylinder. We have clearly shown that the different duration of 13 N-cell and 15 L-cell vortices during one N-cell cycle brings the small phase shift to every vortex pair of N- and L-cell vortex, and finally causes the 'fundamental vortex dislocation cycle'. In addition, there are two kinds of fundamental dislocation cycles, i.e. the symmetric

fundamental dislocation cycle, and the antisymmetric fundamental dislocation cycle, which are determined by whether the same vortex alignment appears on the same side of the step cylinder or not. Last but not least, we discussed challenges of the grid resolution on investigating the long period characteristic. We found that, for the present case, although the detailed information (e.g. the number of N- and L-cell vortices) in one fundamental vortex dislocation cycle varies when continuing to refine the grid, the mechanism of the fundamental vortex dislocation cycle is valid for all cases.

In the future, other Reynolds numbers and diameter ratios will be investigated to explore how the vortex shedding frequencies of N- and L-cell vortices affect the formation and the length of the fundamental vortex dislocation cycle.

## Acknowledgements

## References

[1] Lewis CG, Gharib M. An exploration of the wake three dimensionalities caused by a local discontinuity in cylinder diameter. *Phys. Fluids A: Fluid Dynamics* 1992; **4**(1):104–117.

[2] Dunn W, Tavoularis S. Experimental studies of vortices shed from cylinders with a step-change in diameter. *J. Fluid Mech.* 2006; **555**:409–437.

[3] Morton C, Yarusevych S. Vortex shedding in the wake of a step cylinder. *Phys. Fluids* 2010; **22**(8):083 602.

[4] Morton C, Yarusevych S. Vortex dynamics in the turbulent wake of a single step cylinder. *ASME J. Fluids Eng.* 2014; **136**(031204).

[5] Tian C, Jiang F, Pettersen B, Andersson HI. Numerical investigation of flow around a step cylinder. *Proceedings of 9th National Conference on Computational Mechanics (CIMNE), Trondheim, Norway, May 11-12*, 2017; 369–384.

[6] Tian C, Jiang F, Pettersen B, Andersson HI. Antisymmetric vortex interactions in the wake behind a step cylinder. *Phys. Fluids* 2017; **29**(10):101 704.

[7] Williamson CHK. Oblique and parallel modes of vortex shedding in the wake of a circular cylinder at low Reynolds numbers. *J. Fluid Mech.* 1989; **206**:579–627.

[8] McClure J, Morton C, Yarusevych S. Flow development and structural loading on dual step cylinders in laminar shedding regime. *Phys. Fluids* 2015; **27**:063 602.

[9] Manhart M, Friedrich R. DNS of a turbulent boundary layer with separation. *Int. J. Heat Fluid Flow* 2002; **23**(5):572–581.

[10] Manhart M. A zonal grid algorithm for DNS of turbulent boundary layers. *Computers & Fluids* 2004; **33**(3):435–461.

[11] Williamson JH. Low-storage Runge-Kutta schemes. *J. Comput. Phys.* 1980; **35**:48–56.

[12] Peller N. Numerische simulation turbulenter strömungen mit immersed boundaries. PhD Thesis, Technische Universität München, München, Germany 2010.

[13] Stone HL. Iterative solution of implicit approximations of multidimensional partial differential equations. *SIAM J. Numer. Anal.* 1968; **5**:530–558.

[14] Peller N, Duc AL, Tremblay F, Manhart M. High-order stable interpolations for immersed boundary methods. *Int. J. Numer. Meth. Fl.* 2006; **52**:1175–1193.

[15] Norberg C. An experimental investigation of the flow around a circular cylinder: influence of aspect ratio. *J. Fluid Mech.* 1994; **258**:287–316.

[16] Williamson CHK. Defining a universal and continuous strouhal–reynolds number relationship for the laminar vortex shedding of a circular cylinder. *Physics of Fluids* 1988; **31**(10):2742–2744.

[17] Jeong J, Hussain F. On the identification of a vortex. *J. Fluid Mech.* 1995; **285**:69–94.

[18] Yagita M, Kojima Y, Matsuzaki K. On vortex shedding from circular cylinder with step. *Bulletin of JSME* 1984; **27**(225):426–431.

[19] Norberg C. An experimental study of the flow around cylinders joined with a step in diameter. *Proceedings of the 11th Australasian Fluid Mechanics Conference, Hobart, Australia*, vol. 1, 1992; 507–510.

# Chapter 8

# Article 4: Vortex dislocation mechanisms in the near wake of a step cylinder

Cai Tian[1], Fengjian Jiang[2], Bjørnar Pettersen[1], Helge I. Andersson[3]

## Abstract

Vortex interactions behind step cylinders with diameter ratio $D/d = 2$ and 2.4 at Reynolds number ($Re_D$) 150 were investigated by directly solving the three-dimensional Navier-Stokes equations. In accordance with previous studies, three spanwise vortex cells were captured: S-, N- and L-cell vortices. In this paper, we focused on vortex interactions between the N- and L-cell vortices, especially the vortex dislocations and subsequent formations of vortex loop structures. The phase difference accumulation process of every pair of corresponding N- and L-cell vortices and its effects on the vortex dislocations were investigated. We revealed that the total phase difference between N- and L-cell vortices was accumulated by two physically independent mechanisms, namely different shedding frequencies and different convective velocities of these two cells. The second mechanism has never

[1]Department of Marine Technology, Norwegian University of Science and Technology, No-7491 Trondheim, Norway
[2]SINTEF Ocean, NO-7052 Trondheim, Norway
[3]Department of Energy and Process Engineering, Norwegian University of Science and Technology, No-7491 Trondheim, Norway

been reported before. The relative importance of these two mechanisms varied periodically in the phase difference accumulation process of every pair of corresponding N- and L-cell vortices. This variation caused the vortex dislocation process and the subsequent formation of the loop structures to change from one N-cell cycle to another. Our long-time observations also revealed an interruption of the conventional antisymmetric vortex interactions between two subsequent N-cell cycles in this wake. Moreover, the *trigger value* and the *threshold value* in the phase difference accumulation processes were identified and discussed. Both values contribute to better understanding of the vortex dislocations in this kind of wake flow. Finally, the universality of our discussions and conclusions was investigated.

## 8.1   Introduction

Cylindrical structures are widely used in the marine offshore industry, for example, the hull of a SPAR-platform [1], deep water risers [2], etc. Wake flow behind circular cylinders has been a popular topic of investigation for researchers and engineers for decades. It is well-known that when the Reynolds number ($Re_D$) is less than 50, the wake flow around a circular cylinder is laminar and steady, and there is no vortex shedding behind the cylinder [3]. For $50 \lesssim Re_D \lesssim 180$, periodic two-dimensional vortex shedding occurs in the wake behind the cylinder. When $Re_D$ exceeds 180, the wake becomes three-dimensional. The well-known *Mode A* and *Mode B* appear at $Re_D = 180 - 194$ and $Re_D = 200 - 250$, respectively [3]. Wake turbulence and shear layer instabilities follow as $Re_D$ further increases.

However, even at $Re_D \lesssim 180$, we can observe three-dimensional cylinder wakes under certain circumstances, such as, cylinders with non-uniform inflow, cylinders with varying cross-sections, cylinders with free-ends, etc. In these cases, three dimensionality is triggered by spanwise non-uniformity in either the incoming flow or the configuration itself. Complex three-dimensional wake dynamics appear, such as vortex split, vortex dislocation and oblique shedding. In order to investigate these complex flow phenomena, a single step cylinder becomes an ideal configuration in which geometric complications are removed except for the sudden diameter change.

### 8.1.1   Single step cylinder wake

There are two important parameters in the wake flow behind a single step cylinder, i.e., the Reynolds number ($Re_D$) and the diameter ratio ($D/d$). $D/d$ is the ratio between the large and small diameter part of the step

cylinder, while $Re_D = UD/\nu$ ($U$ represents the uniform inflow velocity, and $\nu$ is the kinematic viscosity of the fluid).

The wake of step cylinders with $1.14 < D/d < 1.76$ at $67 < Re_D < 200$ was initially investigated by Lewis & Gharib [4]. They reported two vortex interaction modes: a direct and an indirect mode. The direct mode occurs when $D/d < 1.25$, where two dominating shedding frequencies ($f_S$ and $f_L$) correspond to vortices shed from the small and large cylinder, respectively. The interactions between these two kinds of vortices take place in a narrow region referred to as the interface. When they are in phase, vortices from the two wake regions connect to each other one by one across the interface. When they are out of phase, the direct connection will be interrupted and at least one half-loop connection between oppositely rotating vortices will appear. The period between two such interruptions is called a *beat cycle*. In the indirect mode ($D/d > 1.55$), in addition to $f_S$ and $f_L$, another distinct frequency $f_3$ (which is referred to as $f_N$ in the present paper) can be detected near the interface behind the large cylinder. This region was first named the modulation zone by Lewis & Gharib [4]. It prevents direct interactions between the vortices with shedding frequency $f_S$ and those with shedding frequency $f_L$. In the modulation zone, the velocity variation is modulated by the main frequency behind the large cylinder, and an inclined interface was found to occur at a beat frequency ($f_L - f_N$). Lewis & Gharib [4] found that the vortex interactions in the indirect mode are more complex than in the direct mode.

Based on the three dominating shedding frequencies, Dunn & Tavoularis [5] identified three types of spanwise vortices: (1) S-cell vortex shed from the small cylinder with the highest shedding frequency $f_S$, (2) N-cell vortex shed in the modulation zone with the lowest shedding frequency $f_N$, (3) L-cell vortex shed from the large cylinder with shedding frequency $f_L$. The terminologies S-, N- and L-cell were thereafter adopted in many studies [6, 7, 8, 9, 10, 11], and are also used in the present study. The regions where these vortex cells occur are indicated in figure 8.1(a).

The interactions between different vortex cells in the indirect mode were investigated in the wake behind a single step cylinder with $D/d \approx 2$ and $Re_D \approx 150$, experimentally by Dunn & Tavoularis [5] and numerically by Morton & Yarusevych [8]. These studies concluded that the S-N cell boundary (the region between the S- and N-cell vortices) is stable and deflects spanwise into the large cylinder direction. At this boundary, one N-cell vortex always connects to a counter-rotating N-cell mate and a S-cell vortex. The vortex dislocations between the S- and N-cell vortices occur at a beat frequency ($f_S - f_N$) at the S-N cell boundary. During this dislocation pro-
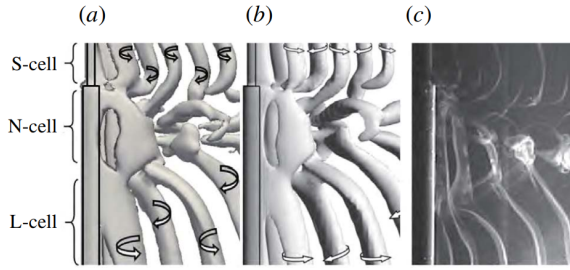
Figure 8.1: Vortex shedding in the wake behind a step cylinder: (a) Isosurfaces of $\lambda_2 = -0.05$ [12] from our simulation, $Re_D = 150$ and $D/d = 2$; (b) Isosurfaces of $Q \approx 2 \times 10^{-3}$ from Morton & Yarusevych [8], $Re_D = 150$ and $D/d = 2$; (b) Flow visualization image from Dunn & Tavoularis [5], $Re_D = 150$ and $D/d = 1.98$.

cess, the half-loop connection between S-cell vortices is dominating. The number of S- and N-cell vortices in a cyclic period (from one dislocation process to the next) is determined by the ratio of the shedding frequencies of these two cells ($f_S/f_N$).

Unlike the S-N cell boundary, the N-L cell boundary (the region between the N- and L-cell vortices) is unstable. As the phase difference between N- and L-cell vortices accumulates, in parallel with the appearance of vortex dislocations between N- and L-cell vortices, the shapes and lengths of the N-cell vortices and the position of the N-L cell boundary vary periodically with the beat frequency ($f_L - f_N$). Morton & Yarusevych [8] defined these cyclic changes as the N-cell cycle. Tian *et al.* [10] further investigated the dislocation processes at the N-L cell boundary. Two new loop structures were identified: the NL-loop (the fake loop) formed between a pair of N- and L-cell vortices with opposite rotating directions, and the NN-loop (the real loop) formed between two subsequent N-cell vortices with opposite rotating directions. In addition, antisymmetric vortex interactions between two adjacent N-cell cycles were reported based on careful observations of the development of these two kinds of loop structures.

When $Re_D$ increases, the wake gradually becomes more complex. However, the three dominating spanwise vortices (S-, N- and L-cell vortices), the vortex dislocation between them and the cyclic variation of the N-cell vortices, are still observable in the wake flow [8]. In addition, Morton & Yarusevych [7, 9] reported that the duration of the N-cell cycle varies and fits a Gaussian distribution at relatively high $Re_D = 1050$.

Other characteristics of the wake behind a single step cylinder with different diameter ratios and different Reynolds numbers have been discussed

in several papers. Ko, Leung & Au [13], Yagita, Yoshihiro & Matsuzaki [14], Norberg [15] and Dunn & Tavoularis [5] found that the vortex shedding behind the small cylinder was seldom influenced, but the flow behind the large cylinder was strongly affected by the step. When this induced effect becomes strong enough, N-cell vortices appear [5, 15]. In addition to the three main vortex cells (S, N and L), two pairs of streamwise vortices (i.e. junction vortices and edge vortices) have also been identified around the step region [5, 6, 11].

### 8.1.2 Vortex dislocation

It is widely accepted that most of the observations mentioned above for the step cylinder are closely related to vortex dislocations. As an interesting physical phenomenon, vortex dislocations have also been investigated in various types of flow, such as in uniform cylinder wakes, mixing layers and nonlinear waves.

The phrase *vortex dislocation* was first introduced by Williamson [16] when he observed multiple vortex cells with different shedding frequencies in his experiments of flow past a circular cylinder at $Re_D < 200$. Neighbouring vortex cells are observed to move either in-phase or out-of-phase with each other due to their different shedding frequencies. When these vortex cells move out of phase, at the boundary between them, the contorted 'tangle' of vortices appears and looks like dislocations that appear in solid materials. Williamson [16] defined this kind of flow phenomenon as vortex dislocation. He reported that, at $Re_D = 100$, vortex dislocations occur at the boundary between cells (the end-plate cell of frequency $f_e$ and the single cell of frequency $f_L$) at a constant beat frequency $f_L - f_e$, accompanied by an obvious minimum amplitude of the velocity fluctuations at the boundary. In addition, by comparing velocity signals from different vortex cell regions, the time trace of phase differences was plotted. Williamson [17] further investigated the dislocation by adding a small 'ring' on a circular cylinder in order to force the dislocation to happen. This study revealed more detailed features of vortex dislocations, such as the vortex dynamics and the effects of vortex dislocations in the wake flow. An interesting long-period characteristic of the vortex dislocation was first reported in McClure, Morton & Yarusevych [18] by investigating flow past dual step cylinders. They defined the time period between two identical vortex dislocations as the fundamental dislocation cycle. Further investigations of this characteristic in the wake behind the single step cylinder can be found in Tian *et al.* [19]. Vortex dislocations in other types of wakes and mixing layers have been reported by many others. For details, the reader is referred to the works of

Gaster [20], Eisenlohr & Eckelmann [21] and Dallard & Browand [22].

### 8.1.3 Objectives of the present study

There have been many attempts to describe the vortex dislocations in the step cylinder wake. Previous studies pointed out that it is the accumulation of phase differences that causes the vortex dislocation between different adjacent spanwise vortex cells. However, the investigations of how phase differences accumulate and how they affect the vortex dislocations are still limited.

Lewis & Gharib [4] and Williamson [16] and experimentally examined the time trace of the phase difference by using probes to monitor velocity signals in different vortex cell regions positioned 10 cylinder diameters downstream. However, at such a location, oblique vortex shedding, complex vortex interactions and the stretching and tilting of the vortices make it difficult to accurately evaluate phase differences. Another interesting phenomenon in the wake flow behind the step cylinder is the cyclic changes of the N-cell vortex, which was defined as the N-cell cycle by Morton & Yarusevych [8]. However, they analyzed this phenomenon in a relatively short time period containing only few N-cell cycles. Whether N-cell cycles have any long-period variations or very low-frequency features is still unknown.

The primary goal of the present numerical study is to thoroughly investigate the mechanisms of phase difference accumulation in the step cylinder wake, and their effect on vortex interactions. Considering that the wake behind the small cylinder part is seldomly influenced by the step, and the contributions of the streamwise vortices on the vortex dislocation between the S- and N-cell vortices are unclear, we only focus on the vortex dislocation between the N- and L-cell vortices. To achieve this objective, we analyze the time and space signals of several flow quantities (velocity, vorticity and $\lambda_2$) obtained from a direct numerical simulation ($DNS$) of flow past two different step cylinders with diameter ratios $D/d = 2$ and 2.4. In order to change the diameter ratio of the step cylinder, we keep $D$ constant, and change $d$. These two cases share the same coordinate system, computational method and data analyze process. First, in §8.2, §8.3, §8.4 and §8.5, the flow problem, the numerical settings and analyses of the wake flow field are described in detail based on the $D/d = 2$ case. Then, in §8.6, the universality of our discussions and conclusions is studied by investigating the $D/d = 2.4$ case. Last but not least, we also aim to present a reliable method that can be used to calculate the phase information ($\varphi$) and phase difference ($\Phi$) of vortices, since such a method is lacking in the literature. Details of the method are included in appendix 8.8.1.

## 8.2 Flow configuration and computational aspects

### 8.2.1 Flow configuration and coordinate system
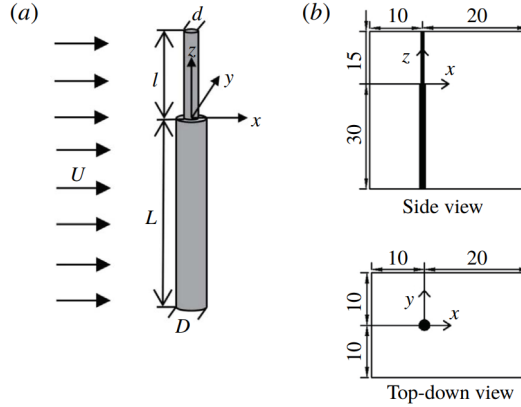


*Figure 8.2: (a) A sketch of the step cylinder geometry ($D/d = 2$); (b) Computational domain, origin and coordinate system are illustrated from two different viewpoints. The diameter of the large cylinder, $D$, is the length unit. The origin locates in the center of the step, the interface between the small and large cylinder.*

A sketch of the $D/d = 2$ step cylinder geometry is shown in figure 8.2(a). $L$ and $l$ represent the length of the large and small part of the cylinder, respectively. In figure 8.2(b), the computational domain and coordinate system are shown, where $x-$, $y-$ and $z-$direction correspond to the streamwise, crossflow and spanwise direction, respectively. The origin locates in the center of the interface between the small and large cylinder. The inlet plane is $10D$ upstream from the center of the step cylinder, while the outlet plane is $20D$ downstream. The spanwise height of the domain is $45D$, of which the small and the large cylinders occupy $15D$ ($l$) and $30D$ ($L$), respectively. The width of the domain is $20D$. This domain is larger than that used by Morton & Yarusevych [8] for the same $D/d$ and $Re_D$. Boundary conditions applied in the present study are as follows:

- The inlet boundary: uniform velocity profile $u=U$, $v=0$, $w=0$;

- The outlet boundary: Neumann boundary condition for velocity components ($\partial u/\partial x$ $= \partial v/\partial x = \partial w/\partial x = 0$) and constant zero pressure condition;

- The other four sides of the computational domain: free-slip boundary conditions (For the two vertical sides: $v = 0$, $\partial u/\partial y = \partial w/\partial y = 0$, For the two horizontal sides: $w = 0$, $\partial u/\partial z = \partial v/\partial z = 0$);

- The step cylinder surfaces: no-slip and impermeable wall.

### 8.2.2    Computational method

For all cases in the present investigation, a thoroughly validated finite-volume based numerical code $MGLET$ [23] is used to directly solve the incompressible Navier-Stokes equations. The midpoint rule is used to approximate the surface integral of flow variables over the faces of the discrete volumes, leading to second-order accuracy in space. A third-order explicit low-storage Runge-Kutta scheme [24] is used for time integration with a constant time step $\triangle t$ that ensures a CFL number smaller than 0.65. The pressure-velocity coupling is handled by solving a Possion equation with Stone's strongly implicit procedure (SIP) [25]. The same code has recently also been used to investigated other complex flows, such as the spheroid wake [26] and the curved cylinder wake [27].

All simulations are conducted on a staggered Cartesian mesh, while the solid surface of the step cylinder is handled by an immersed boundary method (IBM) [28]. The computational domain is divided into cubic Cartesian grid boxes, named level-1 boxes. In each of them, $N \times N \times N$ cubic Cartesian grid cells are uniformly distributed. In order to refine the grid regions, where complex flow phenomena take place, such as the regions close to the step cylinder geometry, the region around the 'step', the regions where vortex dislocations happen, etc., all the grid boxes (the level-1 box) are equally split into eight smaller cubic boxes (the level-2 box). In each level-2 box, there are also $N \times N \times N$ cubic grid cells. Hence, the grid resolution on level-2 is two times finer than that on level-1. This split-process goes on automatically until the finest grid level is reached. The overall properties of the grids for all simulations can be found in table 8.1. A schematic illustration of the mesh design is shown in figure 8.3.

### 8.2.3    Grid convergence study

Table 8.2 shows the Strouhal number ($St$) of the three dominating vortex cells ($St_S = f_S D/U$, $St_N = f_N D/U$ and $St_L = f_L D/U$) behind the step cylinder calculated by Fast Fourier Transform of the time-series of the streamwise velocity $u$ along a vertical sampling line positioned at ($x/D$, $y/D$)=(0.6, 0.2). For these four cases, the differences between $St$ numbers

Table 8.1: *Detailed mesh information of all $D/d = 2$ cases. The Reynolds number for all cases is $Re_D = UD/\nu = 150$.*

| Case | Min grid cell size $(D)$ | Time step $\triangle tU/D$ | Number of grid levels | Number of grid cells in one grid box | Total number of grid cells (million) |
|------|------|------|------|------|------|
| 1 | 0.025 | 0.0080 | 5 | $30 \times 30 \times 30$ | 30.2 |
| 2 | 0.020 | 0.0067 | 5 | $36 \times 36 \times 36$ | 48.8 |
| 3 | 0.015 | 0.0050 | 6 | $24 \times 24 \times 24$ | 81.0 |
| 4 | 0.012 | 0.0040 | 6 | $30 \times 30 \times 30$ | 173.8 |
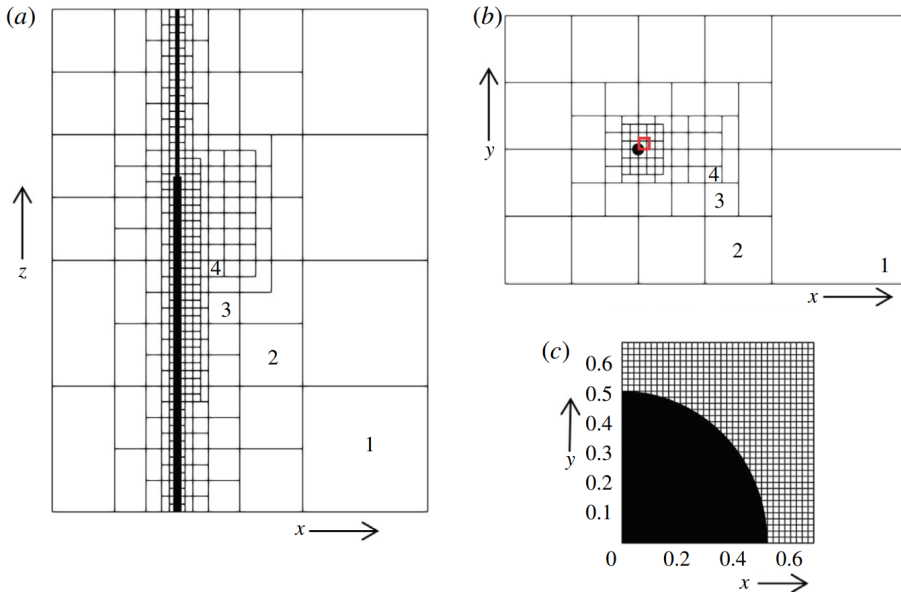


Figure 8.3: *An illustration of the multi-level grids: (a) a slice of the computational domain in the $x - z$ plane at $y/D = 0$, (b) a slice of the computational domain in the $x - y$ plane at $z/D = 0^-$ (at the large diameter $D$ region). Each square represents the slice of a corresponding cubic Cartesian grid box which contains $N \times N \times N$ grid cells. In this figure, there are five levels of grid boxes, where the first four levels are indicated by numbers. Due to different minimum grid sizes, different cases have either five or six levels of grid boxes. (c) a zoom-in plot of the grid cells in the step region (red rectangle in (b)) for Case2.*

Table 8.2: *St of the three dominating vortex cells (S-cell $St_S = f_S D/U$, N-cell $St_N = f_N D/U$ and L-cell $St_L = f_L D/U$) for all cases studied. Results form Morton & Yarusevych [8] are from their numerical simulations for a step cylinder with $D/d = 2$ at $Re_D = 150$. The result from Norberg [29] is calculated by equation 8.1 which was derived by Norberg based on laboratory experiments. [Note: In our cases, $St_S$ is calculated based on the large cylinder diameter, a factor 2 should be used when using Norberg's equation.]*

| Case | 1 | 2 | 3 | 4 | Morton & Yarusevych [8] | Norberg [29] |
|------|------|------|------|------|------|------|
| $St_S$ | 0.294 | 0.295 | 0.290 | 0.292 | 0.320 | 0.297 |
| $St_N$ | 0.153 | 0.153 | 0.155 | 0.154 | 0.157 | - |
| $St_L$ | 0.177 | 0.177 | 0.178 | 0.178 | 0.179 | - |

of the same vortex cell are small. In figure 8.4(a), the distributions of mean streamwise velocity along the line AB (as indicated in the subplot figure 8.4($a_1$)) for all four cases are plotted to illustrate the flow variation on the 'step' just in front of the small cylinder. The curves in figure 8.4(a) and a zoom-in view in figure 8.4($a_2$) clearly show a convergent tendency from Case1 to Case4, and there are only minor differences between Case3 and Case4. Moreover, figure 8.4(b) shows time traces of the spanwise velocity ($w$) in the N-cell formation region where the velocity varies dramatically with time. The fluctuations and the mean values of '$w$' from Case 3 and Case 4 almost coincide. However, the computational cost of Case 4 is significantly higher than that of Case 3, due to large number of grid cells and smaller time step. The long-period features of the flow that we will discuss in later sections require exceptionally long simulations (more than $3000D/U$). All discussions are therefore based on data from Case 3. Case 4 was run only for a limited time for this convergence test.

### 8.2.4   Comparison with previous studies

An overview of the vortical structures in the wake of the step cylinder is illustrated in figure 8.1(a) by plotting the isosurface of $\lambda_2 = -0.05$ [12]. By comparing figures 8.1(a), (b) and (c), one can see that the overall wake structures from the present study compare well with the previous numerical simulations by Morton & Yarusevych [8] and experiments by Dunn & Tavoularis [5]. Behind the step cylinder, as mentioned in §8.1, the shedding
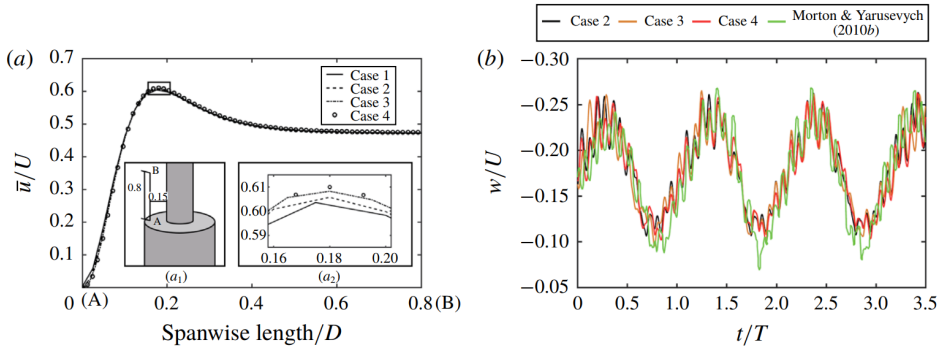
Figure 8.4: (a) Distributions of mean streamwise velocity $\bar{u}/U$ along a sampling line AB in the $x - z$ plane at $y/D = 0$; $(a_1)$ A sketch of the sampling line AB of length $0.8D$, positioned $0.15D$ in front of the small cylinder; $(a_2)$ A zoom-in plot of the upper part of the curves in (a) (black rectangle in (a)); (b) Time traces of the spanwise velocity (w) at point $(x/D, y/D, z/D) = (1, 0, -2.5)$ in the N-cell region. The green line is obtained from Morton & Yarusevych [8]. T is the period of one N-cell cycle which is the same time scale as Morton & Yarusevych [8] used.

of S-cell vortices is barely influenced, which makes it reasonable to introduce the correlation derived by Norberg [29]

$$St = 0.1835 - 3.458/Re + 1.51 \times 10^{-4} Re. \tag{8.1}$$

to validate our $St_S$. From the data in table 8.2, we see that $St_S$ from the present study is slightly lower than that from Morton & Yarusevych [8], but compares better with the experimental value reported in Norberg [29]. In addition, we have obtained spanwise velocity data from Morton & Yarusevych [8] and displayed them in figure 8.4(b). The match between the present study and Morton & Yarusevych [8] is convincing. Based on all these careful comparisons, we believe that the grid resolution in Case 3 is good enough to accurately simulate this flow.

## 8.3 Features of the present wake flow

Generally, the wake behind the two step cylinders ($D/d = 2$ and 2.4) in the present study are very similar. In order to ease the discussions, only the wake flow behind the $D/d = 2$ case is described in §8.3, §8.4 and §8.5. The $D/d = 2.4$ case is presented as a justification case in §8.6.

### 8.3.1   Overview of the flow development
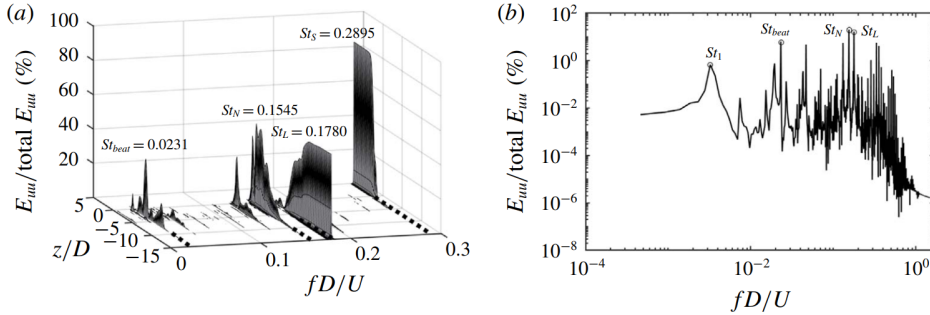


*Figure 8.5: (a) Streamwise velocity spectra along a spanwise line behind the step cylinder at $(x/D, y/D)=(0.6, 0.2)$; (b) Power spectrum plotted at position $(x/D, y/D, z/D) = (0.6, 0.2, -4.4)$, in which $St_N$, $St_L$, $St_{beat}$ and an exceptionally low frequency $St_1$ are marked by small black circles. (Note: there is no S-cell vortex in the wake flow at spanwise position $z/D = -4.4$, so $St_S$ does not show up in this figure.)*

In figure 8.5(a), the streamwise velocity spectrum is obtained by means of Discrete Fourier Transform (DFT) of continuous velocity data along a vertical sampling line parallel to the Z-axis at position $(x/D, y/D) = (0.6, 0.2)$, over a long period of 2500 time units $(D/U)$. As in the previous studies [5, 8, 10], the three dominating frequency components $(St_S = f_S D/U, St_N = f_N D/U$ and $St_L = f_L D/U)$ and the beat frequency $(St_{beat} = f_{beat} D/U)$ are dominating.

The vortex structures in the near wake are illustrated by consecutive snapshots of iso-surface of $\lambda_2$ in figure 8.6. The time $t$ is set to $t = t^* - 2378.1 D/U$, where $t^*$ is the actual time in the simulation. This applies all through §8.3, §8.4 and §8.5. All N- and L-cell vortices are labeled by a combination of capital letters and numbers; 'N' and 'L' represent N- and L-cell vortices, respectively, while the number indicates the shedding order. To differentiate vortices shed from different sides of the step cylinder, we use capital letters with primes (N' and L') to represent vortices shed from the +Y side; and only capital letters (N and L) to represent vortices shed from the -Y side. In figure 8.6(a) to (f), every N-cell vortex has one corresponding L-cell vortex with the same direction of rotation (e.g. N0 and L0; N'1 and L'1...). Due to different shedding frequencies of N- and L-cell vortices, loop structures appear when corresponding N- and L-cell vortices are out of phase. From figure 8.6(g) to (h), loop structures (N8-L'9) and (N'9-L10) form, and are indicated by green and red curves, respectively. Details of
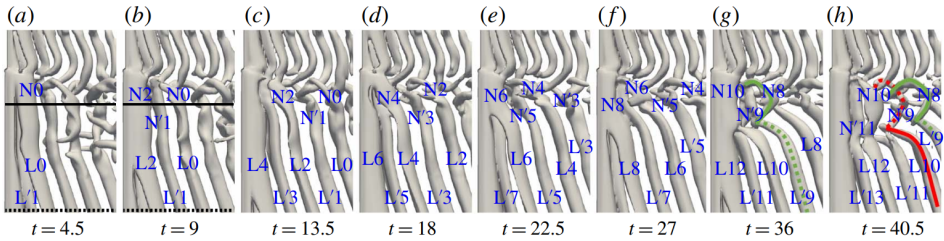
Figure 8.6: Iso-surface of $\lambda_2 = -0.05$ showing developments of vortex structures on the -Y side. The time t is set to $t = t^* - 2378.1D/U$ ($t^*$ is the actual time). Solid and dashed curves in (g) and (h) indicate the loop structures on the -Y and +Y side, respectively. The red and green curves point to different NL-loop structures. In (a) and (b), the black solid line at $z/D = -2.9$ and the black dashed line at $z/D = -14$ indicate the positions of vorticity contours given in figure 8.9.

the formation processes of those loop structures were described in Tian *et al.* [10]. Based on the order of their appearances, the green and red curves are named the NL-loop1 and NL-loop2, respectively.

Based on long-time observations ($2500D/U$), a schematic topology sketch is shown in figure 8.7. This will be used to introduce some important concepts. In figure 8.7, the short and long straight lines represent the N- and L-cell vortices, respectively. Between them, the curved solid lines connect the N-cell vortex and its counterpart L-cell vortex. The dashed curves indicate broken connections that are not able to persist due to dislocations. Detailed visualizations of vortex connections and dislocations in the 1st N-cell cycle are shown in figure 8.6. To ease the observation, we only show the connections between the N- and L-cell vortices. The L-L and N-N loops [10] are not shown in this figure.

We define the side of the N-cell vortex in a NL-loop structure as the side of the loop itself. For example, the NL-loop N8-L'9 (shown by green curves) in figure 8.6(g) is identified to form at the -Y side. As shown in figure 8.7, from the 1st to 7th N-cell cycle, the NL-loop1 (the green curves) appears alternatingly at +Y and -Y side between subsequent N-cell cycles. This is what we called the antisymmetric vortex interactions in Tian *et al.* [10]. However, an unexpected interruption of this antisymmetry is observed between the 7th and 8th N-cell cycles. Figure 8.7 shows, in both the 7th and 8th N-cell cycles, that the NL-loop1 appears at the -Y side (green curves connect to black short lines which represent the N-cell vortex on the -Y side). We introduce the term *long N-cell cycle* to identify the uninter-
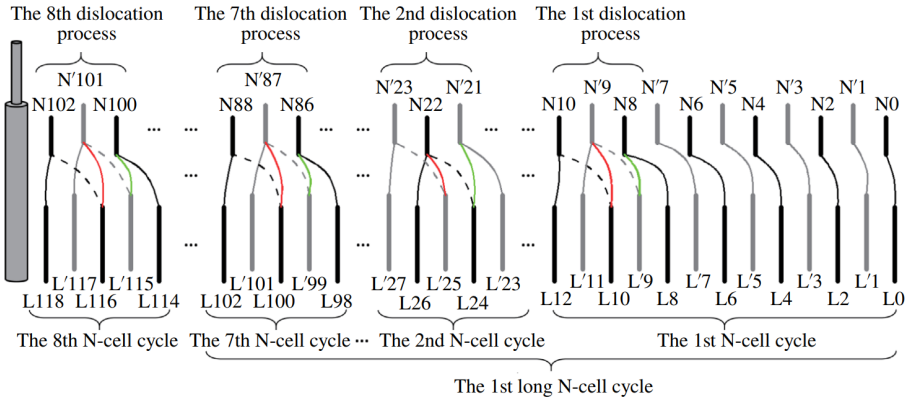
*Figure 8.7: Schematic topology sketches illustrating the long-time history of the vortex connection topology and the vortex shedding. The thick black and gray straight lines represent vortices on the -Y and +Y sides, respectively. Only the N- and L-cell vortices are shown by short and long straight lines. The connections between them are depicted by thin solid curves. Black and gray solid curves indicate the connections between N-cell vortex and its counterpart L-cell vortex. The red and green curves reveal different NL-loop structures (same color code as used in figure 8.6). The dashed curves, on the other hand, indicate broken connections that are not able to persist due to dislocations. We define a new term long N-cell cycle containing several conventional N-cell cycles, while the conventional N-cell cycle was firstly defined by Morton & Yarusevych [8] and adopted also in the present study.*

rupted series of antisymmetric N-cell cycles. Within one long N-cell cycle, antisymmetric vortex interactions appear between subsequent N-cell cycles. However, at the boundary between two long N-cell cycles, this antisymmetry is interrupted. Our long-time observation covering 8 long N-cell cycles shows that there are either 7 or 8 N-cell cycles in one long N-cell cycle. In fact, an exceptionally low frequency ($St_1$) is captured in figure 8.5(b) where a power spectra at position $(x/D, y/D, z/D) = (0.6, 0.2, -4.4)$ is shown. The value of $St_1$ is 0.0032, and is around $St_{beat}/7.5$. This coincides well with our observation that one long N-cell cycle contains either 7 or 8 N-cell cycles. We believe that this low-frequency component is related to the long N-cell cycles. More detailed information on this long-period phenomenon, and the unexpected interruption, will be discussed in §8.5. The other visible frequency components in figure 8.5(b) are combinations of the basic frequency components, i.e. $St_S$, $St_N$, $St_L$ and $St_1$ [30].

### 8.3.2   Necessity of monitoring the phase information of each N- and L-cell vortex

All the interesting physical phenomena, i.e. the formations of NL-loops, the unexpected interruption of the antisymmetry, etc, are directly related to the vortex dislocations in the wake behind the step cylinder. A consensus from the literature [4, 6, 16] is that vortex dislocations are attributed to different shedding frequencies. In the present configuration, if both N- and L-cell vortices shed regularly, it is natural to directly use $f_L$ and $f_N$ to measure the phase difference ($\Phi$) between N- and L-cell vortices. However, the actual wake flow is more complicated. In figures 8.8(a) and (b), we plot time traces of the instantaneous crossflow velocity ($v$) at two locations in the L- and N-cell regions in the symmetry plane. Two dashed sinusoidal curves with constant frequencies $f_L$ and $f_N$ are also plotted in the same figures. By comparing figure 8.8(a) and (b), it is clear that, unlike the regularly shed L-cell vortices, the shedding frequency of the N-cell vortex slightly fluctuates during every N-cell cycle. This was also briefly mentioned by Morton & Yarusevych [8], but not investigated further. The irregularity of the N-cell shedding makes it challenging but necessary to monitor the phase information of every N-cell vortex. Therefore, we developed a method to obtain the phase information ($\varphi$) and the phase difference ($\Phi$) of vortices. Details can be found in appendix 8.8.1.
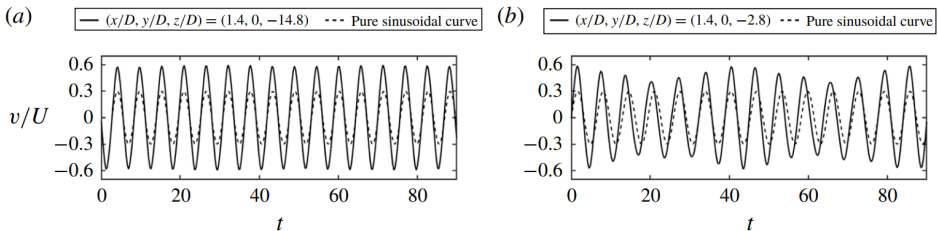


Figure 8.8: Time trace of the oscillating crossflow velocity (v) is plotted as the solid line: (a) at sampling point (x/D, y/D, z/D) = (1.4, 0, -14.8) in the L-cell region; (b) at the sampling point (x/D, y/D, z/D) = (1.4, 0, -2.8) in the N-cell region. For comparison, pure sinusoidal curves are plotted as dashed lines with frequency $f_L$ in (a) and frequency $f_N$ in (b). $f_L$ and $f_N$ are calculated by FFT obtained from figure 8.5.

## 8.4 Two different phase difference accumulation mechanisms and their effects on vortex interactions

### 8.4.1 Two different phase difference accumulation mechanisms
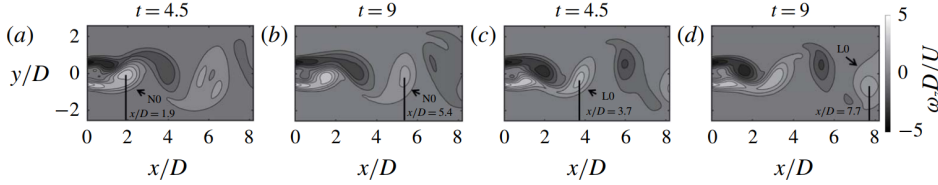


*Figure 8.9: (a) and (c) Instantaneous spanwise vorticity $\omega_z$ ($\omega_z = \partial v/\partial x - \partial u/\partial y$) contour plots in a $(x, y)$ plane at N-cell region $z/D = -2.9$ (black solid line in figure 8.6(a) and (b)); (b) and (d) are the same as (a) and (c) but at L-cell region $z/D = -14$ (black dotted line in figure 8.6(a) and (b)). By detecting the location of concentrated vorticity, the positions of vortices N'9 and L'9 are marked by black lines. (Note: we have compared the position of the center of the concentrated vorticity and the center in the region defined by $\lambda_2$-isolines, and confirmed only tiny differences.)*

From figure 8.6, one can see that both the N- and L-cell vortices are spanwise vortices. This means that the variation of the streamwise distance between corresponding N- and L-cell vortices can reflect the changes in their phase difference ($\Phi$). In the present study, we use the location of the most concentrated spanwise vorticity ($\omega_z$) to indicate the position of the corresponding vortex. In figure 8.9, we plot instantaneous spanwise vorticity $\omega_z$ contours at a (x, y) plane in the N-cell region $z/D = -2.9$ and L-cell region $z/D = -14$. Four black lines indicate the positions of vortices N0 and L0. One can see that from $tU/D = 4.5$ to 9, the streamwise distance between N0 and L0 increases from $1.8D$ ($3.7D$-$1.9D$) to $2.3D$ ($7.7D$-$5.4D$) as they convect downstream. This means that, even after both N0 and L0 disconnect from the shear layer, as shown in figure 8.6(a)), $\Phi$ between them continues to accumulate. By marking the moment when the N-cell vortex just forms as an individual wake-type vortex, we divide the process of $\Phi$ accumulation into two parts. Before this moment, $\Phi$ between the N- and L-cell vortex is dominated by their different shedding frequencies, called $\Phi_f$. After this moment, $\Phi$ is caused by different convective velocities in the N- and L-cell regions, and called $\Phi_c$. Detailed descriptions of monitoring $\Phi_f$

and $\varphi$ can be found in appendix 8.8.1. Due to the spatial inhomogeneity of the convective velocity, it is difficult to accurately assess its effect on $\Phi$. Yet, the distributions of mean streamwise velocity ($\bar{u}$) in different vortex cell regions can roughly indicate the influence.
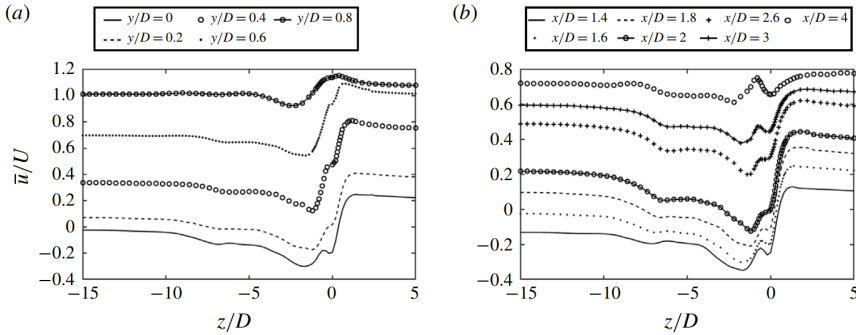


Figure 8.10: (a) Distributions of the mean streamwise velocity ($\bar{u}/U$) along spanwise lines with the same x coordinate (x/D = 1.6), but for different y coordinates. (b) Distributions of mean streamwise velocity $\bar{u}/U$ along spanwise lines with different x coordinates in the symmetry plane (y/D = 0).

In figure 8.10, the spanwise distributions of $\bar{u}$ are plotted at several downstream positions. As shown in figure 8.10(a), the mean streamwise velocity in the N-cell region in the symmetry plane ($y/D = 0$) is nearly $0.2U$ less than that in the L-cell region. At the side plane $y/D = 0.8$, this difference still reaches $0.1U$. From figure 8.10(b), we see that the difference in mean streamwise velocity is clear until a downstream position $x/D = 4$. In other words, at least until $x/D = 4$ in the wake, the convective velocity distribution is distinctly non-uniform in the spanwise direction. This non-uniformity induces an additional $\Phi$ when the vortices convect downstream. We note that this role of the non-uniform convection velocity and its effects have never been addressed before.

## 8.4.2 Effects of two phase difference accumulation mechanisms

### 8.4.2.1 Differences in formation positions of the NL-loop1 and NL-loop2

The formation process of the NL-loop1 in each N-cell cycle is repetitive. An example of this process is presented in figure 8.11, where the vortex structures are shown from both +Y and -Y sides of the step cylinder. In

figure 8.11(a) and (b), and the corresponding zoom-in plots (f) and (g), the foot of vortex N8 completely disconnects from the shear layer at $x/D = 2.8$ (marked by a black line in figure 8.11(b) and (g)). At this moment ($tU/D = 33.3$) the NL-loop1 structure has not yet formed, because there is still no direct connection between N8 and L'9. It takes some more time for N8 to convect downstream and eventually develop into the NL-loop1 with L'9 at $x/D = 3.3$ and $tU/D = 34.5$. This process is indicated in figures 8.11(b-e) and the corresponding zoom-in plots (g-j). By following the same process as described in §8.4.1, we found that from $tU/D = 33.3$ to 34.5, the streamwise distance between vortex N'9 and L'9 increases from $5.3D$ to $6.1D$ as they move downstream. When $\Phi$ between vortex N'9 and L'9 increases, L'9 gradually disconnects from its counterpart N'9 and forms the NL-loop1 with N8 (see figure 8.11(k-o)).

Unlike the NL-loop1 structure which has a distinct formation position, it is difficult to pinpoint where the NL-loop2 forms. As shown in figure 8.12(a-e), in the black circle area, it is not clear how the foot of vortex N'9 completely separates from the shear layer and subsequently connects to L10 as they move downstream. The connection between N'9 and L10 forms in the very near wake before N'9 completely disconnects from the shear layer. In order to compare with the formation process of the NL-loop1 structure shown in figure 8.11, we use the same method to monitor the variation of the streamwise distance between vortices N10 and L10. At $tU/D = 36.9$ (the corresponding instantaneous iso-surface of the vortex structure is shown in figure 8.12(g)), the distance between vortex N10 and L10 reaches $5.9D$. This is very close to the distance between N'9 and L'9 at $tU/D = 34.5$ (figure 8.11(n)), when L'9 successfully induces N8 to connect to itself and together form the NL-loop1 structure. At $tU/D = 36.9$, as shown in figure 8.12(b), the leg of vortex N'9 is at position $x/D = 2.8$. At the same downstream position, the foot of vortex N8 already disconnects from the shear layer, as shown in figure 8.11(b). It is reasonable to speculate that $\Phi$ between N10 and L10 becomes sufficiently large to attract N'9 to connect to L10 before it disconnects from the shear layer. As a consequence, the formation position of NL-loop2 is not so clear.

The time trace of $\Phi_f$ accumulation proves our speculation. By using the method described in appendix 8.8.1, the time trace of $\Phi_f$ accumulation in the 1st N-cell cycle is shown in figure 8.13(b). Circles in this figure represent $\Phi_f$ of corresponding N- and L-cell vortices, in which the green circle represents $\Phi_f$ between N'9 and L'9, and the red circle represents $\Phi_f$ between N10 and L10. Eventually, the dislocations of the vortex pairs corresponding to the green and red circles cause formations of the NL-loop1
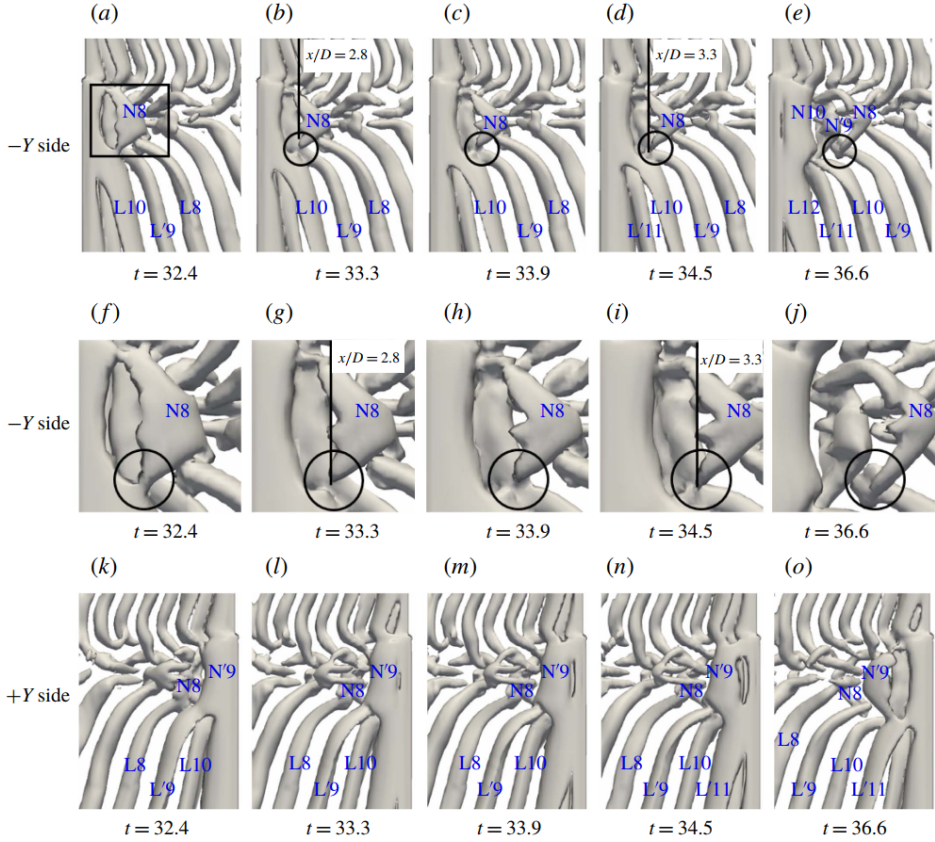
*Figure 8.11: The formation process of the NL-loop1 structure in the 1st
dislocation process (defined in figure 8.7) is shown from the -Y and +Y side
in the first and third row, respectively. In the second row, zoom-in plots of
vortex structures at N-cell region (black rectangle in (a)) are shown. The
black circles highlight the position where the NL-loop1 forms.*

structure (N8-L'9) and the NL-loop2 structure (N'9-L10), respectively.

One can see that the red circle represents a larger $\Phi_f$ value than the
green one, which means that $\Phi_f$ between N10 and L10 is larger than that
between N'9 and L'9. Therefore, compared to the vortex pair N10-L10, the
vortex pair N'9-L'9 needs a larger contribution of $\Phi_c$ to achieve a sufficiently
large $\Phi$ to trigger the vortex dislocation between them, and the subsequent
formation of the NL-loop1 (N8-L'9). In other words, due to the reduced need
of a contribution from $\Phi_c$, the vortex dislocation between N10 and L10 and
the subsequent NL-loop2 (N'9-L10) is formed closer to the cylinder, which
causes the unclear formation position.
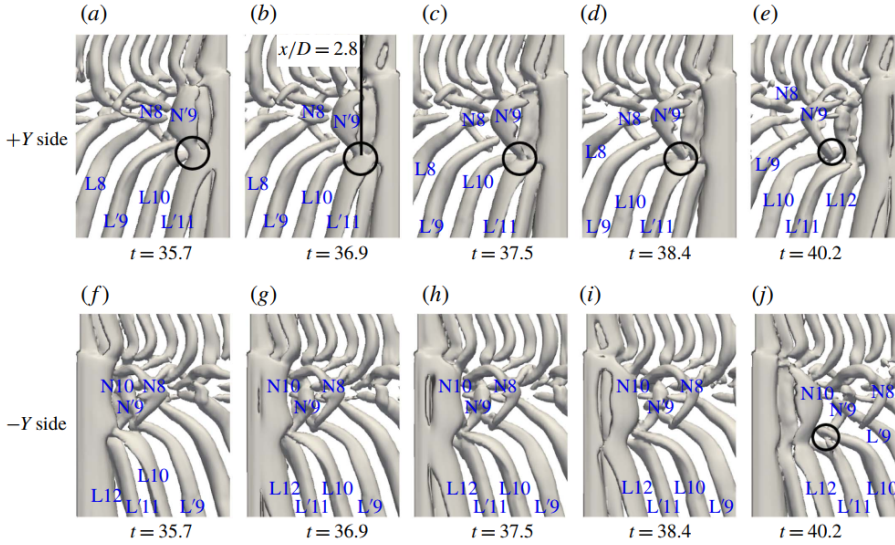
Figure 8.12: The formation process of the NL-loop2 structure in the 1st dislocation process is shown from both +Y and -Y sides. The black circles highlight the position where the NL-loop2 structure is formed.

### 8.4.2.2 Variation of formation positions of the NL-loop1 structures

In figure 8.14, the NL-loop1s in the first eight N-cell cycles are plotted. The black vertical lines show the positions where the NL-loop1 structures just form. Except for the 6th N-cell cycle (figure 8.14(f)), the NL-loop1 structures alternatingly appear at the +Y and -Y side of the step cylinder from the 1st to the 7th N-cell cycles (the first long N-cell cycle). The shape and the formation position of the NL-loop1 structure also vary, as depicted in figure 8.14(a-h).

In table 8.3, the relation between the formation positions of the NL-loop1s in the 1st long N-cell cycle and their $\Phi_f$ are presented. One sees that, except for the 6th N-cell cycle, the formation positions move downstream as the corresponding $\Phi_f$ decreases. This can easily be ascribed to the already discussed two different phase difference accumulation mechanisms. Formation of the NL-loop1 structures require sufficiently large $\Phi$. Since $\Phi_f$ decreases, $\Phi_c$ must contribute more, which consequently leads to a longer formation time and further downstream formation position. To be more clear, the relations between $\Phi_f$ and formation positions of the corresponding NL-loop1s during the 1st-7th long N-cell cycles are plotted in figure
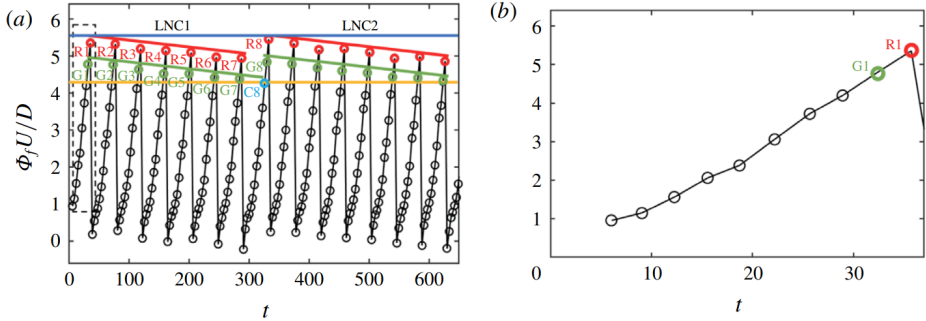
Figure 8.13: (a) Time trace of $\Phi_f$ between corresponding N-cell and L-cell vortices in the 1st (LNC1) and 2nd (LNC2) long N-cell cycle, i.e. from the 1st to the 15th N-cell cycle. The circles represent $\Phi_f$ between a N-cell vortex and its counterpart L-cell vortex. The green and red circles indicate $\Phi_f$ which eventually causes formations of the NL-loop1 and NL-loop2 structures, respectively. From the 1st to the 8th N-cell cycle, the green and red circles are numbered. (b) A zoom-in plot of the time trace of $\Phi_f$ in the 1st N-cell cycle (the black dashed rectangle in (a)). From the left to the right, circles represent $\Phi_f$ between the vortex pair N'1-L'1 to the vortex pair N10-L10, respectively. (Note: The detailed calculation processes can be found in appendix 8.8.1. All detailed data about $\Phi_f$ and the longer time trace of $\Phi_f$ are included in the supplementary file 1. The trigger value and the threshold value are estimated based on 55 N-cell cycles, as shown in supplementary file 3.)
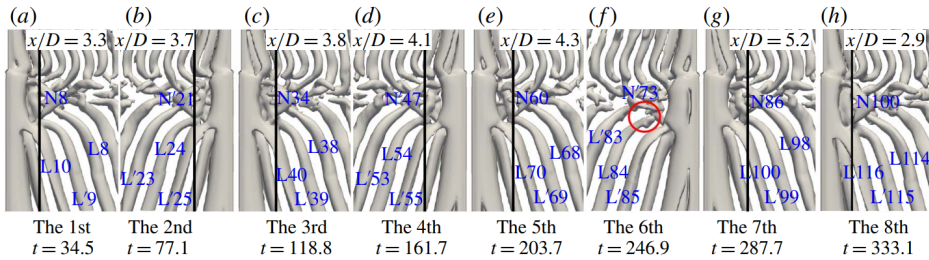


Figure 8.14: The NL-loop1 structures in the 1st to the 8th N-cell cycle are plotted from both the -Y and +Y side (The 1st long N-cell cycle consists of the 1st to the 7th N-cell cycles). From (a) to (h), the just formed NL-loop1 in the 1st - 7th N-cell cycles are plotted, and the black line marks the formation position of NL-loop1. The red circle in (f) highlights an irregular absence of the NL-loop1 structure which will be discussed later.

| N-cell cycle No. | 1 | 2 | 3 | 4 | 5 | 6 | 7 |
|---|---|---|---|---|---|---|---|
| Formation position $x/D$ | 3.3 | 3.7 | 3.8 | 4.1 | 4.3 | - | 5.2 |
| $\Phi_f U/D$ | 4.485 | 4.470 | 4.345 | 4.275 | 4.225 | 4.115 | 4.085 |

*Table 8.3: Formation positions and $\Phi_f$ which causes the NL-loop1s in the 1st to 7th N-cell cycle (the 1st long N-cell cycle). The corresponding vortex structures are shown in figure 8.14(a-g). In the 6th N-cell cycle, there is a loop formation failure.*

8.15. Generally, except for several irregular points, the formation position shifts downstream as $\Phi_f$ decreases. (Note: the appearances of the irregular points will be discussed in §8.5.3.)
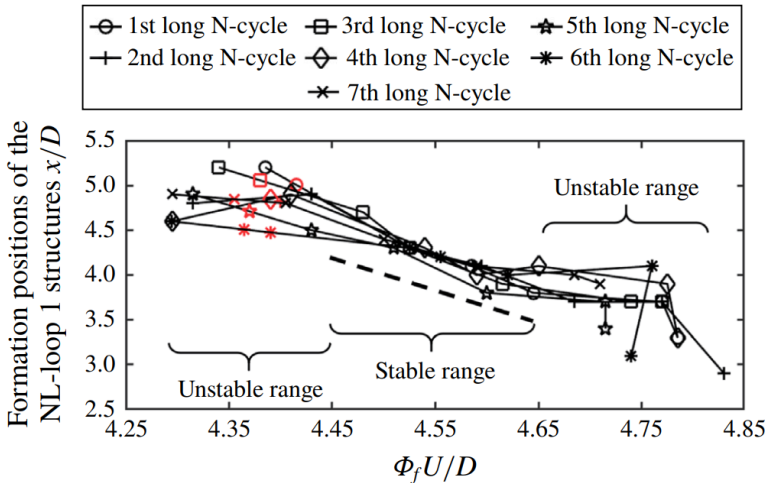


*Figure 8.15: Relation between $\Phi_f$ and the formation position $(x/D)$ of corresponding NL-loop1 structures in the 1st–7th long N-cell cycles (52 N-cell cycles are included). Based on the trends of the curves, one stable range and two unstable ranges are identified. A straight dashed line outlines the trend of the stable range. The occasionally absent NL-loop1 structures in these seven long N-cell cycles are marked by red color at the expected formation positions which can be obtained by linear interpolation.*

Based on the discussions above, we conclude that, for the NL-loop structures, $\Phi$ is accumulated by the joint influence of different shedding frequen-

cies and different convective velocities

$$\Phi = \Phi_f + \Phi_c. \tag{8.2}$$

As the relative magnitude of $\Phi_f$ and $\Phi_c$ varies, the formation processes of the NL-loop structures change.

## 8.5    Characteristics of the long N-cell cycles

### 8.5.1    Trend of $\Phi_f$ variation

The time trace of $\Phi_f$ accumulation between corresponding N- and L-cell vortices is plotted in figure 8.13(a). We use green and red circles to indicate $\Phi_f$ of the pair of N- and L-cell vortices whose dislocation eventually causes the NL-loop1 and NL-loop2, respectively. Two solid lines with the same corresponding colors describe the decreasing tendency in $\Phi_f$ of both NL-loop1 and NL-loop2 over time.

The gradual decrease of $\Phi_f$ in each N-cell cycle can be expressed as:

$$S = \alpha \frac{1}{2f_L} - \beta \frac{1}{2f_N} \tag{8.3}$$

where $S$ (with dimension $D/U$) is a measure of the phase shift of every vortex pair in one N-cell cycle, as compared to the N-cell cycle before it. In this expression, $\alpha$ and $\beta$ represent the number of L- and N-cell vortices in one N-cell cycle. $f_L$ and $f_N$ are the shedding frequencies of L- and N-cell vortices. In the present case, $\alpha = 15$, $\beta = 13$, $f_L D/U = 0.1780$ and $f_N D/U = 0.1545$ (from figure 8.5), from which we obtain $S = 0.064D/U$. This means that, in one N-cell cycle, the duration of 13 N-cell and 15 L-cell vortices is not exactly the same. Although $S$ has a very small value, after a certain number of N-cell cycles, the accumulated difference becomes large enough to influence the dislocation process. Moreover, by checking figure 8.13(a) and the supplementary file 1, one can find that from R1 to R7 or from G1 to G7, $\Phi_f$ decreases by approximately $0.4D/U$, i.e. $\Phi_f$ decreases by around $0.067D/U$ after every N-cell cycle which is close to the $S$ value from expression 8.3.

It is worth mentioning that the numbers $\alpha = 15$, $\beta = 13$ and $S = 0.064D/U$ are related to the particular configuration studied. For different configurations, i.e. different $D/d$ and $Re_D$, these numbers in expression 8.3 may vary. But what we observe in figure 8.13(a) will be a common feature, because it is extremely unlikely to attain a $S$ value exactly equal to zero.

### 8.5.2 Interruption of the antisymmetric phenomenon

From figure 8.14(a) to (h), one can clearly see that the NL-loop1 structure alternatingly appears at the -Y and +Y side of the step cylinder in subsequent N-cell cycles. This is the antisymmetric phenomenon reported in Tian *et al.* [10]. In the present case, the long-time observation reveals that this antisymmetric phenomenon will be interrupted once in a while. As shown in figure 8.14(g) and (h), instead of being antisymmetric, the loop structures in the 7th and 8th N-cell cycles are symmetric. In these two N-cell cycles, both NL-loop1 structures, i.e. N86-L'99 and N100-L'115, are formed at the -Y side.

This interruption is caused by the decreasing tendency in $\Phi_f$, as we discussed in §8.5.1. Normally, there are 13 N-cell and 15 L-cell vortices in one N-cell cycle. The odd number of N-cell vortices causes the antisymmetric phenomenon. However, as shown in figure 8.13(a), when $\Phi_f$ continues to decrease along the green line from G1 to C8, it eventually becomes insufficient in point (C8). Even by including the contribution of $\Phi_c$, $\Phi$ is still not large enough to induce the formation of the expected NL-loop1 (N'99–L114). Therefore, in this N-cell cycle, one additional vortex pair shedding is needed to make $\Phi$ sufficiently large to induce formation of the NL-loop1. The additional one pair of N- and L-cell vortices makes the number of N-cell vortices in the 8th N-cell cycle become even, and thereby interrupts the antisymmetric phenomenon. In the supplementary file 3, the time trace of $\Phi_f$ between N- and L-cell vortices in the 1st to the 8th long N-cell cycles (the 1st to the 55th N-cell cycles) is illustrated.

### 8.5.3 *Trigger value* and *threshold value* of vortex dislocations

Based on the results from earlier papers [8, 16] and our discussions in §8.4 and §8.5.2, it is clear that only when $\Phi$ becomes sufficiently large, the vortex dislocation process can be triggered. We call this value the *trigger value*. Based on equation 8.2, $\Phi$ consists of two parts, $\Phi_f$ and $\Phi_c$. Due to the complexity of $\Phi_c$, an accurate *trigger value* is hard to obtain, but an approximate value is possible to estimate. As we discussed in §8.4, unlike the NL-loop1 structure which has a clear formation position, the NL-loop2 structure forms in the near wake. This makes it hard to define the exact formation position of the NL-loop2. It means that the $\Phi_f$ which induces this NL-loop2 is very close to the *trigger value*, and only a modest contribution from $\Phi_c$ is needed. Therefore, by considering all the largest $\Phi_f$ corresponding to the NL-loop2s, we can draw the blue line in figure 8.13(a)

to approximate the *trigger value* (around $5.60D/U$).

Besides the *trigger value*, there is another interesting value of $\Phi_f$ that should be noticed. As we discussed in §8.5.2, when $\Phi_f$ continues to decrease from G1 to C8 (figure 8.13(a)), the expected formation of the NL-loop1 (N'99-L118) fails. We can speculate that there is a *threshold value* for $\Phi_f$, such that when $\Phi_f$ becomes less than this value, a vortex dislocation will not occur, even when taking the contribution from $\Phi_c$ into account. By connecting all of the smallest values of $\Phi_f$ in green ($\Phi_f$ inducing the NL-loop1), the *threshold value* can be estimated by the yellow line in figure 8.13(a), with a value around $\Phi_f U/D=4.30$.

Due to the complexity of $\Phi_c$, the formation of NL-loop structures becomes quite unstable when $\Phi_f$ is close to the *trigger value* or the *threshold value*. As shown in figure 8.15, one stable $\Phi_f$ range and two unstable $\Phi_f$ ranges can be identified. A dashed straight line outlines the trend in the stable range ($4.45 \lesssim \Phi U/D \lesssim 4.65$), in which the distribution of markers is concentrated, and the formation position decreases almost linearly as $\Phi_f$ increases. Outside this stable range, the tendency becomes unclear. When $\Phi_f$ is smaller than $4.45D/U$, i.e. much smaller than the *trigger value* $5.60D/U$ and close to the *threshold value* $4.30D/U$, the contribution of $\Phi_c$ becomes significant and determines whether the NL-loop1 is able to be formed or not. Figure 8.15 shows that, in the unstable range ($4.30 \lesssim \Phi_f U/D \lesssim 4.45$), all NL-loop1s are generated beyond a downstream position $x/D = 4$, i.e. $\Phi$ of these NL-loop1s can not exceed the *trigger value* upstream of $x/D = 4$. In this situation, how much $\Phi_c$ can accumulate downstream of $x/D = 4$ determines whether these NL-loop1s will appear or not. In figure 8.10(b), we see apparent differences between the convective velocity in the N- and L-cell regions, while these differences diminish as we move downstream. Downstream of $x/D = 4$, the differences become very small. In other words, the accumulation of $\Phi_c$ is modest downstream of $x/D = 4$. Based on the above observation, we can conclude that, for the NL-loop1s with $\Phi_f$ in then range ($4.30D/U - 4.45D/U$), their phase differences are around a critical value, and a small variation in $\Phi_c$ can influence their formation positions, and even lead to unsuccessful formations. The fact that all the red markers in figure 8.15, which represent the occasionally absent NL-loop1s, are located in this range also supports this conclusion.

Another unstable range appears when $\Phi_f$ corresponding to NL-loop1 becomes larger than $4.65D/U$, which is close to the approximate level of the *trigger value*. In this situation, only a small contribution from the convective velocity is needed for NL-loop1 to form. Meanwhile, as shown in figure 8.10(b), when $x/D$ is smaller than 3 ($x/D$=1.4, 1.6, 1.8, 2, 3) the

differences between the convective velocities in the N- and L-cell regions are obvious. These differences are able to increase $\Phi_c$ rapidly. Variations in the convective velocity could also affect the formation position, and lead to a less clear tendency.

Detailed investigations show that many interesting and important features of vortex dislocation in a step cylinder wake may easily be overlooked if the observation time is too short. In the present case, during one long N-cell cycle, most N-cell cycles need an odd number of N- and L-cell vortices to accumulate sufficient $\Phi$, and to trigger the vortex dislocation, which leads to antisymmetry between subsequent N-cell cycles. However, between two long N-cell cycles, the antisymmetry is interrupted. In our earlier paper [10], we did not foresee this interruption, because we tried to conclude that the antisymmetric dislocation process is a result of $f_L/f_{beat} \approx 7.5$, such that two dislocations are needed to compensate for the frequency differences between the N- and L-cells, and that the wake could return to normal one-to-one shedding. However, more detailed observations based on substantially longer simulations show that the small differences (i.e. $S$ in expression 8.3), which were ignored when we obtain the $f_L/f_{beat} \approx 7.5$ relationship, are continuously accumulating and cause a decreasing tendency in the time trace of $\Phi_f$. This is exactly what causes the interruption of the antisymmetry discussed in this section. We note again that these results require exceptionally long simulations. The value of $S$ is so small that it may easily be ignored in short-term observations. But it turns out to lead to very interesting vortex dislocation phenomena. We mentioned that McClure *et al.* [18] also reported similar small differences in the vortex dislocations behind a dual step cylinder. However, instead of investigating how different vortex dislocations vary, they focused on when two identical vortex dislocations appear.

## 8.6   Investigation on universality

In order to investigate the universality of the two different phase difference accumulation mechanisms and their effects on vortex dislocations, the wake behind a step cylinder with $D/d = 2.4$ at the same $Re_D$=150 is investigated. All observations are consistent with our findings from the $D/d = 2.0$ case and support our previous discussions and conclusions.

In general, comparing with the wake in the $D/d = 2$ case, the change in $D/d$ brings no fundamental changes. As shown in figure 8.16, the three dominating frequency components, i.e. $St_S$, $St_N$, $St_L$, and the beat frequency $St_{beat}$ are all captured, similar as in figure 8.5(a). Moreover, similar

non-uniform distributions of the mean streamwise velocity $\bar{u}$ are shown in figure 8.17. This means that, for the $D/d = 2.4$ case, the differences in convective velocities in the N- and L-cell regions can increase $\Phi$ when vortices convect downstream, just as for $D/d = 2.0$ case.
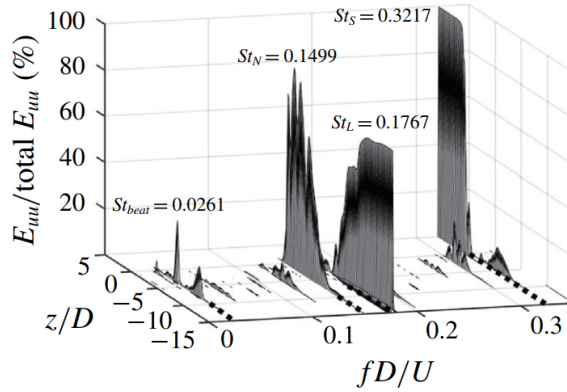


Figure 8.16: *Streamwise velocity spectra in the $D/d = 2.4$ case are calculated based on $1200D/U$ continuous velocity data along a vertical sampling line parallel to the Z-axis at position $(x/D, y/D)=(0.6, 0.2)$.*
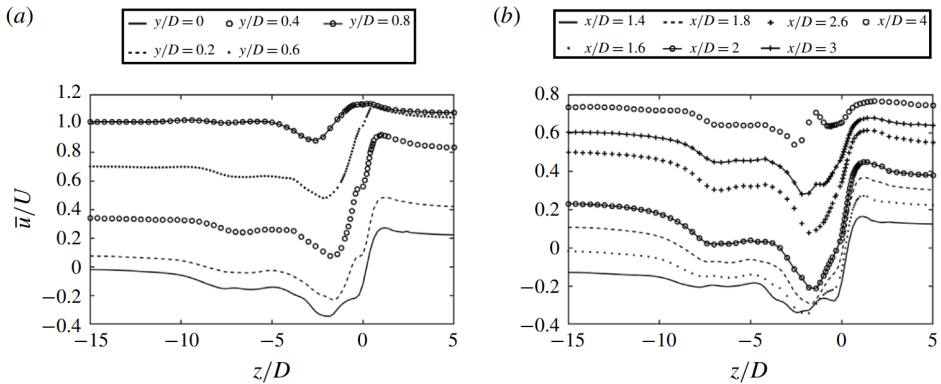


Figure 8.17: *Distributions of mean streamwise velocity $\bar{u}/U$ in the $D/d = 2.4$ case.*

In figure 8.18(a) and (b), the two phase difference accumulation mechanisms (equation 8.2) are examined. As $\Phi_f$ decreases along the red and green lines in figure 8.18(a), larger contributions from $\Phi_c$ are needed to make $\Phi$ sufficiently large to trigger the vortex dislocation, which makes the formation positions of the NL-loop1 structures move downstream during two long
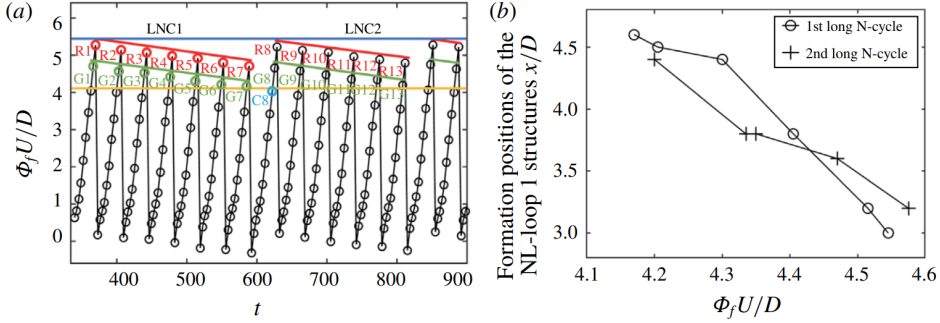
*Figure 8.18: (a) Time traces of $\Phi_f$ between N-cell and L-cell vortices are plotted in the 1st and 2nd long N-cell cycles in the $D/d = 2.4$ case. The same annotations as in figure 8.13 are also used here. (b) Relation between $\Phi_f$ and the formation position (x/D) of NL-loop1 structures in the 1st and 2nd long N-cell cycles in the $D/d = 2.4$ case (same as in Fig. 8.15). (All detailed data about $\varphi$ and $\Phi_f$ is included in the supplementary file 2.)*

N-cell cycles, as shown in figure 8.18(b).

This decreasing tendency in $\Phi_f$ corresponding to the NL-loop1 and NL-loop2 in figure 8.18(a) can be explained by equation 8.3. In figure 8.18(a), from G1 to G7, $\Phi_f$ decreases by $0.52D/U$ ($4.69D/U$-$4.17D/U$=$0.52D/U$), i.e., it decreases by around $0.087D/U$ after every N-cell cycle, which is close to the value from equation 8.3 ($13 \times \frac{1}{2\times0.1767U/D} - 11 \times \frac{1}{2\times0.1499U/D} = 0.094U/D$). As $\Phi_f$ continues to decrease, the expected interruption of the conventional antisymmetry appears in the $D/d = 2.4$ case. The NL-loop1 structures in seven continuous N-cell cycles are plotted in figure 8.19(a) to (g). The NL-loop1 alternatingly appears at the -Y and +Y side in the first six N-cell cycles, i.e. from the 2nd to the 7th N-cell cycle, from figure 8.19(a) to (f). But this conventional antisymmetry is interrupted in the 7th and 8th N-cell cycles. In figure 8.19(f) and (g), the NL-loop1 appears at the same side of the step cylinder. Based on the interruption of the antisymmetry, the long N-cell cycle, the *trigger value* (blue line) and the *threshold value* (yellow line) are also indicated in figure 8.18(a) and (b), similar as in the $D/d = 2$ case.

These investigations prove that our discussions and conclusions in §8.4 and §8.5 are not only valid in the wake behind the step cylinder $D/d$=2 case, but also in other $D/d$ cases.
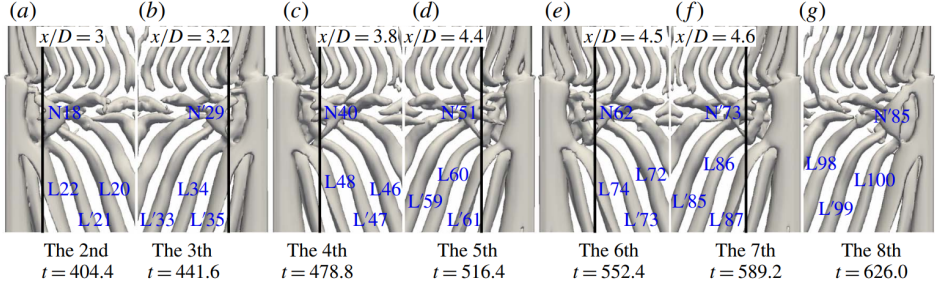
*Figure 8.19: From (a) to (g), the NL-loop1 structures in the 2nd-8th N-cell cycles are plotted from both the -Y and +Y side in the D/d = 2.4 case. The black line marks the formation position of a NL-loop1.*

## 8.7   Conclusions

We use direct numerical simulations to investigate vortex interactions, especially the vortex dislocations between the N- and L-cell vortices, in the near wake behind two single step cylinders with diameter ratio $D/d = 2$ and 2.4 at $Re_D = 150$. Our results of the $D/d = 2$ case show good agreement with previous studies [5, 8, 10], with respect to the three dominating spanwise vortices (i.e. S-, N-, and L-cell vortices), vortex dislocations occurring at the N-L cell boundaries, loop structures (NL-loop1 and NL-loop2) appearing during the dislocation processes, and antisymmetric phenomena between subsequent N-cell cycles. In addition, the numerical results provide more detailed information on how the phase difference ($\Phi$) between the corresponding N- and L-cell vortices is accumulated and finally triggers the formation of vortex dislocations and concomitant NL-loop structures. A phase difference accumulation mechanism is identified for the first time, i.e. $\Phi = \Phi_f + \Phi_c$. We have clearly identified that there are two qualitatively different physical factors contributing to the accumulation of $\Phi$, one is different shedding frequencies ($\Phi_f$), the other one is varying convective velocities in the different vortex cell regions ($\Phi_c$). While $\Phi_f$ is relatively well-known, the contribution from convective velocity $\Phi_c$ has never been examined before.

Based on the new understanding of the phase difference accumulation mechanism, we manage to obtain a clearer insight in various phenomena during the dislocation process. Most importantly, the variations of the formation position of the NL-loop1 and NL-loop2, and the irregularity of the NL-loop1 formation have been fully explained. For a pair of N- and L-cell vortices, as $\Phi_f$ decreases, $\Phi_c$ must contribute more to ensure a sufficiently

large $\Phi$ (we refer to it as the *trigger value*) that can trigger the vortex dislocations. This makes the formation position of the corresponding NL-loop structure move downstream.

Moreover, long-time trace of the accumulation of $\Phi_f$ clearly shows cyclic trends, which are caused by minute differences accumulated during each N-cell cycle (as indicated by $S$ in expression 8.3). Due to the accumulation of this difference, the antisymmetric phenomenon, reported in Tian *et al.* [10], will be cyclically interrupted when $\Phi_f$ decreases below a certain value. We refer to this value as the *threshold value*. The long N-cell cycle is defined based on this phenomenon. Finally, in §8.6, the universality of our discussions and conclusions is justified by investigating the $D/d = 2.4$ case.

The identification of the phase difference accumulation mechanism, explanations of the formation positions of the NL-loops and observations of the long-period characteristics offer a deeper and more complete understanding of the vortex dislocation phenomenon in the wake behind a step cylinder.

Although all investigations in the present paper are based on single step cylinders at Reynolds number 150, the N- and L-cell vortices and their vortex dislocations were observed in other step cylinder cases with $1.55 < D/d < 2$ at $67 < Re_D < 1100$ [5, 7, 8, 15]. In these cases, due to the abrupt change in diameter, vortex shedding frequencies and convective velocities are different in N- and L-cell regions. With these two mechanisms present in the flow, we believe that our discussions and conclusions are also valid for the above mentioned cases. We anticipate that the phase difference accumulation mechanism we report here also exists in other wake flows that contain several adjacent spanwise vortices. In addition, the method we have developed to obtain the phase information and phase differences of vortices may also be applicable in other wake flows.

Declaration of interests. The authors report no conflict of interest.

# Acknowledgements

# Supplementary file

Supplementary files 1, 2, 3 and 4 are attached in the end of this thesis.

## 8.8   Appendix

### 8.8.1   A method used to obtain the phase information and phase difference of vortices

In order to perform detailed investigations on how the phase difference between corresponding N- and L-cell vortices accumulates and triggers the vortex dislocation, we need a reliable method to obtain the phase information ($\varphi$) and the phase difference ($\Phi$) of the wake vortices. According to Green & Gerrard [31] and Griffin [32], the end of the vortex formation region coincides with the location where the vortex strength becomes maximum. By monitoring the time traces of the strength of a vortex and the corresponding vorticity distribution along a center line at $y/D = 0$, we found that in the present low-Reynolds-number case the time instant when the vortex strength reaches its maximum coincides with the instant at which the corresponding largest $\omega_z$ appears at the center line. A detailed example is shown in supplementary file 4. Based on this feature, the *shed position* of a vortex is defined as the position where the corresponding largest $\omega_z$ appears at the center line. Moreover, $\varphi$ of one vortex is defined as the time instant when the corresponding $\omega_z$ reaches its maximum at the sampling point. At a downstream sampling point, $\Phi$ between a pair of the N- and L-cell vortices is the time difference between the time instants when they pass this sampling point:

$$\Phi = \varphi_N - \varphi_L. \tag{8.4}$$

Ideally, we monitor $\varphi_N$ and $\varphi_L$ at the *shed position* of the N- and L-cell vortex, respectively. Then, by using equation (8.4), $\Phi$ can be obtained. However, there are two challenges:

1. Only when both the N- and L-cell vortex are monitored at the same downstream position, we can get $\Phi$ between them without taking the effects from the *convective velocity* into account. Due to different shedding frequencies, the shedding positions of the N- and L-cell vortices are different. Moreover, the fluctuations in the shedding frequencies of N-cell vortices, as discussed in §8.3.2, make the situation even more complicated.

2. In the L-cell region, due to the oblique shedding, the *phases* of the L-cell vortices vary when the sampling point shifts in the spanwise direction.

   The general process developed to overcome these two challenges is: (1) Find the regular shedding regions of the N- and L-cell vortices. (2) Monitor

*shed positions* of the N- and L-cell vortices, and find the suitable sampling positions for both of them. (3) Develop a method to minimize effects of the oblique shedding in the L-cell region. The complete processes of obtaining $\Phi$ in the $D/d = 2$ case are described in the following.

### 8.8.2    Selection of the sampling region and the signal variable

The root mean square ($RMS$) of the spanwise vorticity $\omega_z$ in a part of the N-cell region ($-3.2 < z/D < -2.4$) and the L-cell region ($-18.8 < z/D < -15.8$) are plotted in figure 8.20. From figure 8.20(a), one can see that except for the lowest curve (at $z/D$=-2.4), the trends of the other five curves are the same. Especially at position $z/D$= -2.8 and -2.9, the $RMS$ values coincide, as presented in the zoom-in view figure 8.20(a)-(II). This means that the N-cell vortices can be treated as a regular shed spanwise vortex in the region $-3.2 \lesssim z/D \lesssim -2.6$. In the L-cell region, as illustrated in figure 8.20(b), the differences between the results of four sampling points are negligible. The zoom-in view figure 8.20(b)-II) shows that the largest difference in RMS of $\omega_z$ is about $0.01U/D$, i.e. only 0.3% of the peak value. Generally, the regions ($-3.2 \lesssim z/D \lesssim -2.6$) and ($z/D \lesssim -15.8$) can be treated as the regular shedding region of N- and L-cell vortices, respectively.
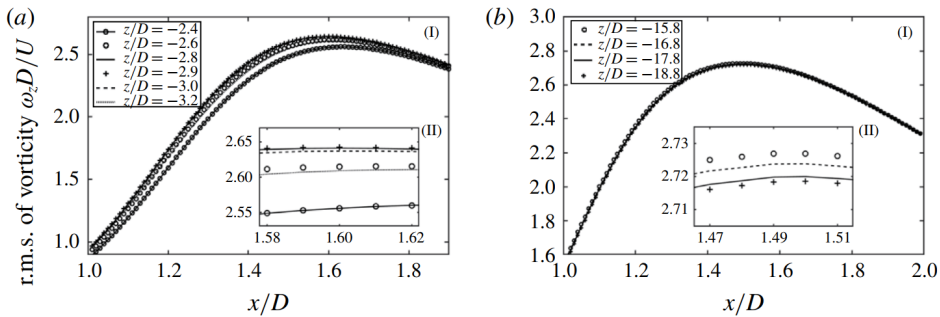


*Figure 8.20: (a): (I) The distribution of RMS of vorticity component $\omega_z D/U$ in a part of the N-cell region ($-3.2 < z/D < -2.4$), (II) A zoom-in view of the peak area of the curves in figure (I); (b): (I) The distribution of RMS of vorticity component $\omega_z D/U$ in a part of the L-cell region ($-18.8 < z/D < -15.8$), (II) A zoom-in view of the peak area of the curves in figure (I).*

As illustrated in §8.3.2, far away from the step position, vortices shed regularly in the L-cell region. In figure 8.21, the vorticity magnitude $|\omega|$, and the three vorticity components ($\omega_x$, $\omega_y$ and $\omega_z$) are checked at point $(x/D,\ y/D,\ z/D) = (1.5,\ 0,\ \text{-15.8})$. The time traces of all three vorticity

components completely repeat themselves with the same period as the L-cell vortex. All vorticity components oscillate regularly enough to be used to monitor $\Phi$ of L-cell vortices. On the other hand, in the N-cell region, the vortex shedding is more complicated. In figure 8.22, at the position ($x/D$, $y/D$, $z/D$) = (1.5, 0, -2.9), which is in the regular shedding region of N-cell vortices, time traces of both $\omega_x$ and $\omega_y$ show substantial irregularities, which are possibly caused by the intensive down-wash [5] and the two pairs of streamwise vortices [5, 6], respectively. However, without disturbances, $\omega_z$ oscillates regularly in figure 8.22(d).
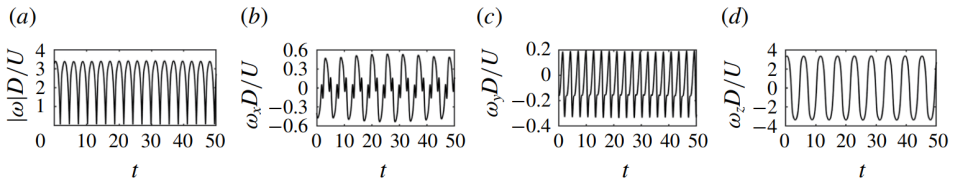


Figure 8.21: *The time traces of magnitude of vorticity ($|\omega|D/U$) and its three components ($\omega_x D/U$, $\omega_y D/U$ and $\omega_z D/U$) in the L-cell region at the point ($x/D$, $y/D$, $z/D$)=(1.5, 0, -15.8) are plotted in (a), (b), (c) and (d), respectively.*
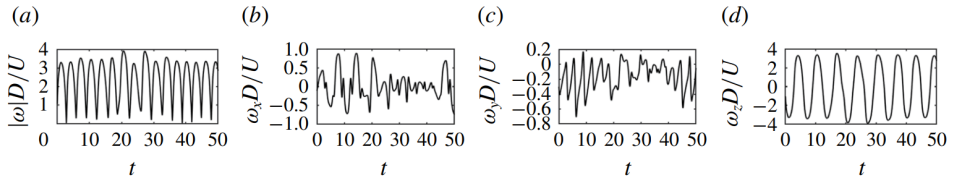


Figure 8.22: *Same as in figure 8.21, but at a different position ($x/D$, $y/D$, $z/D$)=(1.5, 0, -2.9), i.e. in the N-cell region.*

In general, $\omega_z$ of the N- and L-cell vortices oscillate regularly in parts of their shedding regions. It therefore becomes reasonable to select $\omega_z$ as the signal variable.

### 8.8.3   The method for obtaining the phase ($\varphi$) and the *shed position* of vortices

Both the N- and L-cell vortices shed alternatingly from the two sides of the step cylinder. As mentioned in the beginning of Appendix. 8.8.1 and Supplementary file 4, in the present low Reynolds number case, the strength of a vortex and its induced vorticity at the center line ($y/D$=0) approximately

reach their extreme values at the same time. Therefore, we can obtain $\varphi$ and the *shed position* of vortices by monitoring distributions of $\omega_z$ in the symmetry plane. (Note: The following analysis is based on data obtained from high-density (0.01D) sampling lines with sampling frequency $200U/D$. Considering that the shedding frequency of the N- and L-cell vortex is around $0.2U/D$, $200U/D$ is long enough to get the accurate results.)

1. Determination of $\varphi$ and *shed position* of the vortex along a sampling line.

   By checking the variation of $\omega_z$ along a sampling line in the symmetry plane (y/D=0), the *shed position* and $\varphi$ of each vortex can be obtained. In figure 8.23(a), as a vortex passes through a sampling line (from $(x/D,\ y/D,\ z/D)$=(1, 0, -15.8) to (2, 0, -15.8)), the distributions of $\omega_z$ along this line are plotted in the period from $tU/D$=4.205 to 6.205 with a time interval $0.1D/U$. In figure 8.23(a), the maximum of each curve is marked by a small red circle, whose position $(x/D,\ \omega_z D/U)$ represents the core line position and strength of the source vortex. A zoom-in plot of the red circle concentrated area (black rectangular area in (a)) is shown in figure 8.23(b), and the corresponding time trace of these red circles is plotted in figure 8.23(c). The number below each red circle represents its temporal order. One can see that, from the 1st to 10th red circle, the corresponding $\omega_z$ gradually reaches its maximum at $x/D = 1.46$ (as shown in figure 8.23(b)) and at $tU/D$=5.265 (as shown in figure 8.23(c)). This means that the source vortex contains maximum vorticity and separates from the shear layer at $x/D$=1.46 when $tU/D$=5.265. In other words, the *shed position* of this vortex is $x/D$=1.46, and corresponding $\varphi$ at position $(x/D,\ y/D,\ z/D)$=(1.46, 0, -15.8) is $5.265D/U$.

2. Obtaining $\varphi$ of vortices at a fixed sampling point.

   For a fixed sampling point in the symmetry plane ($y/D = 0$), $\omega_z$ will oscillate as vortices pass through the point. When the core lines of vortices pass the sampling point, $\omega_z$ reaches its extremum at this point. Figure 8.23(d) shows the oscillation of $\omega_z$ at position $(x/D,\ y/D,\ z/D) = (1.46, 0, -15.8)$, from which the abscissa of the peaks and troughs of this curve represents $\varphi$ of vortices shed from the -Y and +Y side of the step cylinder, respectively.
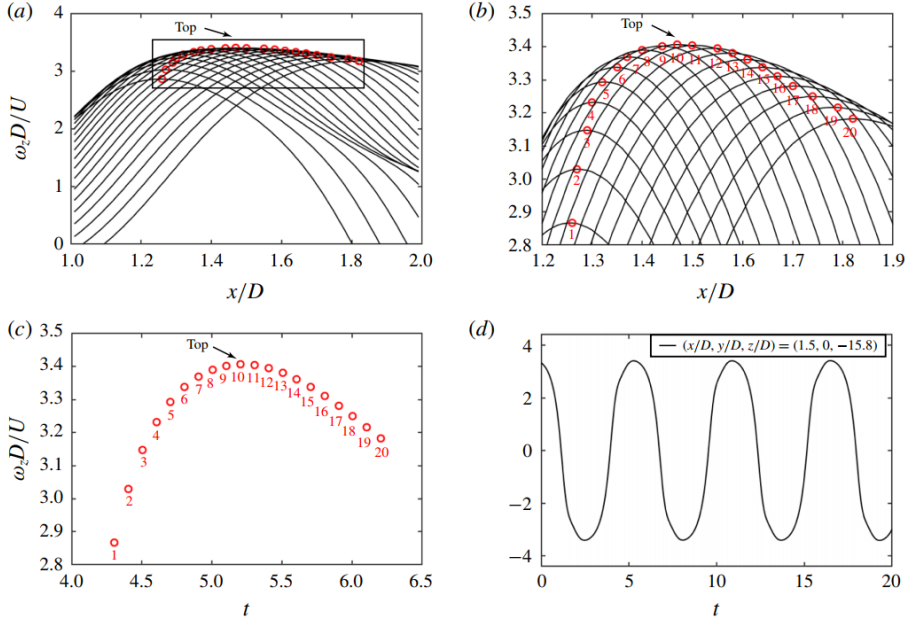
Figure 8.23: a) From $tU/D=4.205$ to 6.205, distributions of vorticity $\omega_z U/D$ along a sampling line (from $(x/D,\ y/D,\ z/D)=(1,\ 0,\ -15.8)$ to $(2,\ 0,\ -15.8))$ are plotted with a time interval of $0.1D/U$. The maximum of each curve is marked by a small red circle; (b) A zoom-in plot of the rectangular area in (a), where the number below each red circle represents the time series of the corresponding curve; (c) Time trace of the maximum vorticity $\omega_z U/D$ (red circles in (a)); (d) Time trace of vorticity $\omega_z$ at sampling point $(x/D,\ y/D,\ z/D)=(1.5,\ 0,\ -15.8)$.

### 8.8.4    Monitoring both the N- and L-cell vortex at the same downstream position

In figure 8.24, the *shed positions* of the N- and L-cell vortices at the first $500D/U$ are examined. Figure 8.24(b) shows that, at two spanwise positions $z/D = -15.8$ and $-17.8$ (which are in the L-cell vortex's regular shedding region discussed in Appendix 8.8.2), most of the L-cell vortices shed at position $x/D=1.46$. Only a few L-cell vortices shed at $x/D=1.47$. Considering that 0.01D is a very small distance and equal to the spatial interval of the sampling points, $x/D=1.46$ can be defined as the *shed position* of L-cell vortices. On the other hand, as illustrated in figure 8.24(a), the *shed position* of N-cell vortices severely fluctuates between $x/D = 1.4$ and 1.6, which makes it hard to define a fixed *shed position* for all N-cell vortices. Luckily,
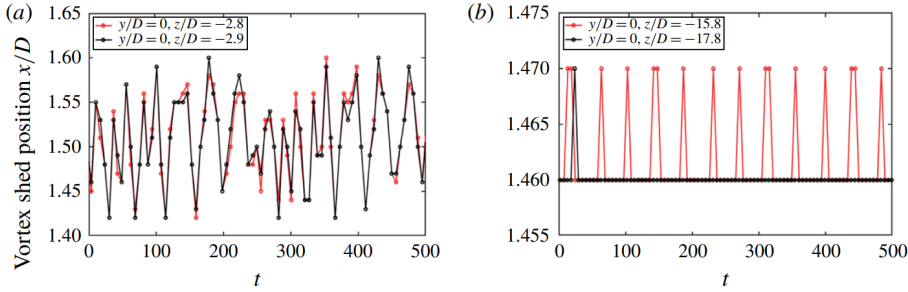
*Figure 8.24: a) Time traces of the shed positions of the N-cell vortices are calculated along two sampling lines (from (x/D, y/D, z/D)=(1, 0, -2.8) to (2, 0, -2.8)) and (from (x/D, y/D, z/D)=(1, 0, -2.9) to (2, 0, -2.9)) are plotted in red and black, respectively. Every small circle represents a N-cell vortex. (b) Time traces of the shed positions of the L-cell vortices are calculated along two sampling lines (from (x/D, y/D, z/D)=(1, 0, -15.8) to (2, 0, -15.8)) and (from (x/D, y/D, z/D)=(1, 0, -17.8) to (2, 0, -17.8)) are plotted in red and black, respectively. Every small circle represents a L-cell vortex.*

as shown in Table 8.4, at the key instant when the vortex dislocations occur, $\varphi$ of the N-cell vortex is stable.

In table 8.4, $\varphi$ of each vortex is calculated in two ways: 1.) In the first column, $\varphi$ is obtained along a sampling line (from $(x/D, y/D, z/D)=(1, 0, -2.9)$ to $(2, 0, -2.9)$) by using the method described in Appendix 8.8.3-(i). 2.) In the second column, $\varphi$ is obtained by using the method described in Appendix 8.8.3-(ii) at a fixed point $(x/D, y/D, z/D)=(1.5, 0, -2.9)$, in which $x/D = 1.5$ is the averaged *shed position* of the N-cell vortices. The differences between these two calculation methods are shown in the third column. The *phases* of the N-cell vortices that induced the vortex dislocations and formations of the NL-loop structures are highlighted with a gray background. At these key instants, the largest difference in $\varphi$ is $0.015D/U$, which is small and equal to the finest grid size (all analysis is based on Case3 in Table 8.1). Differences at the other points are even smaller than $0.1D/U$. The present paper focuses on the trend of $\Phi$ accumulation, rather than the exact value of $\Phi$. We believe that these small differences have negligible influence on our discussions and conclusions.

For the L-cell vortices, at $x/D = 1.5$, they already shed from the shear layer and move regularly downstream. We admit that, from $x/D = 1.46$ (the *shed position* of the L-cell vortices) to 1.5, the convective velocity contributes to the accumulation of $\Phi$. Since these two points are only $0.04D$

apart in $x$-direction, the contributions from the convective velocity will be limited. We believe that $\Phi$ calculated at $x/D = 1.5$ is still dominated by the different shedding frequencies between the N- and L-cell vortices. Therefore, the downstream position $x/D = 1.5$ is selected as the streamwise position of the sampling points for both N- and L-cell vortices. The $\Phi$ between the corresponding N- and L-cell vortices are calculated at this position, and defined as $\Phi_f$.

| $\varphi$ obtained from a sampling line $(D/U)$ | $\varphi$ obtained at a fixed point $(D/U)$ | Difference $(D/U)$ |
|:---:|:---:|:---:|
| 6.095 | 6.05 | 0.045 |
| 9.055 | 9.055 | 0 |
| 12.24 | 12.27 | -0.03 |
| 15.625 | 15.585 | 0.04 |
| 18.78 | 18.73 | 0.05 |
| 22.12 | 22.2 | -0.08 |
| 25.7 | 25.68 | 0.02 |
| 29 | 28.95 | 0.05 |
| 32.325 | 32.315 | 0.01 |
| ... | ... | ... |
| 74.365 | 74.355 | 0.01 |
| ... | ... | ... |
| 116.28 | 116.29 | -0.01 |
| ... | ... | ... |
| 158.29 | 158.3 | -0.01 |
| ... | ... | ... |
| 200.3 | 200.29 | 0.01 |
| ... | ... | ... |
| 242.23 | 242.215 | 0.015 |

Table 8.4: *Phase information $\varphi$ of the N-cell vortices is obtained by two methods. In the first column, we use the method described in appendix 8.8.3-i) to obtain $\varphi$ along a sampling line (from $(x/D, y/D, z/D)=(1, 0, -2.9)$ to $(2, 0, -2.9)$). In the second column, we use the method described in appendix 8.8.3-ii) to obtain $\varphi$ at a fixed sampling point $(x/D, y/D, z/D)=(1.5, 0, -2.9)$. The differences between the first and second column are shown in the third column. The $\varphi$ of the N-cell vortices that induce vortex dislocations are marked by gray shading.*

### 8.8.5   The method to correct L-cell vortices from oblique shedding effects

Due to the oblique shedding in the L-cell region shown in figure 8.1, $\varphi$ of the L-cell vortices varies as the observation position moves in spanwise direction. In order to get rid of this effect, $\varphi$ of the L-cell vortex is divided into two parts.

$$\varphi_{LM} = \varphi_L + \varphi_\theta. \tag{8.5}$$

In equation (8.5), $\varphi_{LM}$ is the phase of the L-cell vortex obtained at a specific sampling position, $\varphi_\theta$ is the component of $\varphi_{LM}$ which can be affected by the oblique shedding, and $\varphi_L$ is the other component that is unaffected. In other words, when the sampling point moves in spanwise direction within the L-cell region, $\varphi_{LM}$ and $\varphi_\theta$ vary, but $\varphi_L$ keeps constant. As an example, we keep the monitoring position of the N-cell vortex at $(x/D, y/D, z/D)$=(1.5, 0, -2.9), and capture $\varphi$ of the L-cell vortices at two sampling points $(x/D, y/D, z/D)$=(1.5, 0, -15.8) and (1.5, 0, -17.8). By using equation (8.4), two time traces of $\Phi_f$ are calculated and shown in figure 8.25(a) and (b), in which the small circles represent $\Phi_f$ between a N-cell vortex and its corresponding L-cell vortex. One can see that the trend of the curves coincide in figure 8.25(a) and (b). When the sampling position of the L-cell vortex moves, the oblique shedding only causes a downward shift of the curves from figure 8.25(a) to (b). By subtracting the average value of all small red circles in each figure, we obtain a green curve (figure 8.25(a)) and a black curve (figure 8.25(b)), and we easily find that these two curves almost coincide. The average value of all the small red circles is $\varphi_\theta$ in equation (8.5). As long as the sampling position of the L-cell vortex is far from the step position, after subtracting $\varphi_\theta$, figure 8.25(c) can always be obtained.

In the $D/d = 2$ case, by using the method described in this appendix, we obtained $\varphi$ of the N- and L-cell vortices at $(x/D, y/D, z/D)$=(1.5, 0, -2.9) and (1.5, 0, -15.8), therefore $\Phi_f$ is calculated on this basis. Following this method, $\Phi_f$ in the $D/d = 2.4$ case can also be obtained. The detailed data of $\varphi$ and $\Phi_f$ for both the $D/d = 2$ and 2.4 cases are included in the supplementary file 1 and 2, respectively.
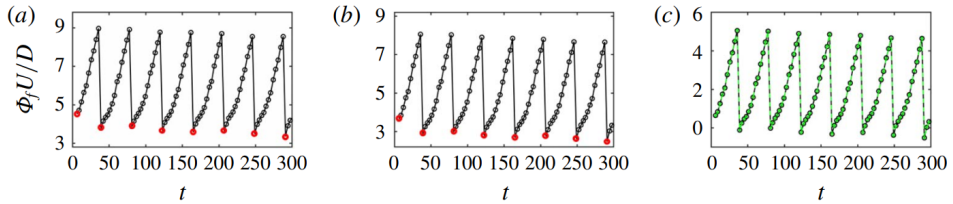
*Figure 8.25: Time traces of $\Phi_f$ during the 1st long N-cell cycle are calculated at two groups of sampling points. (a) The calculations of $\Phi_f$ are based on $\varphi$ of the N- and L-cell vortices which are calculated at $(x/D, y/D, z/D)=(1.5, 0, -2.9)$ and $(1.5, 0, -17.8)$, respectively. (b) The calculations of $\Phi_f$ are based on $\varphi$ of N- and L-cell vortices which are calculated on $(x/D, y/D, z/D)=(1.5, 0, -2.9)$ and $(1.5, 0, -15.8)$, respectively. (c) By using the regression method described in 8.8.5, the results in green and black in (c) have been obtained from (a) and (b), respectively. The circle represents $\Phi_f$ between a N-cell vortex and the corresponding L-cell vortex. In order to ease the observation, we reduce the size of the green circles.*

# References

[1] Saiful-Islam ABM, Jameel M, Jumaat MZ, Shirazi SM, Salman FA. Review of offshore energy in Malaysia and floating spar platform for sustainable exploration. *Renew Sust. Energ. Rev.* 2012; **16**:6268–6284.

[2] Carter BA, Ronalds BF. Deepwater riser technology. *SPE Asia Pacific Oil and Gas Conference and Exhibition, Perth, Australia, October 12-14*, 1998; 461–470.

[3] Williamson CHK. Vortex dynamics in the cylinder wake. *Annu. Rev. Fluid Mech.* 1996; **28**:477–539.

[4] Lewis CG, Gharib M. An exploration of the wake three dimensionalities caused by a local discontinuity in cylinder diameter. *Phys. Fluids A: Fluid Dynamics* 1992; **4**(1):104–117.

[5] Dunn W, Tavoularis S. Experimental studies of vortices shed from cylinders with a step-change in diameter. *J. Fluid Mech.* 2006; **555**:409–437.

[6] Morton C, Yarusevych S, Carvajal-Mariscal I. Study of flow over a step cylinder. *Appl. Mech. Mater.* 2009; **15**:9–14.

[7] Morton C, Yarusevych S. A combined experimental and numerical study of flow past a single step cylinder. *ASME 3rd Joint US-European*

*Fluids Engineering Summer Meeting collocated with 8th International Conference on Nanochannels, Microchannels, and Minichannels, Quebec, Canada, August 1-5*, 2010; 1209–1220.

[8] Morton C, Yarusevych S. Vortex shedding in the wake of a step cylinder. *Phys. Fluids* 2010; **22**(8):083 602.

[9] Morton C, Yarusevych S. Vortex dynamics in the turbulent wake of a single step cylinder. *ASME J. Fluids Eng.* 2014; **136**(031204).

[10] Tian C, Jiang F, Pettersen B, Andersson HI. Antisymmetric vortex interactions in the wake behind a step cylinder. *Phys. Fluids* 2017; **29**(10):101 704.

[11] Tian C, Jiang F, Pettersen B, Andersson HI. Numerical investigation of flow around a step cylinder. *Proceedings of 9th National Conference on Computational Mechanics (CIMNE), Trondheim, Norway, May 11-12*, 2017; 369–384.

[12] Jeong J, Hussain F. On the identification of a vortex. *J. Fluid Mech.* 1995; **285**:69–94.

[13] Ko NWM, Leung WL, Au H. Flow behind two coaxial circular cylinders. *ASME J. Fluids. Eng.* 1982; **104**:223–227.

[14] Yagita M, Kojima Y, Matsuzaki K. On vortex shedding from circular cylinder with step. *Bulletin of JSME* 1984; **27**(225):426–431.

[15] Norberg C. An experimental study of the flow around cylinders joined with a step in diameter. *Proceedings of the 11th Australasian Fluid Mechanics Conference, Hobart, Australia*, vol. 1, 1992; 507–510.

[16] Williamson CHK. Oblique and parallel modes of vortex shedding in the wake of a circular cylinder at low Reynolds numbers. *J. Fluid Mech.* 1989; **206**:579–627.

[17] Williamson CHK. The natural and forced formation of spot-like vortex dislocations in the transition of a wake. *J. Fluid Mech.* 1992; **243**:393–441.

[18] McClure J, Morton C, Yarusevych S. Flow development and structural loading on dual step cylinders in laminar shedding regime. *Phys. Fluids* 2015; **27**:063 602.

[19] Tian C, Jiang F, Pettersen B, Andersson H. The long periodicity of vortex dislocations in the wake behind a step cylinder. *Proceedings of 10th National Conference on Computational Mechanics (CIMNE), Trondheim, Norway, June 3-4*, 2019; 81–99.

[20] Gaster M. Vortex shedding from slender cones at low Reynolds numbers. *J. Fluid Mech.* 1969; **38**:565–576.

[21] Eisenlohr H, Eckelmann H. Vortex splitting and its consequences in the vortex street wake of cylinders at low Reynolds number. *Phys. Fluids A-Fluids* 1989; **1**:189–192.

[22] Dallard T, Browand F. The growth of large scales at defect sites in the plane mixing layer. *J. Fluid Mech.* 1993; **247**:339–368.

[23] Manhart M. A zonal grid algorithm for DNS of turbulent boundary layers. *Computers & Fluids* 2004; **33**(3):435–461.

[24] Williamson JH. Low-storage Runge-Kutta schemes. *J. Comput. Phys.* 1980; **35**:48–56.

[25] Stone HL. Iterative solution of implicit approximations of multidimensional partial differential equations. *SIAM J. Numer. Anal.* 1968; **5**:530–558.

[26] Jiang F, Andersson HI, Gallardo JP, Okulov L. On the peculiar structure of a helical wake vortex behind an inclined prolate spheroid. *J. Fluid Mech.* 2016; **801**:1–12.

[27] Jiang F, Pettersen B, Andersson HI, Kim J, Kim S. Wake behind a concave curved cylinder. *Phys. Rev. Fluids* 2018; **3**(9):094 804.

[28] Peller N, Duc AL, Tremblay F, Manhart M. High-order stable interpolations for immersed boundary methods. *Int. J. Numer. Meth. Fl.* 2006; **52**:1175–1193.

[29] Norberg C. An experimental investigation of the flow around a circular cylinder: influence of aspect ratio. *J. Fluid Mech.* 1994; **258**:287–316.

[30] Gerich D, Eckelmann H. Influence of end plates and free ends on the shedding frequency of circular cylinders. *J. Fluid Mech.* 1982; **122**:109–121.

[31] Green RB, Gerrard JH. Vorticity measurements in the near wake of a circular cylinder at low Reynolds numbers. *J. Fluid Mech.* 1993; **246**:675–691.

[32] Griffin OM. A note on bluff body vortex formation. *J. Fluid Mech.* 1995; **284**:217–224.

# Chapter 9

# Article 5: Diameter ratio effects in the wake flow of single step cylinders

Cai Tian[1], Fengjian Jiang[2], Bjørnar Pettersen[1], Helge I. Andersson[3]

## Abstract

Vortex interactions behind step cylinders with diameter ratio $2 \leq D/d \leq 3$ at Reynolds number ($Re_D$) 150 were investigated by directly solving the three-dimensional Navier-Stokes equations. In accordance with the previous paper [C. Tian, F. Jiang, B. Pettersen, and H. I. Andersson, J. Fluid Mech. 891 (2020)], some interesting characteristics of vortex dislocations, e.g. two phase difference accumulation mechanisms, the trigger and threshold values of vortex dislocations, antisymmetric vortex interactions, and long N-cell cycles, were observed. By performing a detailed investigation of diameter ratio effects, more features of vortex dynamics were discovered. In addition to the known antisymmetric vortex interactions, a symmetric vortex interaction between neighboring N-cell cycles was observed. The long-time

[1]Department of Marine Technology, Norwegian University of Science and Technology, No-7491 Trondheim, Norway

[2]SINTEF Ocean, NO-7052 Trondheim, Norway

[3]Department of Energy and Process Engineering, Norwegian University of Science and Technology, No-7491 Trondheim, Norway

observations revealed an interruption of both these two types of vortex interactions. By using a well-validated phase tracking method, we monitor the time trace of phase difference accumulation process in different $D/d$ cases, from which decreasing (known) and increasing (new) phase difference tendencies were identified. Both caused the interruption of continuous symmetric or antisymmetric phenomena, but through two distinct mechanisms. Meanwhile, the diameter ratio effects on the trigger and threshold values were discussed. Additionally, the likelihood of antisymmetric or symmetric vortex interactions, and increasing or decreasing phase difference tendencies were analyzed. Moreover, diameter ratio effects on shedding frequencies and the extensions of three main vortex cells, i.e. S-, N- and L-cell vortices, were described.

## 9.1   Introduction

In recent years, fluid flow around a step cylinder configuration, as shown in Fig. 9.1, has been the focus of many studies. Flow past structures with a similar shape occurs in many engineering applications, for example, the outer wall of TV-towers, the underwater hull of a SPAR-buoy, the supporting structures for fixed and floating offshore wind turbines, etc. For a sufficiently long single step cylinder, there are mainly two important parameters, i.e. the diameter ratio ($D/d$), and the Reynolds number ($Re_D$). $D/d$ is the diameter ratio between the large- and small-part of the step cylinder, while $Re_D = UD/\nu$ (where $\nu$ is the kinematic viscosity of the fluid, and $U$ represents the uniform inflow velocity).
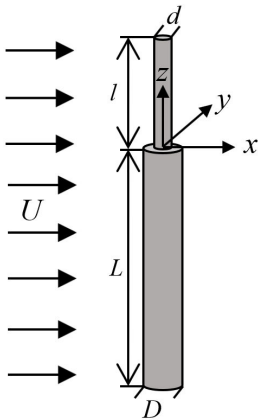


Figure 9.1: A sketch of the step cylinder geometry. The diameter of the small and large cylinder are d and D, respectively. l is the length of the small cylinder, and L is the length of the large cylinder. The origin locates at the center of the interface between the small and large cylinders. The uniform incoming flow U is in the positive x-direction. The three directions are named streamwise (x-direction), crossflow (y-direction) and spanwise (z-direction).

Based on experimental investigations in the wake of a step cylinder with $D/d \approx 2$ at $63 < Re_D < 1100$, Dunn & Tavoularis [1] identified three types

of spanwise vortices: (1) S-cell vortex shed from the small cylinder with
the highest shedding frequency $f_S$, (2) L-cell vortex shed from the large
cylinder with shedding frequency $f_L$ and (3) N-cell vortex located between
the S- and L-cell vortices, with the lowest shedding frequency $f_N$. Lewis &
Gharib [2] found that the N-cell vortex (the modulation zone) only exists
when $D/d > 1.55$, where there is no direct connection between the S- and
L-cell vortices. They called it the *indirect mode*. Meanwhile, a *direct mode*
was identified when $D/d < 1.25$, where the N-cell vortex disappears, and
the corresponding S- and L-cell vortices directly connect to each other.

The N-cell vortex has the lowest shedding frequency among the three
dominating vortex cells, i.e. the S-, N- and L-cell vortices. Similar low-
frequency cells were also observed in the wake behind several other config-
urations, e.g. the wake behind a free-end cylinder [3], the wake behind a
circular cylinder with flat end-plat [4], the wake behind a concave curved
cylinder [5], etc. The previous studies [1, 4, 6, 7] attributed the appear-
ances of such low-frequency cells (N-cell-like vortex) to 3D effects, which
include mainly two mechanisms: downwash and increased base pressure.
Bearman [8] and Williamson [4] found that the increased base pressure has
the effect of increasing the vortex formation region, and causes the vortex
shedding frequency to decrease. Zdravkovich [6] and Williamson [4] found
that the spanwise velocity (downwash) could not merely displace the vortex
formation region further downstream, but also widen the separated shear
layers before they roll up into vortices. These effects would also decrease
the vortex shedding frequency. For the wake behind the step cylinder, by
doing experiments and numerical simulations, Dunn & Tavoularis [1] and
Morton & Yarusevych [7] also concluded that the 3D effect is a plausible
explanation of the formation of the N-cell vortex. However, there is no fur-
ther discussion about the relative importance of these two 3D effects, i.e.
the downwash and the increased base pressure. In Sec. 9.3.2.1, their relative
importance will be discussed.

Whenever there are several spanwise-oriented vortex cells with different
frequencies, these vortices are either in phase or out of phase with each
other. As they move out of phase, a contorted 'tangle' of vortices appears
at the boundary between them, which looks like dislocations that appear
in solid materials. Williamson [4] defined this kind of flow phenomenon
as vortex dislocation. By doing experiments of flow past a circular cylinder
with end-plates at $Re_D < 200$, Williamson found that the vortex dislocation
occurs at the boundary between the central vortex cell of frequency $f_u$ and
the single vortex cell of frequency $f_l$ at a beat frequency $f_u$-$f_l$. Between
two neighboring vortex dislocations, he proposed to estimate the number of

vortex shedding cycles of the central vortex cell ($n_u$) and the single vortex cell ($n_l$) [4] as:

$$n_u = f_u/(f_u - f_l), \tag{9.1}$$

$$n_l = n_u - 1. \tag{9.2}$$

In the wake of a step cylinder, the vortex dislocations between S-, N- and L-cell vortices were also the topic of many investigations [1, 2, 7, 9, 10, 11, 12]. All these studies concluded that the interactions between the S- and N-cell vortices occur in a narrow S-N cell boundary (the region between the S- and N-cell vortices) which is stable and deflects spanwise into the large cylinder region. During the dislocation process, the N-cell vortex splits into at least two filaments. One of these filaments connects to the subsequent N-cell vortex of the opposite sign to form a hairpin-like vortex structure. The other filament connects to the S-cell vortex [1, 11, 12, 13, 13]. Except for the S-cell vortices that connect to the N-cell vortices, the rest of them form S-S half loops [11], which appear at a beat frequency ($f_S - f_N$).

Unlike the S-N cell boundary, the N-L cell boundary (the region between the N- and L-cell vortices) is relatively wide and varies with time. Lewis & Gharib [2] first observed an inclined interface region (the N-L cell boundary) appearing behind the large cylinder at beat frequency ($f_L - f_N$). Morton & Yarusevych [11] explained this phenomenon: as the phase difference between the N- and L-cell vortices accumulates, accompanying with the appearance of vortex dislocations between N- and L-cell vortices, the shapes and lengths of the N-cell vortices and the position of the N-L cell boundary periodically change at the beat frequency ($f_L - f_N$). They defined these cyclic variations as the N-cell cycle [11]. More detailed vortex interactions in the N-cell cycles were investigated by Tian et al. [14, 15, 16, 17]. They observed that, in the wake behind a single step cylinder ($D/d = 2$) at $Re_D$=150, there are two NL-loops (NL-loop 1 and NL-loop2), one NN-loop and at least one LL-half-loop structure in one N-cell cycle. The phrase *antisymmetric vortex interaction* was introduced to describe the phenomenon that the NL-loop structures form at different sides of the step cylinder in the neighboring N-cell cycles. Moreover, Tian et al. [17] reported that the total phase difference, $\Phi$, is accumulated by the joint influence of different shedding frequencies and different convective velocities. This mechanisms was described as

$$\Phi = \Phi_f + \Phi_c \tag{9.3}$$

where $\Phi_f$ and $\Phi_c$ represent the $\Phi$ caused by different shedding frequencies and different convective velocities, respectively. By tracking the phase information of N- and L-cell vortices, they measured $\Phi_f$ of every N-L vortex

pair:

$$\Phi_f = \varphi_N - \varphi_L. \tag{9.4}$$

Here $\varphi_N$ and $\varphi_L$ represent the phase information of the corresponding N- and L-cell vortices, respectively. By plotting the long-time trace of the accumulation of $\Phi_f$, a decreasing tendency of $\Phi_f$ was observed by Tian et al. [17], which makes the formation position of the corresponding NL-loop structure move downstream in subsequent N-cell cycles, and finally causes an interruption of the continuous antisymmetric vortex interactions. An uninterrupted series of antisymmetric N-cell cycles was identified as the long N-cell cycle. The gradual decrease of $\Phi_f$ can be evaluated as:

$$S = \alpha \frac{1}{2f_L} - \beta \frac{1}{2f_N} \tag{9.5}$$

where $S$ (with dimension $D/U$) is a measure of the phase shift of the N-L vortex pair in one N-cell cycle, as compared to the corresponding N-L vortex pair in the previous N-cell cycle. In this expression, $\alpha$ and $\beta$ are the number of L- and N-cell vortices in one N-cell cycle, respectively. Tian et al.[17] found that only when $\Phi_f$ becomes larger than a certain value (as referred to as the *threshold value*), taking $\Phi_c$ into account, $\Phi$ can be sufficiently large (as referred to as the *trigger value*) to induce the vortex dislocation and the formation of the NL-loops.

In previous papers [1, 11, 13, 18], vortex interactions between S- and N-cell vortices were described in detail. The primary goal of the present numerical study is to investigate the effects of the diameter ratio ($D/d$) on the vortex interactions, especially the vortex dislocations between N- and L-cell vortices in the wake behind the step cylinder. Considering that many small streamwise vortices appear when $Re_D$ increases to 300, as shown by Morton and Yarusevych [11]. These vortices disturb the observations of vortex interactions, we choose to stay at $Re_D$=150 to more clearly demonstrate the detailed vortex connections. To achieve this, we analyse the space and time signals of several flow quantities (velocity, vorticity and $\lambda_2$ [19]) obtained from a direct numerical simulation (DNS) of flow past ten different step cylinders with diameter ratios $D/d$=2.0, 2.1, 2.2, 2.3, 2.4, 2.5, 2.6, 2.7, 2.8 and 3.0. All these cases share the same coordinate system, grid resolution and computational method. By using a well validated phase difference tracking method [17], the phase difference accumulation process is further investigated.

All discussions in Sec. 9.2, 9.3 and 9.4 are based on the $D/d$=2.0, 2.2, 2.4, 2.6, 2.8 and 3.0 cases. In Sec. 9.2, the flow problem and the numerical settings used are introduced. Then, the wake and the diameter ratio

effects on the three main vortex cells, i.e. the S-, N- and L-cell vortices, are described in Sec. 9.3. In Sec. 9.4, the diameter ratio effects on the vortex dislocations between N- and L-cell vortices are discussed in detail, and additional characteristics of the vortex dislocations are revealed. In Sec. 9.5, we analyze the likelihood of different characteristics of vortex dislocations. The $D/d$=2.1, 2.3, 2.5 and 2.7 cases are investigated to further support of our discussions and strengthen our conclusions.

## 9.2 Flow configuration and computational aspects

### 9.2.1 Flow configuration and coordinate system
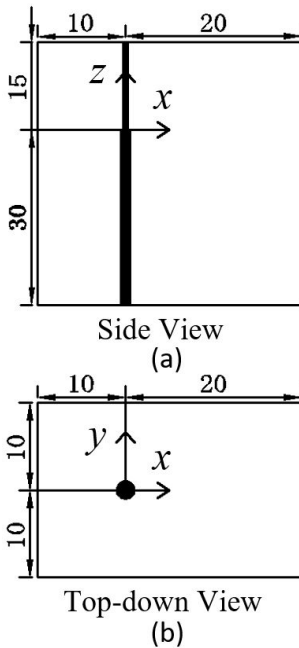


*Figure 9.2: Computational domain, origin and coordinate system are illustrated from (a) side view and (b) top-down view. The diameter of the large cylinder, D, is the length unit. The origin is located in the centre of the step at the interface between the small and large cylinders.*

The step cylinder investigated in the present paper is illustrated in Fig. 9.1. The uniform incoming flow $U$ is in the positive $x$-direction. In Fig. 9.2, a side and a top-down view of the flow domain are shown. The height of the domain is $45D$, of which the small and the large cylinders occupy $15D$ ($l$) and $30D$ ($L$), respectively. The inlet boundary locates at $10D$ upstream from the origin, and the outlet boundary locates at $20D$ downstream. The width of the domain is $20D$. This domain size is comparable to, or exceeds, that used in previous similar studies [11, 15, 17]. Most of the results in the present paper are from the six cases $D/d$=2.0, 2.2, 2.4,

2.6, 2.8 and 3.0. In order to keep the Reynolds number of the large cylinder ($Re_D$) at 150 in all cases, we keep $D$ constant, and change $d$. Boundary conditions used in the present study are as follows:

- The inlet boundary: uniform velocity profile $u=U$, $v=0$, $w=0$;

- The outlet boundary: Neumann boundary condition for velocity components ($\partial u/\partial x$
  $= \partial v/\partial x = \partial w/\partial x = 0$) and constant zero pressure condition;

- The other four sides of the computational domain: free-slip boundary conditions (For the two vertical sides: $v = 0$, $\partial u/\partial y = \partial w/\partial y = 0$, For the two horizontal sides: $w = 0$, $\partial u/\partial z = \partial v/\partial z = 0$);

- The step cylinder surfaces: no-slip and impermeable wall.

### 9.2.2 Computational method

The three-dimensional time-dependent incompressible Navier-Stokes equations are directly solved by a well-verified finite-volume based numerical code $MGLET$ [20]. The surface integral of flow variables over the faces of the discrete volumes is approximated by using the midpoint rule, which leads to second-order accuracy in space. The discretized equations are integrated in time with a third-order explicit low-storage Runge-Kutta scheme [21]. A constant time step $\Delta t$ is used to ensure a CFL number smaller than 0.65. The pressure corrections are handled by solving a Possion equation with Stone's implicit procedure (SIP) [22]. The same code has recently been used to investigate other flows around three-dimensional bluff bodies, such as the step cylinder wake [17], the spheroid wake [23] and the curved cylinder wake [5].

In all simulations, an immersed boundary method (IBM) is used to handle the cylindrical geometry inside the Cartesian grid. The details of this IBM and its validation can be found in Ref. [24]. The overall properties of the grids for all cases are shown in Table 9.1. A schematic illustration of the mesh design can be found in Fig. 3 of Ref. [17]. First, the computational domain is divided into equal-sized cubic Cartesian grid boxes, named the level-1 grid. Each grid box is further equally divided into $N \times N \times N$ cubic grid cells. In the regions where complex flow phenomena take place, e.g. the regions close to the step cylinder geometry, the regions where vortex dislocations happen, etc., the grid boxes (the level-1 box) are equally split into eight smaller cubic grid boxes (the level-2 grid box). There are also $N \times N \times N$ cubic grid cells in every level-2 grid box. Therefore, the grid

resolution in the level-2 grid box is two times finer than that in the level-1 grid box. This refinement-process continuously goes on until a sufficient grid resolution is reached. More detailed information of this local grid refinement method can be found in Ref. [20].

### 9.2.3   Grid convergence

A detailed grid convergence study can be found in our previous paper [17], which proves that in the $D/d$=2.0 case the minimum grid cell size $\Delta/D$=0.015 is fine enough to resolve all physical phenomena of interest to us.
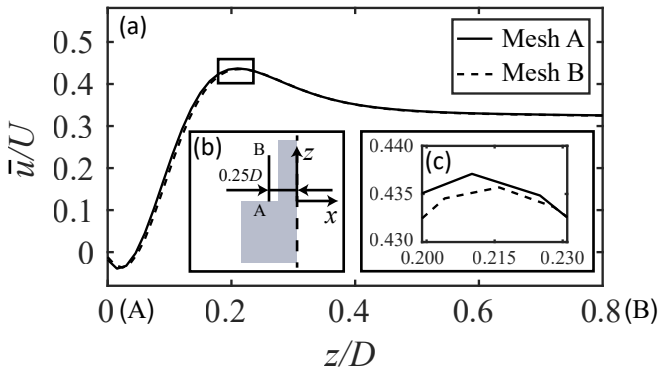


Figure 9.3: (a) Distributions of time-averaged streamwise velocity $\overline{u}/U$ along a sampling line AB in the $x - z$ plane at $y/D$=0 in the $D/d = 2.8$ case. Inset: (b) a sketch of the position of sampling line AB of length 0.8D, at $x/D$=-0.25; and (c) a zoom-in plot of the upper part of the curves in panel (a) (black rectangle in panel).

We note that $\Delta$ is normalized by $D$, therefore when it comes locally around the small cylinder, the grid resolution may be challenged. As we cover different $D/d$ cases in the present study, the grid resolution for small cylinder need to be addressed. When $D/d$=3 the Reynolds number of the small cylinder ($Re_d$) is 50, which is very close to the $Re$ range of the closed wake regime (4-5 $\leq$ Re $\leq$ 30-48). In this $Re$ range, there is no periodic vortex shedding behind the cylinder. Considering that both the vortex shedding and the abrupt change in diameter complicate the flow, the major challenge to the local grid resolution around the small cylinder should appear when $D/d$=2.8 ($Re_d$=53). The grid size in the $D/d$=2.8 case is further refined from $\Delta/D$ =0.015 (Mesh A) to 0.012 (Mesh B) to check the

Table 9.1: *Detailed mesh information. The Reynolds number is $Re_D$ $=UD/\nu$=150. Mesh A is used in all cases. Mesh B is only used in the $D/d = 2.8$ case for the grid convergence test.*

| Mesh | Minimum grid cell size, $\Delta/D$ | Time step, $\triangle tU/D$ | Number of grid levels | Number of grid cells in one grid box | Total number of grid cells (million) |
|---|---|---|---|---|---|
| A | 0.015 | 0.005 | 6 | $24 \times 24 \times 24$ | 124.1 |
| B | 0.012 | 0.004 | 6 | $30 \times 30 \times 30$ | 243.3 |

grid convergence, as shown in Table 9.1. In Fig. 9.3(a), the distributions of time-averaged streamwise velocity along the vertical line AB (as indicated in inset Fig. 9.3(b)) for these two $D/d$=2.8 cases are plotted to illustrate the flow variation on the 'step' in front of the small cylinder. As shown in Fig. 9.3(a) and in the zoom-in view in the inset Fig. 9.3(c), only tiny differences appear when the grid size is refined. Moreover, Fig. 9.4 shows time traces of the crossflow velocity ($v$) in the interaction region between the N- and L-cell vortices where the velocity varies dramatically with time due to the vortex dislocations. The fluctuations and the mean values of $v$ from Mesh A and Mesh B almost coincide. However, the computational cost of Mesh B is significantly higher than that of Mesh A, due to the large number of grid cells and smaller time step. All discussions are therefore based on grid resolution $\Delta/D$ =0.015. To ensure that the flow is properly developed, all cases were simulated first for at least 300 time units ($D/U$), and then continued for at least $2000D/U$ to collect the statistical data.

## 9.3 Diameter ratio effects on the shedding frequencies and the extensions of vortex cells

### 9.3.1 Diameter ratio effects on the S-cell vortex

The diameter ratio $D/d$ dramatically changes the wake, and influences each vortex cell. This is indicated in Fig. 9.5, where the approximate extensions of the S-, N- and L-cell vortices are marked. From Fig. 9.5(a) to (c), one obvious change is the absence of the S-cell vortices in (c), i.e. the $D/d$=3.0 case. As mentioned in Sec. 9.2, when $D/d$ increases from 2 to 3, the Reynolds number of the small cylinder ($Re_d$) decreases from 75 to 50, which is at the border between the steady separation regime ($4-5 < Re < 30-48$)
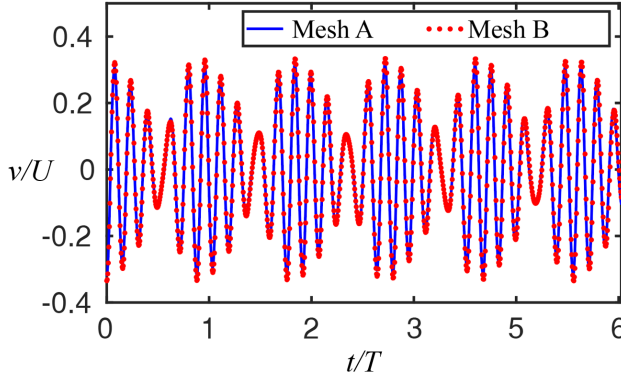
*Figure 9.4: Time traces of the crossflow velocity v at point (x/D, y/D, z/D)=(1, 0, -6) in the D/d=2.8 case by using Mesh A and Mesh B. T is the period of one N-cell cycle.*

and the periodic laminar regime [27] $(30 - 48 < Re < 180 - 200)$. Considering the disturbance caused by the vortex shedding behind the large cylinder, we expected vortex shedding to be triggered also behind the small cylinder. However, no vortex shedding can be observed there. As shown in the 2nd column in Table 9.2, $St_S$ gradually increases as $D/d$ increases. As a result, there is one more S-cell vortex behind the small cylinder ($D/d$=2.4) in Fig. 9.5(b), than in the $D/d$=2.0 case in Fig. 9.5(a). Comparing with the empirical $St'_S$ in the 6th column of Table 9.2, the maximum difference between $St_S$ and $St'_S$ is only 3.2%. The variation of $St_S$ is simply caused by changes in $Re_d$, i.e clearly $D/d$ dependent. In Fig. 9.6, the extensions of the three vortex cells (the S-, N- and L-cell vortices) are shown. To find it, streamwise velocity spectra for all six cases are calculated along a vertical sampling line parallel to the $z$-axis at position $(x/D, y/D)$=(1.6, 0.4). More detailed information about streamwise velocity spectra is shown in Appendix 9.7. For a given spanwise position, only the spectral peaks with the energy accounting for at least 4% of the total energy in the spectra at this spanwise position are taken into consideration. In Fig. 7 in Ref. [11], the authors used a similar method to identify different vortex cell regions. In Fig. 9.6 (a-e), by connecting the lower end of the S-cell extension, a black dashed curve is plotted to illustrate the variation of the S-cell regions. Except for a very small decrease in Fig. 9.6(a), i.e. the $D/d = 2$ case, no obvious change can be observed when $D/d$ increases from 2 (Fig. 9.6(a)) to 2.8 (Fig. 9.6(e)). Generally, in the present low-Reynolds-number step cylinder wakes, the flow behind the small cylinder is seldomly influenced by the abruptly changed diameter at the step position when 2< $D/d$ <3. This

Table 9.2: *Detailed information of the S-, N- and L-cell vortices in six cases. In the 2nd, 3rd and 4th columns, Strouhal numbers of these three dominating vortex cells ($St_S = f_S D/U$, $St_N = f_N D/U$ and $St_L = f_L D/U$) are shown. They are obtained by means of a discrete Fourier transform (DFT) of continuous velocity data along a vertical sampling line with density 0.2D parallel to the z-axis at position (x/D, y/D)=(1.6, 0.4), over at least 2000 time units (D/U). In the 5th column, $\Delta_{NL}$ is calculated by $(St_L - St_N)/St_L$. $\theta_L$ is the oblique shedding angle of the L-cell vortices, as shown in Fig. 9.5. In the 6th column, the empirical Strouhal number of the small cylinder ($St'_s$) is calculated as: $St'_S = (0.2663 - 1.019/Re_d^{0.5}) \times 2$ from Norberg [25]. By means of the Williamson [26] correlation, $St_{L\theta} = (0.2731 - 1.1129/Re_D^{0.5} + 0.4821/Re_D) \times cos(\theta_L)$, the empirical Strouhal number of the large cylinder ($St_{L\theta}$) is calculated and shown in the 8th column. Note: the frequency resolution in this table is between 0.0004 U/D and 0.0005 U/D. A higher frequency resolution may lead to some minor differences in the characteristic frequency in this table. These differences are however small and do not affect our discussions and conclusions.*

| $D/d$ | $St_S$ | $St_N$ | $St_L$ | $\Delta_{NL}$ | $St'_S$ | $\theta_L$ | $St_{L\theta}$ |
|-------|--------|--------|--------|---------------|---------|-----------|----------------|
| 2.0 | 0.2895 | 0.1545 | 0.1780 | 13.2% | 0.2972 | 16° | 0.1776 |
| 2.2 | 0.3084 | 0.1516 | 0.1775 | 14.6% | 0.3142 | 17° | 0.1773 |
| 2.4 | 0.3221 | 0.1501 | 0.1771 | 15.2% | 0.3297 | 17° | 0.1773 |
| 2.6 | 0.3350 | 0.1491 | 0.1768 | 15.7% | 0.3435 | 18° | 0.1764 |
| 2.8 | 0.3444 | 0.1480 | 0.1765 | 16.1% | 0.3558 | 18° | 0.1764 |
| 3.0 | no-shedding | 0.1464 | 0.1761 | 16.9% | - | 18° | 0.1764 |

agrees well with previous studies[1, 9, 17, 28].

## 9.3.2 Diameter ratio effects on the N- and L-cell vortices

### 9.3.2.1 Formation of the N-cell vortex

For the N- and L-cell vortices, the $D/d$ effects are more complicated. Table 9.2 and Fig. 9.5 show that both their shedding frequencies and extensions are influenced. Before taking further steps, we would like to revisit a basic question, i.e. what causes the N-cell vortex. As mentioned in Sec. 9.1, previous studies [1, 11] attributed the appearance of the N-cell vortex to a combination of two 3D effects: downwash and increased base pressure. Both these two 3D effects can increase the vortex formation region and cause the vortex shedding frequency to decrease [4, 6, 8]. Instead of following the
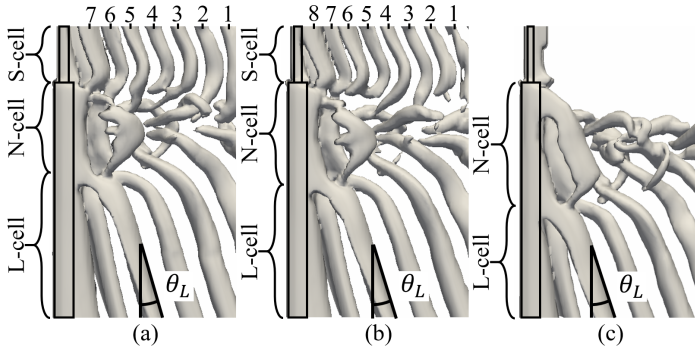
Figure 9.5: Instantaneous iso-surface of $\lambda_2$=-0.05 at $Re_D$=150: (a) the D/d=2.0 case, (b) the D/d=2.4 case, and (c) the D/d=3.0 case. The approximate extensions of the three vortex cells (S-, N- and L-cell vortices) and the oblique shedding angle $\theta_L$ of the L-cell vortices are indicated. The S-cell vortices in (a, b) are labeled by serial numbers. Note: the S-cell vortices disappear in (c) due to $Re_d$=50 in the D/d=3.0 case. $\lambda_2$=-0.05 is selected to be consistent with the value of $\lambda_2$ used in Refs. [15, 17]. The choice of the $\lambda_2$ value affects only the size of the vortex tubes but not their number.
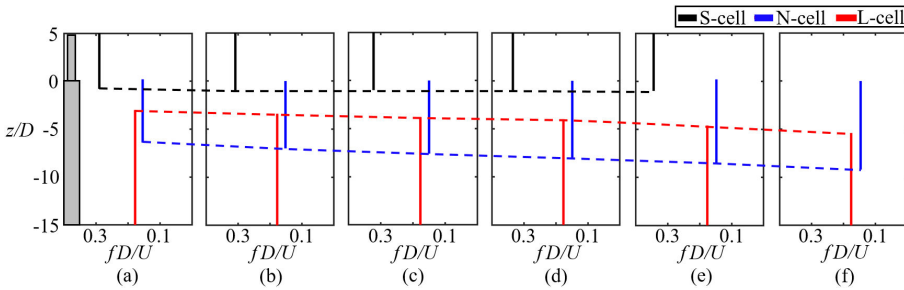


Figure 9.6: Distributions of dimensionless vortex shedding frequency across the span of the step cylinders at $Re_D = 150$, D/d=2.0, 2.2, 2.4, 2.6, 2.8 and 3.0 cases are plotted in (a-f), respectively. By connecting the lower end of the S- and N-cell regions, and the upper end of L-cells, the trend of extensions of these three vortex cells are illustrated by a black, a blue and a red dashed line, respectively.

previous studies to further discuss the N-cell vortex formation mechanism, the relative importance of these two 3D effects is discussed in the following.

In Fig. 9.7(a) and (b), the distributions of time-averaged spanwise velocity $-\overline{w}/U$ and the time averaged base pressure coefficient $\overline{C_{pb}}$ are plotted, respectively. By checking the lower end of N-cell extensions in Fig. 9.6 (blue

dashed line), black circles are added to Fig. 9.7 to illustrate the end position of the N-cell vortex region. Generally, the results agree well with previous investigations [1, 4, 6, 7]. Clear spanwise velocity (downwash) $-\overline{w}/U$ and increased base pressure $\overline{C_{pb}}$ can be observed in the N-cell region (the part of the curves at the right side of the black circles). As $D/d$ increases, this becomes even more obvious. If $-\overline{w}/U$ is assumed to be the key factor that causes the formation of the N-cell vortex, some paradoxical observations arise. For example, by looking at the distribution of $-\overline{w}/U$ in the $D/d$=2.0 case, i.e. the solid blue line in Fig. 9.7(a), one can see that $-\overline{w}/U$ in the L-cell region ($z/D < -10$) is even larger than that in a part of the N-cell vortex area ($-7 < z/D < -6$). In other words, if we assume that it is the strong $-\overline{w}/U$ that induces the formation of the N-cell vortex, the N-cell vortex should extend to the area $z/D < -10$, instead of ending at $z/D = -7$ in the $D/d$=2.0 case. A similar paradox also appears in the $D/d$= 2.2, 2.4 and 2.6 cases. On the other hand, as shown in Fig. 9.7(b), $\overline{C_{pb}}$ in the N-cell region is larger than that outside of the N-cell region for all six cases. In the region $z/D < -10$, $\overline{C_{pb}}$ of the six cases approximately converges to a value around -0.8. In the N-cell region, $\overline{C_{pb}}$ is obviously larger than this. In our opinion, the appearance of the N-cell vortex can be the joint influence of both the spanwise velocity $-\overline{w}/U$ and the increased base pressure $\overline{C_{pb}}$ (the 3D effects). The increased $\overline{C_{pb}}$, however, plays a major role.

### 9.3.2.2 Spanwise extensions and shedding frequencies of the N- and L-cell vortices

Table 9.3: Spanwise range of the S-N and N-L transition regions.

| $D/d$ | S-N transition region | N-L transition region |
|---|---|---|
| 2.0 | $-0.8 \leq z/D \leq 0.2$ | $-6.4 \leq z/D \leq -3.0$ |
| 2.2 | $-1.0 \leq z/D \leq 0$ | $-7.0 \leq z/D \leq -3.4$ |
| 2.4 | $-1.0 \leq z/D \leq 0$ | $-7.6 \leq z/D \leq -3.8$ |
| 2.6 | $-1.0 \leq z/D \leq 0$ | $-8.0 \leq z/D \leq -4.0$ |
| 2.8 | $-1.0 \leq z/D \leq 0.2$ | $-8.6 \leq z/D \leq -4.6$ |
| 3.0 | - | $-9.2 \leq z/D \leq -5.4$ |

In Fig. 9.6(a-e), one can clearly observe two transition regions along the span of the step cylinder: (i) the S-N transition region where both the S- and N-cell vortices may coexist, and (ii) the N-L transition region where
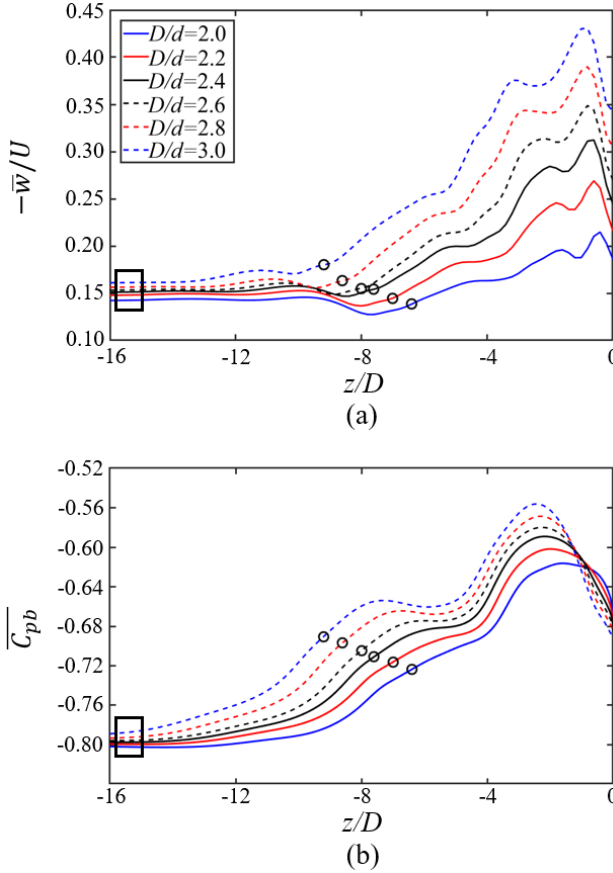
Figure 9.7: (a) Time averaged spanwise velocity $-\overline{w}/U$ along a spanwise sampling line at $(x/D,\ y/D)=(1,\ 0)$ in the large cylinder region, (b) Time-averaged base pressure coefficient $\overline{C_{pb}}$ measured by $\overline{C_{pb}} = (\overline{P_b}-P_0)/(0.5\rho U^2)$, where $P_0$ is the pressure at the inlet boundary, and $\overline{P_b}$ is the time-averaged pressure along a sampling line at $(x/D,\ y/D)=(0.53,\ 0)$ in the large cylinder region. (Note: Due to the way a curved surface is interpreted in IBM, completely smooth surface pressure distributions are hardly obtained. $\overline{P_b}$ is obtained at $(x/D,\ y/D)=(0.53,\ 0)$, instead of at $(x/D,\ y/D)=(0.5,\ 0)$. The distance $h = 0.03D$ is selected because it is slightly larger than the smallest cell's diagonal $(\sqrt{3}\Delta < h = 0.03D < 1.5\sqrt{3}\Delta$, where $\Delta = 0.015D)$, such that we safely avoid wiggles possibly caused by cells directly cut by the cylinder surface, and still stay as close as possible to the surface.) The values of $-\overline{w}/U$ and $\overline{C_{pb}}$ in the L-cell region $(z/D=-16)$ are shown in the ninth and tenth columns in Table 9.4.

both the N- and L-cell vortices may coexist. The spanwise ranges of these two transition regions are shown in Table 9.3. In agreement with previous observations [1, 2, 11], the spanwise length of the S-N transition region is significantly smaller than that of the N-L transition region. In Fig. 7 of Ref. [11], Morton and Yarusevych showed that, both the S-N and the N-L transition region keep constant, when $Re_D$ increases from 150 to 300 in the $D/d$=2.0 case. In the present paper, we define the center position of the transition region as its location. Table 9.3 shows that, at $Re_D$=150, the changed diameter ratios ($2 \leq D/d \leq 3$) have a limited effect on the S-N transition region. The position of the S-N transition region shifts $0.2D$ to the small cylinder side in the $D/d$=2.0 case, and the spanwise length of the S-N transition region decreases from $1D$ to $0.8D$ in the $D/d$=2.8 case. Considering that the frequency analysis is based on data obtained from a sampling line with density ($0.2D$) in spanwise ($z$) direction, these fluctuations in S-N transition region can be neglected. On the other hand, the variation in the N-L transition region is obvious. When $D/d$ increases from 2 to 3 (Fig. 9.6(a-f)), except for a tiny decrease in the $D/d$=3 case, the spanwise length of the N-L transition region gradually increases from $3.4D$ to $4D$. Meanwhile, the position of the N-L transition region continuously moves to the large cylinder side from $z/D$=-4.6$D$ to -7.3$D$. As a result, at the large cylinder side, the spanwise extension of the N-cell vortex increases, whereas the spanwise extension of the L-cell vortex decreases. According to discussions in Sec.9.3.2.1, this can be caused by the increased strength and the increased impact area of the 3D effects (i.e. down wash and increased base pressure), as shown in Fig. 9.7. As the N-cell region continuously expands to the large cylinder side, shrinking of the L-cell region subsequently appears.

The shedding frequencies of both N- and L-cell vortices are affected by this joint influences of the spanwise velocity and the increased $\overline{C_{pb}}$. As mentioned in Sec. 9.1, both the increased $\overline{C_{pb}}$ and $-\overline{w}/U$ can reduce the shedding frequency of the affected vortex. By combining information from Table 9.2 and Fig. 9.7, it is clear that as the base pressure and the strength of the spanwise velocity in the N-cell region increase from the $D/d$=2 to the $D/d$=3.0 case, the corresponding $St_N$ continuous to decrease from 0.1545 to 0.1464, a drop of 5.2%. Meanwhile, $St_L$ only drops 1.1%, i.e. from $St_L$=0.1780 in the $D/d$=2.0 case to $St_L$=0.1761 in the $D/d$=3.0 case. This is because the N-cell region is closer to the step position than the L-cell region is, which makes $\overline{C_{pb}}$ and $-\overline{w}/U$ in the N-cell region more sensitive to the varying $D/d$. In Fig. 9.7 and Table 9.4, when $D/d$ increases from 2 to 3, $\overline{C_{pb}}$ increases around 10% in the N-cell region but only 2% in the

L-cell region. Similarly, $-\overline{w}/U$ in the N-cell region doubles from $D/d$=2 to $D/d$=3.0 case. In the L-cell region, however, the increment is only 15%. The different decline rates of $St_N$ and $St_L$ makes their difference ($\Delta_{NL}$) increases from 13.2% to 16.8%, as seen in the 5th column in Table 9.2. We may speculate that $\Delta_{NL}$ will continue to increase if $D/d$ is further increased. For fixed $D$ and $Re_D$, the maximum $\Delta_{NL}$ can be obtained when $D/d$ tends to infinite, i.e. free end circular cylinder case. In support of this speculation, Ayoub and Karamcheti [3] reported a 23% frequency drop from the main cell to the end cell of a circular cylinder with one free end, which is substantially larger than that in the present study.

## 9.4 Interactions between the N- and L-cell vortices

### 9.4.1 Variation of phase difference between N- and L-cell vortices

The gradual decrease of phase difference $S$ (Eq. 9.5) is an important quantity to characterize vortex dislocations, as discussed in Sec. 9.1. A positive $S$ value and a subsequent decreasing tendency in the time trace of the phase difference were observed in the $D/d$=2 and 2.4 cases [16, 17]. We hypothesized that an increasing tendency may also exist. This is confirmed through more detailed parameter studies in the present paper.

By using the same phase-tracking method introduced by Tian et al. [17], the time trace of $\Phi_f$ between corresponding N- and L-cell vortices in all six $D/d$ cases are illustrated in Fig. 9.8. We use green and red circles to indicate $\Phi_f$ of the N-L vortex pairs whose dislocations eventually cause the NL-loop 1 and NL-loop2, respectively. The trends of these two kinds of circles are illustrated by two solid lines with corresponding colors. Distinct decreasing and increasing tendencies of $\Phi_f$ can be seen in the left and right parts of Fig.9.8, respectively. Moreover, the relation between $S$ and the corresponding tendency of $\Phi_f$ are shown in Table 9.4, which makes it convincing to conclude that the variation tendency of $\Phi_f$ is directly associated with the sign of $S$. This relationship can be explained by some mathematical derivations. Let us assume that the number of N- and L-cell vortices are $\beta$ and $\alpha$ in one N-cell cycle.
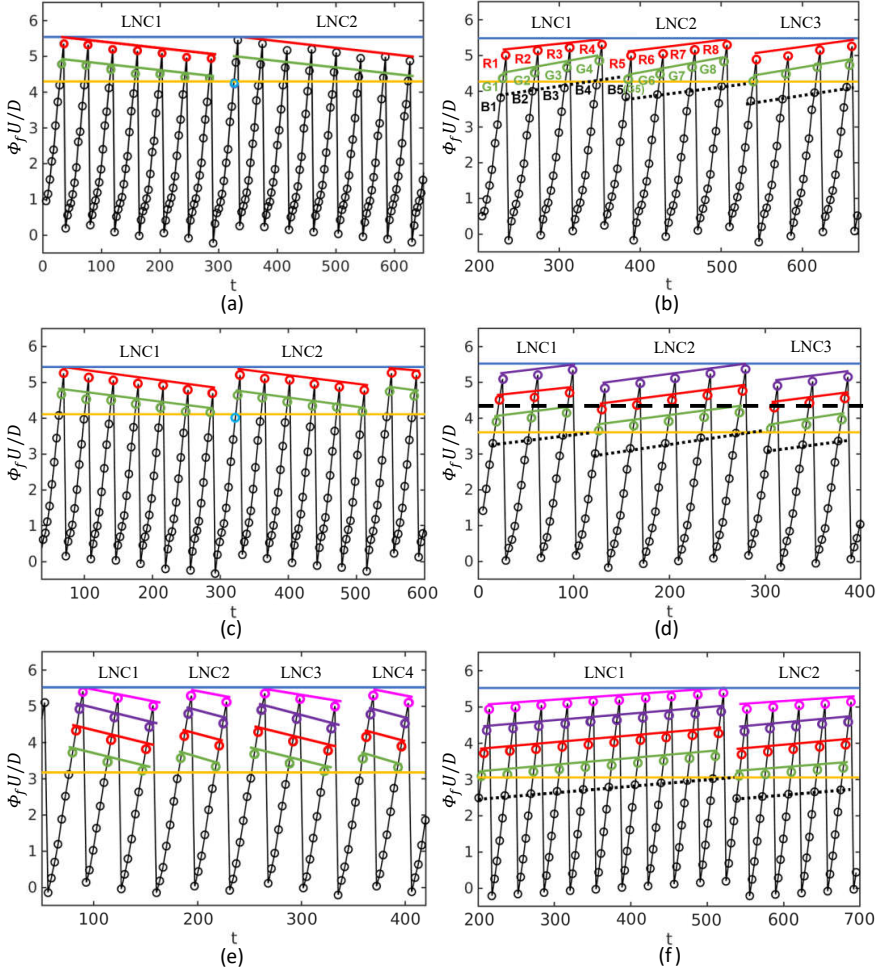
*Figure 9.8: Time trace of $\Phi_f$ between corresponding N-cell and L-cell vortices in several long N-cell cycles. Results at (a) D/d=2.0, (b) D/d=2.2, (c) D/d=2.4, (d) D/d=2.6, (e) D/d=2.8 and (f) D/d=3.0. In (a), the time t is set to t=t*-2378.1D/U, where t* is the actual time in the simulation. In (b-f), t=t*-300D/U. The long N-cell cycles are marked by 'LNC' with serial number. The circles represent the $\Phi_f$ between a N-cell vortex and its counterpart L-cell vortex. The green, red, purple and pink circles indicate the $\Phi_f$ which eventually cause formations of the NL-loop 1, NL-loop2, NL-loop3 and NL-loop4, respectively. Detailed discussions about different NL-loops are given in Sec. 9.4.3. In (b), the red and green circles in the LNC1 and LNC2 are marked by 'R' and 'G' with its serial number. (All the detailed data about the $\Phi_f$ are included in the Supplementary file.) By considering all the highest red points and all the lowest green points, the trigger value and threshold value are marked by the blue and yellow horizontal lines, respectively. The same method is also used in Fig. 13 in Tian et al. [17].*

The phase shift $(\Delta\Phi_f)$ between the N-L vortex pairs with the same serial number (e.g. $k$) in two randomly given neighboring N-cell cycles can be measured:

$$\Delta\Phi_f = \Phi_{f_{(i+1,k)}} - \Phi_{f_{(i,k)}} \tag{9.6}$$

where $\Phi_{f_{(i+1,k)}}$ and $\Phi_{f_{(i,k)}}$ represent the phase difference of the $k$-th N-L vortex pair in the $(i+1)$th and $i$-th N-cell cycles, respectively. According to Eq. 9.4, we can obtain:

$$\Phi_{f_{(i,k)}} = \varphi_{N_{k+(i-1)\beta}} - \varphi_{L_{k+(i-1)\alpha}} \tag{9.7}$$

and reformulate Eq. 9.6 as

$$\begin{aligned}
\Delta\Phi_f &= (\varphi_{N_{k+i\beta}} - \varphi_{L_{k+i\alpha}}) - (\varphi_{N_{k+(i-1)\beta}} - \varphi_{L_{k+(i-1)\alpha}}) \\
&= (\varphi_{N_{k+i\beta}} - \varphi_{N_{k+(i-1)\beta}}) - (\varphi_{L_{k+i\alpha}} - \varphi_{L_{k+(i-1)\alpha}}).
\end{aligned} \tag{9.8}$$

Due to the N- and L-cell vortices are spanwise vortices with dominating shedding frequencies, we can obtain:

$$\varphi_{N_{k+i\beta}} - \varphi_{N_{k+(i-1)\beta}} = \beta\frac{1}{2f_N}, \tag{9.9}$$

$$\varphi_{L_{k+i\alpha}} - \varphi_{L_{k+(i-1)\alpha}} = \alpha\frac{1}{2f_L}. \tag{9.10}$$

Based on Eqs. 9.5, 9.8, 9.9, and 9.10, the phase shift between the $k$-th N-L vortex pair in neighboring N-cell cycles can be measured as

$$\Delta\Phi_f = \beta\frac{1}{2f_N} - \alpha\frac{1}{2f_L} = -S. \tag{9.11}$$

One can easily see that positive $S$ causes a decreasing $\Phi_f$ tendency, and negative $S$ causes an increasing $\Phi_f$ tendency. This is the first time such a relationship is revealed.

By using the same method as described in Sec. 4 of Ref. [17], Fig. 9.9 illustrates the relations between $\Phi_f$ and formation positions of the corresponding NL-loop 1 structures during a long N-cell cycle in all six cases. No matter the tendency of $\Phi_f$ is increasing or decreasing, in a specific $D/d$ case, the smaller the $\Phi_f$ is, the more downstream the formation position of the NL-loop 1 moves. This observation further supplements and validates the relation between $\Phi_f$ and the formation position of the NL-loop 1[17], as mentioned in Sec. 9.1.

Table 9.4: *Detailed information of vortex dislocations in six present $D/d$ cases. The number of N- and L-cell vortices in one N-cell cycle are $\beta$ and $\alpha$, respectively. The variation rate of phase difference (S) is calculated by Eq. 4. In the last two columns, $-\overline{w}/U$ and $\overline{C_{pb}}$ are obtained from Fig. 7 at $z/D=-16$.*

| $D/d$ | $\beta$ | $\alpha$ | Symmetry or Antisymmetry | $SU/D$ | Tendency of $\Phi_f$ | Threshold value | Trigger value | $-\overline{w}/U$ | $\overline{C_{pb}}$ |
|---|---|---|---|---|---|---|---|---|---|
| 2.0 | 13 | 15 | Antisymmetry | 0.064 | Decrease | 4.3 | 5.5 | 0.1422 | -0.8018 |
| 2.2 | 12 | 14 | Symmetry | -0.153 | Increase | 4.2 | 5.5 | 0.1477 | -0.7992 |
| 2.4 | 11 | 13 | Antisymmetry | 0.094 | Decrease | 4.1 | 5.4 | 0.1511 | -0.7974 |
| 2.6 | 11 | 13 | Antisymmetry | -0.104 | Increase | 3.6 | 5.5 | 0.1531 | -0.7958 |
| 2.8 | 10 | 12 | Symmetry | 0.229 | Decrease | 3.2 | 5.5 | 0.1563 | -0.7932 |
| 3.0 | 10 | 12 | Symmetry | -0.059 | Increase | 3.0 | 5.5 | 0.1611 | -0.7888 |
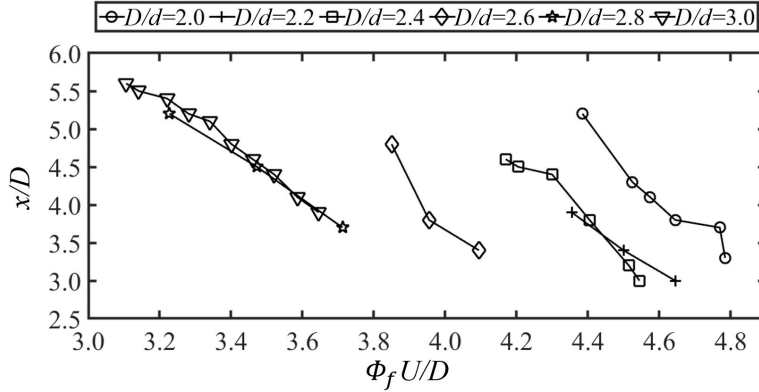


Figure 9.9: *Relation between $\Phi_f$ and the formation position ($x/D$) of corresponding NL-loop 1 structures in a long N-cell cycle. Details of the formation position of the NL-loop 1 in the $D/d$=2.2 and 2.4 cases is shown in Fig. 13 and Fig. 14, respectively. Other cases are shown in Appendix 9.8. Information of $\Phi_f$ is included in the Supplementary file.*

## 9.4.2    $D/d$ influences on the trigger and threshold values of vortex dislocations

The trigger value and the threshold value, as first defined in Tian et al. [17], are important quantities in a vortex dislocation process. They determines when a vortex dislocation eventually takes place. When $\Phi$ is larger than the trigger value, i.e. the corresponding $\Phi_f$ is larger than the threshold value,

vortex dislocations will appear. In the present paper, based on investigations of the six $D/d$ cases, additional features of the trigger value and the threshold value are discovered.

In Fig. 9.8(a-f), the trigger value and the threshold value are obtained and shown by the horizontal blue and yellow lines, respectively. Their specific values are listed in Table 9.4. One can see that, although $D/d$ varies, all the six cases approximately share the same trigger value 5.5 $D/U$. This observation is consistent with McClure et al.[13], in which the authors found that the vortex dislocation happens as vortex filaments approach $2\pi$ phase misalignment. The authors assumed that when two neighboring vortex cells simultaneously shed from the shear layer, they have zero phase difference. However, when the slower shedding vortex sheds one shedding period behind the faster shedding vortex cell, the phase difference between them is $2\pi$. In the present paper, a $2\pi$ phase difference is equal to $1/(St_L) \approx 5.5$. In our opinion, this is because the corresponding N- and L-cell vortices are adjacent spanwise vortices on the same side of the step cylinder. When $\Phi_f$ of a N-L vortex pair exceeds one shedding period of the L-cell vortex, the shear layer of the next L-cell vortex on the other side of the step cylinder will cut down this L-cell vortex and induce a vortex dislocation happen. Furthermore, the number of the N-cell vortex ($\beta$) in one N-cell cycle can be measured as:

$$\beta = nint(2\frac{1}{St_L}/(\frac{1}{St_N} - \frac{1}{St_L})) = nint(\frac{2St_N}{(St_L - St_N)}) \qquad (9.12)$$

where $1/St_L$ is the trigger value (the upper limit of $\Phi_f$), $1/St_N - 1/St_L$ is the accumulating speed of the $\Phi_f$ and $nint$ means rounding to the closest integer. Essentially, the only difference between Eq. 9.12 and Eq. 9.1 from Williamson's work [4] is the factor '2', which is included here to emphasise the importance of counting vortices from the $-Y$ and $+Y$ side independently. Otherwise, it is easy to overlook the antisymmetric vortex interactions. For the same reason, instead of Eq. 9.2, we propose that the number of the L-cell ($\alpha$) vortex can be measured as

$$\alpha = \beta + 2. \qquad (9.13)$$

Detailed information will be discussed in Sec. 9.4.4.

Different from the constant trigger value, the threshold value continues to decrease as $D/d$ increases from 2.0 to 3.0. Eq. 9.3 shows that, for a fixed trigger value, the smaller the $\Phi_f$ is, the higher $\Phi_c$ is needed. To reach the same trigger value, the decreasing tendency of the threshold value should be caused by the increasing capacity of $\Phi_c$. In other words, as $D/d$

increases, if the maximum amount of $\Phi_c$ also increases, the vortex disloca-
tion can be triggered with a smaller $\Phi_f$. Further investigations prove this
assumption. Owing to the spatial inhomogeneity of the convective velocity
and the complex vortex interactions, accurately evaluating $\Phi_c$ is difficult.
However, by comparing the distributions of the time-averaged streamwise
velocity in different vortex cells regions, the capacity of $\Phi_c$ in different cases
can be compared. In Fig. 9.10, the distributions of time-averaged stream-
wise velocity ($\overline{u}/U$) in all six cases are plotted. First, in agreement with the
conclusion of Tian et al. [17], in the near wake ($x/D = 2$), clear differences
between $\overline{u}$ in the N-cell region ($-5 < z/D < 0$) and $\overline{u}$ in the L-cell region
($z/D < -10$) can be observed for all six cases. These differences are sub-
stantially reduced when the sampling line moves downstream from $x/D=2$
to 5. Furthermore, the larger $D/d$ is, the larger difference in $\overline{u}$ between the
N- and L-cell regions can be seen. For example, at $x/D=2$, the maximum
difference between $\overline{u}$ in the N- and L-cell region is $0.33U$ in the $D/d=2.0$
case, but reaches $0.54U$ in the $D/d = 3$ case. This observation clearly indi-
cates that, comparing to the smaller $D/d$ case, a larger amount of $\Phi_c$ can
be accumulated in the larger $D/d$ case.
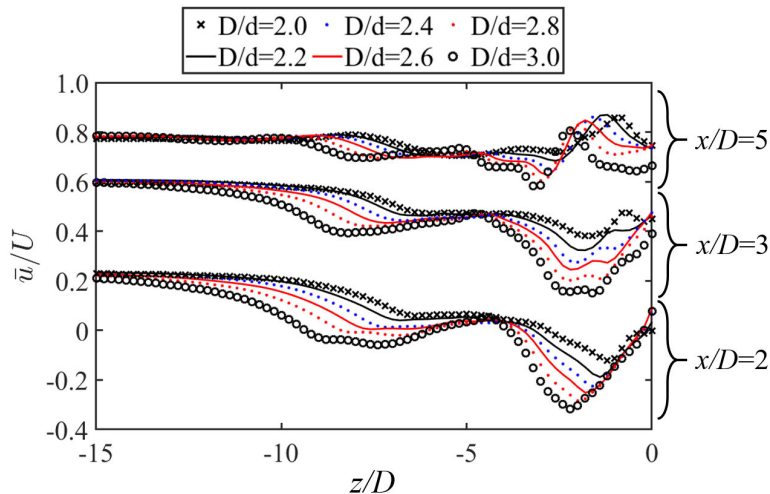


Figure 9.10: Distributions of the time-averaged streamwise velocity ($\overline{u}/U$)
along three vertical sampling lines parallel to the z-axis in the center plane
($y/D=0$) at three positions $x/D=2$, 3 and 5 in the six $D/d$ cases.

### 9.4.3    The number of the NL-loop structures

According to Tian et al.[15, 17], two NL-loop structures, i.e. NL-loop 1 and NL-loop2, one NN-loop and one LL-loop were captured in one N-cell cycle in the $D/d$=2.0 and 2.4 cases. In the present paper, more features of the number of the NL-loop structures are investigated.

In Fig.9.11(a-e), detailed visualizations of vortex connections and dislocations in the 1st N-cell cycle in the $D/d = 2.6$ case are shown. A corresponding topology sketch is plotted in Fig. 9.11(f). The short and long vertical straight lines in the figure represent the N- and L-cell vortices, respectively. Between them, the curved solid lines connect the N-cell vortex and its counterpart L-cell vortex. The dashed curves indicate broken connections that were not able to persist due to vortex dislocations. The three NL-loops, i.e. the NL-loop 1 N4-L'5, the NL-loop2 N'5-L6 and the NL-loop3 N6-L'7, are marked in green, red and purple, respectively, in Fig. 9.11(b), (c) and (d). Compared to the $D/d = 2$ case[17], as shown in Fig. 6 in Ref. [17], a new NL-loop structure (the purple curve in Fig. 9.11(d)) forms after the NL-loop2 (the red curve) in the $D/d = 2.6$ case in Fig. 9.11. Based on the order of occurrences, the new NL-loop is identified as the NL-loop3, which is believed to be caused by the decreasing threshold value. If we hypothesize that the threshold value in the $D/d$=2.6 case was the same as that in the $D/d$=2.0 case, the yellow line will move to the black dashed line in Fig. 9.8(d). This will cause all green circles to become lower than the threshold value. In other words, based on this hypothetical condition, the number of NL-loops will return to 2 in the $D/d$=2.6 case, i.e. there will be no vortex dislocation between N6 and L6.

When $D/d$ continues to increase from 2.6 to 3.0, the threshold value decreases from 3.9 to 3.6. Meanwhile, four NL-loops appear in one N-cell cycle in the $D/d$=2.8 and 3.0 cases, as illustrated in Fig. 9.12. In general, owing to the decreasing trend in the threshold value, the number of NL-loops in one N-cell cycle is expected to continuously increase in the higher $D/d$ cases. For a fixed $Re_D$, the maximum number of NL-loops should appear in the free end cylinder case, i.e. when $D/d$ becomes infinite.

### 9.4.4    Symmetric and antisymmetric vortex interactions

Antisymmetric vortex interactions were reported and discussed in the wake behind the single step cylinders with $D/d$=2.0 and 2.4 by Tian et al.[15, 17]. In the present manuscript, by investigating four more cases $D/d$=2.2, 2.6, 2.8 and 3, an additional symmetric vortex interaction is observed. As examples, the NL-loop 1 structures in the neighboring N-cell cycles are plotted
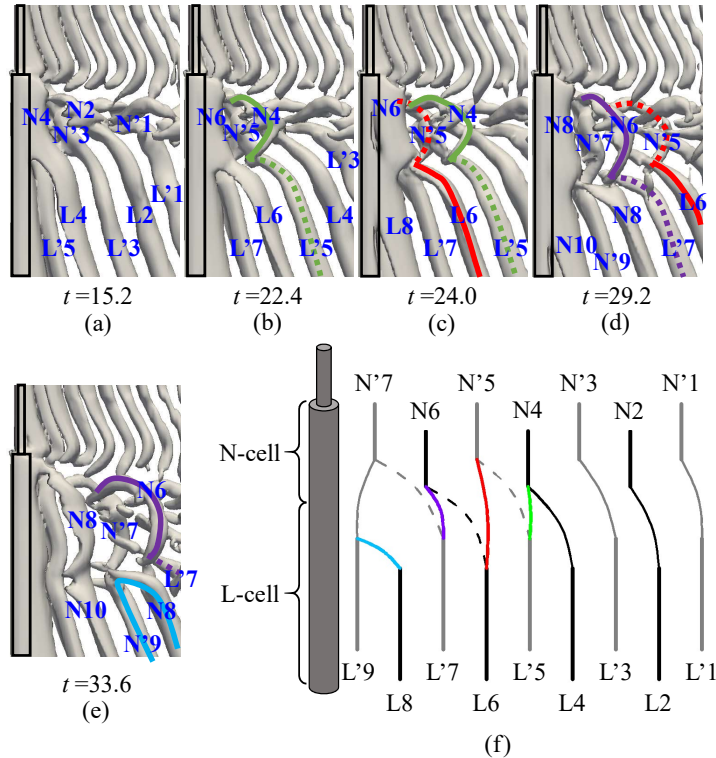
Figure 9.11: (a-e) Iso-surface of $\lambda_2$=-0.05 showing developments of vortex structures on the $-Y$ side in the $D/d = 2.6$ case. Solid and dashed curves indicate the loop structures on the $-Y$ and $+Y$ sides, respectively. (f) Schematic topology illustrating the 1st N-cell cycle in the $D/d$=2.6 case. The time t is t=t*-300D/U, where t* is the actual time in the simulation.

in the D/d=2.4 and 2.6 cases in Fig. 9.13 and 9.14, respectively. The NL-loop 1 structures continuously appear at the -Y side of the step cylinder in Fig. 9.13(a-d). We call this symmetric vortex interaction, in contrast to the antisymmetric vortex interaction shown in Fig. 9.14. From the information in Table 9.4, we learn that, in a certain $D/d$ case, whether vortex dislocations are symmetric or antisymmetric is determined by the parity of the number of N- and L-cell vortices, i.e. $\beta$ and $\alpha$, in one N-cell cycle. When $\beta$ and $\alpha$ are even numbers, symmetric vortex interactions will appear. Oppositely, when $\beta$ and $\alpha$ are odd numbers, antisymmetric vortex interactions will happen. This is because both the N- and L-cell vortices are shed alternatingly from the +Y and -Y side of the step cylinder. When there are an even number of N- and L-cell vortices between the correspond-
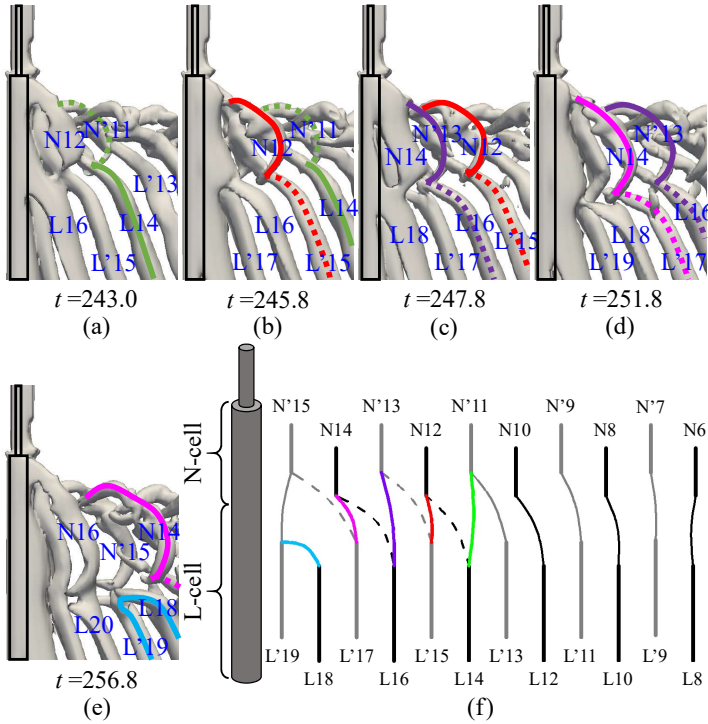
Figure 9.12: (a-e) Iso-surface of $\lambda_2$=-0.05 showing developments of vortex structures on the $-Y$ side in the $D/d$=3.0 case. Solid and dashed curves indicate the loop structures on the $-Y$ and $+Y$ sides, respectively. (f) Schematic topology illustrating the 1st N-cell cycle in the $D/d$=3.0 case. The time $t$ is $t$=$t$*-$300D/U$, where $t$* is the actual time in the simulation.

ing NL-loop 1 structures in the neighboring N-cell cycles, these NL-loop 1 structures appear at the same side of the step cylinder, i.e. symmetric vortex interactions. Otherwise, conventional antisymmetric vortex interactions appear.

Long time observations reveal that not only the decreasing tendency of $\Phi_f$, but also the increasing tendency of $\Phi_f$ can occasionally interrupt the continuous symmetric and antisymmetric vortex interactions. As described in Sec. 9.1, when corresponding $\Phi_f$ continues to decrease in subsequent N-cell cycles, one additional N-L vortex pair will be needed in a certain N-cell cycle to make $\Phi_f$ sufficiently large to induce the formation of the NL-loop structure. It is this one additional N-L vortex pair that changes the parity of the number of N- and L-cell vortices, and further causes the interruption of the repetitive symmetric or antisymmetric vortex interactions. For the
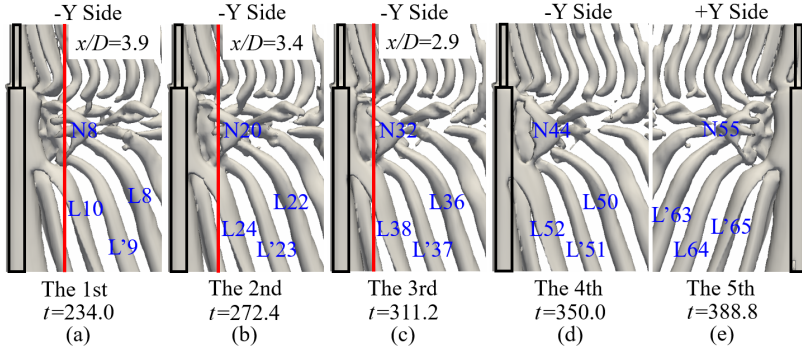
*Figure 9.13: From (a) to (e), the just-formed NL-loop 1 structures in the 1st to 5th N-cell cycles are plotted from both the -Y and +Y side in the D/d=2.2 case. The red line marks the formation position of the NL-loop 1. The time t is set to $t = t^* - 300D/U$.*
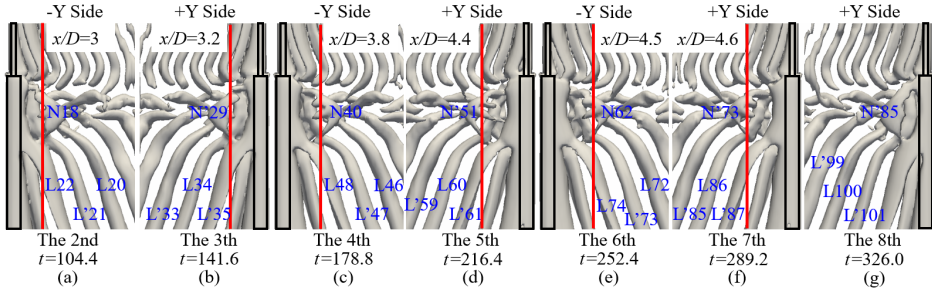


*Figure 9.14: From (a) to (g), the just-formed NL-loop 1 structures in the 2nd to 8th N-cell cycles are plotted from both the -Y and +Y side in the D/d=2.4 case. The red line marks the formation position of the NL-loop 1. The time t is set to $t = t^* - 300D/U$.*

present cases with the discovered increasing tendency of $\Phi_f$, the interruption works in a different way.

In Fig. 9.8(b), (d) and (f), black dotted lines illustrate the increasing tendency of $\Phi_f$ of the N-L vortex pair which is just before the N-L vortex pair whose dislocation finally causes the formation of the NL-loop 1. In the $D/d = 2$ case, along the black dotted line in Fig. 9.8, $\Phi_f$ increases from B1 to B5, and eventually exceeds the threshold value in the 5th N-cell cycle (B5). Under this circumstance, by including the contribution of $\Phi_c$, $\Phi$ is large enough to induce the formation of the NL-loop 1 (N'55-L64) in Fig. 9.13(e). Between neighboring NL-loop 1 structures in Fig. 9.13(a-d), there are 12 N- and 14 L-cell vortices. However, between Fig. 9.8(d) and (e), there are only

11 N- and 13 L-cell vortices in the 5th N-cell cycle, i.e. one N-L vortex pair less than in previous N-cell cycles. It is this one less N-L vortex pair that causes the NL-loop 1 structure (N'55-L64) to form at the +Y side of the step cylinder, and interrupts the continuous symmetric vortex interactions. Similar situations are also observed in the $D/d = 2.6$ and 3.0 cases, which are included in Appendix 9.9. In general, when $\Phi_f$ in advance becomes smaller or larger than the threshold value, one more or one less N-L vortex pair will change the parity of the number of N- or L-cell vortices in one N-cell cycle, and further interrupts the continuously symmetric or antisymmetric vortex interactions. There relationships, as far as the authors know, is the first time to be revealed, could help to understand the vortex dynamics in a vortex dislocation process more clearly.

## 9.5    Likelihood analysis

It's striking to see from Table 9.4 that, among the six cases we investigated here, three cases have the increasing tendency of $\Phi_f$, and the other three have the decreasing tendency. Moreover, three cases show symmetric vortex interactions, while the other three show antisymmetric vortex interactions. It is hard to believe these equal occurrences are all by coincidence. Therefore, we present a likelihood analysis here. Based on $St_N$ and $St_L$, we can obtain

$$E_N = 2St_N/(St_L - St_N), \tag{9.14}$$

$$E_L = 2St_L/(St_L - St_N) \tag{9.15}$$

where $E_N$ and $E_L$ are exact values compared to the rounding value $\alpha$ in Eq. 9.12. The differences ($\delta$, $\delta_N$ and $\delta_L$) between the exact values ($E_N$ and $E_L$) and the rounding values ($\beta$ and $\alpha$) can be expressed as follows:

$$\delta_N = E_N - \beta, \tag{9.16}$$

$$\delta_L = E_L - \alpha. \tag{9.17}$$

According to Eq. 9.12, and 9.13, one can easily obtain:

$$\delta = \delta_N = \delta_L. \tag{9.18}$$

Based on Eq. 9.16, 9.17, and 9.18, the original Eq. 9.5 can be rewritten:

$$\frac{SU}{D} = \alpha\frac{1}{2St_L} - \beta\frac{1}{2St_N} = (E_L - \delta_L)\frac{1}{2St_L} - (E_N - \delta_N)\frac{1}{2St_N} =$$

$$\delta(\frac{1}{2St_N} - \frac{1}{2St_L}) \tag{9.19}$$

Owing to the fact that the N-cell vortices shed slower than the L-cell vortices, i.e. $St_N$ is always smaller than $St_L$, and the value of both $U$ and $D$ are positive, the sign of the $S$ value in Eq. 9.19 is determined by the sign of $\delta$. In other words, when $E_N$ and $E_L$ are rounded to smaller $\beta$ and $\alpha$, respectively, e.g. in the $D/d$=2.0, 2.4 and 2.8 cases, the corresponding $\delta$ value and the $S$ value become positive. Consequently, a decreasing tendency of $\Phi_f$ appears, e.g. as shown in Fig. 9.8(a), (c) and (e). Otherwise, a negative $\delta$ and $S$ lead to an increasing tendency of $\Phi_f$. Meanwhile, based on the parity of $\beta$ and $\alpha$, the characteristic of vortex interactions (symmetry or antisymmetry) can be deduced. Relations between $E_N$ and features of vortex dislocations are shown in Table 9.5.

Table 9.5: Relation between $E_N$ and characteristics of vortex dislocations. In the first column n represents natural (n =1, 2, 3, ...).

| $E_N$ | Tendency of $\Phi_f$ | Symmetry or Antisymmetry |
|---|---|---|
| 2n-1< $E_N$ <2n-0.5 | Decrease | Antisymmetry |
| 2n-0.5< $E_N$ <2n | Increase | Symmetry |
| 2n< $E_N$ <2n+0.5 | Decrease | Symmetry |
| 2n+0.5< $E_N$ <2n+1 | Increase | Antisymmetry |

Table 9.6: Detailed information of vortex dislocations in other four $D/d$ cases, i.e. $D/d$=2.1, 2.3, 2.5 and 2.7.

| $D/d$ | $St_N$ | $St_L$ | $\beta$ | $\alpha$ | Symmetry or Antisymmetry | SU/D | Tendency of $\Phi_f$ |
|---|---|---|---|---|---|---|---|
| 2.1 | 0.1529 | 0.1779 | 12 | 14 | Symmetry | 0.107 | Decrease |
| 2.3 | 0.1509 | 0.1775 | 11 | 13 | Antisymmetry | 0.172 | Decrease |
| 2.5 | 0.1496 | 0.1777 | 11 | 13 | Antisymmetry | -0.042 | Increase |
| 2.7 | 0.1485 | 0.1767 | 11 | 13 | Antisymmetry | -0.252 | Increase |

In Fig. 9.15(a), $E_N$ in the six cases are shown as six black circles. By applying a 5th order interpolation polynomial in curve fitting to these six circles, the black curve in Fig. 9.15(a) is obtained to describe the relation
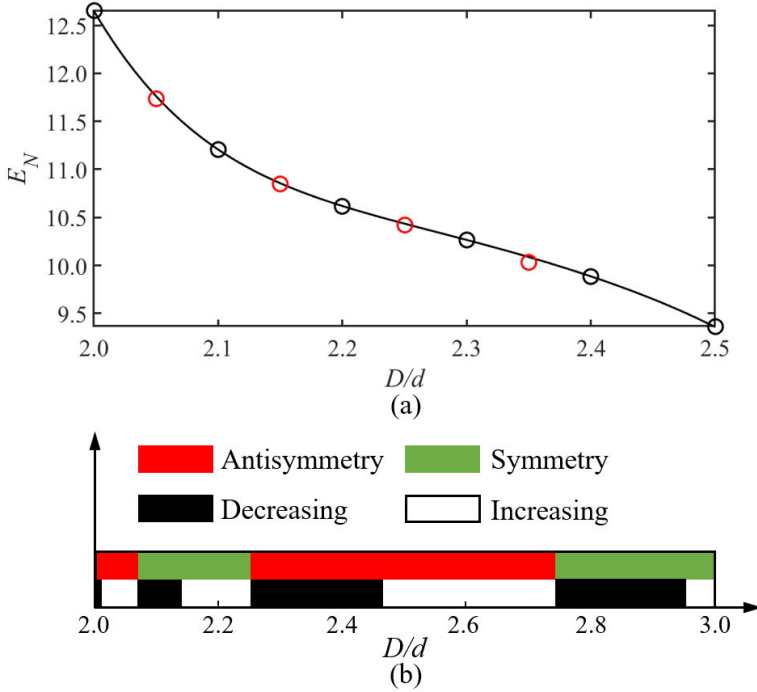
Figure 9.15: (a) $E_N$ in the $D/d=2.0$, 2.2, 2.4, 2.6, 2.8 and 3.0 cases are marked by black circles. By applying a 5th order interpolation polynomial in curve fitting on these six circles, the black curve ($E_N = -5.706(D/d)^5 + 77.805(D/d)^4 - 426.295(D/d)^3 + 1171.735(D/d)^2 - 1615.737(D/d) + 905.749$) is obtained to described the relation between $E_N$ and $D/d$. Moreover, $E_N$ in the $D/d=2.1$, 2.3, 2.5 and 2.7 cases are plotted as red circles to justify the curve fitting function. (b) Following the relation between $E_N$ and characteristics of vortex dislocations in Table 9.5, the black, white, red and green bars are plotted to show the cases with decreasing $\Phi_f$ tendency, the cases with increasing $\Phi_f$ tendency, the cases with antisymmetric vortex interactions and the cases with symmetric vortex interactions, respectively.

between $E_N$ and $D/d$. The justification of this curve is checked by simulating four more cases, i.e. the $D/d=2.1$, 2.3, 2.5 and 2.7 cases. After following the same simulation and analysis processes as described in Sec. 9.4, information of these four cases are shown in Table 9.6. More detailed information is included in Appendix 9.9. By using Eq. 9.14, four red circles are plotted in Fig. 9.15(a), which fit the black curve very well. This indicates a reasonable curve fitting. Based on this curve and Table 9.5, Fig. 9.15(b) can be sketched to show the different characteristics for all cases between $D/d=2$

and 3. One can easily see that the total area of the red bar is larger than that of the green bar. On the other hand, the total areas of the black and white bars are almost the same. Therefore, we can anticipate that, when $D/d$ is randomly chosen between 2 and 3, the likelihood of increasing $\Phi_f$ and decreasing $\Phi_f$ tendencies, are almost the same, whereas the likelihood of antisymmetric vortex interactions is larger than that of symmetric vortex interactions. This anticipation agrees well with our observations shown in Table 9.6. In these four additional cases, the increasing $\Phi_f$ tendency appears in two cases, i.e. the $D/d$=2.5 and 2.7 cases. The other two cases show decreasing $\Phi_f$ tendency. However, only the $D/d = 2.1$ case shows the symmetric vortex interactions. Antisymmetric vortex interactions are observed in the other three cases. The present result indicates that the characteristics of the vortex dislocations are determined by the shedding frequencies of the N- and L-cell vortices. Meanwhile, as described in Sec.9.3.2, by affecting the 3D effects (downwash and increased base pressure), the changed diameter ratio influences the shedding frequencies of the N- and L-cell vortices and the corresponding $E_N$, which in turn affects the characteristics of vortex dislocations. The likelihood of antisymmetric or symmetric vortex interactions, and increasing or decreasing $\Phi_f$ tendencies are determined by the relation between $E_N$ and $D/d$.

## 9.6   Conclusion

In the present paper, we use DNS to investigate vortex dynamics in the near wake behind single step cylinders with $2 \leq D/d \leq 3$ at $Re_D$=150. Our results are consistent with previous studies [1, 11, 15, 17], with respect to the mainly three dominating spanwise vortices (i.e. S-, N- and L-cell vortices) and some interesting characteristics of vortex dislocations (i.e. two phase-difference accumulation mechanisms ($\Phi = \Phi_f + \Phi_c$), the NL-loop structures appearing in the dislocation process, the trigger and threshold value of vortex dislocations, antisymmetric vortex interactions between neighboring N-cell cycles and its interruptions). In addition, the numerical results provide a deeper and more complete information on step cylinder wakes.

First, by a fast Fourier transform (FFT) of time series of the streamwise velocity $u$, shedding frequencies and extensions of three spanwise vortex cells are investigated. As $D/d$ increases from 2 to 3, the extension of the S-cell vortex remain almost constant. The shedding frequency of the S-cell vortex ($St_S$) is simply dependent on $Re_d$. Meanwhile, an expansion of the N-cell region and a shrinking of the L-cell region are observed. For the first time, we report that, as $D/d$ increases, the N-L transition region continues

to move towards the large cylinder part, and its length gradually increases. Since the N-cell region being closer to the step position than the L-cell region, when $D/d$ increases, the shedding frequency of the N-cell vortex $(St_N)$ decreases faster than the shedding frequency of the L-cell vortex $(St_L)$. The oblique shedding angle $(\theta_L)$ of the L-cell vortex remains almost unaffected. In the large cylinder part, the strength of the induced downwash flow $(-w/U)$ and the base pressure become larger, when $D/d$ increases. By carefully checking the distributions of $-w/U$ and base pressure coefficient $(C_{pb})$, we conclude that the formation of N-cell vortices are caused by the joint influence of both increased $-w/U$ and increased $C_{pb}$, but the latter one plays a major role.

Moreover, based on long-time observations on iso-surfaces of $\lambda_2$, we found that, in the $D/d$=2.2, 2.8 and 3.0 cases, the NL-loop 1 structure continues to appear at either the +Y or -Y side of the step cylinder. In comparison with the already known antisymmetric phenomenon [15, 17], we call this symmetric vortex interactions. By analyzing the number of N- and L-cell vortices, i.e. $\beta$ and $\alpha$, in one N-cell cycle in different $D/d$ cases, we found that it is the parity of $\beta$ and $\alpha$ that determines whether symmetric or antisymmetric vortex interactions appears in a certain $D/d$ case.

By using a reliable phase tracking method, we monitored the time trace of $\Phi_f$ in the $D/d$=2.0, 2.2, 2.4, 2.6, 2.8 and 3.0 cases. An increasing tendency of $\Phi_f$ is first captured in $D/d$=2.2, 2.6 and 3.0 cases. In these cases, the formation position of NL-loop 1 structures is observed to continuously move upstream as $\Phi_f$ increases. Similar as the decreasing tendency of $\Phi_f$ reported in Ref. [17], the discovered increasing $\Phi_f$ tendency also can cause the interruption of continuous antisymmetric or symmetric vortex interaction phenomena, but in a different way. According to the time trace of $\Phi_f$, the trigger value of vortex dislocations is found to remain constant when $D/d$ varies. The threshold value of vortex dislocations decreases as D/d increases, which further causes the number of NL-loop structures in one N-cell cycle to increase from 2 in the $D/d$=2.0 case to 4 in the $D/d$=3.0 case. Based on the application of a constant trigger value, we propose Eq. 9.12 and 9.13 to measure $\beta$ and $\alpha$. Comparing with the conventional Eq. 9.1 and 9.2, a new factor '2' is introduced to emphasize the importance of counting vortices from the -Y and +Y side independently. Otherwise, the antisymmetric phenomenon is easy overlooked. Furthermore, a universal rule of anticipating the qualitative features of vortex dislocations are summarized in Table 9.5.

Finally, we analyze the likelihood of appearance of antisymmetric or symmetric vortex interactions, and the likelihood of increasing or decreas-

ing phase differences. Based on the investigations of $D/d$=2.0, 2.2, 2.4, 2.6, 2.8 and 3.0 cases, we predicted that, when $2 \leq D/d \leq 3$, the likelihood of increasing $\Phi_f$ and decreasing $\Phi_f$ are almost the same, but the antisymmetric phenomenon is more likely to appear than the symmetric phenomenon. Further observations in $D/d$=2.1, 2.3, 2.5 and 2.7 cases prove our anticipation.

In summary, by simulating altogether ten different $D/d$ cases, the present paper provides more in-depth and complete understanding of the vortex dislocation phenomenon. Some new observations, e.g. an increasing tendency of $\Phi_f$, the symmetric features and increased number of NL-loop structures in the vortex dislocation process, help to outline a better picture and lead to the identification of several important relationships. These include the relationship between $\alpha$ ($\beta$) and (anti-) symmetry, and the relationship between tendency of $\Phi_f$ and $S$. Moreover, the method and formulas we used to analyze the likelihood of appearance of different features of vortex dislocations may also be applicable in other wake flows.

## Supplementary Material

By using the phase tracking method described in Ref.[17], the phase information of N- and L-cell vortices and their phase differences in the $D/d$=2.0, 2.2, 2.4, 2.6, 2.8, and 3.0 cases are shown in the supplementary file 1, 5, 2, 6, 7, and 8, respectively. The N-L vortex pair whose phase difference induces vortex dislocations is highlighted in gray.

## Data Availability Statement

The data that support the findings of this study are available from the corresponding author upon reasonable request.

## Acknowledgments

## 9.7 Appendix A: Streamwise velocity spectra in the $D/d$=2.0, 2.2, 2.4, 2.6, 2.8 and 3.0 cases

In this appendix, all velocity spectra are calculated by a fast Fourier transform (FFT) of at least $2000D/U$ continuous streamwise velocity ($u$) data along a vertical sampling line parallel to the $z$-axis with density $0.2D$ positioned at $(x/D, y/D)$=(1.6, 0.4).



(a)　　　　　　　(b)
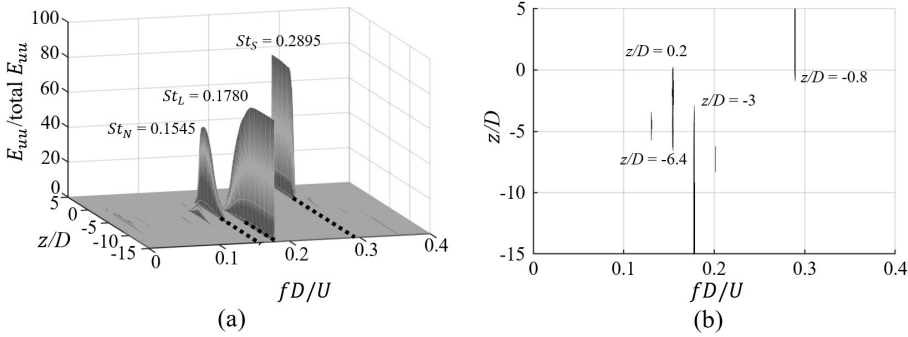
Figure 9.16: In the $D/d$=2.0 case, (a) a 3D version of velocity spectra along a spanwise line behind the step cylinder at $(x/D, y/D)$=(1.6, 0.4), where the shedding frequencies of the three main vortex cells (S-cell: $St_S = f_S D/U$, N-cell: $St_N = f_N D/U$ and L-cell: $St_L = f_L D/U$) are marked. (b) The projection of the panel (a) on the top-down view. Only points with $E_{uu}/(Total\ E_{uu}) \geq 4$ are shown.



(a)　　　　　　　(b)
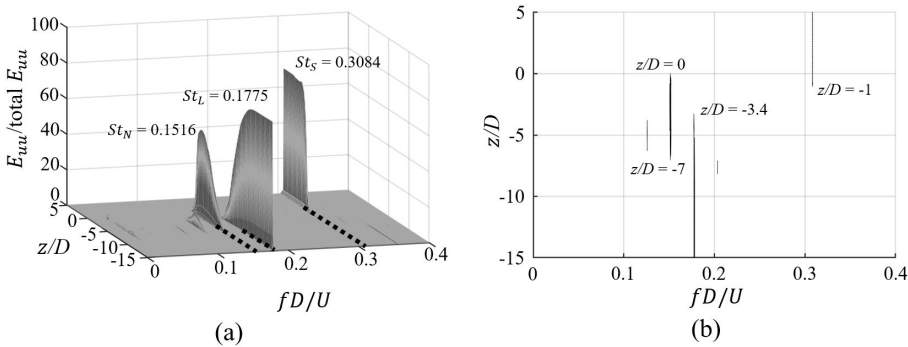
Figure 9.17: (a, b) are same as Fig. 9.16(a, b), but in a different case $D/d$=2.2.
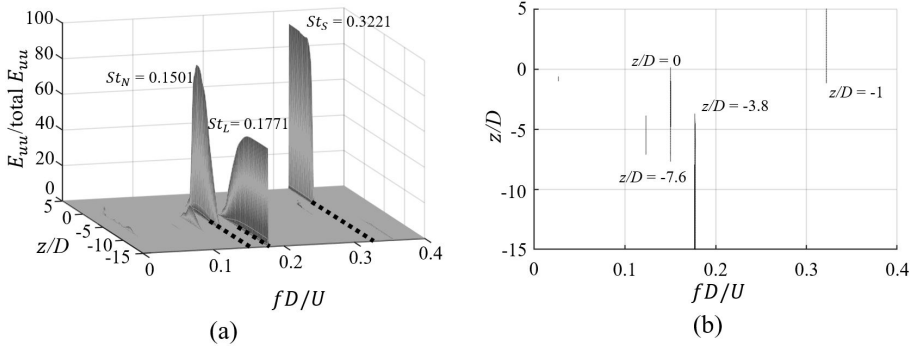
Figure 9.18: (a, b) are same as Fig. 9.16(a, b), but in a different case $D/d$=2.4.
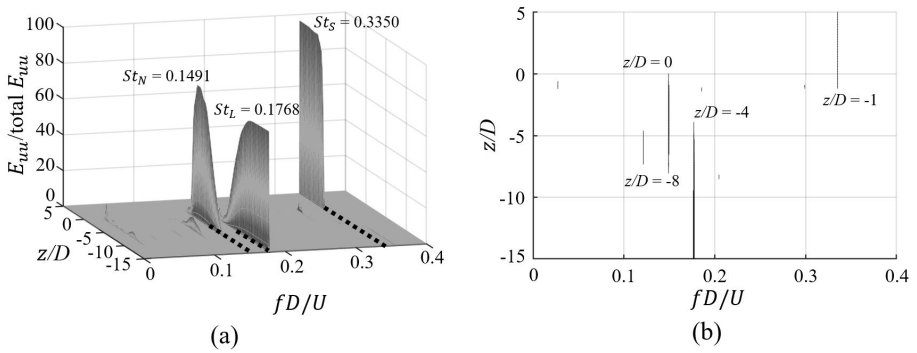


Figure 9.19: (a, b) are same as Fig. 9.16(a, b), but in a different case $D/d$=2.6.
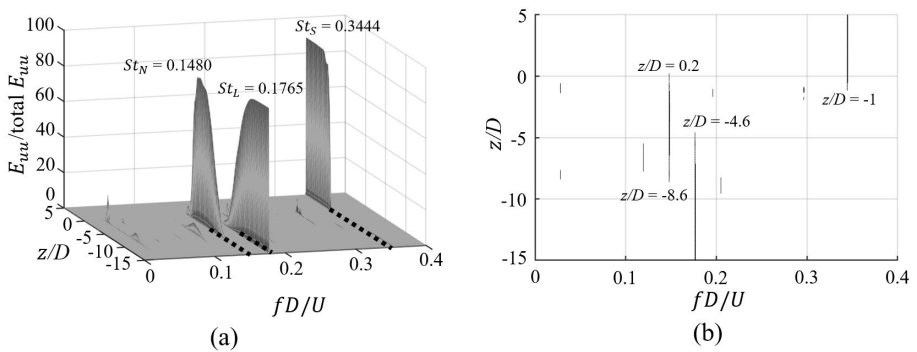


Figure 9.20: (a, b) are same as Fig. 9.16(a, b), but in a different case $D/d$=2.8.
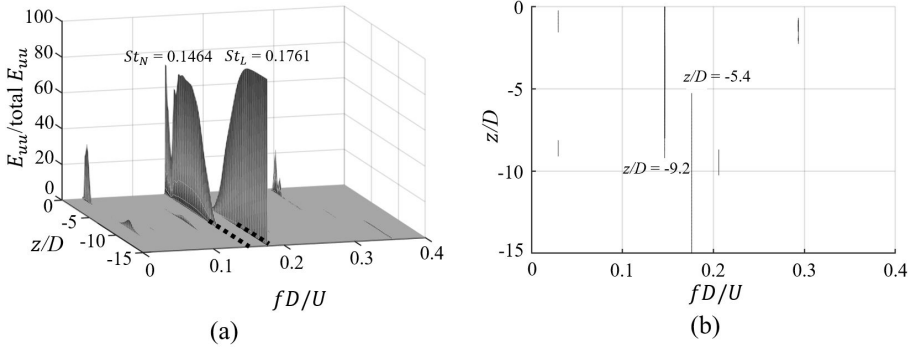
Figure 9.21: (a, b) are same as Fig. 9.16(a, b), but in a different case $D/d=3.0$.

## 9.8 Appendix B: Detailed information of vortex dislocations in the $D/d=2.0$, 2.6, 2.8 and 3.0 cases

In this appendix, the just-formed NL-loop 1 structures in the first long N-cell cycle are plotted in the $D/d=2.0$, 2.6, 2.8 and 3.0 cases from both the $-Y$ and $+Y$ sides (in Figs. 9.22, 9.23, 9.24, and 9.8, respectively). The red line marks the formation position of NL-loop 1. As discussed in Sec. 9.4.4, when the NL-loop 1 structure appears alternately at the $+Y$ and $-Y$ sides between subsequent N-cell cycles, the antisymmetric vortex interactions appear. On the other hand, when the NL-loop 1 structure continuously appears at the $+Y$ or $-Y$ side in the neighboring N-cell cycles, the symmetric vortex interactions appear.
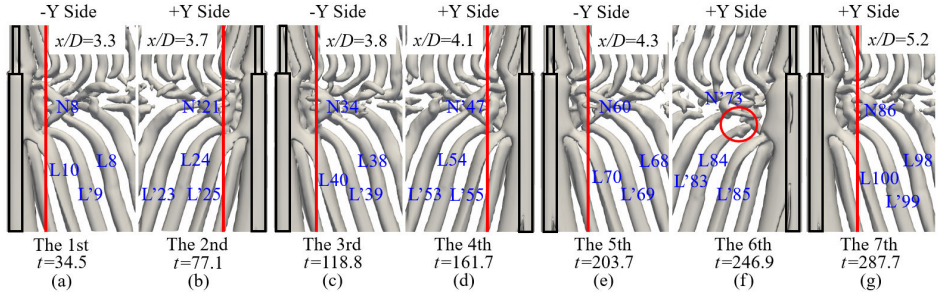
**Figure 9.22:** *From (a) to (g), isosurfaces of $\lambda_2$=-0.05 showing formation position and the side of the NL-loop 1 structure in the 1st long N-cell cycle in the $D/d$=2.0 case. The antisymmetric phenomenon appears. The red circle in panel (f) highlights an irregular absence of the NL-loop 1 structure, which was discussed in Ref. [17]. The time t is set to $t = t^* - 2378.1D/U$.*
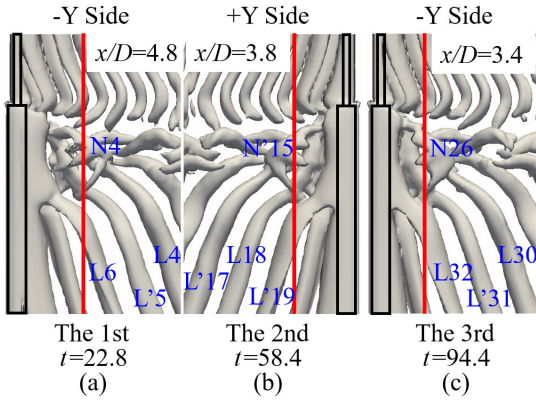


**Figure 9.23:** *From (a) to (c), isosurfaces of $\lambda_2$=-0.05 showing formation position and the side of the NL-loop 1 structure in the 1st long N-cell cycle in the $D/d$=2.6 case. The antisymmetric phenomenon appears. The time t is set to $t = t^* - 300D/U$.*
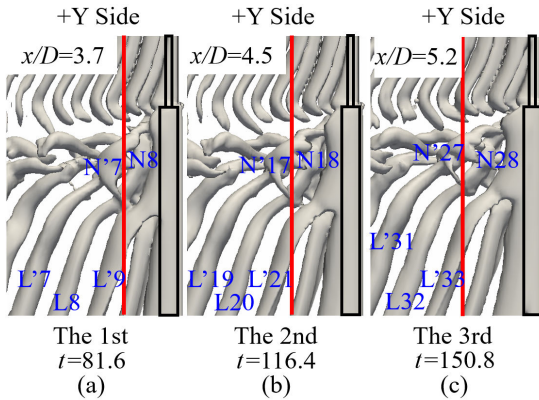


**Figure 9.24:** *From (a) to (c), isosurface of $\lambda_2$=-0.05 showing formation position and the side of the NL-loop 1 structure in the 1st long N-cell cycle in the $D/d$=2.8 case. The symmetric phenomenon appears. The time t is set to $t = t^* - 300D/U$.*
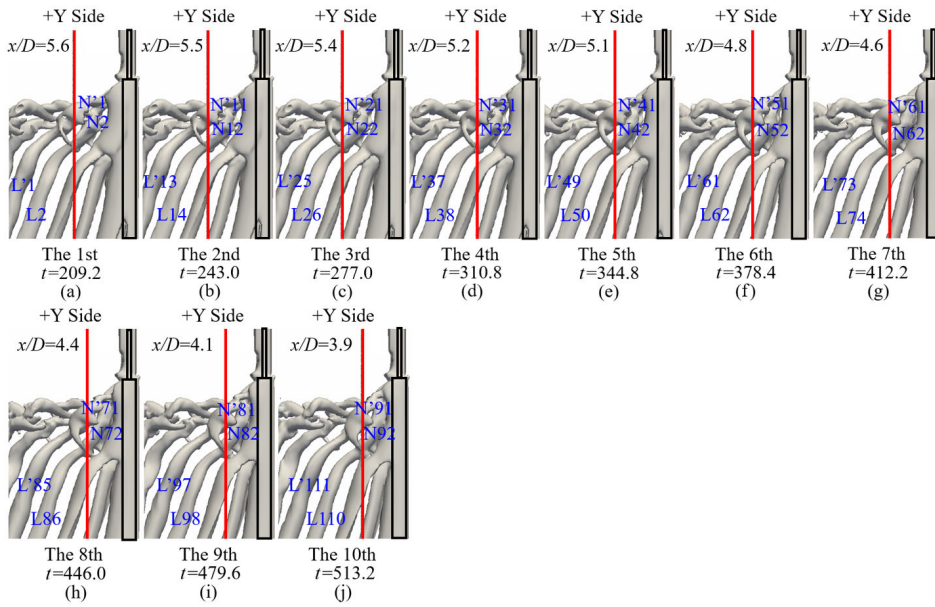
Figure 9.25: From (a) to (j), isosurface of $\lambda_2$=-0.05 showing formation position and the side of the NL-loop 1 structure in the 1st long N-cell cycle in the $D/d$=3.0 case. The symmetric phenomenon appears. The time $t$ is set to $t = t^* - 300D/U$.

## 9.9    Appendix C: Detailed information in $D/d$=2.1, 2.3, 2.5 and 2.7 cases

This appendix includes four figures, i.e., Fig. 9.26-9.29. All velocity spectra are calculated by a fast Fourier transform (FFT) of at least $2000D/U$ continuous streamwise velocity ($u$) data along a vertical sampling line parallel to the $z$-axis with density $0.2D$ positioned at $(x/D, y/D)$=(1.6, 0.4). The just-formed NL-loop 1 structures in the first long N-cell cycle are plotted in the $D/d$=2.1, 2.3, 2.5 and 2.7 cases from both the $-Y$ and $+Y$ sides. The red line marks the formation position of NL-loop 1. As discussed in Sec. 9.4.4, when the NL-loop 1 structure appears alternately at the $+Y$ and $-Y$ sides between subsequent N-cell cycles, the antisymmetric vortex interactions appear. On the other hand, when the NL-loop 1 structure continuously appears at the $+Y$ or $-Y$ side in the neighboring N-cell cycles, the symmetric vortex interactions appear. Based on Sec. 9.4.1, by observing the tendency of formation position of NL- loop 1 structures, the variation of $\Phi_f$ can be obtained. When the formation position of NL-loop 1 structures continuously moves downstream or upstream in a long N-cell cycles, the corresponding decreasing or increasing tendency of $\Phi_f$ appears, respectively.
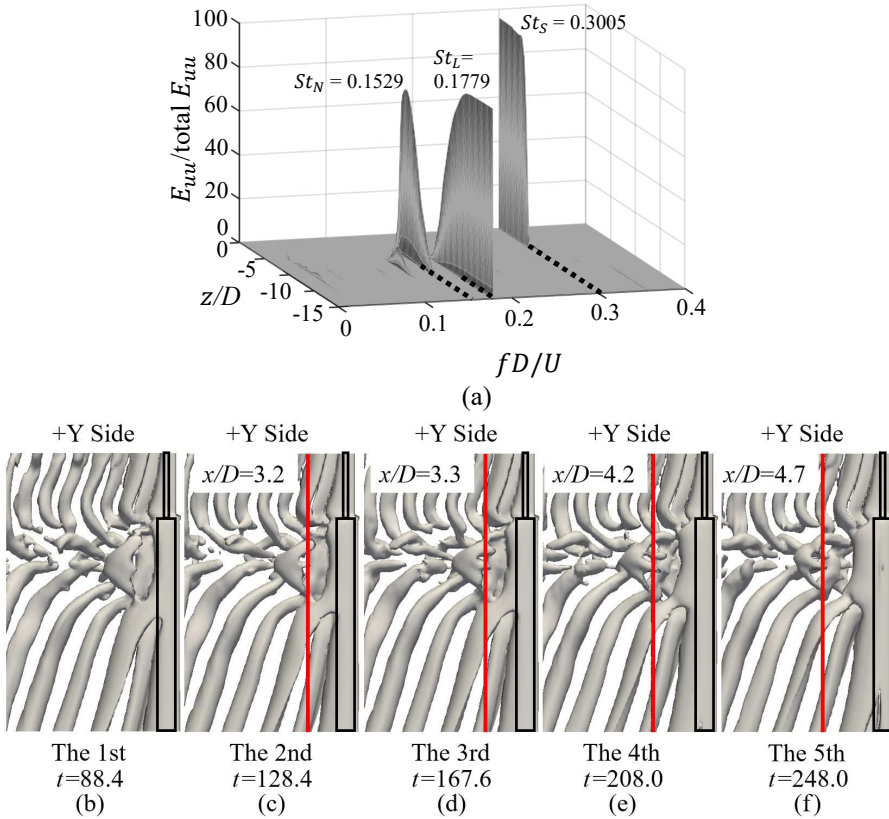
Figure 9.26: In the $D/d=2.1$ case, (a) a 3D velocity spectra along a spanwise line behind the step cylinder at $(x/D,\ y/D)=(1.6,\ 0.4)$, where the shedding frequencies of the three main vortex cells (S-cell: $St_S = f_S D/U$, N-cell: $St_N = f_N D/U$ and L-cell: $St_L = f_L D/U$) are marked. From (b) to (f), isosurface of $\lambda_2=-0.05$ showing formation position and the side of the NL-loop 1 structure in the 1st long N-cell cycle in the $D/d=2.1$ case. The symmetric phenomenon and decreasing tendency of $\Phi_f$ appear. The time $t$ is set to $t = t^* - 300D/U$.
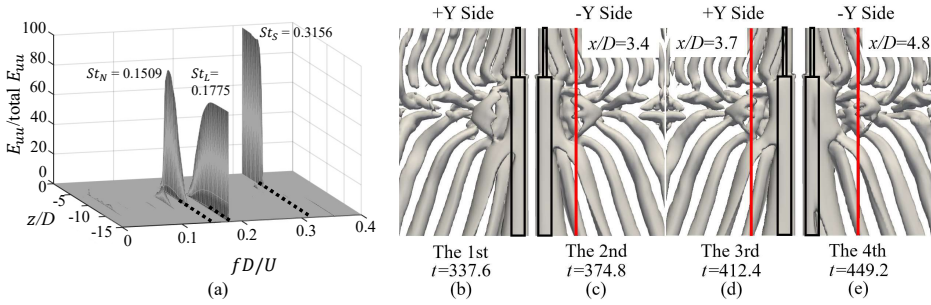
Figure 9.27: (a) is same as Fig. 9.26(a), but in a different case $D/d$=2.3. From (b) to (e), isosurface of $\lambda_2$=-0.05 showing formation position and the side of the NL-loop 1 structure in the 1st long N-cell cycle in the $D/d$=2.3 case. The antisymmetric phenomenon and decreasing tendency of $\Phi_f$ appear. The time $t$ is set to $t = t^* - 300D/U$.
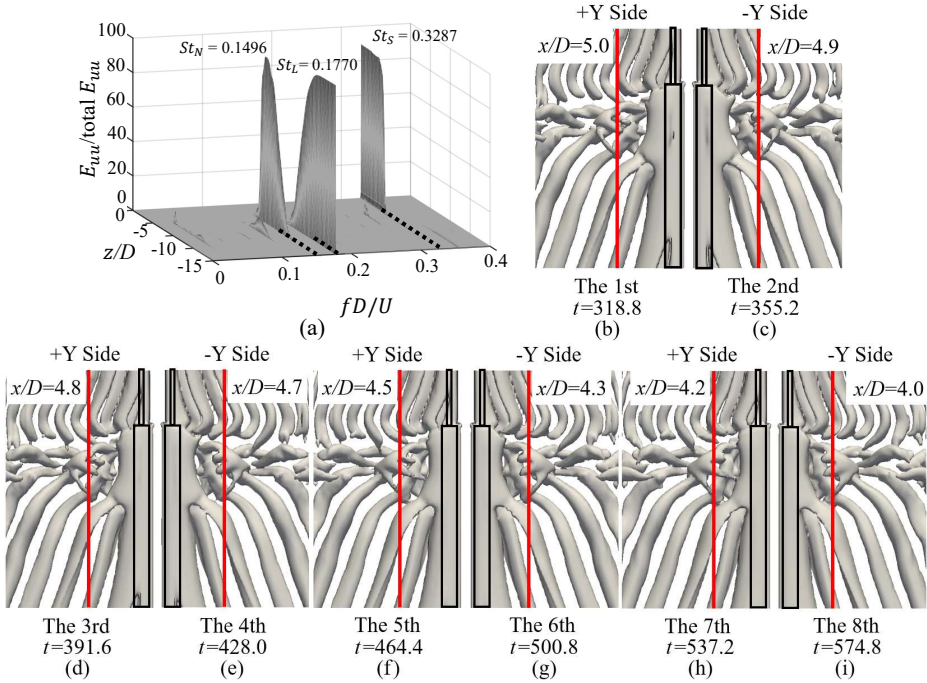


Figure 9.28: (a) is same as Fig. 9.26(a), but in a different case $D/d$=2.5. From (b) to (i), isosurface of $\lambda_2$=-0.05 showing formation position and the side of the NL-loop 1 structure in the 1st long N-cell cycle in the $D/d$=2.5 case. The antisymmetric phenomenon and increasing tendency of $\Phi_f$ appear. The time $t$ is set to $t = t^* - 300D/U$.
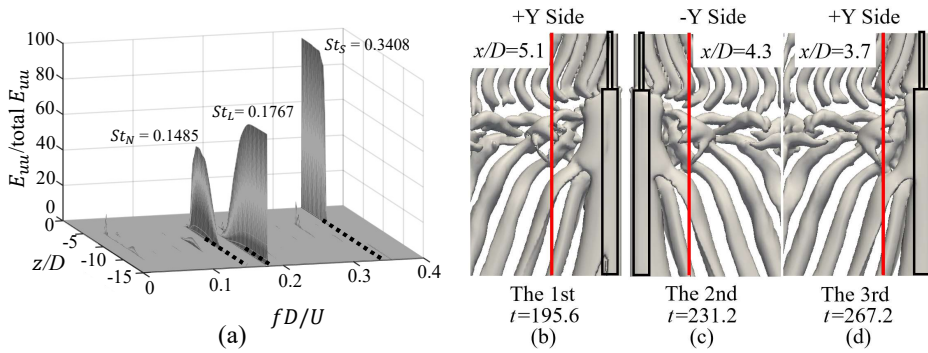
Figure 9.29: (a) is same as Fig. 9.26(a), but in a different case $D/d=2.7$. From (b) to (d), isosurface of $\lambda_2=-0.05$ showing formation position and the side of the NL-loop 1 structure in the 1st long N-cell cycle in the $D/d=2.7$ case. The antisymmetric phenomenon and increasing tendency of $\Phi_f$ appear. The time $t$ is set to $t = t^* - 300D/U$.

# References

[1] Dunn W, Tavoularis S. Experimental studies of vortices shed from cylinders with a step-change in diameter. *J. Fluid Mech.* 2006; **555**:409–437.

[2] Lewis CG, Gharib M. An exploration of the wake three dimensionalities caused by a local discontinuity in cylinder diameter. *Phys. Fluids A: Fluid Dynamics* 1992; **4**(1):104–117.

[3] Ayoub A, Karamcheti K. An experiment on the flow past a finite circular cylinder at high subcritical and supercritical Reynolds numbers. *J. Fluid Mech.* 1982; **118**:1–26.

[4] Williamson CHK. Oblique and parallel modes of vortex shedding in the wake of a circular cylinder at low Reynolds numbers. *J. Fluid Mech.* 1989; **206**:579–627.

[5] Jiang F, Pettersen B, Andersson HI, Kim J, Kim S. Wake behind a concave curved cylinder. *Phys. Rev. Fluids* 2018; **3**(9):094 804.

[6] Zdravkovich MM, Brand VP, Mathew G, Weston A. Flow past short circular cylinders with two free ends. *J. Fluid Mech.* 1989; **203**:557–575.

[7] Morton C, Yarusevych S, Carvajal-Mariscal I. Study of flow over a step cylinder. *Appl. Mech. Mater.* 2009; **15**:9–14.

[8] Bearman PW. Investigation of the flow behind a two-dimensional model with a blunt trailing edge and fitted with splitter plates. *J. Fluid Mech.* 1965; **21**(2):241–255.

[9] Norberg C. An experimental study of the flow around cylinders joined with a step in diameter. *Proceedings of the 11th Australasian Fluid Mechanics Conference, Hobart, Australia*, vol. 1, 1992; 507–510.

[10] Vallès B, Andersson HI, Jenssen CB. Direct-mode interactions in the wake behind a stepped cylinder. *Phys. Fluids* 2002; **14**(4):1548–1551.

[11] Morton C, Yarusevych S. Vortex shedding in the wake of a step cylinder. *Phys. Fluids* 2010; **22**(8):083 602.

[12] Morton C, Yarusevych S. Vortex dynamics in the turbulent wake of a single step cylinder. *ASME J. Fluids Eng.* 2014; **136**(031204).

[13] McClure J, Morton C, Yarusevych S. Flow development and structural loading on dual step cylinders in laminar shedding regime. *Phys. Fluids* 2015; **27**(6):063 602.

[14] Tian C, Jiang F, Pettersen B, Andersson HI. Numerical investigation of flow around a step cylinder. *Proceedings of 9th National Conference on Computational Mechanics (CIMNE), Trondheim, Norway, May 11-12*, 2017; 369–384.

[15] Tian C, Jiang F, Pettersen B, Andersson HI. Antisymmetric vortex interactions in the wake behind a step cylinder. *Phys. Fluids* 2017; **29**(10):101 704.

[16] Tian C, Jiang F, Pettersen B, HI Andersson. The long periodicity of vortex dislocations in the wake behind a step cylinder. *Proceedings of 10th National Conference on Computational Mechanics (CIMNE), Trondheim, Norway, June 3-4*, 2019; 81–99.

[17] Tian C, Jiang F, Pettersen B, Andersson HI. Vortex dislocation mechanisms in the near wake of a step cylinder. *J. Fluid Mech.* 2020; **891**.

[18] Ji C, Yang X, Yu Y, Cui Y, Srinil N. Numerical simulations of flows around a dual step cylinder with different diameter ratios at low Reynolds number. *Eur. J. Mech. B/Fluids* 2020; **79**:332–344.

[19] Jeong J, Hussain F. On the identification of a vortex. *J. Fluid Mech.* 1995; **285**:69–94.

[20] Manhart M. A zonal grid algorithm for DNS of turbulent boundary layers. *Computers & Fluids* 2004; **33**(3):435–461.

[21] Williamson JH. Low-storage Runge-Kutta schemes. *J. Comput. Phys.* 1980; **35**:48–56.

[22] Stone HL. Iterative solution of implicit approximations of multidimensional partial differential equations. *SIAM J. Numer. Anal.* 1968; **5**:530–558.

[23] Jiang F, Andersson HI, Gallardo JP, Okulov L. On the peculiar structure of a helical wake vortex behind an inclined prolate spheroid. *J. Fluid Mech.* 2016; **801**:1–12.

[24] Peller N, Duc AL, Tremblay F, Manhart M. High-order stable interpolations for immersed boundary methods. *Int. J. Numer. Meth. Fl.* 2006; **52**:1175–1193.

[25] Norberg C. Fluctuating lift on a circular cylinder: review and new measurements. *J. Fluid Struct.* 2003; **17**(1):57–96.

[26] Williamson CHK, Brown GL. A series in $1/\sqrt{Re}$ to represent the Strouhal–Reynolds number relationship of the cylinder wake. *J. Fluid Struct.* 1998; **12**(8):1073–1085.

[27] Zdravkovich MM. *Flow around circular cylinders: Volume 1: Fundamentals.* Oxford university press, 1997.

[28] Yagita M, Kojima Y, Matsuzaki K. On vortex shedding from circular cylinder with step. *Bulletin of JSME* 1984; **27**(225):426–431.

# Chapter 10

# Article 6: Diameter ratio effects in the wake flow of single step cylinders

Cai Tian[1], Fengjian Jiang[2], Bjørnar Pettersen[1], Helge I. Andersson[3]

## Abstract

The vortex system around the step surface of a step cylinder with diameter ratio $D/d = 2$ at Reynolds number ($Re_D$) 3900 was investigated by directly solving the three-dimensional Navier-Stokes equations. Formation mechanisms and vortex dynamics of the complex vortex system were studied by performing a detailed investigation of both the time-averaged and instantaneous flow fields. For the time-averaged flow, including the known *junction* and *edge vortices*, in total, four horseshoe vortices were observed to form above the step surface in front of the upper small cylinder. The crossflow width of four horseshoe vortices varies differently as they convect downstream. Moreover, we captured a pair of *base vortices* and a back-side horizontal vortex in the rear part of the step surface behind the small cylinder. For the instantaneous flow, hairpin vortices were found to form

[1]Department of Marine Technology, Norwegian University of Science and Technology, No-7491 Trondheim, Norway
[2]SINTEF Ocean, NO-7052 Trondheim, Norway
[3]Department of Energy and Process Engineering, Norwegian University of Science and Technology, No-7491 Trondheim, Norway

between the legs of two counter-rotating horseshoe vortices located on the same side of the step cylinder. Furthermore, in the small step cylinder wake, Kelvin-Helmholtz vortices were observed to shed at an unexpectedly high shedding frequency.

## 10.1    Introduction

The flow around a uniform circular cylinder has been a popular research topic for several decades because of its simple geometry and vast flow phenomena in its wakes. As the Reynolds number $Re_D = UD/\nu$ varies ($D$ represents the diameter of the circular cylinder, $U$ and $\nu$ are the free-stream velocity and the kinematic viscosity, respectively), the cylinder wake flow exhibits distinctly different behaviors[1, 2]. When $Re_D$ is less than 5, there is no flow separation around the cylinder. As $Re_D$ increases to the range $5 < Re_D < 40$, the flow separates on the cylinder wall to form a fixed pair of vortices behind the cylinder, and there is no vortex shedding. For $40 < Re_D < 180$, periodic two-dimensional vortex shedding occurs. When $Re_D$ exceeds 180, the wake becomes three-dimensional. Williamson [1] reported the well-known mode A and mode B at $Re_D = 184 - 194$ and $Re_D = 200 - 250$, respectively. When the Reynolds number becomes larger than $Re_D \approx 300$, the cylinder wake flow becomes completely turbulent. While the boundary layer over the cylinder surface stays laminar in a wide Reynolds number regime $300 < Re_D < 2 \times 10^5$, which is known as the sub-critical flow regime[2]. In this regime, the particular Reynolds number 3900 is a benchmark, at which there are many accurate numerical simulations [3, 4, 5, 6] and experimental studies [7, 8].

Besides the circular cylinder, due to the extensive applications in marine engineering, e.g., the underwater hull of SPAR-buoy floating offshore wind turbines [9] and the steel lazy wave risers [10, 11], the flow around the step cylinder illustrated in Fig. 10.1(a) has also attracted attention in the recent years.

In 1992, Lewis and Gharib[13] experimentally investigated the wake of a single step cylinder with $1 < D/d < 2$ at Reynolds number $Re_D = UD/\nu$ in the range $35 < Re_D < 200$. They identified three vortex interaction modes, namely *direct mode* when $D/d < 1.25$, *indirect mode* when $D/d > 1.55$, and *transition mode* when $1.25 < D/d < 1.55$. In *direct mode*, vortices shed from the small cylinder directly interact with those from the large cylinder in a narrow region. The wake is dominated by two frequencies $f_S$ and $f_L$ corresponding to shedding frequencies of the spanwise vortex structures behind the small and large cylinder, respectively. In the *indirect mode*, one
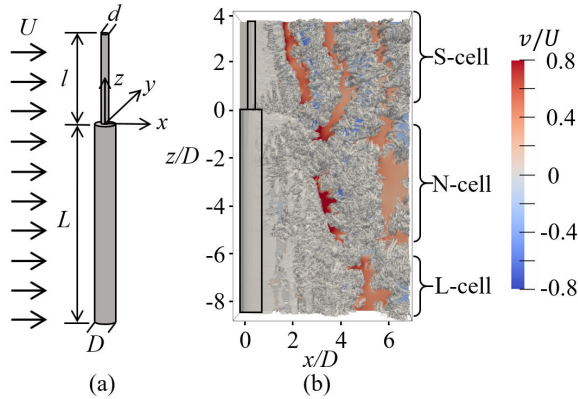
Figure 10.1: (a) A sketch of the step cylinder geometry. Diameter of the small and large cylinders are d and D, respectively. l and L denote the length of the small and large cylinders, respectively. The origin locates at the center of the interface between the small and large cylinders. The uniform incoming flow U is in the positive x-direction. The three directions are referred to as streamwise (x-direction), crossflow (y-direction) and spanwise (z-direction). (b) Perspective view of the instantaneous wake behind a single step cylinder with $D/d = 2$ at $Re_D = 3900$, taken at an arbitrary moment with the flow fully developed. The wake structures are shown by the isosurfaces of $\lambda_2 = -2$ (Ref. [12]) from our simulation. To ease the observation, color contours of crossflow velocity $v/U$ are plotted in the (x, z)-plane at $y/D = 0$.

more frequency $f_3$ (which is also referred to as $f_N$ by Dunn and Tavoularis [14]) was identified in a so-called modulation zone, in which no direct inter-action was found between vortices with $f_S$ and $f_L$. Dunn and Tavoularis [14] validated the *indirect mode* through experimental investigations in the wake of a step cylinder with $D/d \approx 2$ at $63 < Re_D < 1100$. Based on the three dominating frequency components behind the step cylinder, they identified three types of spanwise vortex cells: (1) S-cell vortex with the highest shedding frequency $f_S$ behind the small cylinder, (2) L-cell vortex shed from the large cylinder with shedding frequency $f_L$, and (3) N-cell vor-tex with the lowest shedding frequency $f_N$ located between the S- and L-cell regions. An illustration of these three vortex cells are shown in Fig. 10.1(b). According to Refs. [15, 16], the average length of the N-cell vortex was found to decrease with increasing $Re_D$ or decreasing $D/d$. Due to the different shedding frequencies of S-, N- and L-cell vortices, complex vortex interac-tions and dislocations occurring between these three main vortex cells were observed and analysed in Refs. [16, 17, 18, 19, 20]. Similar spanwise vor-

tex cells and the vortex interactions between them were also observed and investigated in the dual step cylinder wakes [21, 22, 23].

In addition to the three main spanwise vortex structures, the streamwise vortex system around the step surface has also been investigated in several previous studies[14, 24, 25]. In an experimental study of the flow around a single step cylinder with $D/d = 2$ at $Re_D = 1100$, Dunn and Tavoularis[14] identified two kinds of streamwise vortices: a pair of *edge vortices* and a *junction vortex*. Edge vortices form around the leading edge of the step surface, while a *junction vortex* originates upstream of where the small cylinder interacts with the step. On the same side ($+Y$ or $-Y$ side) of the step cylinder, these two types of vortices rotate in opposite directions. Morton et al.[24] verified the existence of the *junction* and *edge vortices* in their numerical investigations at a slightly higher Reynolds number, $Re_D$=2000. Besides, McClure et al.[25] and Ji et al.[26, 27] reported the existence of a similar streamwise vortex system in flow around dual-step cylinders. McClure et al.[25] further concluded that the *junction vortex* primarily connects to the vortices shed from the large cylinder, while the *edge vortex* mainly connects to the small cylinder vortices. However, despite these well verified findings, there still exist more flow details needed to be thoroughly described and investigated. For example; how different types of streamwise vortices develop in the flow around the step cylinder, how these vortices interact with each other, and whether other types of streamwise vortices exist around the step surface when $Re_D$ increases.

Besides the step cylinder, the time-averaged streamwise vortex system has also been investigated in the wake of both surface-mounted finite circular and square cylinders. Sumner and Heseltine[28], Sumner et al.[29], and Zhang et al.[30] reported that a dipole type, a quadrupole type, or a six-vortices type appears depending on the aspect ratio and the Reynolds number of the surface-mounted cylinder. Moreover, near the free-end, Park and Lee [31], Krajnovic [32], and Hain et al. [33] observed a pair of streamwise tip vortices. By investigating the instantaneous and phase-averaged flow around surface-mounted cylinders, recent studies [34, 35] suggested that the tip vortices is primarily caused by the deformed main spanwise vortices that connect back to the free end.

As mentioned before, $Re_D = 3900$ is a benchmark for the flow past a uniform circular cylinder, where there are many accurate numerical and experimental studies. However, until now, no one has investigated flow around a step cylinder at such Reynolds number. As a pioneer, the present study investigates the flow around a single step cylinder with $D/d = 2$ at $Re_D = 3900$ by using direct numerical simulations (DNS). Our primary

objectives are to investigate the formation mechanisms, vortex dynamics, and interactions between the vortices around the step position. Therefore, we restrict our analysis and discussions to the flow regions close to the step surface. Sec. 10.2 introduces the flow problem and the numerical methodology. In Sec. 10.3, by analyzing the time-averaged flow, the vortex system around the step surface is described. In addition to the conventional *junction* and *edge vortices*, four other vortices are discussed. In Sec. 10.4, based on the instantaneous flow field, the formations of hair-pin vortices and Kelvin-Helmholtz vortices with an unexpectedly high shedding frequency are described.

## 10.2 Numerical simulations

### 10.2.1 Flow configuration

In the present study, we investigate the flow around a step cylinder as shown in Fig. 10.1(a). The uniform incoming flow $U$ is in the positive $x-$direction. The side and top-down views of the flow domain are illustrated in Fig. 10.2. The streamwise length and the crossflow width of the computational domain are $L_x$ and $L_y$. The inlet plane is located $L_{x1}$ upstream from the centre of the step cylinder, and the outlet plane is placed $L_{x2}$ downstream. In the crossflow direction, the step cylinder is located in the middle of the domain. The spanwise height of the domain is $L_z$, where the length of the small and large cylinders occupy $l$ and $L$, respectively. Detailed information of the flow domains used in the present study is summarized in Table 10.1. Boundary conditions are as follows:

- The inlet boundary: uniform velocity profile $u=U$, $v=0$, $w=0$;

- The outlet boundary: Neumann boundary condition for velocity components ($\partial u/\partial x = \partial v/\partial x = \partial w/\partial x = 0$) and constant zero pressure condition ($p=0$);

- The other four sides of the computational domain: free-slip boundary conditions (For the two vertical sides: $v = 0$, $\partial u/\partial y = \partial w/\partial y = 0$, For the two horizontal sides: $w = 0$, $\partial u/\partial z = \partial v/\partial z = 0$);

- The step cylinder surfaces: no-slip and impermeable wall.
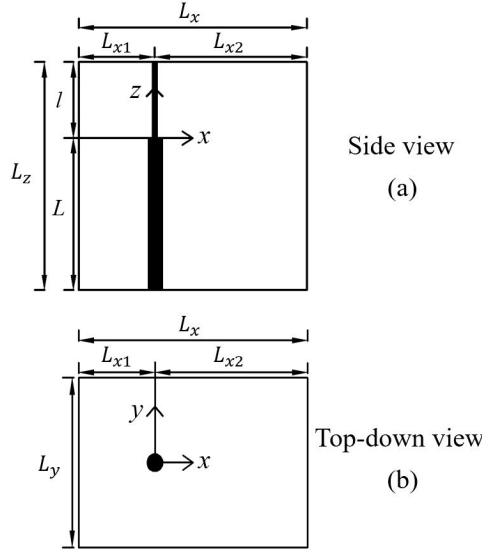
Figure 10.2: Computational domain, origin and coordinate system are illustrated from (a) side view and (b) top-down view.

### 10.2.2    Computational method

In the present DNS study, the governing equations contain a mass conservation equation (10.1) and a time-dependent full three-dimensional incompressible Navier-Stokes equation (10.2):

$$\boldsymbol{\nabla} \cdot \boldsymbol{u} = 0, \tag{10.1}$$

$$\frac{\partial \boldsymbol{u}}{\partial t} + (\boldsymbol{u} \cdot \boldsymbol{\nabla})\boldsymbol{u} = \nu \boldsymbol{\nabla}^2 \boldsymbol{u} - \frac{1}{\rho}\boldsymbol{\nabla} p, \tag{10.2}$$

where $\bigtriangledown$ is the Del operator, $\nu$ is the kinematic viscosity of the fluid, and $\rho$ is the constant fluid density. For all simulations, a thoroughly validated finite-volume-based numerical code MGLET [36, 37] is used to directly solve the governing equations (10.1 and 10.2) without introducing any turbulence model. In MGLET, Eq. 10.1 and Eq. 10.2 are first discretized on a 3-D staggered Cartesian grid. Then, by using the midpoint approximation, the discretized equations are integrated over the surfaces of the discrete volumes. This leads to a second-order accuracy in space. In time, the discretized equations are integrated with Williamson's third-order low-storage Runge-Kutta scheme [38]. A constant time step $\Delta t$ is used to ensure a CFL number smaller than 0.5. The pressure corrections are achieved by using Stone's implicit procedure (SIP) [39].

The solid surface of the step cylinder is handled by an immersed boundary method (IBM). We use an unstructured triangular mesh to represent the surface of the geometry, and transfer information to IBM to block grid cells bounded by this surface. Detailed description and validation of this IBM can be found in Peller et al. [40]. The computational domain is first divided into equal-sized cubic grid boxes, named the level-1 box. In each grid box, there are $N \times N \times N$ equal-sized cubic grid cells. For the region where complex flow phenomena appear, e.g., the regions close to the step cylinder and the region where vortices form, the grid boxes (the level-1 box) are equally divided into eight small cubic grid boxes, named the level-2 box. In every level-2 grid box, there are also $N \times N \times N$ grid cells. This means that the grid resolution in the level-2 box is two times finer than that in the level-1 box. This grid refinement-process goes on automatically until the finest grid level is reached. The grid structure in case Fine-B in the geometrical symmetry plane (the $(x, z)$-plane at $y/D=0$) is plotted in Fig. 10.3 to schematically illustrate the grid structure.
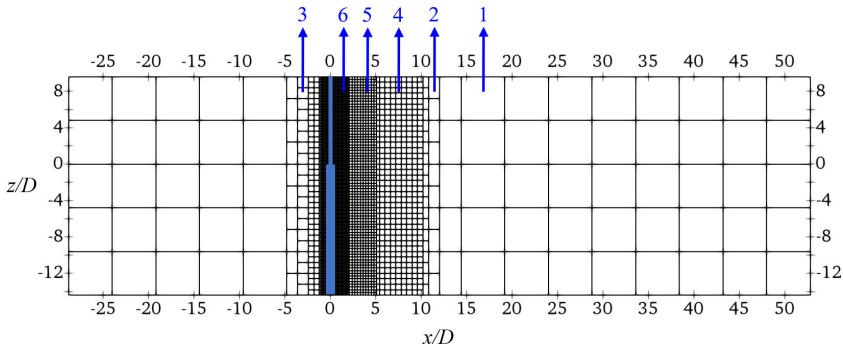


*Figure 10.3: An illustration of the multi-level grids in the $(x, z)$-plane at $y/D = 0$. Each square represents a slice of corresponding cubic Cartesian grid box that contains $N \times N \times N$ grid cells. Here, there are six levels of grid boxes as indicated by numbers. Owing to different minimum grid cell sizes, different cases studied in the present study have either five or six levels of grid boxes.*

Details of the mesh used in simulations are summarized in Table 10.1. Since all grid cells are cubic, the minimum grid cell size ($\Delta_c/D$) is the same in x, y, and z directions. The four cases with the different minimum grid cell sizes ($\Delta_c/D$), i.e., the Coarse, Medium, Fine-A and Very Fine cases, are set up for the grid study. In the geometry study, the mesh in the Fine-A case is also used with the cases Fine-B and Fine-C, in which the vertical lengths

Table 10.1: *Detailed mesh and domain information of all simulations in the present study. The case Coarse has five levels of grids, and the other cases all have six levels of grids. The cases Coarse, Medium, Fine-A, and Very Fine are used for the grid study. The cases, Fine-A, Fine-B, and Fine-C are used for the spanwise-length study. As shown in Fig. 10.3, the minimum grid cells $(\Delta_c/D)$ cover the region around the step cylinder.*

| Case | Min. Cell size $\Delta_c/D$ | Time step $\Delta t U/D$ | Domain Size $(L_x \times L_y \times L_z)/D$ | $l/D$ | $L/D$ | $L_{x1}$ | $L_{x2}$ | Number of grid cells ($\times 10^9$) |
|---|---|---|---|---|---|---|---|---|
| Coarse | 0.010 | 0.0025 | $81.60 \times 38.40 \times 14.40$ | 4.80 | 9.60 | 28.80 | 52.80 | 0.20 |
| Medium | 0.00625 | 0.0015 | $74.80 \times 40.80 \times 18.00$ | 6.00 | 12.00 | 27.20 | 47.60 | 0.84 |
| Fine-A | 0.005 | 0.0012 | $81.60 \times 38.40 \times 14.40$ | 4.80 | 9.60 | 28.80 | 52.80 | 1.21 |
| Very Fine | 0.004 | 0.0010 | $81.92 \times 40.96 \times 15.36$ | 5.12 | 10.24 | 30.72 | 51.20 | 2.67 |
| Fine-B | 0.005 | 0.0012 | $81.60 \times 38.40 \times 24.00$ | 9.60 | 14.40 | 28.80 | 52.80 | 2.02 |
| Fine-C | 0.005 | 0.0012 | $87.04 \times 43.52 \times 32.64$ | 10.88 | 21.76 | 32.64 | 54.40 | 2.71 |

of the small ($l$) and large cylinder ($L$) parts are varied.

### 10.2.3 Grid convergence, spanwise length convergence, and statistical convergence

The detailed discussions about grid convergence, spanwise length convergence, and statistical convergence are provided in Appendix 10.6. Based on the outcome of these considerations, we conclude that the mesh and configuration in the Fine-B case (see in Table 10.1) are sufficiently good for reliable DNS simulations in the present study. The statistical results obtained during the time period $tU/D = 350 - 850$ is sufficiently steady for the investigations in the present study. All simulations were performed on an SGI ALTIX ICE X SLES - 11sp3 cluster at NTNU. In the case Fine-B, there are six levels of grids containing in total $2.02 \times 10^9$ grid cells, with minimum grid cell size $\Delta_c/D = 0.005$. To run this case, we used 3360 processors (2 GB memory per processor) for at least 800 000 time steps. This single case consumed in total approximately 1.87 million CPU hours. Recently, the same code MGLET has been used for simulations of wake flow behind other cylindrical structures at the same Reynolds number 3900 in Refs. [5, 41, 42], where similar minimum grid cell size and CFL criteria were used.

## 10.3    Time-averaged flow around the step surface

Similar to the flow around a finite-length cylinder[28, 30, 35], the appearance of the time-averaged streamwise vortices is also a distinctive feature of the flow around the step surface of the step cylinder. In Fig. 10.4(a) By plotting the isosurfaces of time-averaged $\lambda_2$=-9, a four horseshoe vortex system is identified in Fig. 10.4(a), where H1, H2, H3, and H4 are clear. Besides the conventional *junction vortex* (H1) and *edge vortex* (H3) reported in Refs. [14, 24, 25], two new-observed vortices (H2 and H4) are identified. Fig. 10.5(a) illustrates the evolution of these horseshoe vortices by projecting streamlines on several planes. To ease the observation, vortex cores (red lines in Fig. 10.5(a) and (b)) are calculated by using Tecplot post-processing software, which uses algorithms based on techniques outlined by Ref. [44]. Additional information about the flow and vortices is shown in Fig. 10.5(b), where the vortex core lines and the limiting streamlines are projected on the step surface. Moreover, the time-averaged streamlines in the symmetry plane ($y/D = 0$) are plotted in Fig. 10.6(a) and (b). Based on Fig. 10.5 and Fig. 10.6(a), one can see that the main horseshoe vortex H1 is caused by both the leading edge separation and the impingement of the flow at the upstream surface of the step cylinder. When the flow approaches the step cylinder, an upward flow along the large cylinder is driven by the pressure difference between the stagnation pressure on the large cylinder and the pressure above the step surface at the same streamwise position. As the upward flow reaches the leading edge of the large cylinder, it separates and deflects to the incoming flow direction. After imping the upstream surface of the small cylinder in the symmetry plane at the attachment saddle point $A_1$ (the blue dot at $z/D$=0.26) in Fig. 10.6(a), a part of the flow is directed upward and some move downward. The majority of the downward flow attaches to the step surface at the attachment saddle point $A_2$ (the green dot at $x/D$=-0.28), and recirculates into the main horseshoe vortex H1. The other downward flow separates along the small cylinder wall at the separation saddle point $S_1$ (the red triangle at $z/D$=0.03) and induces the formation of vortex H2. The formation of vortex H3 is caused by the separation of the backward flow beneath the vortex H1 on its way back to the leading edge of the large cylinder at the separation point $S_2$ (the red dot at $x/D$=-0.42). The corresponding local separation line is marked by the green dashed curve in Fig. 10.5(b). The neighboring H1 and H3 vortices are counter-rotating. Due to topological reasons, the vortex H4 appears upstream of H3 and rotates in the same direction as H1. As shown in Fig. 10.6(a), without formation of H4, the flow induced by the counter-
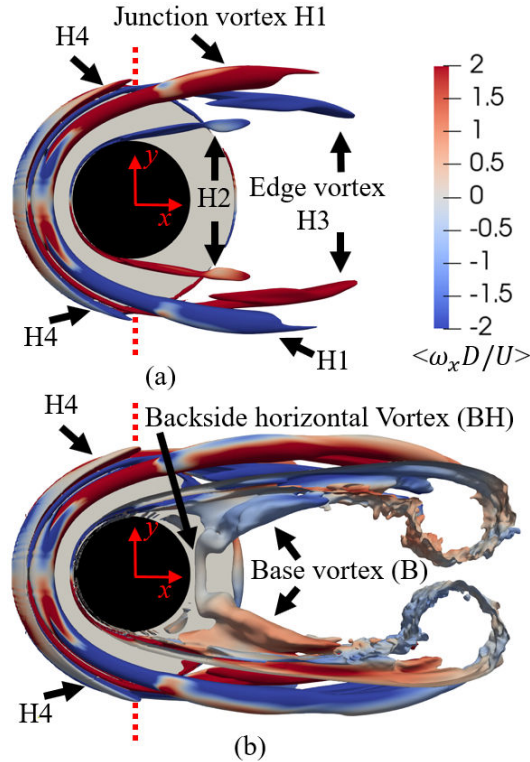
Figure 10.4: (a) The time-averaged vortex structures around the step surface are illustrated by the isosurface of the time-averaged $\lambda_2 = -9$ at the top-down viewpoints coloured by the time-averaged streamwise vorticity $\omega_x$ ($\omega_x = \partial w/\partial y - \partial v/\partial z$). (b) Same as (a) but $\lambda_2 = -0.2$. In (a) and (b), the main vortices around the step surface are indicated. The red dotted lines mark the position $x/D = 0$. (Note: The vortex structures in the present paper were checked by plotting both the isosurfaces of $\lambda_2$ (Ref.[12]) and Q (Ref.[43]). No obvious difference was observed. To ease the presentation and discussion, only the isosurface of $\lambda_2$ is used.)

clockwise rotating vortex H3 would conflict with the incoming flow. Between the counter-rotating vortices H3 and H4, a reattachment saddle point $A_3$ is observed, as shown by the green triangle at $x/D = -0.46$ in Fig. 10.6(a). In Fig. 10.5(c) and (d), the horseshoe vortices H1-H4 are illustrated by three-dimensional streamlines in different colors.

After these four horseshoe vortices (H1, H2, H3 and H4) form in front of the step cylinder, they wrap around the small cylinder and advect downstream. Based on Fig. 10.5(a) and Fig. 10.6(a), one can see that the con-
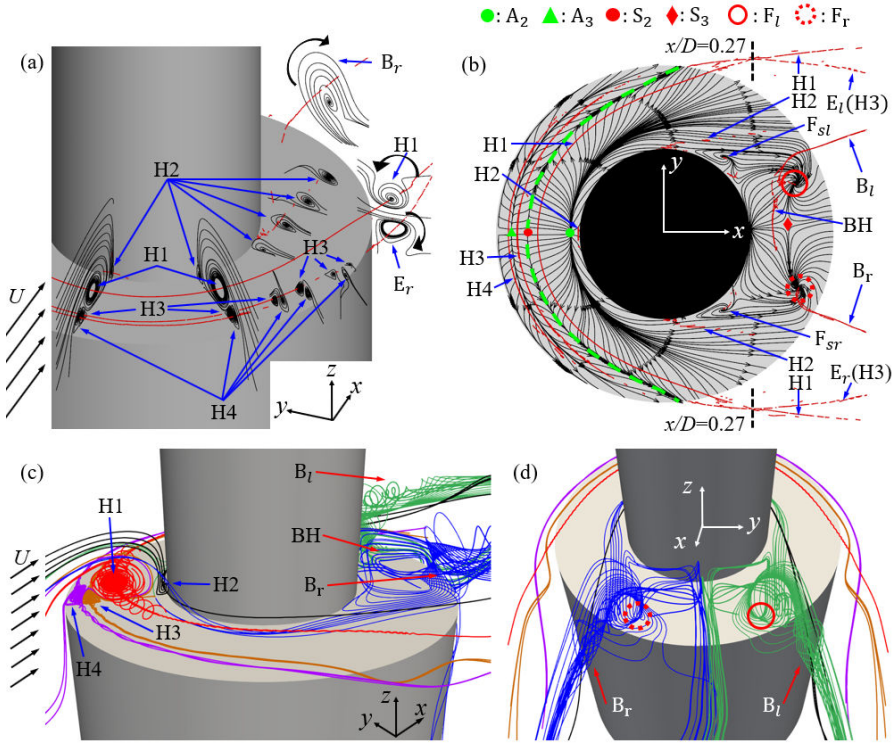
Figure 10.5: (a) Time-averaged streamlines projected on several planes close to the step surface. The main vortex components are indicated. (b) Time-averaged streamlines projected on the step surface. The attachment saddle point $A_2$, the reattachment saddle point $A_3$, the separation saddle point $S_2$, a backside separation saddle point $S_3$, and two focal points $F_l$ and $F_r$ are marked by the green dot, green triangle, red dot, red diamond, red circle and red dotted circle, respectively. The critical point for H1 and H3 is illustrated by two dashed black lines at $x/D = 0.27$. The local separation line is illustrated by a green dashed line in (b). In (a) and (b), the vortex core lines are plotted as red curves. (c) Three-dimensional flow evolution pattern with H1 in red, H2 in black, H3 in brown, H4 in purple, $B_r$ in blue, and $B_l$ in green. (d) Same as (c) but view from behind.

ventional *edge vortex* [14, 24] ($E_r$) rotates in the same direction as H3. Furthermore, the time-averaged isosurface of $\lambda_2$ in Fig. 10.4(a) and the instantaneous isosurface of $\lambda_2$ in Fig. 10.9(b) clearly show that as the horseshoe vortex H3 forms and wraps to the downstream, this vortex takes the role as the conventional *edge vortex*. However, this formation mechanism of
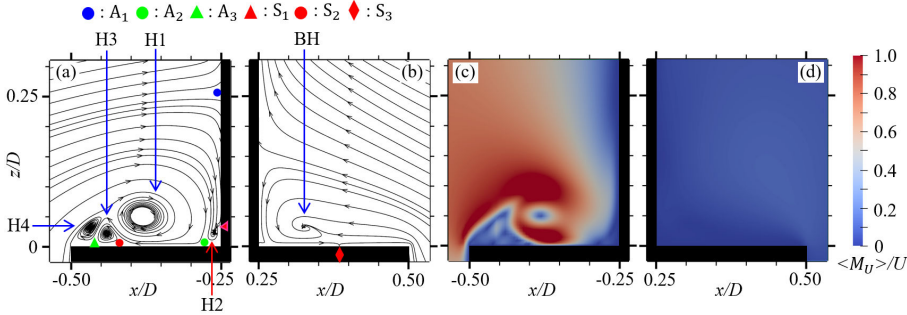
*Figure 10.6: (a) Time-averaged streamlines in a (x, z)-plane at $y/D = 0$
in the fore part of the step cylinder, the four horseshoe vortices (H1, H2,
H3, and H4) are indicated. The same markers used in Fig. 10.5(a) are used
here: the attachment saddle point $A_2$, the reattachment saddle point $A_3$, the
separation saddle point $S_2$, a backside separation saddle point $S_3$ are marked
by the green dot, green triangle, red dot, and red diamond, respectively.
Moreover, an attachment saddle point $A_1$ and a separation saddle point $S_1$
are marked by a blue dot and red triangle, respectively. (b) Same as (a) but
in the rear part of the step cylinder, the backside horizontal vortex (BH)
is marked. (c) and (d) show the corresponding time-averaged magnitude of
velocity $< M_U > /U$ contours in (a) and (b), respectively.*

the *edge vortex* (H3) is different from that reported by Dunn and Tavoularis
[14]. They suggested that when the incoming flow is blocked by the small
cylinder and pushed sideways by the rotating *junction vortex*, it spills over
the edges of the step surface and rolls up into the *edge vortex*. However,
Fig. 10.4 and 10.5 in the present study clearly show that the *edge vortex* is
a horseshoe vortex caused by the local separation of the backward flow be-
neath the *junction vortex* H1. Indeed, both the junction and *edge vortex* are
close to each other and the step surface, making it difficult to isolate them
and investigate their formation mechanisms experimentally. Different from
H1, H2 and H3 that extend relatively far into the wake flow ($x/D >$0.5), H4
ends at $x/D \approx 0$. As shown in Fig. 10.4(a) and (b), when $\lambda_2$ changes from
-9 to -0.2, H1, H2 and H3 extend further downstream and merge into mean
recirculation wakes. However, H4 still ends around $x/D = 0$, as marked by
the red dashed lines in Fig. 10.4(b). Further discussions about how H4 ends
will be provided in Sec. 10.4.

   Another obvious feature is the different developments of H1 and H3.
Fig. 10.5(b) clearly shows that for $x/D > 0$ the width of H1 gradually
increases as moving to the downstream, while the width of H3 gradually

decreases. The width here is referred to the crossflow distance between the legs of the horseshoe vortex. Due to the different development tendencies, we define a critical position $x/D = 0.27$ for H1 and H3 as marked by the black dashed lines in Fig. 10.5(b). Upstream of it, the width of H3 is larger than that of H1. Downstream of it, the scenario is opposite. We find that it is the fact that H1 and H3 locate in different spanwise regions that causes their qualitatively different spatial evolution. As shown in Fig. 10.5(a), Fig. 10.6(a), and Fig. 10.7(a), when H1 and H3 wrap around the small cylinder and extend to $x/D = 0.1$, H1 is still located above the step surface ($z/D > 0$), while H3 already extends outside and below the step surface. In Fig. 10.8, in comparison, the time-averaged streamlines behind the small and large cylinder are plotted in the $(x, y)$-planes at $z/D = 0.1$ and $z/D = -0.05$. The vortex core lines of H1, H2, and H3 are also projected in these planes. One can see that around the small cylinder, at $0 < x/D < 0.75$, the incoming flow has an outward flow direction. The width of the recirculation region gradually increases. On the contrary, behind the large cylinder part, the incoming flow has an inward flow direction at $0 < x/D < 0.75$. According to these different flow directions, from $x/D = 0.1$ to $x/D = 0.7$, the width of H1 increases from $0.98D$ in Fig. 10.7(a) to $1.15D$ Fig. 10.7(b), while the width of H3 decreases from $1.00D$ to $0.90D$. Moreover, due to the same reason, the width of H2 also slightly increases as extends downstream above the step surface, as shown in Fig. 10.5(b) and Fig. 10.6(a). At spanwise position far away from the step surface, due to the diameter ratio, the wake width behind the small cylinder is smaller than that behind the large cylinder. Close to the step surface, however, for the wakes behind the small and large cylinders to smoothly connect with each other, the flow behaves differently behind the small and the large cylinders. A similar four-horseshoe vortex system has also been reported in flow past a wall-mounted cylinder [45, 46, 47], but never been observed before in the flow around a step cylinder. Moreover, the newly observed opposite tendencies of crossflow widths of the horseshoe vortices are unique. The behavior of the crossflow width is normally the same for different vortex components of a horseshoe vortex system in the near wake of flow around wall-mounted cylinders.

In addition to these four characteristic horseshoe vortices, we capture a pair of counter-rotating *base vortices* ($B_r$ and $B_l$) generated from two focal points $F_r$ and $F_l$ on the step surface behind the small cylinder, as shown in Fig. 10.5(b). Between them, another backside horizontal vortex (BH) is identified. Although, similar focal points and vortex structures have been reported in the flow around a wall-mounted cylinder [48, 49, 50], it is sur-
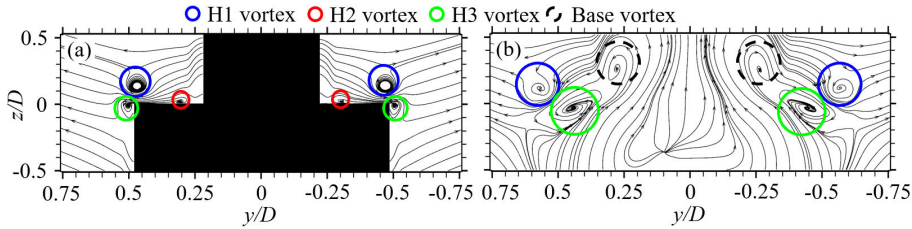
Figure 10.7: (a) Time-averaged streamlines in a (y, z)-plane at x/D=0.1.
(b) Same as (a) but at $x/D = 0.7$. The horseshoe vortex H1, H2, and H3
and the base vortex are marked. Note: the slight asymmetry in (b) is caused
by the marginal statistical time-sampling. The detailed discussion can be
found in Appendix 10.6.3.
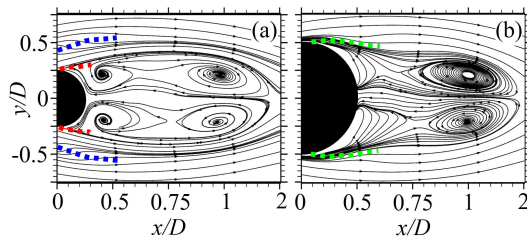


Figure 10.8: (a) Time-averaged streamlines in a (x, y)-plane at $z/D =
-0.1$. (b) Same as (a) but at $z/D = 0.05$. The vortex core lines correspond-
ing to H1, H2, and H3 are projected in (a) and (b) by the blue, red and
green dotted lines, respectively.

prising to observe the formation of these vortices in such a narrow step
surface with only $0.25D$ radial width. Fig. 10.5(b) and Fig. 10.6(b) show
that when the back-flow caused by the recirculations reaches the trailing
edge of the large cylinder in the (x, z)-plane at $y/D = 0$, vortex BH forms
in the same way as H1 dose, as explained in the previous paragraph. The
corresponding backside separation saddle point is marked by the red di-
amond in Fig. 10.5(b) and Fig. 10.6(b). Moreover, Fig. 10.6(c) and (d)
show that the strength of the back-flow is much weaker than that of the
incoming flow. Consequently, different from the incoming flow that induces
four vortices (H1, H2, H3, and H4) in the forepart of the step surface, the
weak back-flow only induces one backside horizontal vortex (BH) on the
rear part of the step surface. Additionally, when the recirculation flow be-
hind the small cylinder reaches the two focal points $F_r$ and $F_l$ on the step
surface, it spirals upwards and moves into the positive $x-$direction to form
a pair of base vortices ($B_r$ and $B_l$), as indicated in Fig. 10.5(c) and (d).

The corresponding swirls caused by these *base vortices* are seen in the $(y, z)$-plane at $x/D = 0.7$ in Fig. 10.7(b), as highlighted by the black dashed circles. Due to the modest strength of the recirculation flow, the backside horizontal vortex (BH) and the pair of *base vortices* ($B_r$ and $B_l$) are weaker compared to the horseshoe vortices. We can only observe four horseshoe vortices in the isosurface plot of $\lambda_2 = -9$ in Fig. 10.4(a). BH, $B_r$, and $B_l$ become visible only in the isosurface plot of $\lambda_2 = -0.2$. Moreover, the colors of the streamwise vorticity $\omega_x$ on the isosurfaces of $B_r$ and $B_l$ are obviously lighter than those of H1 and H3. These facts confirm the weak strength of BH, $B_r$, and $B_l$.

## 10.4    Instantaneous flow around the step surface

The instantaneous isosurface of $\lambda_2$ is presented in the step region in Fig. 10.9 and Fig. 10.10. The boundary layer is laminar in the fore part of the step cylinder, therefore the four horseshoe vortices seen in the time-averaged flow field are also clearly observed in the instantaneous flow field at $x/D < 0$. On the other hand, the vortex structures corresponding to BH, $B_r$, and $B_l$ are difficult to be identified in the instantaneous flow. These vortices are located in the turbulent wake of the small cylinder, which makes them indistinguishable in the small turbulent eddies. For $x/D > 0$, complex vortex interactions and small turbulent eddies appear. Two instantaneous features are remarkable: the formation of hairpin vortices between the horseshoe vortices, and the formation of secondary spanwise vortices close to the rear part of the small cylinder.

By plotting iso-surfaces of $\lambda_2 = -0.2$ at six consecutive time instants in Fig. 10.10, two stages are identified in the formation process of the hairpin vortices: the initial stage (from Fig. 10.10(a) to (c)) and the developed stage (in Fig. 10.10(d) and (f)) which are marked by the red and black colors, respectively. Unlike the hairpin vortex structures that form between two counter-rotating streamwise vortices located on different sides of the obstacle structures [51, 52], in the present study, the hairpin vortex forms between the legs of two counter-rotating vortices H1 and H3 on the same side of the step cylinder. Additionally, before the hairpin vortex forms, a special vortex bridge forms between two co-rotating vortices H1 and H4. This stage is referred to as the initial stage. From Fig. 10.10(a) to (c), as H4 extends from $x/D = 0$ to $x/D \approx 0.12$ a vortex bridge gradually forms between H1 and H4 as marked by a black circle. In Fig. 10.10(d), when the vortex bridge separates from H4 and reconnects to H3, a hairpin vortex forms between two counter-rotating vortices H1 and H3, as indicated by
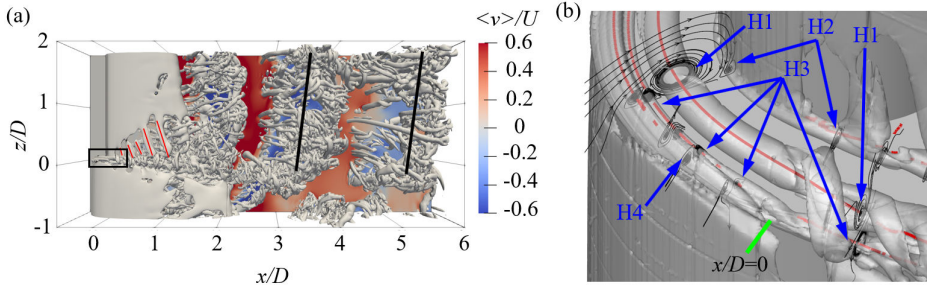
Figure 10.9: (a) Instantaneous isosurface of the $\lambda_2$=-2 together with color contours of crossflow velocity $v/U$ in the (x, y)-plane at $y/D = 0$. The Kelvin-Helmholtz vortex and the S-cell vortex are marked by the red and black lines, respectively. (b) A zoomed-in view of the step region (black rectangle) in (a). The streamwise position $x/D = 0$ is marked by a short green line.
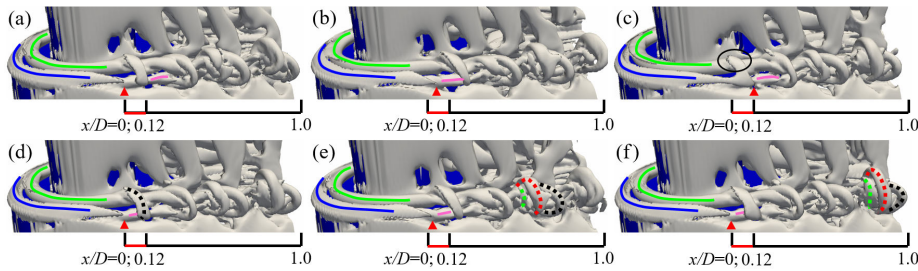


Figure 10.10: Consecutive instantaneous isosurfaces of $\lambda_2$=-0.2 showing developments of vortex structures around the step position in the $Re_D = 3900$ case. The vortices H1, H3, and H4 are marked by the green, pink and blue lines, respectively. (a) $tU/D$=860.052, (b) $tU/D$=860.172, (c) $tU/D$=860.292, (d) $tU/D$=860.364, (e) $tU/D$=861.060, (f) $tU/D$=861.300. The end position of H4 (the blue curve) is marked by the red triangle.

the black dotted curve. In parallel, H4 shrinks back to $x/D = 0$, which explains the fact that the time-averaged H4 ends at $x/D \approx 0$ in Fig. 10.4, as mentioned in Sec. 10.3. At the developed stage, from Fig. 10.10(d) to (e), just in front of the hairpin vortex marked by the black dashed curve, two more hairpin vortices form, as indicated by the red and green dashed curves. These three hairpin vortices nest together to form a hairpin vortex group. From Fig. 10.10(e) to (f), this vortex group convects downstream from $x/D \approx 0.7$ to $x/D \approx 1$. To clearly show the formation process of the

hairpin vortices, we upload an animation to the supplementary file, from which one can clearly see that, in every vortex group, two or three hairpin vortices form in every $0.3D/U$.
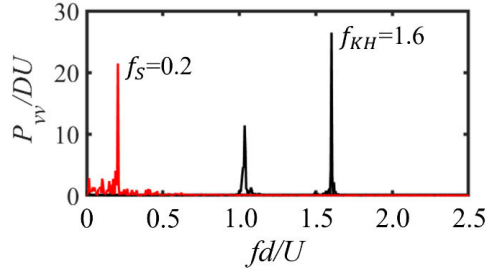


Figure 10.11: Crossflow velocity (v) spectra at positions $(x/D, y/D, z/D) = (0.53, 0.4, 0.2)$ and $(3, 0.6, 0.2)$ are plotted in black and red, respectively. The frequency components corresponding to $f_S$ and $f_{KH}$ are marked. Note that the frequency is nondimensionalized based on the small cylinder's diameter $(d)$. (The value of $f_{KH}$ can also be measured from the movie in the supplementary file.)
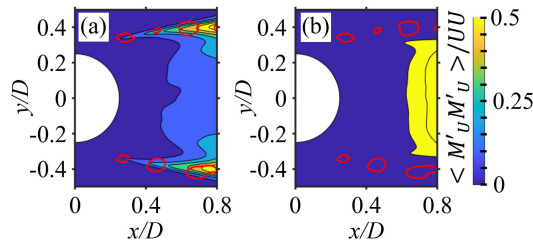


Figure 10.12: (a) Contours of time-averaged magnitude velocity fluctuation $< M'_U M'_U > /UU$ plots in a horizontal plane at $z/D=0.2$, together with instantaneous contours of $\lambda_2 = -9$ at $tU/D = 860.36$ plot in red color; (b) Same as (a) but at $z/D = 3$. The same instantaneous contours of $\lambda_2 = -9$ in (a) are directly projected in (b).

Another remarkable instantaneous phenomenon is the secondary spanwise vortices as highlighted by the red lines in Fig. 10.9(a). These vortices, similar to those caused by the Kelvin-Helmholtz (KH) instability, are formed before the main spanwise S-cell vortices (the black lines in Fig. 10.9(a)) shed from the small cylinder. A pair of corresponding spiral flows ($F_{sr}$ and $F_{sl}$) are clearly captured in the time-averaged streamlines on the step surface in

Fig. 10.5(b). The frequency of conventional KH vortices [53, 54] follows

$$f_{KH}/f_K = 0.0235 \times Re^{0.67} \tag{10.3}$$

, in which $f_{KH}$ and $f_K$ represent the shedding frequency of the KH vortex and the corresponding main Karman vortex, respectively. The main Karman vortex behind the small cylinder in the present study is referred to as $f_S$ in Fig. 10.11. The ratio between the KH and main Karman vortices in the present study (i.e., $f_{KH}/f_S$=1.6/0.2 $\approx$ 8) is two times higher than the empirical value from Eq. 10.3 (i.e., $0.0235 \times 1950^{0.67} \approx 4$ where $Re_d$ instead of $Re_D$ is used because the focused KH vortex appears behind the small cylinder). The conventional KH vortex is caused by the KH instability, that amplifies the convection of perturbations in the shear layer. According to the previous study by Robinson[55], in which flow along a solid wall was considered, the formation of the hairpin vortices was observed to help promote convection of velocity perturbations from the wall to the flow in the upper region. Fig. 10.12 shows that closer to the group of hairpin vortices the velocity fluctuation clearly becomes stronger in the region where KH vortices form. This implies that the KH vortex in the present study is caused by the combined effects of both the KH instability and the instability transported by the horseshoe vortex. This causes the unexpectedly high shedding frequency $f_{KH}$.

## 10.5    Conclusions

In the present study, we use DNS to investigate both the time-averaged and instantaneous flow fields around the step cylinder with $D/d = 2$ at $Re_D = 3900$. In general, our results show good agreement with previous studies [14, 24, 25, 26] with respect to the formation of the *junction* and *edge vortices* around the step surface of the step cylinder. Moreover, similar *base vortices* identified in the flow past a wall-mounted cylinder by Refs. [48, 49, 50] are also captured in the rear part of the step surface. Furthermore, our numerical results provide more complete and detailed information about the flow around the step surface.

The time-averaged iso-surfaces of $\lambda_2$ and time-averaged streamlines show that, due to the flow impingement, flow recirculation and flow separations on the junction surfaces between the root of the small cylinder and the step surface, four horseshoe vortices (H1, H2, H3, and H4) form above the step surface in front of the upper small cylinder. In addition to the conventional *junction vortex* (H1) and the *edge vortex* (H3), two additional horseshoe vortices H2 and H4 are clearly identified. The resulting four

horseshoe vortex system is therefore identified. Under the influence of the different flow behaviors in the wakes of the small and large cylinders, the H1, H2, and H3 vortices develop differently. When they reach $x/D > 0$ and extend downstream, the crossflow width of H1 and H2 continue to increase, however, the crossflow width of H3 decreases. Consequently, a critical point for H1 and H3 is defined. Moreover, in the rear part of the step surface ($x/D > 0$), we capture a pair of *base vortices* ($B_r$ and $B_l$) and a backside horizontal vortex (BH).

By detailed investigations in the instantaneous flow, we find that the four horseshoe vortices clearly exist in both the time-averaged and instantaneous flow field. In the forepart of the step surface ($x/D < 0$), the vortices H1, H2, H3, and H4 are quite stable and only slightly fluctuate in time. On the other hand, vortices $B_r$, $B_l$, and BH are difficult to be identified in the instantaneous flow due to their weak strength. As H4 extends to $x/D > 0$, a vortex bridge gradually forms between the legs of two co-rotating horseshoe vortices H1 and H4. After this vortex bridge separates from the end of H4 at $x/D \approx 0.12$, a hairpin vortex forms between the legs of two counter-rotating horseshoe vortices H1 and H3 located on the same side of the step cylinder. In the neighboring region upstream of this hairpin vortex, either one or two more hairpin vortices form before convecting to the wake region dominated by small turbulent eddies. Another remarkable phenomenon is
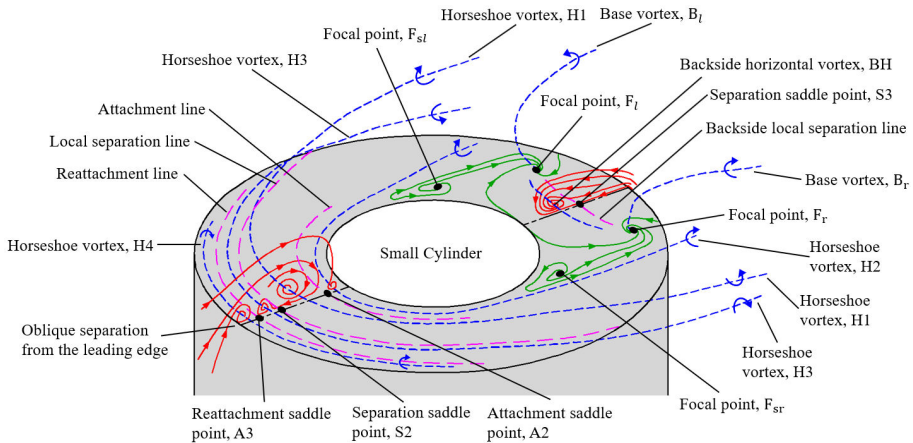


*Figure 10.13: Schematic of the flow field for the single step cylinder with $D/d = 2$ at $Re_D = 3900$ showing the main flow features. To ease observations, the surface of the small cylinder is omitted.*

the appearance of Kelvin-Helmholtz (KH) vortices with an unexpectedly high shedding frequency behind the small cylinder. Our results suggest

that their appearances are caused by the combined effects of both the KH instability and the instability transported by the horseshoe vortices.

Based on the discussions in the present paper, an overall schematic of the flow around the step surface of the step cylinder with $D/d = 2$ at $Re_D = 3900$ is illustrated in Fig. 10.13, where the main time-averaged vortex structures and flow features are identified. To ease observations, the geometry of the small cylinder is omitted.

## Supplementary Material

Supplementary movies are attached along with the submission.

## Data Availability Statement

The data that support the findings of this study are available from the corresponding author upon reasonable request.

## Acknowledgments

## 10.6    Appendix: Grid convergence, spanwise length convergence, and statistical convergence

The present study focuses on the flow around the step surface of the step cylinder. Therefore, in this section, we execute the convergence tests in the region close to the step surface, i.e., the S- and N-cell regions (see in Fig. 10.1(b)).

### 10.6.1    Grid convergence

Table 10.2 shows the Strouhal number ($St$) and the time-averaged drag coefficient ($\overline{C_D}$) obtained in the S- and N-cell regions. In these two regions, we capture two dominating frequencies $St_S$ and $St_N$, corresponding to the shedding frequencies of the main S- and N-cell vortices. The time-averaged

*Table 10.2: Strouhal numbers of the two dominating vortex cells (S-cell, $St_S = f_S D/U$, and N-cell, $St_N = f_N D/U$) are shown in the second and third columns. They are obtained by means of a discrete Fourier transform (DFT) of continuous velocity data along a vertical sampling line with density 0.01D parallel to the $z-$axis at position $(x/D, y/D)=(2.02, 0)$, over at least 300 time units $(D/U)$. In the last two columns, the time-averaged drag force coefficients are calculated by using Eq. 10.4. Subscript S stands for the small cylinder part 1< z/D <4, N stands for the large cylinder part in the N-cell region -4< z/D <-1.*

| Case | $St_S$ | $St_N$ | $\overline{C_{DS}}$ | $\overline{C_{DN}}$ |
|---|---|---|---|---|
| Coarse | 0.42 | 0.18 | 1.02 | 0.87 |
| Medium | 0.42 | 0.19 | 0.97 | 0.86 |
| Fine-A | 0.43 | 0.19 | 0.95 | 0.85 |
| Very Fine | 0.44 | 0.19 | 0.94 | 0.85 |

drag coefficient is normalized as

$$\overline{C_{Dj}} = \frac{\overline{F_{xj}}}{0.5\rho A_j U^2}, \quad j = S, N, \tag{10.4}$$

where the subscript $S$ represents the small cylinder part covered by the S-cell vortex at $1 < z/D < 4$, and $N$ represents the large cylinder part covered by the N-cell vortex at $-4 < z/D < -1$. $A_j$ is the projected areas of the different parts in the $(y, z)$-plane. One can easily calculate: $A_S/D^2 = 1.5$, and $A_N/D^2=3$. When the mesh is refined from the case Coarse to Very Fine, the data in Table 10.2 shows converging trends of all quantities listed. Moreover, in Fig. 10.14, we plot the time-averaged streamwise velocity $< u > /U$ and the time-averaged pressure coefficient $(< C_P >)$ along a vertical sampling line located at $(x/D, y/D)=(2.02, 0)$. $< C_P >$ is defined as

$$< C_P >= \frac{< P > -P_0}{0.5\rho U^2}, \tag{10.5}$$

where $< P >$ is the time-averaged pressure along the sampling line and $P_0$ is the pressure at the inlet boundary. The curves in Fig. 10.14 clearly show a converging tendency from the Coarse case to the Very Fine case. Especially in the region (-5< z/D <3) close to the step position $(z/D = 0)$, we barely see any difference between the Fine-A and Very Fine cases.
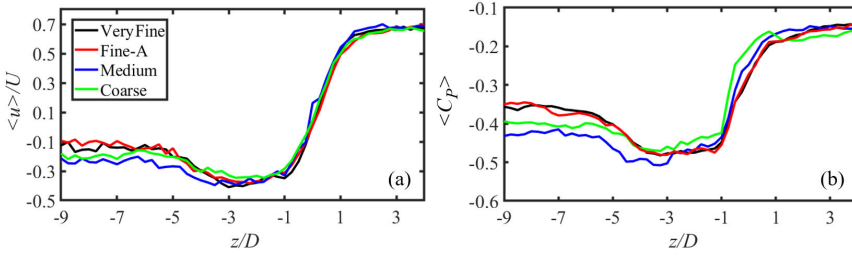
Figure 10.14: (a) Distribution of time-averaged streamwise velocity ($< u >$ /U) along a sampling line at (x/D, y/D)=(2.02, 0) in the Coarse, Medium, Fine-A, and Very Fine cases. (b) Same as (a) but for the time-averaged pressure coefficient ($< C_P > /U$).
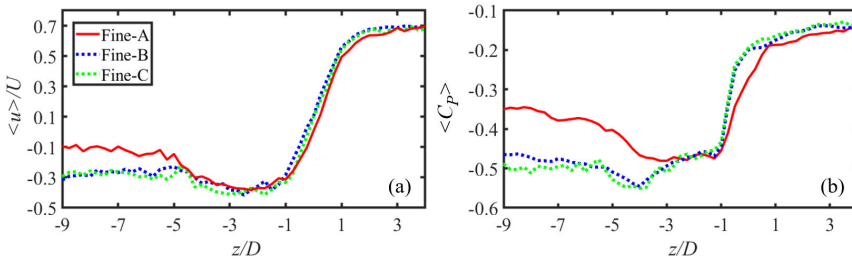


Figure 10.15: (a) Distribution of time-averaged streamwise velocity ($< u >$ /U) along a sampling line at (x/D, y/D)=(2.02, 0) in the Fine-A, Fine-B and Fine-C cases. (b) Same as (a) but for the time-averaged pressure coefficient ($< C_P > /U$).

### 10.6.2   Spanwise length convergence

Due to the large number of grid cells and the smaller time step, the computational cost of the Very Fine case is significantly higher than that of the Fine-A case. Therefore, in the spanwise length convergence test, we built Fine-B and Fine-C by using the same grid structures in Fine-A, and changed the lengths of both the small ($l$) and large cylinder ($L$) cylinders (see in Table 10.1).

Fig. 10.15 shows the distributions of $< u > /U$ and $< C_P >$ along a vertical sampling line at $(x/D, y/D)$=(2.02, 0) in the Fine-A, Fine-B and Fine-C cases. The results show that the free-slip wall boundary condition at the top and bottom of the domain have relatively strong influences on the results in the Fine-A case. Especially at $z/D = -9$ which is close to the bottom boundary ($z/D = -9.6$) in Fine-A, $< u > /U$ and $< C_P >$ in Fine-A are only one-third and half of those in Fine-B and Fine-C, respectively.
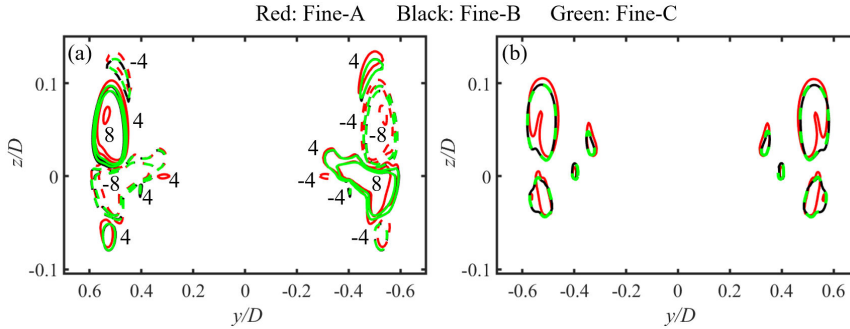
*Figure 10.16: (a) Contours of time-averaged streamwise vorticity $< \omega_x >$ $D/U = \pm 4$ and $\pm 8$ plotted in a (y, z)-plane at $x/D=0.3$. Solid and dashed lines represent positive and negative values. (b) Contours of time-averaged $\lambda_2 = -9$ (Ref. [12]) plotted in the same plane used in (a).*

On the other hand, the difference between the blue (Fine-B) and green (Fine-C) dotted curves is very small, especially in the region around the step position at $-5 < z/D < 3$. Furthermore, in Fig. 10.16, we plot the time-averaged streamwise vorticity $< \omega_x > D/U$ contours and the time-averaged $\lambda_2$ contours in a (y, z)-plane at $x/D = 0.3$, which is in the step area just behind the small cylinder. The results of Fine-A show obvious differences when comparing with the results of Fine-B and Fine-C. On the other hand, the difference between results of Fine-B (the black curves) and Fine-C (the green curves) is negligible. The overlap between the green and black curves proves that the spanwise length in Fine-B and Fine-C cases converge well in the flow field close to the step surface.

### 10.6.3 Statistical convergence

The discussions in Sec. 10.3 and Sec. 10.4 are based on both the instantaneous and time-averaged flows, therefore a careful examination of the statistical convergence is necessary. We first simulated case Fine-B for 350 time units $(D/U)$ to ensure that the flow is properly developed. Then the time-averaged streamlines on the step surface are calculated based on the velocity data with three different sampling times: $tU/D$ from 350 to 650 in Fig. 10.17(a), $tU/D$ from 350 to 850 in Fig. 10.17(b), and $tU/D$ from 350 to 950 in Fig. 10.17(c). Similar time-averaged flow fields are shown in the upstream part of the step surface (i.e., $x/D < 0$), where an attachment line, a reattachment line, and one separation line are indicated. The detailed formation mechanisms of these three special lines are described in

Sec. 10.3. At their intersection points with the $x-$axis, the corresponding attachment saddle point $A_2$, reattachment saddle point $A_3$, and separation saddle point $S_2$ are marked in Fig. 10.17. To describe the position of the attachment, reattachment, and separation lines, we define the position of their corresponding saddle points as their own position. Based on Fig. 10.17 and Table 10.3, one can easily see that the variation tendencies of these three lines are similar. Moreover, the position of the attachment and reattachment lines keep constant in all three subplots in Fig. 10.17. Only the location of the local separation line moves $0.02D$ upstream from Fig. 10.17(a) to Fig. 10.17(b), then remains unchanged from Fig. 10.17(b) to Fig. 10.17(c). Moreover, in Fig. 10.17(d), the time-averaged streamlines are plotted based on the velocity data within $tU/D$=650-950. The negligible difference between Fig.10.17(c) and (d) proves that no temporal feature appears after $tU/D$=650. Morton and Yarusevych [56] used the hydrogen bubble technique to illustrate the flow on the step surface of a dual step cylinder with $D/d = 2$ at $Re_D$=2100, as shown in Fig. 10.17(e). Although the configuration and the Reynolds number are not the same as in the present paper, both the attachment line and the local separation line are similar and clear in their study and ours.

The 2nd order statistical convergence is also checked. In Fig. 10.18, the contours of time-averaged magnitude velocity fluctuations $< M'_U M'_U > /UU$ are plotted in a horizontal plane at $z/D$=0.2, based on three different time periods. Based on the same time periods, Fig. 10.19 (a) and (b) show the time-averaged Reynolds shear stress $< u'v' > /UU$ at $(x/D, z/D)$=(1, 7) and $(x/D, z/D)$=(2, -14), respectively. Both Fig. 10.18 and 10.19 indicate that the differences in the 2nd order velocity fluctuations between the time periods $tU/D$=350-850 and $tU/D$=350-950 are negligible.

Table 10.3: Location of singular points for different sampling periods.

| Time period $(tU/D)$ | $A_2$ $(x/D, y/D)$ | $A_3$ $(x/D, y/D)$ | $S_2$ $(x/D, y/D)$ | $S_3$ $(x/D, y/D)$ |
|---|---|---|---|---|
| $350 - 650$ | (-0.40, 0) | (-0.46, 0) | (-0.28, 0) | (0.38, 0.05) |
| $350 - 850$ | (-0.42, 0) | (-0.46, 0) | (-0.28, 0) | (0.36, 0.03) |
| $350 - 950$ | (-0.42, 0) | (-0.46, 0) | (-0.28, 0) | (0.36, 0.02) |

Considering that the step cylinder configuration used in the present study is symmetric about the $x - z$ coordinate surface, under the uniform
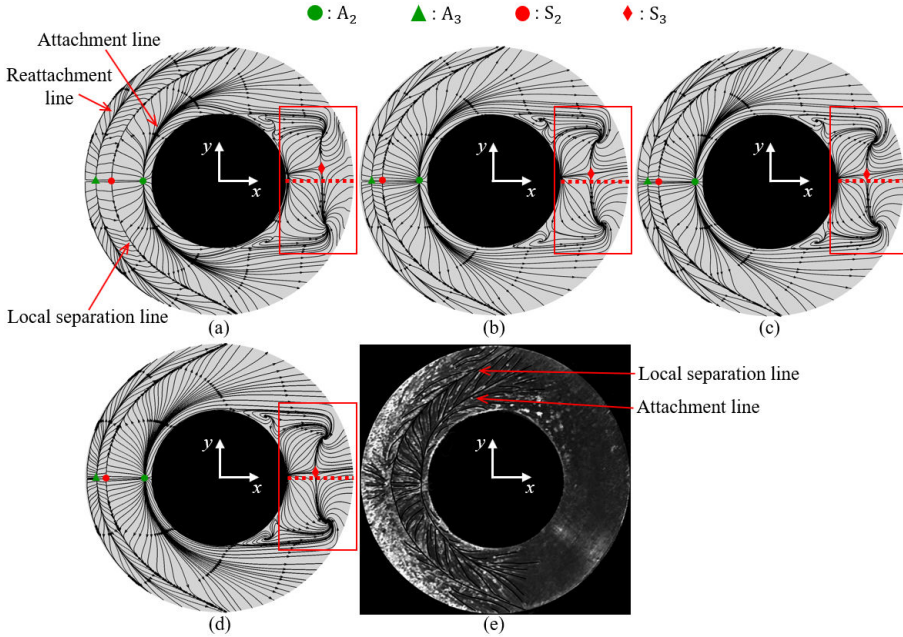
*Figure 10.17: (a) Time-averaged streamlines projected on the step surface based on the velocity data in the time range $tU/D = 350 - 650$. (b) Same as (a) but based on the velocity data within $tU/D = 350 - 850$. (c) Same as (a) but based on the velocity data within $tU/D = 350 - 950$. (d) Same as (a) but based on the velocity data within $tU/D = 650 - 950$. (e) Hydrogen bubble surface visualization on the step junction of a dual-step cylinder for $Re_D = 2,100$, $D/d = 2$ from Morton and Yarusevych [56]. The attachment saddle point $A_2$, the reattachment saddle point $A_3$, the separation saddle point $S_2$, and the backside separation saddle point $S_3$ are marked by the green dot, green triangle, red dot, and red diamond, respectively.*

incoming flow in the $x-$direction, the time-averaged wake flow is also expected to be symmetric about the $x-$axis. However, as highlighted by the red rectangle in Fig. 10.17, an unexpected asymmetry appears on the rear part of the step surface at $x/D > 0$, where a separation saddle point is marked by a red diamond. The crossflow distance between the red diamond and the center red dotted line ($y/D = 0$) can reflect the strength of the asymmetry. As shown in Fig. 10.17 and Table 10.3, the red diamond continuously moves closer to the center red dotted line ($y/D = 0$) as the simulation time increases, i.e.,the strength of the asymmetry in wake flow continues to decrease with increasing simulation time length. If the simula-
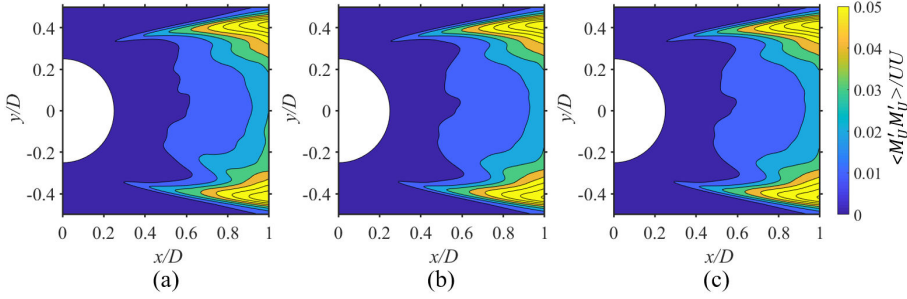
*Figure 10.18: (a) Contours of time-averaged magnitude velocity fluctuation*
$(< M_U' M_U' > /UU)$ *plots in a horizontal plane at* $z/D = 0.2$ *based on the velocity data* $tU/D = 350\text{-}650$. *(b) Same as (a) but based on the velocity data* $tU/D = 350\text{-}850$. *(c) Same as (a) but based on the velocity data* $tU/D=350\text{-}950$.

tion time further increases to sufficiently long, a symmetric wake flow can be expected, where the red diamond will locate exactly on the center red dotted line. However, we think it is too time-consuming and unnecessary to run the simulation even longer just to obtain a completely symmetric time-averaged wake. Because first the asymmetry in Fig. 10.17(b) and (c) are already weak, the red diamond only deflects $0.02-0.03D$ away from the center line. And more importantly, this slight asymmetry has no effect on our discussions in the present study.

In general, based on the results presented in this section, we conclude that the mesh and configuration in the Fine-B case (see in Table 10.1) are sufficiently good for reliable DNS simulations in the present study. The statistical results obtained during both time periods $tU/D = 350-850$ and $tU/D = 350-950$ are sufficiently converged for the investigations in the present study.
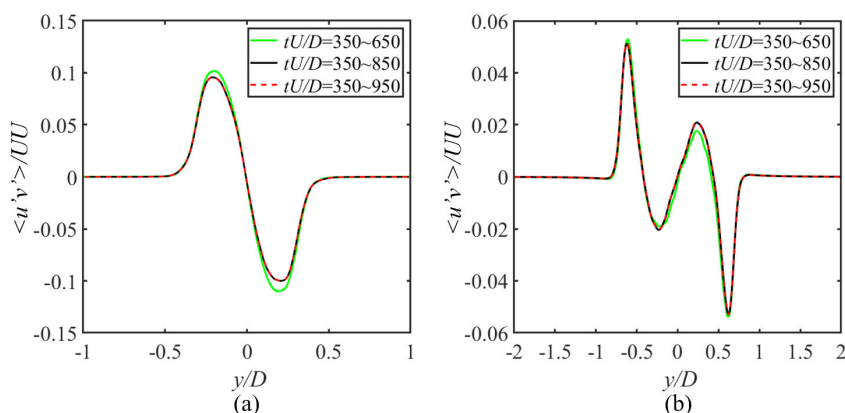
*Figure 10.19: (a) Co-variance of the velocity fluctuations ($< u'v' > /UU$) at $(x/D, z/D)=(1, 7)$. (b) Same as (a) but at $(x/D, z/D)=(2, -14)$.*

## References

[1] Williamson CHK. Vortex dynamics in the cylinder wake. *Annu. Rev. Fluid Mech.* 1996; **28**:477–539.

[2] Sumer B, Fredsøe J. *Hydrodynamics around cylindrical structures-Volume 26.* World Scientific: Singapore, 1997.

[3] Lehmkuhl O, Rodríguez I, Borrell R, Oliva A. Low-frequency unsteadiness in the vortex formation region of a circular cylinder. *Phys. Fluids* 2013; **25**(8):085 109.

[4] Rajani BN, Kandasamy A, Majumdar S. LES of flow past circular cylinder at Re= 3900. *J. Appl. Fluid Mech.* 2016; **9**(3).

[5] Strandenes H, Pettersen B, Andersson HI, Manhart M. Influence of spanwise no-slip boundary conditions on the flow around a cylinder. *Comput. Fluids* 2017; **156**:48–57.

[6] Tian G, Xiao Z. New insight on large-eddy simulation of flow past a circular cylinder at subcritical Reynolds number 3900. *AIP Adv.* 2020; **10**(8):085 321.

[7] Parnaudeau P, Carlier J, Heitz D, Lamballais E. Experimental and numerical studies of the flow over a circular cylinder at Reynolds number 3900. *Phys. Fluids* 2013; **20**(8):085 101.

[8] Molochnikov VM, Mikheev NI, Mikheev AN, Paereliy AA, Dushin NS, Dushina OA. SIV measurements of flow structure in the near wake of a circular cylinder at Re= 3900. *Fluid Dyn. Res.* 2019; **51**(5):055 505.

[9] Rodriguez S, Jaworski J. Strongly-coupled aeroelastic free-vortex wake framework for floating offshore wind turbine rotors. part 2: Application. *Renew. Energy* 2019; **149**:1018–1032.

[10] Felisita A, Gudmestad OT, Karunakaran D, Martinsen LO. Review of steel lazy wave riser concepts for the north sea. *J. Offshore Mech. Arct. Eng.* 2017; **139**(1).

[11] Yin D, Lie H, Wu J. Structural and hydrodynamic aspects of steel lazy wave riser in deepwater. *J. Offshore Mech. Arct. Eng.* 2020; **142**(2).

[12] Jeong J, Hussain F. On the identification of a vortex. *J. Fluid Mech.* 1995; **285**:69–94.

[13] Lewis CG, Gharib M. An exploration of the wake three dimensionalities caused by a local discontinuity in cylinder diameter. *Phys. Fluids A: Fluid Dynamics* 1992; **4**(1):104–117.

[14] Dunn W, Tavoularis S. Experimental studies of vortices shed from cylinders with a step-change in diameter. *J. Fluid Mech.* 2006; **555**:409–437.

[15] Norberg C. An experimental study of the flow around cylinders joined with a step in diameter. *Proceedings of the 11th Australasian Fluid Mechanics Conference, Hobart, Australia*, vol. 1, 1992; 507–510.

[16] Tian C, Jiang F, Pettersen B, Andersson HI. Diameter ratio effects in the wake flow of single step cylinders. *Phys. Fluids* 2020; **32**(9):093 603.

[17] Morton C, Yarusevych S. Vortex shedding in the wake of a step cylinder. *Phys. Fluids* 2010; **22**(8):083 602.

[18] Tian C, Jiang F, Pettersen B, Andersson HI. Antisymmetric vortex interactions in the wake behind a step cylinder. *Phys. Fluids* 2017; **29**(10):101 704.

[19] Tian C, Jiang F, Pettersen B, HI Andersson. The long periodicity of vortex dislocations in the wake behind a step cylinder. *Proceedings of 10th National Conference on Computational Mechanics (CIMNE), Trondheim, Norway, June 3-4*, 2019; 81–99.

[20] Tian C, Jiang F, Pettersen B, Andersson HI. Vortex dislocation mechanisms in the near wake of a step cylinder. *J. Fluid Mech.* 2020; **891**.

[21] Morton C, Yarusevych S, Scarano F. A tomographic particle image velocimetry investigation of the flow development over dual step cylinders. *Phys. Fluids* 2016; **28**(2):025 104.

[22] Morton C, Yarusevych S. Vortex shedding from cylinders with two step discontinuities in diameter. *J. Fluid Mech.* 2020; **902**.

[23] Yan Y, Ji C, Srinil N. Three-dimensional flip-flopping flow around a pair of dual-stepped circular cylinders in a side-by-side arrangement. *Phys. Fluids* 2020; **32**(12):123 608.

[24] Morton C, Yarusevych S, Carvajal-Mariscal I. Study of flow over a step cylinder. *Appl. Mech. Mater.* 2009; **15**:9–14.

[25] McClure J, Morton C, Yarusevych S. Flow development and structural loading on dual step cylinders in laminar shedding regime. *Phys. Fluids* 2015; **27**(6):063 602.

[26] Ji C, Cui Y, Xu D, Yang X, Srinil N. Vortex-induced vibrations of dual-step cylinders with different diameter ratios in laminar flows. *Phys. Fluids* 2019; **31**(7):073 602.

[27] Ji C, Yang X, Yu Y, Cui Y, Srinil N. Numerical simulations of flows around a dual step cylinder with different diameter ratios at low Reynolds number. *Eur. J. Mech. B/Fluids* 2020; **79**:332–344.

[28] Sumner D, Heseltine J. Tip vortex structure for a circular cylinder with a free end. *J. Wind. Eng. Ind. Aerodyn.* 2008; **29**(6-7):1185–1196.

[29] Sumner D, Heseltine J, Dansereau O. Wake structure of a finite circular cylinder of small aspect ratio. *Exp. Fluids* 2004; **37**(5):720–730.

[30] Zhang D, Cheng L, An H, Zhao M. Direct numerical simulation of flow around a surface-mounted finite square cylinder at low reynolds numbers. *Phys. Fluids* 2017; **29**(4):045 101.

[31] Part C, Lee S. Flow structure around a finite circular cylinder embedded in various atmospheric boundary layers. *Fluid Dyn. Res.* 2002; **30**(4):197–215.

[32] Krajnovic S. Flow around a tall finite cylinder explored by large eddy simulation. *J. Fluid Mech.* 2011; **676**:294–317.

[33] Hain R, Kähler C, Michaelis D. Tomographic and time resolved PIV measurements on a finite cylinder mounted on a flat plate. *Exp. Fluids* 2008; **45**(4):715–724.

[34] Sumner D. Flow above the free end of a surface-mounted finite-height circular cylinder: A review. *J. Fluids Struct.* 2013; **43**:41–63.

[35] Bourgeois JA, Sattari P, Martinuzzi RJ. Alternating half-loop shedding in the turbulent wake of a finite surface-mounted square cylinder with a thin boundary layer. *Phys. Fluids* 2011; **23**(9):095 101.

[36] Manhart M, Friedrich R. DNS of a turbulent boundary layer with separation. *Int. J. Heat Fluid Flow* 2002; **23**(5):572–581.

[37] Manhart M. A zonal grid algorithm for DNS of turbulent boundary layers. *Computers & Fluids* 2004; **33**(3):435–461.

[38] Williamson JH. Low-storage Runge-Kutta schemes. *J. Comput. Phys.* 1980; **35**:48–56.

[39] Stone HL. Iterative solution of implicit approximations of multidimensional partial differential equations. *SIAM J. Numer. Anal.* 1968; **5**:530–558.

[40] Peller N, Duc AL, Tremblay F, Manhart M. High-order stable interpolations for immersed boundary methods. *Int. J. Numer. Meth. Fl.* 2006; **52**:1175–1193.

[41] Gallardo JP, Andersson HI, Pettersen B. Turbulent wake behind a concave curved cylinder. *J. Fluid Mech.* 2014; **742**:192.

[42] Jiang F, Pettersen B, Andersson HI. Turbulent wake behind a concave curved cylinder. *J. Fluid Mech.* 2019; **878**:663–699.

[43] Hunt JCR, Wray A, Moin P. Eddies, stream, and convergence zones in turbulent flows. *Center for Turbulent Research Report CTR-S88* 1988; :193–208.

[44] Sujudi D, Haimes R. Identification of swirling flow in 3-d vector fields. *12th Computational Fluid Dynamics Conference, San Diego, CA, U.S.A, June 19-22*, 1995; 1715.

[45] Ishii J, Honami S. A three-dimensional turbulent detached flow with a horseshoe vortex. *J. Eng. Gas Turbines Power* 1986; :125–130.

[46] Simpson RL. Junction flows. *Annu. Rev. Fluid Mech.* 2001; **33**(1):415–443.

[47] Praisner TJ, Smith CR. The dynamics of the horseshoe vortex and associated endwall heat transfer—part ii: Time-mean results. *J. Turbomach.* 2005; **128**(4):755–762.

[48] Sau A, Hwang RR, Sheu TW, Yang WC. Interaction of trailing vortices in the wake of a wall-mounted rectangular cylinder. *Phys. Rev. E* 2003; **68**(5):056 303.

[49] Palau-Salvador G, Stoesser T, Fröhlich J, Kappler M, Rodi W. Large eddy simulations and experiments of flow around finite-height cylinders. *Flow Turbul. Combust.* 2010; **84**(2):239.

[50] Dousset V, Pothérat A. Formation mechanism of hairpin vortices in the wake of a truncated square cylinder in a duct. *J. Fluid Mech.* 2010; **653**:519–536.

[51] Gretta W, Smith C. The flow structure and statistics of a passive mixing tab. *J. Fluids Eng.* 1993; :255–263.

[52] Elavarasan R, Meng H. Flow visualization study of role of coherent structures in a tab wake. *Fluid Dyn. Res.* 2000; **27**(3):183.

[53] Wei T, Smith C. Secondary vortices in the wake of circular cylinders. *J. Fluid Mech.* 1986; **168**:513–533.

[54] McClure J, Pavan C, Yarusevych S. Secondary vortex dynamics in the cylinder wake during laminar-to-turbulent transition. *Phys. Rev. Fluids* 2019; **4**(12).

[55] Robinson S. Coherent motions in the turbulent boundary layer. *Annu. Rev. Fluid Mech.* 1991; **23**(1):601–639.

[56] Morton C, Yarusevych S. Three-dimensional flow and surface visualization using hydrogen bubble technique. *J. Vis.* 2015; :47–58.

# Chapter 11

# Supplementary file

## 11.1 Supplementary file 1

## Supplementary file 1: Detailed information about the N- and L-cell vortices for the D/d=2 case.

| | Vortices in the '-Y' side of the step cylinder | | | | | Vortices in the '+Y' side of the step cylinder | | | | | |
|---|---|---|---|---|---|---|---|---|---|---|---|
| N-cell cycle No. | L-cell Vortex No. | N-cell vortex No. | $\Phi_f$ | $\varphi_N$ | $\varphi_L$ | $\varphi_N$ | $\varphi_L$ | $\Phi_f$ | N-cell vortex No. | L-cell Vortex No. | N-cell cycle No. |
| | 2 | 2 | 1.15 | 9.055 | 7.905 | 6.05 | 5.095 | 0.955 | 1 | 1 | |
| | 4 | 4 | 2.06 | 15.585 | 13.525 | 12.27 | 10.71 | 1.56 | 3 | 3 | |
| | 6 | 6 | 3.06 | 22.2 | 19.14 | 18.73 | 16.345 | 2.385 | 5 | 5 | |
| | 8 | 8 | 4.2 | 28.95 | 24.75 | 25.68 | 21.955 | 3.725 | 7 | 7 | |
| | 10 | 10 | 5.32 | 35.7 | 30.38 | 32.315 | 27.53 | 4.785 | 9 | 9 | 1 |
| | 12 | | | | 35.985 | | 33.175 | | | 11 | |
| | 14 | 12 | 0.555 | 42.12 | 41.565 | 38.965 | 38.775 | 0.19 | 11 | 13 | |
| | 16 | 14 | 0.89 | 48.055 | 47.165 | 45.11 | 44.35 | 0.76 | 13 | 15 | |
| | 18 | 16 | 1.465 | 54.225 | 52.76 | 51.11 | 49.965 | 1.145 | 15 | 17 | |
| | 20 | 18 | 2.61 | 60.96 | 58.35 | 57.45 | 55.555 | 1.895 | 17 | 19 | |
| | 22 | 20 | 3.61 | 67.59 | 63.98 | 64.08 | 61.18 | 2.9 | 19 | 21 | |
| 2 | 24 | 22 | 4.77 | 74.355 | 69.585 | 70.965 | 66.775 | 4.19 | 21 | 23 | |
| | 26 | | | | 75.185 | 77.705 | 72.375 | 5.33 | 23 | 25 | |
| | 28 | 24 | 0.29 | 81.075 | 80.785 | | 77.975 | | | 27 | |
| | 30 | 26 | 0.81 | 87.19 | 86.38 | 84.155 | 83.585 | 0.57 | 25 | 29 | |
| | 32 | 28 | 1.2 | 93.17 | 91.97 | 90.15 | 89.175 | 0.975 | 27 | 31 | |
| | 34 | 30 | 1.84 | 99.435 | 97.595 | 96.275 | 94.795 | 1.48 | 29 | 33 | |
| | 36 | 32 | 3.06 | 106.28 | 103.22 | 102.805 | 100.4 | 2.405 | 31 | 35 | |
| | 38 | 34 | 4.12 | 112.96 | 108.84 | 109.48 | 106.02 | 3.46 | 33 | 37 | |
| | 40 | 36 | 5.2 | 119.64 | 114.44 | 116.29 | 111.645 | 4.645 | 35 | 39 | 3 |
| | 42 | | | | 120.055 | | 117.26 | | | 41 | |
| | 44 | 38 | 0.525 | 126.19 | 125.665 | 122.95 | 122.865 | 0.085 | 37 | 43 | |
| | 46 | 40 | 0.89 | 132.155 | 131.265 | 129.185 | 128.46 | 0.725 | 39 | 45 | |
| | 48 | 42 | 1.43 | 138.29 | 136.86 | 135.13 | 134.06 | 1.07 | 41 | 47 | |
| | 50 | 44 | 2.21 | 144.685 | 142.475 | 141.525 | 139.67 | 1.855 | 43 | 49 | |
| | 52 | 46 | 3.47 | 151.575 | 148.105 | 148.185 | 145.305 | 2.88 | 45 | 51 | |
| 4 | 54 | 48 | 4.575 | 158.3 | 153.725 | 154.88 | 150.925 | 3.955 | 47 | 53 | |
| | 56 | | | | 159.335 | 161.675 | 156.525 | 5.15 | 49 | 55 | |
| | 58 | 50 | -0.015 | 164.92 | 164.935 | | 162.145 | | | 57 | |
| | 60 | 52 | 0.675 | 171.21 | 170.535 | 168.17 | 167.74 | 0.43 | 51 | 59 | |
| | 62 | 54 | 1.02 | 177.165 | 176.145 | 174.145 | 173.335 | 0.81 | 53 | 61 | |
| | 64 | 56 | 1.72 | 183.46 | 181.74 | 180.21 | 178.94 | 1.27 | 55 | 63 | |
| | 66 | 58 | 2.63 | 189.995 | 187.365 | 186.865 | 184.545 | 2.32 | 57 | 65 | |
| | 68 | 60 | 3.93 | 196.88 | 192.95 | 193.57 | 190.15 | 3.42 | 59 | 67 | |
| | 70 | 62 | 5.095 | 203.67 | 198.575 | 200.29 | 195.765 | 4.525 | 61 | 69 | 5 |
| | 72 | | | | 204.175 | | 201.385 | | | 71 | |
| | 74 | 64 | 0.41 | 210.19 | 209.78 | 207.05 | 206.985 | 0.065 | 63 | 73 | |
| | 76 | 66 | 0.88 | 216.255 | 215.375 | 213.305 | 212.58 | 0.725 | 65 | 75 | |
| | 78 | 68 | 1.32 | 222.3 | 220.98 | 219.23 | 218.18 | 1.05 | 67 | 77 | |
| | 80 | 70 | 2.215 | 228.8 | 226.585 | 225.435 | 223.78 | 1.655 | 69 | 79 | |
| | 82 | 72 | 3.23 | 235.43 | 232.2 | 232.175 | 229.38 | 2.795 | 71 | 81 | |
| 6 | 84 | 74 | 4.415 | 242.215 | 237.8 | 238.93 | 235 | 3.93 | 73 | 83 | |
| | 86 | | | | 243.42 | 245.6 | 240.63 | 4.97 | 75 | 85 | |
| | 88 | 76 | -0.08 | 248.935 | 249.015 | | 246.22 | | | 87 | |
| | 90 | 78 | 0.645 | 255.27 | 254.625 | 252.24 | 251.83 | 0.41 | 77 | 89 | |
| | 92 | 80 | 1.03 | 261.24 | 260.21 | 258.275 | 257.41 | 0.865 | 79 | 91 | |
| | 94 | 82 | 1.675 | 267.505 | 265.83 | 264.36 | 263.03 | 1.33 | 81 | 93 | |
| | 96 | 84 | 2.71 | 274.16 | 271.45 | 270.655 | 268.63 | 2.025 | 83 | 95 | |
| | 98 | 86 | 3.725 | 280.815 | 277.09 | 277.49 | 274.25 | 3.24 | 85 | 97 | |
| | 100 | 88 | 4.945 | 287.615 | 282.67 | 284.265 | 279.88 | 4.385 | 87 | 99 | 7 |
| | 102 | | | | 288.305 | | 285.495 | | | 101 | |
| | 104 | 90 | 0.33 | 294.235 | 293.905 | 290.875 | 291.09 | -0.215 | 89 | 103 | |
| | 106 | 92 | 0.735 | 300.25 | 299.515 | 297.325 | 296.7 | 0.625 | 91 | 105 | |
| | 108 | 94 | 1.16 | 306.28 | 305.12 | 303.255 | 302.325 | 0.93 | 93 | 107 | |
| | 110 | 96 | 2.03 | 312.775 | 310.745 | 309.45 | 307.925 | 1.525 | 95 | 109 | |
| | 112 | 98 | 3.165 | 319.53 | 316.365 | 315.945 | 313.545 | 2.4 | 97 | 111 | |
| | 114 | 100 | 4.21 | 326.205 | 321.995 | 322.77 | 319.17 | 3.6 | 99 | 113 | |
| | 116 | 102 | 5.46 | 333.015 | 327.555 | 329.595 | 324.765 | 4.83 | 101 | 115 | 8 |
| | 118 | | | | 333.155 | | 330.365 | | | 117 | |
| | 120 | 104 | 0.65 | 339.405 | 338.755 | 336.22 | 335.965 | 0.255 | 103 | 119 | |
| | 122 | 106 | 0.995 | 345.325 | 344.33 | 342.35 | 341.535 | 0.815 | 105 | 121 | |
| | 124 | 108 | 1.53 | 351.475 | 349.945 | 348.335 | 347.145 | 1.19 | 107 | 123 | |
| | 126 | 110 | 2.555 | 358.105 | 355.55 | 354.76 | 352.73 | 2.03 | 109 | 125 | |
| | 128 | 112 | 3.765 | 364.915 | 361.15 | 361.365 | 358.355 | 3.01 | 111 | 127 | |
| 9 | 130 | 114 | 4.78 | 371.555 | 366.775 | 368.14 | 363.96 | 4.18 | 113 | 129 | |
| | 132 | | | | 372.39 | 374.925 | 369.575 | 5.35 | 115 | 131 | |
| | 134 | 116 | 0.24 | 378.245 | 378.005 | | 375.19 | | | 133 | |
| | 136 | 118 | 0.8 | 384.395 | 383.595 | 381.365 | 380.8 | 0.565 | 117 | 135 | |
| | 138 | 120 | 1.19 | 390.39 | 389.2 | 387.34 | 386.4 | 0.94 | 119 | 137 | |
| | 140 | 122 | 1.84 | 396.66 | 394.82 | 393.495 | 392.02 | 1.475 | 121 | 139 | |
| | 142 | 124 | 2.94 | 403.375 | 400.435 | 400.14 | 397.615 | 2.525 | 123 | 141 | |
| | 144 | 126 | 4.19 | 410.24 | 406.05 | 406.755 | 403.23 | 3.525 | 125 | 143 | |
| | 146 | 128 | 5.17 | 416.84 | 411.67 | 413.54 | 408.855 | 4.685 | 127 | 145 | 10 |
| | 148 | | | | 417.285 | | 414.47 | | | 147 | |
| | 150 | 130 | 0.505 | 423.38 | 422.875 | 420.23 | 420.08 | 0.15 | 129 | 149 | |
| | 152 | 132 | 0.845 | 429.35 | 428.505 | 426.38 | 425.685 | 0.695 | 131 | 151 | |
| | 154 | 134 | 1.365 | 435.475 | 434.11 | 432.35 | 431.29 | 1.06 | 133 | 153 | |
| | 156 | 136 | 2.195 | 441.905 | 439.71 | 438.72 | 436.89 | 1.83 | 135 | 155 | |
| | 158 | 138 | 3.39 | 448.7 | 445.31 | 445.505 | 442.515 | 2.99 | 137 | 157 | |
| 11 | 160 | 140 | 4.595 | 455.53 | 450.935 | 452.17 | 448.14 | 4.03 | 139 | 159 | |
| | 162 | | | | 456.53 | 458.935 | 453.74 | 5.195 | 141 | 161 | |
| | 164 | 142 | 0.09 | 462.2 | 462.11 | | 459.32 | | | 163 | |
| | 166 | 144 | 0.76 | 468.45 | 467.69 | 465.465 | 464.92 | 0.545 | 143 | 165 | |
| | 168 | 146 | 1.125 | 474.43 | 473.305 | 471.425 | 470.495 | 0.93 | 145 | 167 | |
| | 170 | 148 | 1.84 | 480.74 | 478.9 | 477.51 | 476.105 | 1.405 | 147 | 169 | |
| | 172 | 150 | 2.79 | 487.295 | 484.505 | 484 | 481.69 | 2.31 | 149 | 171 | |
| | 174 | 152 | 3.935 | 494.06 | 490.125 | 490.885 | 487.315 | 3.57 | 151 | 173 | |
| | 176 | 154 | 5.11 | 500.855 | 495.745 | 497.49 | 492.935 | 4.555 | 153 | 175 | 12 |
| | 178 | | | | 501.36 | | 498.55 | | | 177 | |
| | 180 | 156 | 0.435 | 507.405 | 506.97 | 504.21 | 504.165 | 0.045 | 155 | 179 | |
| | 182 | 158 | 0.84 | 513.42 | 512.58 | 510.49 | 509.775 | 0.715 | 157 | 181 | |
| | 184 | 160 | 1.305 | 519.49 | 518.185 | 516.44 | 515.38 | 1.06 | 159 | 183 | |
| | 186 | 162 | 2.27 | 526.075 | 523.805 | 522.665 | 520.995 | 1.67 | 161 | 185 | |
| | 188 | 164 | 3.27 | 532.695 | 529.425 | 529.285 | 526.615 | 2.67 | 163 | 187 | |
| 13 | 190 | 166 | 4.43 | 539.47 | 535.04 | 536.195 | 532.235 | 3.96 | 165 | 189 | |
| | 192 | | | | 540.65 | 542.79 | 537.845 | 4.945 | 167 | 191 | |
| | 194 | 168 | -0.045 | 546.21 | 546.255 | | 543.455 | | | 193 | |

| | | | | | | | | | | | |
|---|---|---|---|---|---|---|---|---|---|---|---|
| | 196 | 170 | 0.615 | 552.475 | 551.86 | 549.415 | 549.055 | 0.36 | 169 | 195 | |
| | 198 | 172 | 0.96 | 558.42 | 557.46 | 555.465 | 554.66 | 0.805 | 171 | 197 | |
| | 200 | 174 | 1.62 | 564.68 | 563.06 | 561.52 | 560.26 | 1.26 | 173 | 199 | |
| | 202 | 176 | 2.785 | 571.46 | 568.675 | 567.89 | 565.865 | 2.025 | 175 | 201 | |
| | 204 | 178 | 3.805 | 578.09 | 574.285 | 574.61 | 571.48 | 3.13 | 177 | 203 | |
| | 206 | 180 | 4.99 | 584.875 | 579.885 | 581.485 | 577.085 | 4.4 | 179 | 205 | 14 |
| | 208 | | | | 585.48 | | 582.68 | | | 207 | |
| | 210 | 182 | 0.435 | 591.51 | 591.075 | 588.17 | 588.28 | -0.11 | 181 | 209 | |
| | 212 | 184 | 0.86 | 597.525 | 596.665 | 594.545 | 593.87 | 0.675 | 183 | 211 | |
| | 214 | 186 | 1.29 | 603.555 | 602.265 | 600.505 | 599.465 | 1.04 | 185 | 213 | |
| | 216 | 188 | 2.055 | 609.93 | 607.875 | 606.72 | 605.065 | 1.655 | 187 | 215 | |
| | 218 | 190 | 3.325 | 616.82 | 613.495 | 613.255 | 610.685 | 2.57 | 189 | 217 | |
| 15 | 220 | 192 | 4.315 | 623.43 | 619.115 | 619.97 | 616.305 | 3.665 | 191 | 219 | |
| | 222 | | | | 624.725 | 626.785 | 621.92 | 4.865 | 193 | 221 | |
| | 224 | 194 | -0.195 | 630.145 | 630.34 | | 627.535 | | | 223 | |
| | 226 | 196 | 0.635 | 636.58 | 635.945 | 633.41 | 633.14 | 0.27 | 195 | 225 | |
| | 228 | 198 | 0.965 | 642.515 | 641.55 | 639.525 | 638.745 | 0.78 | 197 | 227 | |
| | 230 | 200 | 1.545 | 648.7 | 647.155 | 645.53 | 644.35 | 1.18 | 199 | 229 | |
| | 232 | 202 | 2.415 | 655.19 | 652.775 | 652.01 | 649.965 | 2.045 | 201 | 231 | |
| | 234 | 204 | 3.73 | 662.13 | 658.4 | 658.63 | 655.585 | 3.045 | 203 | 233 | |
| 16 | 236 | 206 | 4.72 | 668.735 | 664.015 | 665.385 | 661.205 | 4.18 | 205 | 235 | |
| | 238 | | | | 669.62 | 672.15 | 666.82 | 5.33 | 207 | 237 | |
| | 240 | 208 | 0.175 | 675.4 | 675.225 | | 672.42 | | | 239 | |
| | 242 | 210 | 0.74 | 681.56 | 680.82 | 678.555 | 678.02 | 0.535 | 209 | 241 | |
| | 244 | 212 | 1.13 | 687.55 | 686.42 | 684.495 | 683.62 | 0.875 | 211 | 243 | |
| | 246 | 214 | 1.855 | 693.875 | 692.02 | 690.65 | 689.22 | 1.43 | 213 | 245 | |
| | 248 | 216 | 2.88 | 700.515 | 697.635 | 697.38 | 694.83 | 2.55 | 215 | 247 | |
| | 250 | 218 | 4.165 | 707.41 | 703.245 | 704.02 | 700.44 | 3.58 | 217 | 249 | |
| | 252 | 220 | 5.27 | 714.12 | 708.85 | 710.795 | 706.05 | 4.745 | 219 | 251 | 17 |
| | 254 | | | | 714.45 | | 711.65 | | | 253 | |
| | 256 | 222 | 0.555 | 720.605 | 720.05 | 717.52 | 717.25 | 0.27 | 221 | 255 | |
| | 258 | 224 | 0.95 | 726.6 | 725.65 | 723.635 | 722.85 | 0.785 | 223 | 257 | |
| | 260 | 226 | 1.465 | 732.715 | 731.25 | 729.61 | 728.45 | 1.16 | 225 | 259 | |
| | 262 | 228 | 2.35 | 739.215 | 736.865 | 735.885 | 734.055 | 1.83 | 227 | 261 | |
| | 264 | 230 | 3.41 | 745.895 | 742.485 | 742.735 | 739.675 | 3.06 | 229 | 263 | |
| 18 | 266 | 232 | 4.615 | 752.71 | 748.095 | 749.385 | 745.29 | 4.095 | 231 | 265 | |
| | 268 | | | | 753.7 | 756.095 | 750.9 | 5.195 | 233 | 267 | |
| | 270 | 234 | 0.095 | 759.4 | 759.305 | | 756.505 | | | 269 | |
| | 272 | 236 | 0.73 | 765.635 | 764.905 | 762.65 | 762.105 | 0.545 | 235 | 271 | |
| | 274 | 238 | 1.105 | 771.61 | 770.505 | 768.625 | 767.705 | 0.92 | 237 | 273 | |
| | 276 | 240 | 1.855 | 777.97 | 776.115 | 774.75 | 773.31 | 1.44 | 239 | 275 | |
| | 278 | 242 | 2.86 | 784.595 | 781.735 | 781.115 | 778.925 | 2.19 | 241 | 277 | |
| | 280 | 244 | 3.95 | 791.305 | 787.355 | 788.04 | 784.545 | 3.495 | 243 | 279 | |
| | 282 | 246 | 5.115 | 798.085 | 792.97 | 794.69 | 790.165 | 4.525 | 245 | 281 | 19 |
| | 284 | | | | 798.585 | | 795.775 | | | 283 | |
| | 286 | 248 | 0.425 | 804.615 | 804.19 | 801.355 | 801.385 | -0.03 | 247 | 285 | |
| | 288 | 250 | 0.795 | 810.585 | 809.79 | 807.66 | 806.99 | 0.67 | 249 | 287 | |
| | 290 | 252 | 1.26 | 816.655 | 815.395 | 813.605 | 812.595 | 1.01 | 251 | 289 | |
| | 292 | 254 | 2.285 | 823.295 | 821.01 | 819.88 | 818.2 | 1.68 | 253 | 291 | |
| | 294 | 256 | 3.34 | 829.965 | 826.625 | 826.425 | 823.815 | 2.61 | 255 | 293 | |
| 20 | 296 | 258 | 4.48 | 836.715 | 832.235 | 833.325 | 829.43 | 3.895 | 257 | 295 | |
| | 298 | | | | 837.84 | 840.06 | 835.04 | 5.02 | 259 | 297 | |
| | 300 | 260 | 0.05 | 843.49 | 843.44 | | 840.64 | | | 299 | |
| | 302 | 262 | 0.705 | 849.74 | 849.035 | 846.635 | 846.24 | 0.395 | 261 | 301 | |
| | 304 | 264 | 1.045 | 855.675 | 854.63 | 852.7 | 851.835 | 0.865 | 263 | 303 | |
| | 306 | 266 | 1.65 | 861.88 | 860.23 | 858.735 | 857.43 | 1.305 | 265 | 305 | |
| | 308 | 268 | 2.795 | 868.64 | 865.845 | 865.2 | 863.035 | 2.165 | 267 | 307 | |
| | 310 | 270 | 3.905 | 875.36 | 871.455 | 871.83 | 868.65 | 3.18 | 269 | 309 | |
| | 312 | 272 | 4.985 | 882.05 | 877.065 | 878.64 | 874.26 | 4.38 | 271 | 311 | 21 |
| | 314 | | | | 882.67 | | 879.865 | | | 313 | |
| | 316 | 274 | 0.425 | 888.695 | 888.27 | 885.39 | 885.47 | -0.08 | 273 | 315 | |
| | 318 | 276 | 0.875 | 894.745 | 893.87 | 891.74 | 891.07 | 0.67 | 275 | 317 | |
| | 320 | 278 | 1.325 | 900.8 | 899.475 | 897.705 | 896.675 | 1.03 | 277 | 319 | |
| | 322 | 280 | 2 | 907.09 | 905.09 | 903.95 | 902.28 | 1.67 | 279 | 321 | |
| | 324 | 282 | 3.23 | 913.94 | 910.71 | 910.575 | 907.9 | 2.675 | 281 | 323 | |
| 22 | 326 | 284 | 4.34 | 920.67 | 916.33 | 917.245 | 913.52 | 3.725 | 283 | 325 | |
| | 328 | | | | 921.945 | 924.025 | 919.14 | 4.885 | 285 | 327 | |
| | 330 | 286 | -0.25 | 927.31 | 927.56 | | 924.755 | | | 329 | |
| | 332 | 288 | 0.595 | 933.76 | 933.165 | 930.65 | 930.365 | 0.285 | 287 | 331 | |
| | 334 | 290 | 0.92 | 939.695 | 938.775 | 936.7 | 935.97 | 0.73 | 289 | 333 | |
| | 336 | 292 | 1.515 | 945.9 | 944.385 | 942.705 | 941.58 | 1.125 | 291 | 335 | |
| | 338 | 294 | 2.355 | 952.36 | 950.005 | 949.215 | 947.195 | 2.02 | 293 | 337 | |
| | 340 | 296 | 3.62 | 959.24 | 955.62 | 955.935 | 952.815 | 3.12 | 295 | 339 | |
| 23 | 342 | 298 | 4.785 | 966.015 | 961.23 | 962.645 | 958.425 | 4.22 | 297 | 341 | |
| | 344 | | | | 966.825 | 969.44 | 964.03 | 5.41 | 299 | 343 | |
| | 346 | 300 | 0.225 | 972.64 | 972.415 | | 969.625 | | | 345 | |
| | 348 | 302 | 0.795 | 978.8 | 978.005 | 975.83 | 975.21 | 0.62 | 301 | 347 | |
| | 350 | 304 | 1.19 | 984.785 | 983.595 | 981.76 | 980.8 | 0.96 | 303 | 349 | |
| | 352 | 306 | 1.99 | 991.185 | 989.195 | 987.9 | 986.39 | 1.51 | 305 | 351 | |
| | 354 | 308 | 2.97 | 997.775 | 994.805 | 994.545 | 992 | 2.545 | 307 | 353 | |
| | 356 | 310 | 4.15 | 1004.57 | 1000.42 | 1001.34 | 997.61 | 3.73 | 309 | 355 | |
| | 358 | 312 | 5.325 | 1011.355 | 1006.03 | 1008 | 1003.225 | 4.775 | 311 | 357 | 24 |
| | 360 | | | | 1011.64 | | 1008.835 | | | 359 | |
| | 362 | 314 | 0.57 | 1017.815 | 1017.245 | 1014.7 | 1014.445 | 0.255 | 313 | 361 | |
| | 364 | 316 | 0.945 | 1023.795 | 1022.85 | 1020.855 | 1020.05 | 0.805 | 315 | 363 | |
| | 366 | 318 | 1.48 | 1029.94 | 1028.46 | 1026.845 | 1025.655 | 1.19 | 317 | 365 | |
| | 368 | 320 | 2.475 | 1036.55 | 1034.075 | 1033.09 | 1031.265 | 1.825 | 319 | 367 | |
| | 370 | 322 | 3.49 | 1043.185 | 1039.695 | 1039.845 | 1036.885 | 2.96 | 321 | 369 | |
| 25 | 372 | 324 | 4.65 | 1049.965 | 1045.315 | 1046.66 | 1042.505 | 4.155 | 323 | 371 | |
| | 374 | | | | 1050.925 | 1053.27 | 1048.12 | 5.15 | 325 | 373 | |
| | 376 | 326 | 0.125 | 1056.66 | 1056.535 | | 1053.73 | | | 375 | |
| | 378 | 328 | 0.67 | 1062.815 | 1062.145 | 1059.83 | 1059.34 | 0.49 | 327 | 377 | |
| | 380 | 330 | 1.035 | 1068.785 | 1067.75 | 1065.805 | 1064.945 | 0.86 | 329 | 379 | |
| | 382 | 332 | 1.805 | 1075.165 | 1073.36 | 1071.935 | 1070.555 | 1.38 | 331 | 381 | |
| | 384 | 334 | 2.935 | 1081.915 | 1078.98 | 1078.33 | 1076.17 | 2.16 | 333 | 383 | |
| | 386 | 336 | 3.99 | 1088.58 | 1084.59 | 1085.15 | 1081.785 | 3.365 | 335 | 385 | |
| | 388 | 338 | 5.19 | 1095.38 | 1090.19 | 1091.98 | 1087.39 | 4.59 | 337 | 387 | 26 |
| | 390 | | | | 1095.785 | | 1092.99 | | | 389 | |
| | 392 | 340 | 0.525 | 1101.9 | 1101.375 | 1098.625 | 1098.58 | 0.045 | 339 | 391 | |
| | 394 | 342 | 0.895 | 1107.855 | 1106.96 | 1104.9 | 1104.165 | 0.735 | 341 | 393 | |
| | 396 | 344 | 1.385 | 1113.94 | 1112.555 | 1110.855 | 1109.755 | 1.1 | 343 | 395 | |

| | | | | | | | | | | | |
|---|---|---|---|---|---|---|---|---|---|---|---|
|  | 398 | 346 | 2.3 | 1120.46 | 1118.16 | 1117.165 | 1115.355 | 1.81 | 345 | 397 |  |
|  | 400 | 348 | 3.525 | 1127.305 | 1123.78 | 1123.72 | 1120.97 | 2.75 | 347 | 399 |  |
| 27 | 402 | 350 | 4.54 | 1133.935 | 1129.395 | 1130.49 | 1126.585 | 3.905 | 349 | 401 |  |
|  | 404 |  |  |  | 1135.01 | 1137.3 | 1132.2 | 5.1 | 351 | 403 |  |
|  | 406 | 352 | 0.045 | 1140.665 | 1140.62 |  | 1137.815 |  |  | 405 |  |
|  | 408 | 354 | 0.725 | 1146.95 | 1146.225 | 1143.855 | 1143.425 | 0.43 | 353 | 407 |  |
|  | 410 | 356 | 1.065 | 1152.895 | 1151.83 | 1149.885 | 1149.03 | 0.855 | 355 | 409 |  |
|  | 412 | 358 | 1.67 | 1159.11 | 1157.44 | 1155.945 | 1154.635 | 1.31 | 357 | 411 |  |
|  | 414 | 360 | 2.685 | 1165.745 | 1163.06 | 1162.505 | 1160.25 | 2.255 | 359 | 413 |  |
|  | 416 | 362 | 3.955 | 1172.635 | 1168.68 | 1169.12 | 1165.87 | 3.25 | 361 | 415 |  |
|  | 418 | 364 | 4.93 | 1179.225 | 1174.295 | 1175.895 | 1171.485 | 4.41 | 363 | 417 | 28 |
|  | 420 |  |  |  | 1179.905 |  | 1177.1 |  |  | 419 |  |
|  | 422 | 366 | 0.35 | 1185.86 | 1185.51 | 1182.63 | 1182.705 | -0.075 | 365 | 421 |  |
|  | 424 | 368 | 0.8 | 1191.91 | 1191.11 | 1188.92 | 1188.31 | 0.61 | 367 | 423 |  |
|  | 426 | 370 | 1.26 | 1197.97 | 1196.71 | 1194.865 | 1193.91 | 0.955 | 369 | 425 |  |
|  | 428 | 372 | 1.995 | 1204.315 | 1202.32 | 1201.125 | 1199.515 | 1.61 | 371 | 427 |  |
|  | 430 | 374 | 3.125 | 1211.06 | 1207.935 | 1207.88 | 1205.13 | 2.75 | 373 | 429 |  |
| 29 | 432 | 376 | 4.39 | 1217.93 | 1213.54 | 1214.515 | 1210.74 | 3.775 | 375 | 431 |  |
|  | 434 |  |  |  | 1219.14 | 1221.31 | 1216.34 | 4.97 | 377 | 433 |  |
|  | 436 | 378 | -0.145 | 1224.595 | 1224.74 |  | 1221.94 |  |  | 435 |  |
|  | 438 | 380 | 0.65 | 1230.985 | 1230.335 | 1227.945 | 1227.535 | 0.41 | 379 | 437 |  |
|  | 440 | 382 | 1.01 | 1236.94 | 1235.93 | 1233.96 | 1233.13 | 0.83 | 381 | 439 |  |
|  | 442 | 384 | 1.62 | 1243.15 | 1241.53 | 1239.985 | 1238.73 | 1.255 | 383 | 441 |  |
|  | 444 | 386 | 2.52 | 1249.665 | 1247.145 | 1246.38 | 1244.335 | 2.045 | 385 | 443 |  |
|  | 446 | 388 | 3.64 | 1256.405 | 1252.765 | 1253.255 | 1249.955 | 3.3 | 387 | 445 |  |
|  | 448 | 390 | 4.85 | 1263.23 | 1258.38 | 1259.87 | 1255.575 | 4.295 | 389 | 447 | 30 |
|  | 450 |  |  |  | 1263.99 |  | 1261.185 |  |  | 449 |  |
|  | 452 | 392 | 0.27 | 1269.86 | 1269.59 | 1266.605 | 1266.79 | -0.185 | 391 | 451 |  |
|  | 454 | 394 | 0.795 | 1275.99 | 1275.195 | 1273.04 | 1272.395 | 0.645 | 393 | 453 |  |
|  | 456 | 396 | 1.195 | 1281.99 | 1280.795 | 1278.975 | 1277.995 | 0.98 | 395 | 455 |  |
|  | 458 | 398 | 2.045 | 1288.45 | 1286.405 | 1285.15 | 1283.6 | 1.55 | 397 | 457 |  |
|  | 460 | 400 | 3.035 | 1295.06 | 1292.025 | 1291.65 | 1289.215 | 2.435 | 399 | 459 |  |
|  | 462 | 402 | 4.165 | 1301.81 | 1297.645 | 1298.58 | 1294.835 | 3.745 | 401 | 461 |  |
|  | 464 | 404 | 5.315 | 1308.575 | 1303.26 | 1305.17 | 1300.455 | 4.715 | 403 | 463 | 31 |
|  | 466 |  |  |  | 1308.87 |  | 1306.065 |  |  | 465 |  |
|  | 468 | 406 | 0.52 | 1314.995 | 1314.475 | 1311.845 | 1311.67 | 0.175 | 405 | 467 |  |
|  | 470 | 408 | 0.865 | 1320.94 | 1320.075 | 1318.01 | 1317.275 | 0.735 | 407 | 469 |  |
|  | 472 | 410 | 1.42 | 1327.095 | 1325.675 | 1324 | 1322.875 | 1.125 | 409 | 471 |  |
|  | 474 | 412 | 2.525 | 1333.815 | 1331.29 | 1330.305 | 1328.48 | 1.825 | 411 | 473 |  |
|  | 476 | 414 | 3.54 | 1340.44 | 1336.9 | 1336.96 | 1334.095 | 2.865 | 413 | 475 |  |
| 32 | 478 | 416 | 4.715 | 1347.225 | 1342.51 | 1343.86 | 1339.705 | 4.155 | 415 | 477 |  |
|  | 480 |  |  |  | 1348.115 | 1350.535 | 1345.31 | 5.225 | 417 | 479 |  |
|  | 482 | 418 | 0.235 | 1353.95 | 1353.715 |  | 1350.915 |  |  | 481 |  |
|  | 484 | 420 | 0.755 | 1360.07 | 1359.315 | 1357.045 | 1356.515 | 0.53 | 419 | 483 |  |
|  | 486 | 422 | 1.125 | 1366.04 | 1364.915 | 1363.04 | 1362.115 | 0.925 | 421 | 485 |  |
|  | 488 | 424 | 1.81 | 1372.33 | 1370.52 | 1369.145 | 1367.715 | 1.43 | 423 | 487 |  |
|  | 490 | 426 | 3.04 | 1379.18 | 1376.14 | 1375.625 | 1373.33 | 2.295 | 425 | 489 |  |
|  | 492 | 428 | 4.065 | 1385.815 | 1381.75 | 1382.32 | 1378.945 | 3.375 | 427 | 491 |  |
|  | 494 | 430 | 5.19 | 1392.545 | 1387.355 | 1389.155 | 1384.555 | 4.6 | 429 | 493 | 33 |
|  | 496 |  |  |  | 1392.955 |  | 1390.155 |  |  | 495 |  |
|  | 498 | 432 | 0.55 | 1399.105 | 1398.555 | 1395.85 | 1395.755 | 0.095 | 431 | 497 |  |
|  | 500 | 434 | 0.93 | 1405.08 | 1404.15 | 1402.095 | 1401.35 | 0.745 | 433 | 499 |  |
|  | 502 | 436 | 1.445 | 1411.195 | 1409.75 | 1408.065 | 1406.95 | 1.115 | 435 | 501 |  |
|  | 504 | 438 | 2.205 | 1417.57 | 1415.365 | 1414.405 | 1412.555 | 1.85 | 437 | 503 |  |
|  | 506 | 440 | 3.505 | 1424.495 | 1420.99 | 1421.015 | 1418.175 | 2.84 | 439 | 505 |  |
| 34 | 508 | 442 | 4.51 | 1431.12 | 1426.61 | 1427.73 | 1423.8 | 3.93 | 441 | 507 |  |
|  | 510 |  |  |  | 1432.225 | 1434.505 | 1429.415 | 5.09 | 443 | 509 |  |
|  | 512 | 444 | -0.045 | 1437.795 | 1437.84 |  | 1435.03 |  |  | 511 |  |
|  | 514 | 446 | 0.665 | 1444.11 | 1443.445 | 1441.05 | 1440.64 | 0.41 | 445 | 513 |  |
|  | 516 | 448 | 1 | 1450.05 | 1449.05 | 1447.035 | 1446.25 | 0.785 | 447 | 515 |  |
|  | 518 | 450 | 1.65 | 1456.31 | 1454.66 | 1453.095 | 1451.855 | 1.24 | 449 | 517 |  |
|  | 520 | 452 | 2.58 | 1462.86 | 1460.28 | 1459.725 | 1457.47 | 2.255 | 451 | 519 |  |
|  | 522 | 454 | 3.89 | 1469.785 | 1465.895 | 1466.38 | 1463.085 | 3.295 | 453 | 521 |  |
|  | 524 | 456 | 4.97 | 1476.475 | 1471.505 | 1473.13 | 1468.7 | 4.43 | 455 | 523 | 35 |
|  | 526 |  |  |  | 1477.105 |  | 1474.305 |  |  | 525 |  |
|  | 528 | 458 | 0.365 | 1483.065 | 1482.7 | 1479.915 | 1479.905 | 0.01 | 457 | 527 |  |
|  | 530 | 460 | 0.845 | 1489.14 | 1488.295 | 1486.175 | 1485.5 | 0.675 | 459 | 529 |  |
|  | 532 | 462 | 1.28 | 1495.17 | 1493.89 | 1492.11 | 1491.095 | 1.015 | 461 | 531 |  |
|  | 534 | 464 | 2.11 | 1501.605 | 1499.495 | 1498.315 | 1496.69 | 1.625 | 463 | 533 |  |
|  | 536 | 466 | 3.145 | 1508.25 | 1505.105 | 1505.095 | 1502.3 | 2.795 | 465 | 535 |  |
| 36 | 538 | 468 | 4.37 | 1515.085 | 1510.715 | 1511.78 | 1507.91 | 3.87 | 467 | 537 |  |
|  | 540 |  |  |  | 1516.32 | 1518.495 | 1513.52 | 4.975 | 469 | 539 |  |
|  | 542 | 470 | -0.09 | 1521.83 | 1521.92 |  | 1519.12 |  |  | 541 |  |
|  | 544 | 472 | 0.675 | 1528.195 | 1527.52 | 1525.15 | 1524.72 | 0.43 | 471 | 543 |  |
|  | 546 | 474 | 1.04 | 1534.16 | 1533.12 | 1531.2 | 1530.32 | 0.88 | 473 | 545 |  |
|  | 548 | 476 | 1.665 | 1540.39 | 1538.725 | 1537.245 | 1535.92 | 1.325 | 475 | 547 |  |
|  | 550 | 478 | 2.645 | 1546.99 | 1544.345 | 1543.53 | 1541.535 | 1.995 | 477 | 549 |  |
|  | 552 | 480 | 3.69 | 1553.66 | 1549.97 | 1550.4 | 1547.155 | 3.245 | 479 | 551 |  |
|  | 554 | 482 | 4.85 | 1560.44 | 1555.59 | 1557.095 | 1552.78 | 4.315 | 481 | 553 | 37 |
|  | 556 |  |  |  | 1561.205 |  | 1558.395 |  |  | 555 |  |
|  | 558 | 484 | 0.26 | 1567.075 | 1566.815 | 1563.74 | 1564.01 | -0.27 | 483 | 557 |  |
|  | 560 | 486 | 0.725 | 1573.15 | 1572.425 | 1570.205 | 1569.62 | 0.585 | 485 | 559 |  |
|  | 562 | 488 | 1.115 | 1579.15 | 1578.035 | 1576.14 | 1575.23 | 0.91 | 487 | 561 |  |
|  | 564 | 490 | 2.005 | 1585.655 | 1583.65 | 1582.345 | 1580.84 | 1.505 | 489 | 563 |  |
|  | 566 | 492 | 3.075 | 1592.345 | 1589.27 | 1588.79 | 1586.46 | 2.33 | 491 | 565 |  |
|  | 568 | 494 | 4.185 | 1599.07 | 1594.885 | 1595.695 | 1592.08 | 3.615 | 493 | 567 |  |
|  | 570 | 496 | 5.37 | 1605.86 | 1600.49 | 1602.43 | 1597.69 | 4.74 | 495 | 569 | 38 |
|  | 572 |  |  |  | 1606.08 |  | 1603.285 |  |  | 571 |  |
|  | 574 | 498 | 0.59 | 1612.26 | 1611.67 | 1609.065 | 1608.875 | 0.19 | 497 | 573 |  |
|  | 576 | 500 | 0.93 | 1618.19 | 1617.26 | 1615.24 | 1614.465 | 0.775 | 499 | 575 |  |
|  | 578 | 502 | 1.48 | 1624.33 | 1622.85 | 1621.22 | 1620.055 | 1.165 | 501 | 577 |  |
|  | 580 | 504 | 2.54 | 1631 | 1628.46 | 1627.595 | 1625.655 | 1.94 | 503 | 579 |  |
|  | 582 | 506 | 3.68 | 1637.75 | 1634.07 | 1634.19 | 1631.265 | 2.925 | 505 | 581 |  |
| 39 | 584 | 508 | 4.76 | 1644.44 | 1639.68 | 1641.005 | 1636.875 | 4.13 | 507 | 583 |  |
|  | 586 |  |  |  | 1645.29 | 1647.8 | 1642.485 | 5.315 | 509 | 585 |  |
|  | 588 | 510 | 0.26 | 1651.155 | 1650.895 |  | 1648.095 |  |  | 587 |  |
|  | 590 | 512 | 0.81 | 1657.31 | 1656.5 | 1654.265 | 1653.7 | 0.565 | 511 | 589 |  |
|  | 592 | 514 | 1.19 | 1663.295 | 1662.105 | 1660.255 | 1659.3 | 0.955 | 513 | 591 |  |
|  | 594 | 516 | 1.815 | 1669.53 | 1667.715 | 1666.385 | 1664.91 | 1.475 | 515 | 593 |  |
|  | 596 | 518 | 2.965 | 1676.3 | 1673.335 | 1672.965 | 1670.525 | 2.44 | 517 | 595 |  |
|  | 598 | 520 | 4.13 | 1683.085 | 1678.955 | 1679.6 | 1676.145 | 3.455 | 519 | 597 |  |

| | | | | | | | | | | |
|---|---|---|---|---|---|---|---|---|---|---|---|
| | 600 | 522 | 5.135 | 1689.705 | 1684.57 | 1686.385 | 1681.765 | 4.62 | 521 | 599 | 40 |
| | 602 | | | | 1690.18 | | 1687.375 | | | 601 | |
| | 604 | 524 | 0.485 | 1696.275 | 1695.79 | 1693.075 | 1692.985 | 0.09 | 523 | 603 | |
| | 606 | 526 | 0.86 | 1702.255 | 1701.395 | 1699.265 | 1698.595 | 0.67 | 525 | 605 | |
| | 608 | 528 | 1.38 | 1708.385 | 1707.005 | 1705.23 | 1704.2 | 1.03 | 527 | 607 | |
| | 610 | 530 | 2.14 | 1714.76 | 1712.62 | 1711.605 | 1709.81 | 1.795 | 529 | 609 | |
| | 612 | 532 | 3.37 | 1721.605 | 1718.235 | 1718.33 | 1715.43 | 2.9 | 531 | 611 | |
| 41 | 614 | 534 | 4.555 | 1728.4 | 1723.845 | 1725.005 | 1721.04 | 3.965 | 533 | 613 | |
| | 616 | | | | 1729.445 | 1731.805 | 1726.645 | 5.16 | 535 | 615 | |
| | 618 | 536 | 0.015 | 1735.05 | 1735.035 | | 1732.24 | | | 617 | |
| | 620 | 538 | 0.71 | 1741.335 | 1740.625 | 1738.33 | 1737.83 | 0.5 | 537 | 619 | |
| | 622 | 540 | 1.065 | 1747.285 | 1746.22 | 1744.285 | 1743.42 | 0.865 | 539 | 621 | |
| | 624 | 542 | 1.765 | 1753.585 | 1751.82 | 1750.365 | 1749.015 | 1.35 | 541 | 623 | |
| | 626 | 544 | 2.705 | 1760.135 | 1757.43 | 1756.91 | 1754.625 | 2.285 | 543 | 625 | |
| | 628 | 546 | 3.875 | 1766.925 | 1763.05 | 1763.72 | 1760.24 | 3.48 | 545 | 627 | |
| | 630 | 548 | 5.09 | 1773.75 | 1768.66 | 1770.38 | 1765.855 | 4.525 | 547 | 629 | 42 |
| | 632 | | | | 1774.27 | | 1771.465 | | | 631 | |
| | 634 | 550 | 0.425 | 1780.3 | 1779.875 | 1777.125 | 1777.075 | 0.05 | 549 | 633 | |
| | 636 | 552 | 0.87 | 1786.35 | 1785.48 | 1783.41 | 1782.675 | 0.735 | 551 | 635 | |
| | 638 | 554 | 1.32 | 1792.4 | 1791.08 | 1789.35 | 1788.28 | 1.07 | 553 | 637 | |
| | 640 | 556 | 2.235 | 1798.93 | 1796.695 | 1795.555 | 1793.885 | 1.67 | 555 | 639 | |
| | 642 | 558 | 3.23 | 1805.545 | 1802.315 | 1802.205 | 1799.505 | 2.7 | 557 | 641 | |
| 43 | 644 | 560 | 4.39 | 1812.32 | 1807.93 | 1809.07 | 1805.125 | 3.945 | 559 | 643 | |
| | 646 | | | | 1813.545 | 1815.665 | 1810.74 | 4.925 | 561 | 645 | |
| | 648 | 562 | -0.105 | 1819.05 | 1819.155 | | 1816.35 | | | 647 | |
| | 650 | 564 | 0.61 | 1825.365 | 1824.755 | 1822.31 | 1821.955 | 0.355 | 563 | 649 | |
| | 652 | 566 | 0.955 | 1831.315 | 1830.36 | 1828.365 | 1827.56 | 0.805 | 565 | 651 | |
| | 654 | 568 | 1.61 | 1837.575 | 1835.965 | 1834.42 | 1833.16 | 1.26 | 567 | 653 | |
| | 656 | 570 | 2.725 | 1844.305 | 1841.58 | 1840.75 | 1838.775 | 1.975 | 569 | 655 | |
| | 658 | 572 | 3.75 | 1850.945 | 1847.195 | 1847.515 | 1844.39 | 3.125 | 571 | 657 | |
| | 660 | 574 | 4.935 | 1857.735 | 1852.8 | 1854.365 | 1850 | 4.365 | 573 | 659 | 44 |
| | 662 | | | | 1858.4 | | 1855.6 | | | 661 | |
| | 664 | 576 | 0.375 | 1864.375 | 1864 | 1861.015 | 1861.2 | -0.185 | 575 | 663 | |
| | 666 | 578 | 0.8 | 1870.395 | 1869.595 | 1867.425 | 1866.795 | 0.63 | 577 | 665 | |
| | 668 | 580 | 1.215 | 1876.41 | 1875.195 | 1873.375 | 1872.395 | 0.98 | 579 | 667 | |
| | 670 | 582 | 2.025 | 1882.83 | 1880.805 | 1879.58 | 1878 | 1.58 | 581 | 669 | |
| | 672 | 584 | 3.255 | 1889.68 | 1886.425 | 1886.08 | 1883.615 | 2.465 | 583 | 671 | |
| 45 | 674 | 586 | 4.295 | 1896.325 | 1892.03 | 1892.84 | 1889.235 | 3.605 | 585 | 673 | |
| | 676 | | | | 1897.65 | 1899.68 | 1894.845 | 4.835 | 587 | 675 | |
| | 678 | 588 | -0.185 | 1903.065 | 1903.25 | | 1900.45 | | | 677 | |
| | 680 | 590 | 0.645 | 1909.495 | 1908.85 | 1906.305 | 1906.05 | 0.255 | 589 | 679 | |
| | 682 | 592 | 0.985 | 1915.43 | 1914.445 | 1912.45 | 1911.645 | 0.805 | 591 | 681 | |
| | 684 | 594 | 1.545 | 1921.59 | 1920.045 | 1918.445 | 1917.245 | 1.2 | 593 | 683 | |
| | 686 | 596 | 2.45 | 1928.11 | 1925.66 | 1924.885 | 1922.85 | 2.035 | 595 | 685 | |
| | 688 | 598 | 3.745 | 1935.025 | 1931.28 | 1931.485 | 1928.47 | 3.015 | 597 | 687 | |
| 46 | 690 | 600 | 4.71 | 1941.61 | 1936.9 | 1938.24 | 1934.09 | 4.15 | 599 | 689 | |
| | 692 | | | | 1942.51 | 1945 | 1939.705 | 5.295 | 601 | 691 | |
| | 694 | 602 | 0.175 | 1948.295 | 1948.12 | | 1945.315 | | | 693 | |
| | 696 | 604 | 0.74 | 1954.465 | 1953.725 | 1951.44 | 1950.925 | 0.515 | 603 | 695 | |
| | 698 | 606 | 1.12 | 1960.45 | 1959.33 | 1957.395 | 1956.525 | 0.87 | 605 | 697 | |
| | 700 | 608 | 1.805 | 1966.74 | 1964.935 | 1963.545 | 1962.13 | 1.415 | 607 | 699 | |
| | 702 | 610 | 2.855 | 1973.41 | 1970.555 | 1970.24 | 1967.745 | 2.495 | 609 | 701 | |
| | 704 | 612 | 4.145 | 1980.31 | 1976.165 | 1976.865 | 1973.36 | 3.505 | 611 | 703 | |
| | 706 | 614 | 5.18 | 1986.955 | 1981.775 | 1983.655 | 1978.97 | 4.685 | 613 | 705 | 47 |
| | 708 | | | | 1987.38 | | 1984.575 | | | 707 | |
| | 710 | 616 | 0.505 | 1993.485 | 1992.98 | 1990.38 | 1990.18 | 0.2 | 615 | 709 | |
| | 712 | 618 | 0.9 | 1999.48 | 1998.58 | 1996.505 | 1995.78 | 0.725 | 617 | 711 | |
| | 714 | 620 | 1.405 | 2005.585 | 2004.18 | 2002.47 | 2001.38 | 1.09 | 619 | 713 | |
| | 716 | 622 | 2.245 | 2012.04 | 2009.795 | 2008.775 | 2006.99 | 1.785 | 621 | 715 | |
| | 718 | 624 | 3.345 | 2018.755 | 2015.41 | 2015.62 | 2012.6 | 3.02 | 623 | 717 | |
| 48 | 720 | 626 | 4.59 | 2025.605 | 2021.015 | 2022.25 | 2018.215 | 4.035 | 625 | 719 | |
| | 722 | | | | 2026.615 | 2029 | 2023.815 | 5.185 | 627 | 721 | |
| | 724 | 628 | 0.085 | 2032.295 | 2032.21 | | 2029.415 | | | 723 | |
| | 726 | 630 | 0.745 | 2038.55 | 2037.805 | 2035.56 | 2035.005 | 0.555 | 629 | 725 | |
| | 728 | 632 | 1.125 | 2044.52 | 2043.395 | 2041.535 | 2040.6 | 0.935 | 631 | 727 | |
| | 730 | 634 | 1.845 | 2050.845 | 2049 | 2047.635 | 2046.2 | 1.435 | 633 | 729 | |
| | 732 | 636 | 2.815 | 2057.435 | 2054.62 | 2054.03 | 2051.81 | 2.22 | 635 | 731 | |
| | 734 | 638 | 3.91 | 2064.155 | 2060.245 | 2060.95 | 2057.43 | 3.52 | 637 | 733 | |
| | 736 | 640 | 5.065 | 2070.93 | 2065.865 | 2067.555 | 2063.055 | 4.5 | 639 | 735 | 49 |
| | 738 | | | | 2071.48 | | 2068.67 | | | 737 | |
| | 740 | 642 | 0.39 | 2077.485 | 2077.095 | 2074.24 | 2074.29 | -0.05 | 641 | 739 | |
| | 742 | 644 | 0.79 | 2083.49 | 2082.7 | 2080.565 | 2079.9 | 0.665 | 643 | 741 | |
| | 744 | 646 | 1.235 | 2089.545 | 2088.31 | 2086.505 | 2085.505 | 1 | 645 | 743 | |
| | 746 | 648 | 2.235 | 2096.16 | 2093.925 | 2092.75 | 2091.12 | 1.63 | 647 | 745 | |
| | 748 | 650 | 3.255 | 2102.8 | 2099.545 | 2099.305 | 2096.735 | 2.57 | 649 | 747 | |
| 50 | 750 | 652 | 4.405 | 2109.565 | 2105.16 | 2106.24 | 2102.355 | 3.885 | 651 | 749 | |
| | 752 | | | | 2110.765 | 2112.89 | 2107.965 | 4.925 | 653 | 751 | |
| | 754 | 654 | -0.025 | 2116.34 | 2116.365 | | 2113.565 | | | 753 | |
| | 756 | 656 | 0.645 | 2122.605 | 2121.96 | 2119.5 | 2119.165 | 0.335 | 655 | 755 | |
| | 758 | 658 | 0.985 | 2128.54 | 2127.555 | 2125.58 | 2124.755 | 0.825 | 657 | 757 | |
| | 760 | 660 | 1.6 | 2134.755 | 2133.155 | 2131.61 | 2130.35 | 1.26 | 659 | 759 | |
| | 762 | 662 | 2.78 | 2141.54 | 2138.76 | 2138.02 | 2135.955 | 2.065 | 661 | 761 | |
| | 764 | 664 | 3.83 | 2148.2 | 2144.37 | 2144.68 | 2141.565 | 3.115 | 663 | 763 | |
| | 766 | 666 | 4.965 | 2154.94 | 2149.975 | 2151.53 | 2147.175 | 4.355 | 665 | 765 | 51 |
| | 768 | | | | 2155.575 | | 2152.775 | | | 767 | |
| | 770 | 668 | 0.425 | 2161.6 | 2161.175 | 2158.27 | 2158.375 | -0.105 | 667 | 769 | |
| | 772 | 670 | 0.88 | 2167.65 | 2166.77 | 2164.645 | 2163.97 | 0.675 | 669 | 771 | |
| | 774 | 672 | 1.31 | 2173.68 | 2172.37 | 2170.615 | 2169.57 | 1.045 | 671 | 773 | |
| | 776 | 674 | 1.995 | 2179.975 | 2177.98 | 2176.825 | 2175.175 | 1.65 | 673 | 775 | |
| | 778 | 676 | 3.25 | 2186.855 | 2183.605 | 2183.4 | 2180.795 | 2.605 | 675 | 777 | |
| 52 | 780 | 678 | 4.295 | 2193.52 | 2189.225 | 2190.08 | 2186.415 | 3.665 | 677 | 779 | |
| | 782 | | | | 2194.845 | 2196.865 | 2192.035 | 4.83 | 679 | 781 | |
| | 784 | 680 | -0.275 | 2200.185 | 2200.46 | | 2197.655 | | | 783 | |
| | 786 | 682 | 0.585 | 2206.655 | 2206.07 | 2203.5 | 2203.265 | 0.235 | 681 | 785 | |
| | 788 | 684 | 0.915 | 2212.595 | 2211.68 | 2209.6 | 2208.875 | 0.725 | 683 | 787 | |
| | 790 | 686 | 1.5 | 2218.79 | 2217.29 | 2215.6 | 2214.485 | 1.115 | 685 | 789 | |
| | 792 | 688 | 2.315 | 2225.225 | 2222.91 | 2222.09 | 2220.1 | 1.99 | 687 | 791 | |
| | 794 | 690 | 3.625 | 2232.155 | 2228.53 | 2228.76 | 2225.72 | 3.04 | 689 | 793 | |
| 53 | 796 | 692 | 4.71 | 2238.85 | 2234.14 | 2235.49 | 2231.335 | 4.155 | 691 | 795 | |
| | 798 | | | | 2239.74 | 2242.28 | 2236.94 | 5.34 | 693 | 797 | |
| | 800 | 694 | 0.16 | 2245.49 | 2245.33 | | 2242.535 | | | 799 | |

| | | | | | | | | | | |
|---|---|---|---|---|---|---|---|---|---|---|
| | 802 | 696 | 0.755 | 2251.675 | 2250.92 | 2248.69 | 2248.13 | 0.56 | 695 | 801 | |
| | 804 | 698 | 1.135 | 2257.65 | 2256.515 | 2254.62 | 2253.715 | 0.905 | 697 | 803 | |
| | 806 | 700 | 1.9 | 2264.01 | 2262.11 | 2260.755 | 2259.31 | 1.445 | 699 | 805 | |
| | 808 | 702 | 2.885 | 2270.61 | 2267.725 | 2267.45 | 2264.915 | 2.535 | 701 | 807 | |
| | 810 | 704 | 4.115 | 2277.45 | 2273.335 | 2274.16 | 2270.53 | 3.63 | 703 | 809 | |
| | 812 | 706 | 5.295 | 2284.235 | 2278.94 | 2280.88 | 2276.14 | 4.74 | 705 | 811 | 54 |
| | 814 | | | | 2284.545 | | 2281.745 | | | 813 | |
| | 816 | 708 | 0.56 | 2290.71 | 2290.15 | 2287.605 | 2287.35 | 0.255 | 707 | 815 | |
| | 818 | 710 | 0.96 | 2296.71 | 2295.75 | 2293.76 | 2292.95 | 0.81 | 709 | 817 | |
| | 820 | 712 | 1.47 | 2302.825 | 2301.355 | 2299.735 | 2298.555 | 1.18 | 711 | 819 | |
| | 822 | 714 | 2.405 | 2309.38 | 2306.975 | 2305.97 | 2304.165 | 1.805 | 713 | 821 | |
| | 824 | 716 | 3.425 | 2316.02 | 2312.595 | 2312.755 | 2309.785 | 2.97 | 715 | 823 | |
| 55 | 826 | 718 | 4.595 | 2322.805 | 2318.21 | 2319.51 | 2315.4 | 4.11 | 717 | 825 | |
| | 828 | | | | 2323.82 | 2326.15 | 2321.015 | 5.135 | 719 | 827 | |
| | 830 | 720 | 0.07 | 2329.5 | 2329.43 | | 2326.625 | | | 829 | |
| | 832 | 722 | 0.68 | 2335.715 | 2335.035 | 2332.725 | 2332.235 | 0.49 | 721 | 831 | |
| | 834 | 724 | 1.04 | 2341.685 | 2340.645 | 2338.705 | 2337.84 | 0.865 | 723 | 833 | |
| | 836 | 726 | 1.795 | 2348.05 | 2346.255 | 2344.835 | 2343.445 | 1.39 | 725 | 835 | |
| | 838 | 728 | 2.87 | 2354.745 | 2351.875 | 2351.195 | 2349.065 | 2.13 | 727 | 837 | |
| | 840 | 730 | 3.94 | 2361.43 | 2357.49 | 2358.06 | 2354.685 | 3.375 | 729 | 839 | |
| | 842 | 732 | 5.13 | 2368.225 | 2363.095 | 2364.825 | 2360.295 | 4.53 | 731 | 841 | 56 |
| | 844 | | | | 2368.695 | | 2365.895 | | | 843 | |
| | 846 | 734 | 0.465 | 2374.755 | 2374.29 | 2371.47 | 2371.495 | -0.025 | 733 | 845 | |
| | 848 | 736 | 0.83 | 2380.715 | 2379.885 | 2377.775 | 2377.085 | 0.69 | 735 | 847 | |
| | 850 | 738 | 1.305 | 2386.785 | 2385.48 | 2383.72 | 2382.68 | 1.04 | 737 | 849 | |
| | 852 | 740 | 2.27 | 2393.36 | 2391.09 | 2390.01 | 2388.285 | 1.725 | 739 | 851 | |
| | 854 | 742 | 3.425 | 2400.13 | 2396.705 | 2396.545 | 2393.9 | 2.645 | 741 | 853 | |
| 57 | 856 | 744 | 4.495 | 2406.815 | 2402.32 | 2403.365 | 2399.515 | 3.85 | 743 | 855 | |
| | 858 | | | | 2407.93 | 2410.185 | 2405.125 | 5.06 | 745 | 857 | |
| | 860 | 746 | 0.04 | 2413.575 | 2413.535 | | 2410.73 | | | 859 | |
| | 862 | 748 | 0.725 | 2419.86 | 2419.135 | 2416.745 | 2416.335 | 0.41 | 747 | 861 | |
| | 864 | 750 | 1.07 | 2425.8 | 2424.73 | 2422.805 | 2421.93 | 0.875 | 749 | 863 | |
| | 866 | 752 | 1.655 | 2431.99 | 2430.335 | 2428.845 | 2427.535 | 1.31 | 751 | 865 | |
| | 868 | 754 | 2.715 | 2438.665 | 2435.95 | 2435.355 | 2433.145 | 2.21 | 753 | 867 | |
| | 870 | 756 | 3.93 | 2445.5 | 2441.57 | 2441.965 | 2438.76 | 3.205 | 755 | 869 | |
| | 872 | 758 | 4.925 | 2452.11 | 2447.185 | 2448.745 | 2444.375 | 4.37 | 757 | 871 | 58 |

## 11.2   Supplementary file 2

**Supplementary file 2: Detailed information about the N- and L-cell vortices for the D/d=2.4 case.**

| | | Vortices in the '-Y' side of the step cylinder | | | | Vortices in the '+Y' side of the step cylinder | | | | | |
|---|---|---|---|---|---|---|---|---|---|---|---|
| N-cell cycle No. | L-cell Vortex No. | N-cell vortex No. | $\Phi_f$ | $\varphi_N$ | $\varphi_L$ | $\varphi_N$ | $\varphi_L$ | $\Phi_f$ | N-cell vortex No. | L-cell Vortex No. | N-cell cycle No. |
| | 0 | 0 | 0.635 | 339.98 | 339.345 | 342.975 | 342.155 | 0.82 | 1 | 1 | |
| | 2 | 2 | 1.135 | 346.095 | 344.96 | 349.34 | 347.775 | 1.565 | 3 | 3 | |
| | 4 | 4 | 2.175 | 352.765 | 350.59 | 356.2 | 353.41 | 2.79 | 5 | 5 | |
| | 6 | 6 | 3.46 | 359.69 | 356.23 | 363.115 | 359.08 | 4.035 | 7 | 7 | |
| 1 | 8 | 8 | 4.69 | 366.56 | 361.87 | 369.96 | 364.69 | 5.27 | 9 | 9 | |
| | 10 | | | | 367.505 | | 370.32 | | | 11 | |
| | 12 | 10 | 0.17 | 373.305 | 373.135 | 376.525 | 375.945 | 0.58 | 11 | 13 | |
| | 14 | 12 | 0.82 | 379.58 | 378.76 | 382.605 | 381.57 | 1.035 | 13 | 15 | |
| | 16 | 14 | 1.495 | 385.88 | 384.385 | 389.225 | 387.2 | 2.025 | 15 | 17 | |
| | 18 | 16 | 2.73 | 392.75 | 390.02 | 396.125 | 392.84 | 3.285 | 17 | 19 | |
| | 20 | 18 | 4 | 399.625 | 395.625 | 403.02 | 398.475 | 4.545 | 19 | 21 | 2 |
| | 22 | 20 | 5.145 | 406.43 | 401.285 | | 404.095 | | | 23 | |
| | 24 | | | | 406.905 | 409.81 | 409.715 | 0.095 | 21 | 25 | |
| | 26 | 22 | 0.51 | 413.035 | 412.525 | 416.12 | 415.335 | 0.785 | 23 | 27 | |
| | 28 | 24 | 1.02 | 419.165 | 418.145 | 422.35 | 420.955 | 1.395 | 25 | 29 | |
| | 30 | 26 | 1.955 | 425.73 | 423.775 | 429.22 | 426.595 | 2.625 | 27 | 31 | |
| | 32 | 28 | 3.28 | 432.7 | 429.42 | 436.1 | 432.24 | 3.86 | 29 | 33 | |
| 3 | 34 | 30 | 4.515 | 439.575 | 435.06 | 442.945 | 437.875 | 5.07 | 31 | 35 | |
| | 36 | | | | 440.69 | | 443.5 | | | 37 | |
| | 38 | 32 | 0.055 | 446.365 | 446.31 | 449.595 | 449.12 | 0.475 | 33 | 39 | |
| | 40 | 34 | 0.715 | 452.645 | 451.93 | 455.745 | 454.74 | 1.005 | 35 | 41 | |
| | 42 | 36 | 1.3 | 458.855 | 457.555 | 462.23 | 460.37 | 1.86 | 37 | 43 | |
| | 44 | 38 | 2.465 | 465.65 | 463.185 | 469.21 | 466.005 | 3.205 | 39 | 45 | |
| | 46 | 40 | 3.76 | 472.585 | 468.825 | 476.05 | 471.645 | 4.405 | 41 | 47 | 4 |
| | 48 | 42 | 4.975 | 479.435 | 474.46 | | 477.27 | | | 49 | |
| | 50 | | | | 480.08 | 482.845 | 482.89 | -0.045 | 43 | 51 | |
| | 52 | 44 | 0.47 | 486.17 | 485.7 | 489.22 | 488.51 | 0.71 | 45 | 53 | |
| | 54 | 46 | 0.95 | 492.265 | 491.315 | 495.445 | 494.13 | 1.315 | 47 | 55 | |
| | 56 | 48 | 1.78 | 498.72 | 496.94 | 502.17 | 499.76 | 2.41 | 49 | 57 | |
| | 58 | 50 | 3.05 | 505.63 | 502.58 | 509.15 | 505.4 | 3.75 | 51 | 59 | |
| 5 | 60 | 52 | 4.3 | 512.52 | 508.22 | 515.965 | 511.04 | 4.925 | 53 | 61 | |
| | 62 | | | | 513.855 | | 516.67 | | | 63 | |
| | 64 | 54 | -0.18 | 519.3 | 519.48 | 522.67 | 522.295 | 0.375 | 55 | 65 | |
| | 66 | 56 | 0.68 | 525.785 | 525.105 | 528.78 | 527.92 | 0.86 | 57 | 67 | |
| | 68 | 58 | 1.215 | 531.95 | 530.735 | 535.22 | 533.55 | 1.67 | 59 | 69 | |
| | 70 | 60 | 2.325 | 538.695 | 536.37 | 542.11 | 539.19 | 2.92 | 61 | 71 | |
| | 72 | 62 | 3.61 | 545.62 | 542.01 | 549.035 | 544.83 | 4.205 | 63 | 73 | 6 |
| | 74 | 64 | 4.805 | 552.45 | 547.645 | | 550.455 | | | 75 | |
| | 76 | | | | 553.265 | 555.85 | 556.075 | -0.225 | 65 | 77 | |
| | 78 | 66 | 0.3 | 559.185 | 558.885 | 562.345 | 561.69 | 0.655 | 67 | 79 | |
| | 80 | 68 | 0.885 | 565.385 | 564.5 | 568.45 | 567.31 | 1.14 | 69 | 81 | |
| | 82 | 70 | 1.645 | 571.765 | 570.12 | 575.16 | 572.94 | 2.22 | 71 | 83 | |
| | 84 | 72 | 2.915 | 578.675 | 575.76 | 582.05 | 578.58 | 3.47 | 73 | 85 | |
| 7 | 86 | 74 | 4.17 | 585.565 | 581.395 | 588.93 | 584.215 | 4.715 | 75 | 87 | |
| | 88 | | | | 587.03 | | 589.84 | | | 89 | |
| | 90 | 76 | -0.315 | 592.34 | 592.655 | 595.68 | 595.465 | 0.215 | 77 | 91 | |
| | 92 | 78 | 0.57 | 598.845 | 598.275 | 601.925 | 601.09 | 0.835 | 79 | 93 | |
| | 94 | 80 | 1.08 | 604.98 | 603.9 | 608.235 | 606.715 | 1.52 | 81 | 95 | |
| | 96 | 82 | 2.09 | 611.625 | 609.535 | 615.16 | 612.355 | 2.805 | 83 | 97 | |
| | 98 | 84 | 3.415 | 618.595 | 615.18 | 622.035 | 618 | 4.035 | 85 | 99 | |
| 8 | 100 | 86 | 4.655 | 625.47 | 620.815 | 628.85 | 623.63 | 5.22 | 87 | 101 | |
| | 102 | | | | 626.44 | | 629.25 | | | 103 | |
| | 104 | 88 | 0.21 | 632.27 | 632.06 | 635.43 | 634.87 | 0.56 | 89 | 105 | |
| | 106 | 90 | 0.79 | 638.465 | 637.675 | 641.585 | 640.485 | 1.1 | 91 | 107 | |
| | 108 | 92 | 1.44 | 644.735 | 643.295 | 648.145 | 646.11 | 2.035 | 93 | 109 | |
| | 110 | 94 | 2.65 | 651.58 | 648.93 | 655.135 | 651.745 | 3.39 | 95 | 111 | |
| | 112 | 96 | 3.925 | 658.49 | 654.565 | 661.96 | 657.385 | 4.575 | 97 | 113 | 9 |
| | 114 | 98 | 5.125 | 665.32 | 660.195 | | 663.01 | | | 115 | |
| | 116 | | | | 665.82 | 668.74 | 668.63 | 0.11 | 99 | 117 | |
| | 118 | 100 | 0.545 | 671.985 | 671.44 | 675.005 | 674.25 | 0.755 | 101 | 119 | |
| | 120 | 102 | 1.03 | 678.09 | 677.06 | 681.29 | 679.875 | 1.415 | 103 | 121 | |
| | 122 | 104 | 1.95 | 684.64 | 682.69 | 688.085 | 685.51 | 2.575 | 105 | 123 | |
| | 124 | 106 | 3.235 | 691.57 | 688.335 | 695.05 | 691.155 | 3.895 | 107 | 125 | |
| 10 | 126 | 108 | 4.47 | 698.445 | 693.975 | 701.87 | 696.795 | 5.075 | 109 | 127 | |
| | 128 | | | | 699.61 | | 702.42 | | | 129 | |
| | 130 | 110 | -0.015 | 705.22 | 705.235 | 708.525 | 708.045 | 0.48 | 111 | 131 | |
| | 132 | 112 | 0.735 | 711.595 | 710.86 | 714.605 | 713.67 | 0.935 | 113 | 133 | |
| | 134 | 114 | 1.34 | 717.825 | 716.485 | 721.115 | 719.3 | 1.815 | 115 | 135 | |
| | 136 | 116 | 2.5 | 724.62 | 722.12 | 728.02 | 724.94 | 3.08 | 117 | 137 | |
| | 138 | 118 | 3.78 | 731.54 | 727.76 | 734.925 | 730.575 | 4.35 | 119 | 139 | 11 |
| | 140 | 120 | 4.955 | 738.345 | 733.39 | | 736.2 | | | 141 | |
| | 142 | | | | 739.01 | 741.73 | 741.82 | -0.09 | 121 | 143 | |
| | 144 | 122 | 0.405 | 745.03 | 744.625 | 748.15 | 747.435 | 0.715 | 123 | 145 | |
| | 146 | 124 | 0.94 | 751.18 | 750.24 | 754.3 | 753.05 | 1.25 | 125 | 147 | |
| | 148 | 126 | 1.785 | 757.65 | 755.865 | 761.1 | 758.68 | 2.42 | 127 | 149 | |
| | 150 | 128 | 3.09 | 764.59 | 761.5 | 767.985 | 764.325 | 3.66 | 129 | 151 | |
| 12 | 152 | 130 | 4.335 | 771.475 | 767.14 | 774.845 | 769.96 | 4.885 | 131 | 153 | |
| | 154 | | | | 772.775 | | 775.59 | | | 155 | |
| | 156 | 132 | -0.14 | 778.26 | 778.4 | 781.555 | 781.215 | 0.34 | 133 | 157 | |
| | 158 | 134 | 0.64 | 784.665 | 784.025 | 787.745 | 786.84 | 0.905 | 135 | 159 | |
| | 160 | 136 | 1.16 | 790.815 | 789.655 | 794.135 | 792.47 | 1.665 | 137 | 161 | |
| | 162 | 138 | 2.245 | 797.535 | 795.29 | 801.095 | 798.11 | 2.985 | 139 | 163 | |
| | 164 | 140 | 3.555 | 804.485 | 800.93 | 807.95 | 803.75 | 4.2 | 141 | 165 | 13 |
| | 166 | 142 | 4.79 | 811.355 | 806.565 | | 809.375 | | | 167 | |
| | 168 | | | | 812.185 | 814.75 | 814.995 | -0.245 | 143 | 169 | |
| | 170 | 144 | 0.34 | 818.14 | 817.8 | 821.24 | 820.605 | 0.635 | 145 | 171 | |
| | 172 | 146 | 0.865 | 824.28 | 823.415 | 827.42 | 826.22 | 1.2 | 147 | 173 | |
| | 174 | 148 | 1.59 | 830.625 | 829.035 | 834.06 | 831.85 | 2.21 | 149 | 175 | |
| | 176 | 150 | 2.845 | 837.515 | 834.67 | 841.05 | 837.49 | 3.56 | 151 | 177 | |
| | 178 | 152 | 4.06 | 844.39 | 840.33 | 847.87 | 843.125 | 4.745 | 153 | 179 | 14 |
| | 180 | 154 | 5.275 | 851.215 | 845.94 | | 848.755 | | | 181 | |
| | 182 | | | | 851.57 | 854.625 | 854.38 | 0.245 | 155 | 183 | |
| | 184 | 156 | 0.61 | 857.8 | 857.19 | 860.8 | 860.005 | 0.795 | 157 | 185 | |
| | 186 | 158 | 1.105 | 863.925 | 862.82 | 867.145 | 865.635 | 1.51 | 159 | 187 | |
| | 188 | 160 | 2.12 | 870.57 | 868.635 | 873.995 | 871.275 | 2.72 | 161 | 189 | |
| | 190 | 162 | 3.41 | 877.505 | 874.095 | 880.92 | 876.925 | 3.995 | 163 | 191 | |
| 15 | 192 | 164 | 4.63 | 884.36 | 879.73 | | | | | | |

| | | | | | | | | | | | |
|---|---|---|---|---|---|---|---|---|---|---|---|
| | 194 | | | | 885.36 | 887.765 | 882.545 | 5.22 | 165 | 193 | |
| | 196 | 166 | 0.145 | 891.125 | 890.98 | | 888.17 | | | 195 | |
| | 198 | 168 | 0.805 | 897.405 | 896.6 | 894.36 | 893.79 | 0.57 | 167 | 197 | |
| | 200 | 170 | 1.485 | 903.705 | 902.22 | 900.435 | 899.41 | 1.025 | 169 | 199 | |
| | 202 | 172 | 2.69 | 910.545 | 907.855 | 907.04 | 905.04 | 2 | 171 | 201 | |
| | 204 | 174 | 3.965 | 917.46 | 913.495 | 913.935 | 910.675 | 3.26 | 173 | 203 | |
| | 206 | 176 | 5.115 | 924.245 | 919.13 | 920.825 | 916.315 | 4.51 | 175 | 205 | 16 |
| | 208 | | | | 924.75 | | 921.94 | | | 207 | |
| | 210 | 178 | 0.485 | 930.855 | 930.37 | 927.605 | 927.565 | 0.04 | 177 | 209 | |
| | 212 | 180 | 0.985 | 936.98 | 935.995 | 933.95 | 933.18 | 0.77 | 179 | 211 | |
| | 214 | 182 | 1.915 | 943.535 | 941.62 | 940.17 | 938.805 | 1.365 | 181 | 213 | |
| | 216 | 184 | 3.225 | 950.49 | 947.265 | 947.035 | 944.44 | 2.595 | 183 | 215 | |
| 17 | 218 | 186 | 4.475 | 957.38 | 952.905 | 953.92 | 950.085 | 3.835 | 185 | 217 | |
| | 220 | | | | 958.535 | 960.76 | 955.72 | 5.04 | 187 | 219 | |
| | 222 | 188 | 0.025 | 964.18 | 964.155 | | 961.345 | | | 221 | |
| | 224 | 190 | 0.71 | 970.485 | 969.775 | 967.42 | 966.965 | 0.455 | 189 | 223 | |
| | 226 | 192 | 1.28 | 976.675 | 975.395 | 973.575 | 972.585 | 0.99 | 191 | 225 | |
| | 228 | 194 | 2.44 | 983.465 | 981.025 | 980.04 | 978.21 | 1.83 | 193 | 227 | |
| | 230 | 196 | 3.72 | 990.385 | 986.665 | 987.02 | 983.845 | 3.175 | 195 | 229 | |
| | 232 | 198 | 4.94 | 997.235 | 992.295 | 993.86 | 989.485 | 4.375 | 197 | 231 | 18 |
| | 234 | | | | 997.92 | | 995.11 | | | 233 | |
| | 236 | 200 | 0.445 | 1003.98 | 1003.535 | 1000.65 | 1000.73 | -0.08 | 199 | 235 | |
| | 238 | 202 | 0.94 | 1010.095 | 1009.155 | 1007.035 | 1006.345 | 0.69 | 201 | 237 | |
| | 240 | 204 | 1.75 | 1016.53 | 1014.78 | 1013.25 | 1011.965 | 1.285 | 203 | 239 | |
| | 242 | 206 | 3.035 | 1023.455 | 1020.42 | 1019.97 | 1017.6 | 2.37 | 205 | 241 | |
| 19 | 244 | 208 | 4.275 | 1030.335 | 1026.06 | 1026.955 | 1023.24 | 3.715 | 207 | 243 | |

## 11.3    Supplementary file 3

**Supplementary file 3: Time trace of the $\Phi_f$ between N- and L-cell vortices in the D/d=2 case.**
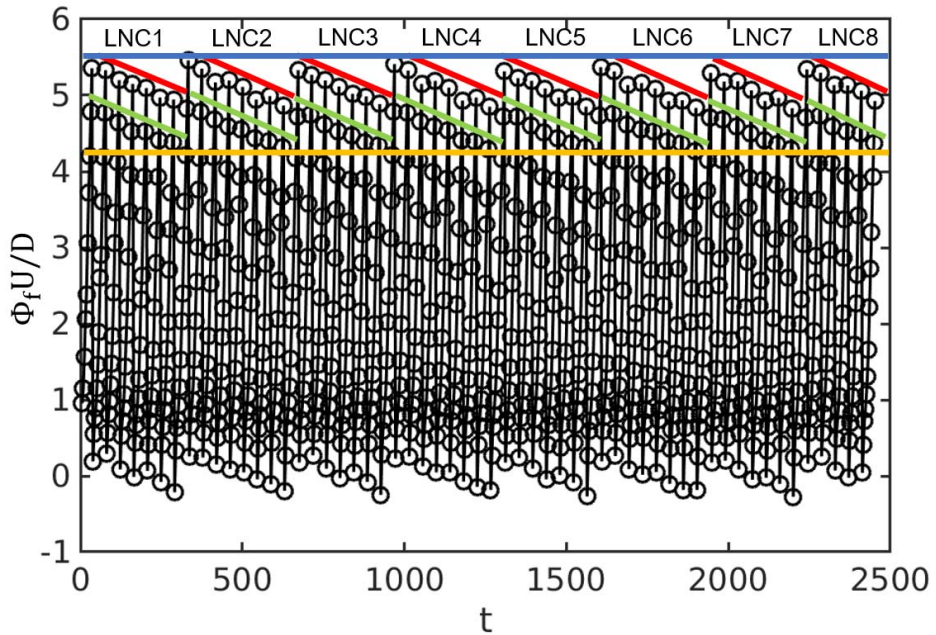


Time trace of $\Phi_f$ between N- and L-cell vortices is plotted in the 1st-8th N-cell cycles. Green and red lines are plotted to describel the tendency of $\Phi_f$ of the NL-loop1s and NL-loop2s. The long N-cell cycles are marked by 'LNC' with serial number. The 'trigger value' and 'threshold value' of vortex dislocations are marked by a blue and yellow line, respectively.

## 11.4 Supplementary file 4
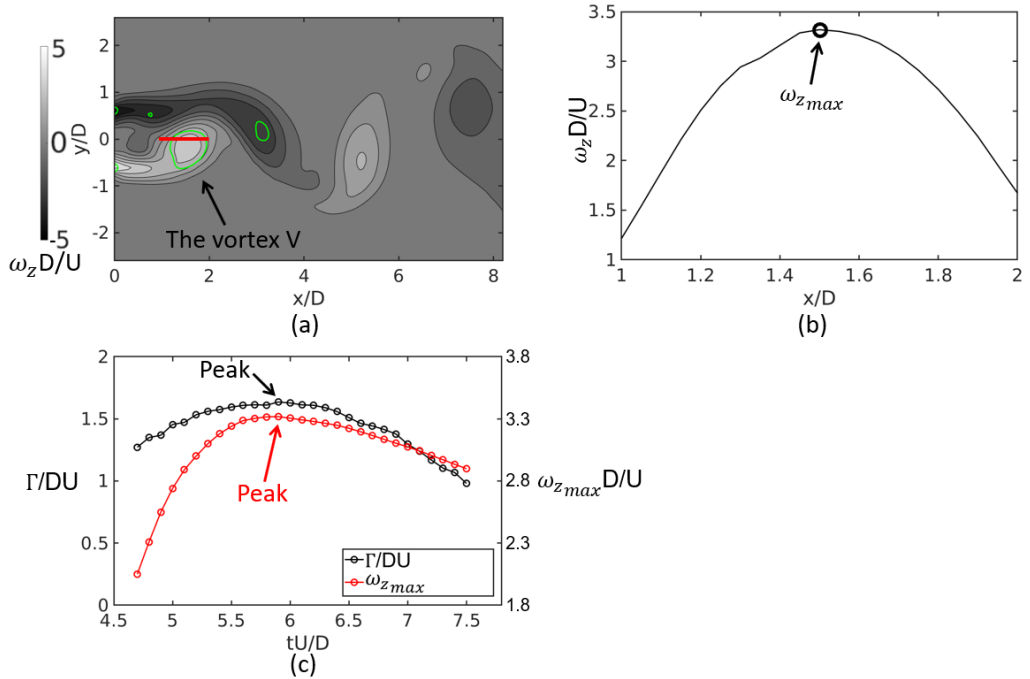
Figure 1. (a) Instantaneous spanwise vorticity $\omega_z$ ($\omega_z = \partial v/\partial x - \partial u/\partial y$) contour plots in a (x,y) plane at z/D = -14 at tU/D = 5.9. An isoline with $\lambda_2 = -1$ is plotted in green. (b) Distribution of $\omega_z$ is plotted along a sampling line at (y/D, z/D) = (0, -14) within the range 1< x/D <2, shown as a red line in subplot (a). (c) Time traces of maximum vorticity $\omega_{z_{max}}D/U$ (black circle in (b)) and the vortex strength $\Gamma/DU$ are plotted from tU/D = 4.6 to 7.5 with a time interval of 0.1D/U. The resolution of the sampling line is 0.05D.

According to Green & Gerrard [1] and Griffin [2], the end of the vortex formation region coincides with the location where the vortex strength becomes maximum. For a spanwise (z-dir.) vortex, the vortex strength in terms of circulation ($\Gamma$) can be measured as: .

$$\Gamma = \int_A \vec{\omega} \cdot d\vec{A} \approx \int_A \omega_z dA$$

In the present case, the integration area is defined as the region within the corresponding isoline $\lambda_2 = -1$. By monitoring the time traces of the strength of a vortex and the corresponding vorticity distribution along the center line at y/D = 0, we found that in the present low-Reynolds-number case the instant when vortex strength reaches its maximum is also the instant when the corresponding largest $\omega_z$ appears at the center line. As an example, the formation process of the vortex $V$ is monitored and plotted in figure 1. In figure 1(a), the $\omega_z$-contour and the isoline for $\lambda_2 = -1$ are plotted in the (x, y)-plane at the L-cell area z/D = -14 at tU/D = 5.9, in which the vortex $V$ is marked. By integrating $\omega_z$ within the green circle surrounding vortex $V$, the vortex strength $\Gamma$ at tU/D = 5.9 can be obtained. At the same instant, the $\omega_z$-distribution along a sampling line (the red line in figure 1(a)) at (y/D, z/D)=(0, -14) is plotted in figure 1(b). The peak of this distribution curve is marked and defined as $\omega_{z_{max}}$. By repeating this process, we were able to plot figure 1(c), from which one can see that the vortex strength and $\omega_{z_{max}}$ at the center line reach their maximum at the same time. This means that in the present low-Reynolds-number case the time instant when the largest $\omega_{z_{max}}$ appears at the center line, is the approximate instant when the corresponding vortex is formed.

REFERENCES:
[1] GREEN, R.B. & GERRARD, J.H. 1993 Vorticity measurements in the near wake of a circular cylinder at low Reynolds numbers. *J. Fluid Mech.* **246,** 675-691.
[2] GRIFFIN, O.M. 1995 A note on bluff body vortex formation. J. Fluid Mech. **284**, 217-224.

## 11.5 Supplementary file 5

Supplementary file 5: Detailed information about the N- and L-cell vortices for the D/d=2.2 case.

### Vortices in the '-Y' side of the step cylinder

| N-cell cycle No. | L-cell Vortex No. | N-cell vortex No. | $\Phi_f$ | $\varphi_N$ | $\varphi_L$ |
|---|---|---|---|---|---|
|  | 2 | 2 | 0.655 | 207.675 | 207.02 |
|  | 4 | 4 | 1.36 | 213.895 | 212.535 |
|  | 6 | 6 | 2.54 | 220.695 | 218.155 |
|  | 8 | 8 | 3.815 | 227.595 | 223.78 |
|  | 10 | 10 | 5 | 234.395 | 229.395 |
|  | 12 |  |  |  | 235.005 |
|  | 14 | 12 | 0.36 | 240.965 | 240.605 |
|  | 16 | 14 | 0.845 | 247.055 | 246.21 |
|  | 18 | 16 | 1.54 | 253.36 | 251.82 |
|  | 20 | 18 | 2.77 | 260.21 | 257.44 |
|  | 22 | 20 | 4.005 | 267.07 | 263.065 |
|  | 24 | 22 | 5.135 | 273.815 | 268.68 |
|  | 26 |  |  |  | 274.295 |
|  | 28 | 24 | 0.42 | 280.325 | 279.905 |
|  | 30 | 26 | 0.88 | 286.395 | 285.515 |
|  | 32 | 28 | 1.635 | 292.77 | 291.135 |
|  | 34 | 30 | 2.84 | 299.605 | 296.765 |
|  | 36 | 32 | 4.09 | 306.49 | 302.4 |
|  | 38 | 34 | 5.205 | 313.23 | 308.025 |
|  | 40 |  |  |  | 313.645 |
|  | 42 | 36 | 0.42 | 319.68 | 319.26 |
|  | 44 | 38 | 0.88 | 325.755 | 324.875 |
|  | 46 | 40 | 1.655 | 332.15 | 330.495 |
|  | 48 | 42 | 2.87 | 338.99 | 336.12 |
|  | 50 | 44 | 4.175 | 345.915 | 341.74 |
|  | 52 | 46 | 5.305 | 352.66 | 347.355 |
|  | 54 |  |  |  | 352.955 |
|  | 56 | 48 | 0.555 | 359.115 | 358.56 |
|  | 58 | 50 | 1.05 | 365.21 | 364.16 |
|  | 60 | 52 | 1.83 | 371.6 | 369.77 |
|  | 62 | 54 | 3.075 | 378.465 | 375.39 |
| 5 | 64 | 56 | 4.33 | 385.345 | 381.015 |
|  | 66 |  |  |  | 386.63 |
|  | 68 | 58 | -0.17 | 392.075 | 392.245 |
|  | 70 | 60 | 0.645 | 398.505 | 397.86 |
|  | 72 | 62 | 1.125 | 404.6 | 403.475 |
|  | 74 | 64 | 1.98 | 411.08 | 409.1 |
|  | 76 | 66 | 3.245 | 417.98 | 414.735 |
| 6 | 78 | 68 | 4.465 | 424.83 | 420.365 |
|  | 80 |  |  |  | 425.99 |
|  | 82 | 70 | -0.06 | 431.545 | 431.605 |
|  | 84 | 72 | 0.635 | 437.855 | 437.22 |
|  | 86 | 74 | 1.125 | 443.96 | 442.835 |
|  | 88 | 76 | 2.155 | 450.61 | 448.455 |
|  | 90 | 78 | 3.445 | 457.53 | 454.085 |
| 7 | 92 | 80 | 4.66 | 464.365 | 459.705 |
|  | 94 |  |  |  | 465.315 |
|  | 96 | 82 | 0.105 | 471.02 | 470.915 |
|  | 98 | 84 | 0.72 | 477.235 | 476.515 |
|  | 100 | 86 | 1.27 | 483.385 | 482.115 |
|  | 102 | 88 | 2.39 | 490.12 | 487.73 |
|  | 104 | 90 | 3.665 | 497.015 | 493.35 |
| 8 | 106 | 92 | 4.83 | 503.8 | 498.97 |
|  | 108 |  |  |  | 504.59 |
|  | 110 | 94 | 0.205 | 510.41 | 510.205 |
|  | 112 | 96 | 0.755 | 516.575 | 515.82 |
|  | 114 | 98 | 1.34 | 522.78 | 521.44 |
|  | 116 | 100 | 2.435 | 529.5 | 527.065 |
|  | 118 | 102 | 3.725 | 536.425 | 532.7 |
|  | 120 | 104 | 4.88 | 543.21 | 538.33 |
|  | 122 |  |  |  | 543.945 |
|  | 124 | 106 | 0.205 | 549.765 | 549.56 |
|  | 126 | 108 | 0.735 | 555.915 | 555.18 |
|  | 128 | 110 | 1.375 | 562.17 | 560.795 |
|  | 130 | 112 | 2.465 | 568.89 | 566.425 |
|  | 132 | 114 | 3.78 | 575.83 | 572.05 |
|  | 134 | 116 | 4.985 | 582.655 | 577.67 |
|  | 136 |  |  |  | 583.275 |
|  | 138 | 118 | 0.325 | 589.2 | 588.875 |
|  | 140 | 120 | 0.88 | 595.35 | 594.47 |
|  | 142 | 122 | 1.545 | 601.62 | 600.075 |
|  | 144 | 124 | 2.68 | 608.37 | 605.69 |
|  | 146 | 126 | 3.955 | 615.27 | 611.315 |
|  | 148 | 128 | 5.145 | 622.08 | 616.935 |
|  | 150 |  |  |  | 622.555 |

### Vortices in the '+Y' side of the step cylinder

| $\varphi_N$ | $\varphi_L$ | $\Phi_f$ | N-cell vortex No. | L-cell Vortex No. | N-cell cycle No. |
|---|---|---|---|---|---|
| 204.615 | 204.11 | 0.505 | 1 | 1 |  |
| 210.695 | 209.725 | 0.97 | 3 | 3 |  |
| 217.155 | 215.345 | 1.81 | 5 | 5 |  |
| 224.035 | 220.97 | 3.065 | 7 | 7 |  |
| 230.945 | 226.59 | 4.355 | 9 | 9 | 1 |
|  | 232.2 |  |  | 11 |  |
| 237.635 | 237.805 | -0.17 | 11 | 13 |  |
| 244.035 | 243.41 | 0.625 | 13 | 15 |  |
| 250.15 | 249.015 | 1.135 | 15 | 17 |  |
| 256.605 | 254.625 | 1.98 | 17 | 19 |  |
| 263.5 | 260.25 | 3.25 | 19 | 21 |  |
| 270.375 | 265.875 | 4.5 | 21 | 23 | 2 |
|  | 271.485 |  |  | 25 |  |
| 277.07 | 277.1 | -0.03 | 23 | 27 |  |
| 283.415 | 282.71 | 0.705 | 25 | 29 |  |
| 289.545 | 288.325 | 1.22 | 27 | 31 |  |
| 296.105 | 293.95 | 2.155 | 29 | 33 |  |
| 303.015 | 299.585 | 3.43 | 31 | 35 |  |
| 309.86 | 305.215 | 4.645 | 33 | 37 | 3 |
|  | 310.835 |  |  | 39 |  |
| 316.55 | 316.455 | 0.095 | 35 | 41 |  |
| 322.765 | 322.07 | 0.695 | 37 | 43 |  |
| 328.925 | 327.685 | 1.24 | 39 | 45 |  |
| 335.655 | 333.305 | 2.35 | 41 | 47 |  |
| 342.57 | 338.93 | 3.64 | 43 | 49 |  |
| 349.39 | 344.55 | 4.84 | 45 | 51 | 4 |
|  | 350.155 |  |  | 53 |  |
| 356.005 | 355.76 | 0.245 | 47 | 55 |  |
| 362.145 | 361.36 | 0.785 | 49 | 57 |  |
| 368.37 | 366.965 | 1.405 | 51 | 59 |  |
| 375.17 | 372.58 | 2.59 | 53 | 61 |  |
| 382.05 | 378.205 | 3.845 | 55 | 63 |  |
| 388.815 | 383.82 | 4.995 | 57 | 65 |  |
|  | 389.435 |  |  | 67 |  |
| 395.375 | 395.05 | 0.325 | 59 | 69 |  |
| 401.48 | 400.665 | 0.815 | 61 | 71 |  |
| 407.77 | 406.285 | 1.485 | 63 | 73 |  |
| 414.55 | 411.92 | 2.63 | 65 | 75 |  |
| 421.46 | 417.55 | 3.91 | 67 | 77 |  |
| 428.225 | 423.18 | 5.045 | 69 | 79 |  |
|  | 428.8 |  |  | 81 |  |
| 434.73 | 434.41 | 0.32 | 71 | 83 |  |
| 440.83 | 440.025 | 0.805 | 73 | 85 |  |
| 447.155 | 445.64 | 1.515 | 75 | 87 |  |
| 453.94 | 451.27 | 2.67 | 77 | 89 |  |
| 460.875 | 456.895 | 3.98 | 79 | 91 |  |
| 467.665 | 462.51 | 5.155 | 81 | 93 |  |
|  | 468.115 |  |  | 95 |  |
| 474.17 | 473.715 | 0.455 | 83 | 97 |  |
| 480.275 | 479.315 | 0.96 | 85 | 99 |  |
| 486.6 | 484.92 | 1.68 | 87 | 101 |  |
| 493.42 | 490.54 | 2.88 | 89 | 103 |  |
| 500.305 | 496.16 | 4.145 | 91 | 105 |  |
| 507.08 | 501.78 | 5.3 | 93 | 107 |  |
|  | 507.395 |  |  | 109 |  |
| 513.59 | 513.01 | 0.58 | 95 | 111 |  |
| 519.665 | 518.625 | 1.04 | 97 | 113 |  |
| 526.06 | 524.25 | 1.81 | 99 | 115 |  |
| 532.935 | 529.885 | 3.05 | 101 | 117 |  |
| 539.8 | 535.515 | 4.285 | 103 | 119 | 9 |
|  | 541.14 |  |  | 121 |  |
| 546.54 | 546.755 | -0.215 | 105 | 123 |  |
| 552.945 | 552.37 | 0.575 | 107 | 125 |  |
| 559.015 | 557.985 | 1.03 | 109 | 127 |  |
| 565.57 | 563.61 | 1.96 | 111 | 129 |  |
| 572.485 | 569.24 | 3.245 | 113 | 131 |  |
| 579.335 | 574.86 | 4.475 | 115 | 133 | 10 |
|  | 580.475 |  |  | 135 |  |
| 586.025 | 586.075 | -0.05 | 117 | 137 |  |
| 592.325 | 591.67 | 0.655 | 119 | 139 |  |
| 598.42 | 597.27 | 1.15 | 121 | 141 |  |
| 605.075 | 602.88 | 2.195 | 123 | 143 |  |
| 611.985 | 608.505 | 3.48 | 125 | 145 |  |
| 618.785 | 614.125 | 4.66 | 127 | 147 | 11 |
|  | 619.745 |  |  | 149 |  |

| | | | | | | | | | | | |
|---|---|---|---|---|---|---|---|---|---|---|---|
| | 152 | 130 | 0.49 | 628.66 | 628.17 | 625.43 | 625.36 | 0.07 | 129 | 151 | |
| | 154 | 132 | 0.96 | 634.74 | 633.78 | 631.675 | 630.975 | 0.7 | 131 | 153 | |
| | 156 | 134 | 1.66 | 641.06 | 639.4 | 637.81 | 636.59 | 1.22 | 133 | 155 | |
| | 158 | 136 | 2.87 | 647.9 | 645.03 | 644.46 | 642.215 | 2.245 | 135 | 157 | |
| | 160 | 138 | 4.115 | 654.775 | 650.66 | 651.395 | 647.845 | 3.55 | 137 | 159 | |
| | 162 | 140 | 5.26 | 661.545 | 656.285 | 658.2 | 653.475 | 4.725 | 139 | 161 | 12 |
| | 164 | | | | 661.9 | | 659.095 | | | 163 | |
| | 166 | 142 | 0.515 | 668.035 | 667.52 | 664.795 | 664.71 | 0.085 | 141 | 165 | |
| | 168 | 144 | 0.95 | 674.085 | 673.135 | 671.015 | 670.325 | 0.69 | 143 | 167 | |
| | 170 | 146 | 1.785 | 680.545 | 678.76 | 677.205 | 675.945 | 1.26 | 145 | 169 | |
| | 172 | 148 | 3.065 | 687.455 | 684.39 | 683.855 | 681.575 | 2.28 | 147 | 171 | |
| 13 | 174 | 150 | 4.305 | 694.315 | 690.01 | 690.785 | 687.205 | 3.58 | 149 | 173 | |
| | | | | | | 697.645 | 692.82 | 4.825 | 151 | 175 | |

## 11.6   Supplementary file 6

## Vortices in the '-Y' side of the step cylinder

| N-cell cycle No. | L-cell Vortex No. | N-cell vortex No. | $\Phi_f$ | $\varphi_N$ | $\varphi_L$ |
|---|---|---|---|---|---|
| | 2 | 2 | 1.97 | 8.375 | 6.405 |
| | 4 | 4 | 3.25 | 15.335 | 12.085 |
| | 6 | 6 | 4.45 | 22.175 | 17.725 |
| | 8 | | | | 23.365 |
| | 10 | 8 | -0.025 | 28.97 | 28.995 |
| | 12 | 10 | 0.555 | 35.185 | 34.63 |
| | 14 | 12 | 1.465 | 41.73 | 40.265 |
| | 16 | 14 | 2.78 | 48.695 | 45.915 |
| 2 | 18 | 16 | 3.955 | 55.52 | 51.565 |
| | 20 | 18 | 5.16 | 62.36 | 57.2 |
| | 22 | | | | 62.825 |
| | 24 | 20 | 0.36 | 68.81 | 68.45 |
| | 26 | 22 | 1.065 | 75.14 | 74.075 |
| | 28 | 24 | 2.26 | 81.975 | 79.715 |
| | 30 | 26 | 3.47 | 88.84 | 85.37 |
| | 32 | 28 | 4.665 | 95.68 | 91.015 |
| | 34 | | | | 96.65 |
| | 36 | 30 | 0.125 | 102.405 | 102.28 |
| | 38 | 32 | 0.7 | 108.61 | 107.91 |
| | 40 | 34 | 1.685 | 115.235 | 113.55 |
| | 42 | 36 | 2.965 | 122.165 | 119.2 |
| | 44 | 38 | 4.195 | 129.04 | 124.845 |
| | 46 | | | | 130.48 |
| | 48 | 40 | -0.22 | 135.885 | 136.105 |
| | 50 | 42 | 0.44 | 142.17 | 141.73 |
| | 52 | 44 | 1.235 | 148.595 | 147.36 |
| | 54 | 46 | 2.525 | 155.525 | 153 |
| 5 | 56 | 48 | 3.745 | 162.4 | 158.655 |
| | 58 | 50 | 4.93 | 169.225 | 164.295 |
| | 60 | | | | 169.925 |
| | 62 | 52 | 0.225 | 175.78 | 175.555 |
| | 64 | 54 | 0.89 | 182.075 | 181.185 |
| | 66 | 56 | 2.01 | 188.835 | 186.825 |
| | 68 | 58 | 3.25 | 195.725 | 192.475 |
| | 70 | 60 | 4.44 | 202.555 | 198.115 |
| | 72 | | | | 203.75 |
| | 74 | 62 | -0.035 | 209.34 | 209.375 |
| | 76 | 64 | 0.605 | 215.605 | 215 |
| | 78 | 66 | 1.475 | 222.105 | 220.63 |
| | 80 | 68 | 2.74 | 229.02 | 226.28 |
| 7 | 82 | 70 | 3.975 | 235.905 | 231.93 |
| | 84 | 72 | 5.195 | 242.76 | 237.565 |
| | 86 | | | | 243.195 |
| | 88 | 74 | 0.36 | 249.18 | 248.82 |
| | 90 | 76 | 1.035 | 255.485 | 254.45 |
| | 92 | 78 | 2.26 | 262.35 | 260.09 |
| | 94 | 80 | 3.54 | 269.28 | 265.74 |
| | 96 | 82 | 4.71 | 276.095 | 271.385 |
| | 98 | | | | 277.015 |
| | 100 | 84 | 0.115 | 282.755 | 282.64 |
| | 102 | 86 | 0.74 | 289.005 | 288.265 |
| | 104 | 88 | 1.79 | 295.69 | 293.9 |
| | 106 | 90 | 3.07 | 302.62 | 299.55 |
| | 108 | 92 | 4.245 | 309.445 | 305.2 |
| | 110 | | | | 310.835 |
| | 112 | 94 | -0.205 | 316.255 | 316.46 |
| | 114 | 96 | 0.515 | 322.6 | 322.085 |
| | 116 | 98 | 1.29 | 329.005 | 327.715 |
| | 118 | 100 | 2.54 | 335.9 | 333.36 |
| 10 | 120 | 102 | 3.765 | 342.775 | 339.01 |
| | 122 | 104 | 4.98 | 349.63 | 344.65 |
| | 124 | | | | 350.28 |
| | 126 | 106 | 0.285 | 356.19 | 355.905 |
| | 128 | 108 | 0.875 | 362.41 | 361.535 |
| | 130 | 110 | 2.015 | 369.19 | 367.175 |
| | 132 | 112 | 3.32 | 376.145 | 372.825 |
| | 134 | 114 | 4.505 | 382.97 | 378.465 |
| | 136 | | | | 384.1 |
| | 138 | 116 | 0.01 | 389.735 | 389.725 |
| | 140 | 118 | 0.6 | 395.95 | 395.35 |
| | 142 | 120 | 1.555 | 402.54 | 400.985 |
| | 144 | 122 | 2.865 | 409.5 | 406.635 |
| 12 | 146 | 124 | 4.04 | 416.325 | 412.285 |
| | 148 | 126 | 5.235 | 423.155 | 417.92 |
| | 150 | | | | 423.55 |
| | 152 | 128 | 0.4 | 429.575 | 429.175 |
| | 154 | 130 | 1.12 | 435.925 | 434.805 |

## Vortices in the '+Y' side of the step cylinder

| $\varphi_N$ | $\varphi_L$ | $\Phi_f$ | N-cell vortex No. | L-cell Vortex No. | N-cell cycle No. |
|---|---|---|---|---|---|
| 4.985 | 3.62 | 1.365 | 1 | 1 | |
| 11.915 | 9.26 | 2.655 | 3 | 3 | |
| 18.755 | 14.905 | 3.85 | 5 | 5 | 1 |
| 25.59 | 20.545 | 5.045 | 7 | 7 | |
| | 26.18 | | | 9 | |
| 32.135 | 31.81 | 0.325 | 9 | 11 | |
| 38.38 | 37.445 | 0.935 | 11 | 13 | |
| 45.165 | 43.09 | 2.075 | 13 | 15 | |
| 52.07 | 48.74 | 3.33 | 15 | 17 | |
| 58.925 | 54.385 | 4.54 | 17 | 19 | |
| | 60.015 | | | 21 | |
| 65.7 | 65.64 | 0.06 | 19 | 23 | |
| 71.885 | 71.26 | 0.625 | 21 | 25 | |
| 78.465 | 76.895 | 1.57 | 23 | 27 | |
| 85.435 | 82.54 | 2.895 | 25 | 29 | |
| 92.285 | 88.19 | 4.095 | 27 | 31 | 3 |
| 99.13 | 93.83 | 5.3 | 29 | 33 | |
| | 99.465 | | | 35 | |
| 105.485 | 105.095 | 0.39 | 31 | 37 | |
| 111.875 | 110.725 | 1.15 | 33 | 39 | |
| 118.77 | 116.375 | 2.395 | 35 | 41 | |
| 125.625 | 122.025 | 3.6 | 37 | 43 | 4 |
| 132.45 | 127.665 | 4.785 | 39 | 45 | |
| | 133.295 | | | 47 | |
| 139.095 | 138.915 | 0.18 | 41 | 49 | |
| 145.35 | 144.54 | 0.81 | 43 | 51 | |
| 152.03 | 150.18 | 1.85 | 45 | 53 | |
| 158.93 | 155.83 | 3.1 | 47 | 55 | |
| 165.79 | 161.475 | 4.315 | 49 | 57 | |
| | 167.11 | | | 59 | |
| 172.625 | 172.74 | -0.115 | 51 | 61 | |
| 178.88 | 178.37 | 0.51 | 53 | 63 | |
| 185.335 | 184 | 1.335 | 55 | 65 | |
| 192.26 | 189.65 | 2.61 | 57 | 67 | |
| 199.16 | 195.295 | 3.865 | 59 | 69 | 6 |
| 206 | 200.935 | 5.065 | 61 | 71 | |
| | 206.56 | | | 73 | |
| 212.47 | 212.185 | 0.285 | 63 | 75 | |
| 218.775 | 217.815 | 0.96 | 65 | 77 | |
| 225.605 | 223.455 | 2.15 | 67 | 79 | |
| 232.515 | 229.105 | 3.41 | 69 | 81 | |
| 239.33 | 234.75 | 4.58 | 71 | 83 | |
| | 240.38 | | | 85 | |
| 246.045 | 246.01 | 0.035 | 73 | 87 | |
| 252.32 | 251.635 | 0.685 | 75 | 89 | |
| 258.905 | 257.27 | 1.635 | 77 | 91 | |
| 265.82 | 262.915 | 2.905 | 79 | 93 | |
| 272.665 | 268.565 | 4.1 | 81 | 95 | 8 |
| 279.515 | 274.2 | 5.315 | 83 | 97 | |
| | 279.825 | | | 99 | |
| 285.89 | 285.45 | 0.44 | 85 | 101 | |
| 292.23 | 291.08 | 1.15 | 87 | 103 | |
| 299.105 | 296.725 | 2.38 | 89 | 105 | |
| 306.03 | 302.375 | 3.655 | 91 | 107 | 9 |
| 312.865 | 308.015 | 4.85 | 93 | 109 | |
| | 313.645 | | | 111 | |
| 319.47 | 319.275 | 0.195 | 95 | 113 | |
| 325.695 | 324.9 | 0.795 | 97 | 115 | |
| 332.44 | 330.54 | 1.9 | 99 | 117 | |
| 339.4 | 336.19 | 3.21 | 101 | 119 | |
| 346.21 | 341.83 | 4.38 | 103 | 121 | |
| | 347.465 | | | 123 | |
| 352.995 | 353.095 | -0.1 | 105 | 125 | |
| 359.28 | 358.72 | 0.56 | 107 | 127 | |
| 365.785 | 364.35 | 1.435 | 109 | 129 | |
| 372.71 | 369.995 | 2.715 | 111 | 131 | |
| 379.55 | 375.645 | 3.905 | 113 | 133 | 11 |
| 386.39 | 381.285 | 5.105 | 115 | 135 | |
| | 386.915 | | | 137 | |
| 392.89 | 392.54 | 0.35 | 117 | 139 | |
| 399.155 | 398.17 | 0.985 | 119 | 141 | |
| 405.975 | 403.81 | 2.165 | 121 | 143 | |
| 412.88 | 409.46 | 3.42 | 123 | 145 | |
| 419.73 | 415.105 | 4.625 | 125 | 147 | |
| | 420.735 | | | 149 | |
| 426.465 | 426.365 | 0.1 | 127 | 151 | |
| 432.65 | 431.99 | 0.66 | 129 | 153 | |

| | | | | | | | | | | | |
|---|---|---|---|---|---|---|---|---|---|---|---|
| 156 | 132 | 2.33 | 442.78 | 440.45 | | 439.28 | 437.625 | 1.655 | 131 | 155 | |
| 158 | 134 | 3.545 | 449.645 | 446.1 | | 446.255 | 443.275 | 2.98 | 133 | 157 | |
| 160 | 136 | 4.75 | 456.49 | 451.74 | | 453.09 | 448.92 | 4.17 | 135 | 159 | 13 |
| 162 | | | | 457.37 | | 459.925 | 454.555 | 5.37 | 137 | 161 | |
| 164 | 138 | 0.175 | 463.175 | 463 | | | 460.185 | | | 163 | |
| 166 | 140 | 0.74 | 469.365 | 468.625 | | 466.24 | 465.81 | 0.43 | 139 | 165 | |
| 168 | 142 | 1.78 | 476.045 | 474.265 | | 472.67 | 471.44 | 1.23 | 141 | 167 | |
| 170 | 144 | 3.075 | 482.985 | 479.91 | | 479.58 | 477.085 | 2.495 | 143 | 169 | |
| 172 | 146 | 4.285 | 489.845 | 485.56 | | 486.43 | 482.735 | 3.695 | 145 | 171 | 14 |

## 11.7   Supplementary file 7

Supplementary file 7: Detailed information about the N- and L-cell vortices for the D/d=2.8 case.

| N-cell cycle No. | L-cell Vortex No. | N-cell vortex No. | $\Phi_f$ | $\varphi_N$ | $\varphi_L$ | $\varphi_N$ | $\varphi_L$ | $\Phi_f$ | N-cell vortex No. | L-cell Vortex No. | N-cell cycle No. |
|---|---|---|---|---|---|---|---|---|---|---|---|
| | 2 | 2 | 0.2575 | 59.14 | 58.8825 | 55.93 | 56.0675 | -0.1375 | 1 | 1 | |
| | 4 | 4 | 1.1975 | 65.715 | 64.5175 | 62.395 | 61.6975 | 0.6975 | 3 | 3 | |
| | 6 | 6 | 2.5225 | 72.695 | 70.1725 | 69.23 | 67.3425 | 1.8875 | 5 | 5 | |
| 1 | 8 | 8 | 3.7125 | 79.54 | 75.8275 | 76.11 | 72.9975 | 3.1125 | 7 | 7 | |
| | 10 | 10 | 4.9275 | 86.4 | 81.4725 | 82.975 | 78.6525 | 4.3225 | 9 | 9 | |
| | 12 | | | | 87.1075 | 89.71 | 84.2925 | 5.4175 | 11 | 11 | |
| | 14 | 12 | 0.1425 | 92.885 | 92.7425 | | 89.9275 | | | 13 | |
| | 16 | 14 | 1.0275 | 99.41 | 98.3825 | 96.04 | 95.5625 | 0.4775 | 13 | 15 | |
| | 18 | 16 | 2.2475 | 106.29 | 104.0425 | 102.845 | 101.2075 | 1.6375 | 15 | 17 | |
| 2 | 20 | 18 | 3.4725 | 113.175 | 109.7025 | 109.765 | 106.8725 | 2.8925 | 17 | 19 | |
| | 22 | 20 | 4.6975 | 120.055 | 115.3575 | 116.6 | 112.5325 | 4.0675 | 19 | 21 | |
| | 24 | | | | 120.9975 | 123.41 | 118.1825 | 5.2275 | 21 | 23 | |
| | 26 | 22 | -0.0425 | 126.595 | 126.6375 | | 123.8175 | | | 25 | |
| | 28 | 24 | 0.7925 | 133.07 | 132.2775 | 129.82 | 129.4525 | 0.3675 | 23 | 27 | |
| | 30 | 26 | 2.0225 | 139.95 | 137.9275 | 136.43 | 135.0975 | 1.3325 | 25 | 29 | |
| 3 | 32 | 28 | 3.2275 | 146.82 | 143.5925 | 143.395 | 140.7625 | 2.6325 | 27 | 31 | |
| | 34 | 30 | 4.4375 | 153.685 | 149.2475 | 150.245 | 146.4225 | 3.8225 | 29 | 33 | |
| | 36 | | | | 154.8925 | 157.1 | 152.0725 | 5.0275 | 31 | 35 | |
| | 38 | 32 | -0.1425 | 160.385 | 160.5275 | | 157.7125 | | | 37 | |
| | 40 | 34 | 0.5625 | 166.725 | 166.1625 | 163.53 | 163.3425 | 0.1875 | 33 | 39 | |
| | 42 | 36 | 1.7325 | 173.545 | 171.8125 | 170.13 | 168.9875 | 1.1425 | 35 | 41 | |
| | 44 | 38 | 2.9975 | 180.475 | 177.4775 | 177.015 | 174.6425 | 2.3725 | 37 | 43 | |
| | 46 | 40 | 4.1825 | 187.315 | 183.1325 | 183.88 | 180.3075 | 3.5725 | 39 | 45 | 4 |
| | 48 | 42 | 5.2975 | 194.075 | 188.7775 | 190.765 | 185.9575 | 4.8075 | 41 | 47 | |
| | 50 | | | | 194.4175 | | 191.5975 | | | 49 | |
| | 52 | 44 | 0.4475 | 200.505 | 200.0575 | 197.27 | 197.2375 | 0.0325 | 43 | 51 | |
| | 54 | 46 | 1.4575 | 207.16 | 205.7025 | 203.745 | 202.8775 | 0.8675 | 45 | 53 | |
| | 56 | 48 | 2.7325 | 214.1 | 211.3675 | 210.67 | 208.5325 | 2.1375 | 47 | 55 | |
| | 58 | 50 | 3.9225 | 220.95 | 217.0275 | 217.535 | 214.1975 | 3.3375 | 49 | 57 | 5 |
| | 60 | 52 | 5.1275 | 227.8 | 222.6725 | 224.4 | 219.8525 | 4.5475 | 51 | 59 | |
| | 62 | | | | 228.3125 | | 225.4925 | | | 61 | |
| | 64 | 54 | 0.2375 | 234.18 | 233.9425 | 231.05 | 231.1275 | -0.0775 | 53 | 63 | |
| | 66 | 56 | 1.2525 | 240.84 | 239.5875 | 237.43 | 236.7625 | 0.6675 | 55 | 65 | |
| | 68 | 58 | 2.5025 | 247.745 | 245.2425 | 244.255 | 242.4125 | 1.8425 | 57 | 67 | |
| 6 | 70 | 60 | 3.6825 | 254.59 | 250.9075 | 251.135 | 248.1275 | 3.0075 | 59 | 69 | |
| | 72 | 62 | 4.9175 | 261.475 | 256.5575 | 258.035 | 253.7375 | 4.2975 | 61 | 71 | |
| | 74 | | | | 262.2025 | 264.745 | 259.3825 | 5.3625 | 63 | 73 | |
| | 76 | 64 | 0.1175 | 267.955 | 267.8375 | | 265.0225 | | | 75 | |
| | 78 | 66 | 0.9525 | 274.43 | 273.4775 | 271.18 | 270.6575 | 0.5225 | 65 | 77 | |
| | 80 | 68 | 2.2475 | 281.385 | 279.1375 | 277.9 | 276.3075 | 1.5925 | 67 | 79 | |
| 7 | 82 | 70 | 3.4475 | 288.25 | 284.8025 | 284.81 | 281.9675 | 2.8425 | 69 | 81 | |
| | 84 | 72 | 4.6625 | 295.115 | 290.4525 | 291.665 | 287.6275 | 4.0375 | 71 | 83 | |
| | 86 | | | | 296.0925 | 298.495 | 293.2725 | 5.2225 | 73 | 85 | |
| | 88 | 74 | -0.0175 | 301.71 | 301.7275 | | 298.9075 | | | 87 | |
| | 90 | 76 | 0.7825 | 308.145 | 307.3625 | 304.845 | 304.5425 | 0.3025 | 75 | 89 | |
| | 92 | 78 | 1.9575 | 314.97 | 313.0125 | 311.545 | 310.1875 | 1.3575 | 77 | 91 | |
| 8 | 94 | 80 | 3.2075 | 321.89 | 318.6825 | 318.47 | 315.8475 | 2.6225 | 79 | 93 | |
| | 96 | 82 | 4.4075 | 328.745 | 324.3375 | 325.305 | 321.5125 | 3.7925 | 81 | 95 | |
| | 98 | | | | 329.9825 | 332.17 | 327.1625 | 5.0075 | 83 | 97 | |
| | 100 | 84 | -0.2025 | 335.42 | 335.6225 | | 332.8025 | | | 99 | |
| | 102 | 86 | 0.5775 | 341.84 | 341.2625 | 338.635 | 338.4425 | 0.1925 | 85 | 101 | |
| | 104 | 88 | 1.7275 | 348.64 | 346.9125 | 345.135 | 344.0825 | 1.0525 | 87 | 103 | |
| | 106 | 90 | 2.9525 | 355.53 | 352.5775 | 352.095 | 349.7425 | 2.3525 | 89 | 105 | |
| | 108 | 92 | 4.1475 | 362.38 | 358.2325 | 358.96 | 355.4075 | 3.5525 | 91 | 107 | 9 |
| | 110 | 94 | 5.3075 | 369.18 | 363.8725 | 365.835 | 361.0525 | 4.7825 | 93 | 109 | |
| | 112 | | | | 369.5075 | | 366.6925 | | | 111 | |
| | 114 | 96 | 0.3775 | 375.52 | 375.1425 | 372.355 | 372.3225 | 0.0325 | 95 | 113 | |
| | 116 | 98 | 1.4575 | 382.24 | 380.7825 | 378.86 | 377.9625 | 0.8975 | 97 | 115 | |
| | 118 | 100 | 2.7425 | 389.19 | 386.4475 | 385.705 | 383.6125 | 2.0925 | 99 | 117 | |
| | 120 | 102 | 3.9075 | 396.02 | 392.1125 | 392.595 | 389.2825 | 3.3125 | 101 | 119 | 10 |
| | 122 | 104 | 5.0925 | 402.855 | 397.7625 | 399.465 | 394.9375 | 4.5275 | 103 | 121 | |
| | 124 | | | | 403.4025 | | 400.5825 | | | 123 | |
| | 126 | 106 | 0.2725 | 409.315 | 409.0425 | 406.1 | 406.2225 | -0.1225 | 105 | 125 | |
| | 128 | 108 | 1.1725 | 415.86 | 414.6875 | 412.5 | 411.8625 | 0.6375 | 107 | 127 | |
| | 130 | 110 | 2.4525 | 422.8 | 420.3475 | 419.365 | 417.5125 | 1.8525 | 109 | 129 | |
| 11 | 132 | 112 | 3.6575 | 429.665 | 426.0075 | 426.25 | 423.2275 | 3.0225 | 111 | 131 | |
| | 134 | 114 | 4.8925 | 436.55 | 431.6575 | 433.095 | 428.8325 | 4.2625 | 113 | 133 | |
| | 136 | | | | 437.2925 | 439.86 | 434.4725 | 5.3875 | 115 | 135 | |
| | 138 | 116 | 0.0825 | 443.005 | 442.9225 | | 440.1075 | | | 137 | |
| | 140 | 118 | 1.0025 | 449.565 | 448.5625 | 446.215 | 445.7425 | 0.4725 | 117 | 139 | |
| | 142 | 120 | 2.2225 | 456.44 | 454.2175 | 452.945 | 451.3875 | 1.5575 | 119 | 141 | |
| 12 | 144 | 122 | 3.4225 | 463.305 | 459.8825 | 459.9 | 457.0475 | 2.8525 | 121 | 143 | |
| | 146 | 124 | 4.6475 | 470.185 | 465.5375 | 466.74 | 462.7125 | 4.0275 | 123 | 145 | |

Vortices in the '-Y' side of the step cylinder      Vortices in the '+Y' side of the step cylinder

# 11.8   Supplementary file 8

Supplementary file 8: Detailed information about the N- and L-cell vortices for the D/d=3.0 case.

### Vortices in the '-Y' side of the step cylinder

| N-cell cycle No. | L-cell Vortex No. | N-cell vortex No. | $\Phi_f$ | $\varphi_N$ | $\varphi_L$ |
|---|---|---|---|---|---|
| 1 | 2 | 2 | 3.106 | 204.64 | 201.534 |
|  | 4 | 4 | 4.356 | 211.555 | 207.199 |
|  | 6 |  |  |  | 212.849 |
|  | 8 | 6 | -0.204 | 218.295 | 218.499 |
|  | 10 | 8 | 0.756 | 224.92 | 224.164 |
|  | 12 | 10 | 1.931 | 231.785 | 229.854 |
| 2 | 14 | 12 | 3.141 | 238.685 | 235.544 |
|  | 16 | 14 | 4.421 | 245.61 | 241.189 |
|  | 18 |  |  |  | 246.844 |
|  | 20 | 16 | -0.159 | 252.335 | 252.494 |
|  | 22 | 18 | 0.806 | 258.965 | 258.159 |
|  | 24 | 20 | 1.996 | 265.845 | 263.849 |
| 3 | 26 | 22 | 3.221 | 272.75 | 269.529 |
|  | 28 | 24 | 4.481 | 279.665 | 275.184 |
|  | 30 |  |  |  | 280.839 |
|  | 32 | 26 | -0.114 | 286.375 | 286.489 |
|  | 34 | 28 | 0.861 | 293.015 | 292.154 |
|  | 36 | 30 | 2.056 | 299.9 | 297.844 |
| 4 | 38 | 32 | 3.281 | 306.805 | 303.524 |
|  | 40 | 34 | 4.541 | 313.72 | 309.179 |
|  | 42 |  |  |  | 314.829 |
|  | 44 | 36 | -0.069 | 320.415 | 320.484 |
|  | 46 | 38 | 0.911 | 327.065 | 326.154 |
|  | 48 | 40 | 2.111 | 333.955 | 331.844 |
| 5 | 50 | 42 | 3.341 | 340.86 | 337.519 |
|  | 52 | 44 | 4.601 | 347.775 | 343.174 |
|  | 54 |  |  |  | 348.824 |
|  | 56 | 46 | -0.024 | 354.455 | 354.479 |
|  | 58 | 48 | 0.966 | 361.115 | 360.149 |
|  | 60 | 50 | 2.176 | 368.015 | 365.839 |
| 6 | 62 | 52 | 3.401 | 374.915 | 371.514 |
|  | 64 | 54 | 4.656 | 381.825 | 377.169 |
|  | 66 |  |  |  | 382.819 |
|  | 68 | 56 | 0.021 | 388.495 | 388.474 |
|  | 70 | 58 | 1.021 | 395.165 | 394.144 |
|  | 72 | 60 | 2.236 | 402.07 | 399.834 |
| 7 | 74 | 62 | 3.461 | 408.97 | 405.509 |
|  | 76 | 64 | 4.716 | 415.88 | 411.164 |
|  | 78 |  |  |  | 416.814 |
|  | 80 | 66 | 0.071 | 422.535 | 422.464 |
|  | 82 | 68 | 1.081 | 429.22 | 428.139 |
|  | 84 | 70 | 2.296 | 436.125 | 433.829 |
| 8 | 86 | 72 | 3.521 | 443.025 | 439.504 |
|  | 88 | 74 | 4.771 | 449.93 | 445.159 |
|  | 90 |  |  |  | 450.809 |
|  | 92 | 76 | 0.116 | 456.575 | 456.459 |
|  | 94 | 78 | 1.131 | 463.27 | 462.139 |
|  | 96 | 80 | 2.356 | 470.185 | 467.829 |
| 9 | 98 | 82 | 3.586 | 477.085 | 473.499 |
|  | 100 | 84 | 4.826 | 483.98 | 479.154 |
|  | 102 |  |  |  | 484.804 |
|  | 104 | 86 | 0.161 | 490.615 | 490.454 |
|  | 106 | 88 | 1.191 | 497.325 | 496.134 |
|  | 108 | 90 | 2.416 | 504.24 | 501.824 |
| 10 | 110 | 92 | 3.646 | 511.14 | 507.494 |
|  | 112 | 94 | 4.881 | 518.03 | 513.149 |
|  | 114 |  |  |  | 518.799 |
|  | 116 | 96 | 0.201 | 524.655 | 524.454 |
|  | 118 | 98 | 1.246 | 531.375 | 530.129 |
|  | 120 | 100 | 2.476 | 538.295 | 535.819 |
|  | 122 | 102 | 3.706 | 545.195 | 541.489 |
|  | 124 | 104 | 4.931 | 552.075 | 547.144 |
|  | 126 |  |  |  | 552.794 |
|  | 128 | 106 | 0.246 | 558.695 | 558.449 |
|  | 130 | 108 | 1.301 | 565.43 | 564.129 |
|  | 132 | 110 | 2.536 | 572.35 | 569.814 |
|  | 134 | 112 | 3.766 | 579.25 | 575.484 |
|  | 136 | 114 | 4.986 | 586.125 | 581.139 |
|  | 138 |  |  |  | 586.784 |
|  | 140 | 116 | 0.291 | 592.735 | 592.444 |
|  | 142 | 118 | 1.361 | 599.485 | 598.124 |
|  | 144 | 120 | 2.601 | 606.41 | 603.809 |
|  | 146 | 122 | 3.826 | 613.305 | 609.479 |
|  | 148 |  | 5.036 | 620.17 | 615.134 |
|  | 150 | 124 |  |  | 620.779 |
|  | 152 | 126 | 0.336 | 626.775 | 626.439 |
|  | 154 | 128 | 1.421 | 633.54 | 632.119 |

### Vortices in the '+Y' side of the step cylinder

| $\varphi_N$ | $\varphi_L$ | $\Phi_f$ | N-cell vortex No. | L-cell Vortex No. | N-cell cycle No. |
|---|---|---|---|---|---|
| 201.195 | 198.699 | 2.496 | 1 | 1 |  |
| 208.09 | 204.369 | 3.721 | 3 | 3 |  |
| 214.97 | 210.024 | 4.946 | 5 | 5 |  |
|  | 215.674 |  |  | 7 |  |
| 221.59 | 221.329 | 0.261 | 7 | 9 |  |
| 228.325 | 227.009 | 1.316 | 9 | 11 |  |
| 235.25 | 232.694 | 2.556 | 11 | 13 |  |
| 242.15 | 238.364 | 3.786 | 13 | 15 |  |
| 249.02 | 244.019 | 5.001 | 15 | 17 |  |
|  | 249.664 |  |  | 19 |  |
| 255.63 | 255.324 | 0.306 | 17 | 21 |  |
| 262.38 | 261.004 | 1.376 | 19 | 23 |  |
| 269.305 | 266.694 | 2.611 | 21 | 25 |  |
| 276.205 | 272.359 | 3.846 | 23 | 27 |  |
| 283.065 | 278.014 | 5.051 |  | 29 |  |
|  | 283.659 |  | 25 | 31 |  |
| 289.67 | 289.319 | 0.351 | 27 | 33 |  |
| 296.435 | 294.999 | 1.436 | 29 | 35 |  |
| 303.36 | 300.689 | 2.671 | 31 | 37 |  |
| 310.26 | 306.354 | 3.906 | 33 | 39 |  |
| 317.11 | 312.009 | 5.101 |  | 41 |  |
|  | 317.654 |  | 35 | 43 |  |
| 323.715 | 323.314 | 0.401 | 37 | 45 |  |
| 330.495 | 328.999 | 1.496 | 39 | 47 |  |
| 337.415 | 334.684 | 2.731 | 41 | 49 |  |
| 344.315 | 340.349 | 3.966 | 43 | 51 |  |
| 351.155 | 345.999 | 5.156 | 45 | 53 |  |
|  | 351.649 |  |  | 55 |  |
| 357.755 | 357.309 | 0.446 | 47 | 57 |  |
| 364.55 | 362.994 | 1.556 | 49 | 59 |  |
| 371.47 | 368.679 | 2.791 | 51 | 61 |  |
| 378.375 | 374.344 | 4.031 | 53 | 63 |  |
| 385.195 | 379.994 | 5.201 |  | 65 |  |
|  | 385.644 |  | 55 | 67 |  |
| 391.8 | 391.304 | 0.496 | 57 | 69 |  |
| 398.605 | 396.989 | 1.616 | 59 | 71 |  |
| 405.525 | 402.674 | 2.851 | 61 | 73 |  |
| 412.43 | 408.339 | 4.091 | 63 | 75 |  |
| 419.24 | 413.989 | 5.251 |  | 77 |  |
|  | 419.639 |  | 65 | 79 |  |
| 425.845 | 425.299 | 0.546 | 67 | 81 |  |
| 432.66 | 430.989 | 1.671 | 69 | 83 |  |
| 439.58 | 436.669 | 2.911 | 71 | 85 |  |
| 446.49 | 442.334 | 4.156 | 73 | 87 |  |
| 453.28 | 447.984 | 5.296 |  | 89 |  |
|  | 453.634 |  | 75 | 91 |  |
| 459.89 | 459.299 | 0.591 | 77 | 93 |  |
| 466.72 | 464.984 | 1.736 | 79 | 95 |  |
| 473.635 | 470.664 | 2.971 | 81 | 97 |  |
| 480.545 | 476.329 | 4.216 | 83 | 99 |  |
| 487.325 | 481.979 | 5.346 |  | 101 |  |
|  | 487.629 |  | 85 | 103 |  |
| 493.935 | 493.289 | 0.646 | 87 | 105 |  |
| 500.775 | 498.979 | 1.796 | 89 | 107 |  |
| 507.69 | 504.659 | 3.031 | 91 | 109 |  |
| 514.6 | 510.319 | 4.281 | 93 | 111 |  |
| 521.365 | 515.974 | 5.391 | 95 | 113 |  |
|  | 521.624 |  |  | 115 |  |
| 527.98 | 527.289 | 0.691 | 97 | 117 |  |
| 534.835 | 532.974 | 1.861 | 99 | 119 |  |
| 541.745 | 538.654 | 3.091 | 101 | 121 | 11 |
| 548.66 | 544.319 | 4.341 | 103 | 123 |  |
|  | 549.969 |  |  | 125 |  |
| 555.405 | 555.619 | -0.214 | 105 | 127 |  |
| 562.025 | 561.284 | 0.741 | 107 | 129 |  |
| 568.89 | 566.974 | 1.916 | 109 | 131 |  |
| 575.795 | 572.654 | 3.141 | 111 | 133 | 12 |
| 582.715 | 578.309 | 4.406 | 113 | 135 |  |
|  | 583.964 |  |  | 137 |  |
| 589.445 | 589.614 | -0.169 | 115 | 139 |  |
| 596.075 | 595.279 | 0.796 | 117 | 141 |  |
| 602.945 | 600.969 | 1.976 | 119 | 143 |  |
| 609.855 | 606.644 | 3.211 | 121 | 145 | 13 |
| 616.77 | 612.304 | 4.466 | 123 | 147 |  |
|  | 617.954 |  |  | 149 |  |
| 623.485 | 623.609 | -0.124 | 125 | 151 |  |
| 630.12 | 629.274 | 0.846 | 127 | 153 |  |

| | | | | | | | | | | | |
|---|---|---|---|---|---|---|---|---|---|---|---|
| 156 | 130 | 2.661 | 640.465 | 637.804 | | 637.005 | 634.964 | 2.041 | 129 | 155 | |
| 158 | 132 | 3.891 | 647.365 | 643.474 | | 643.91 | 640.644 | 3.266 | 131 | 157 | 14 |
| 160 | | 5.091 | 654.215 | 649.124 | | 650.825 | 646.299 | 4.526 | 133 | 159 | |
| 162 | 134 | | | 654.774 | | | 651.949 | | | 161 | |
| 164 | 136 | 0.386 | 660.82 | 660.434 | | 657.525 | 657.604 | -0.079 | 135 | 163 | |
| 166 | 138 | 1.481 | 667.595 | 666.114 | | 664.17 | 663.274 | 0.896 | 137 | 165 | |
| 168 | 140 | 2.716 | 674.52 | 671.804 | | 671.06 | 668.959 | 2.101 | 139 | 167 | |
| 170 | 142 | 3.951 | 681.42 | 677.469 | | 677.965 | 674.639 | 3.326 | 141 | 169 | 15 |
| 172 | | 5.141 | 688.26 | 683.119 | | 684.88 | 680.294 | 4.586 | 143 | 171 | |
| 174 | 144 | | | 688.769 | | | 685.944 | | | 173 | |
| 176 | 146 | 0.436 | 694.865 | 694.429 | | 691.565 | 691.594 | -0.029 | 145 | 175 | |